Towards integration of optically active defects in silicon photonics

by

Adam DeAbreu

M.Sc., Simon Fraser University, 2018
B.Sc., Simon Fraser University, 2016

Thesis Submitted in Partial Fulfillment of the
Requirements for the Degree of
Doctor of Philosophy

in the
Department of Physics
Faculty of Science

SIMON FRASER UNIVERSITY
Spring 2024

Declaration of Committee

Name:	**Adam DeAbreu**
Degree:	**Doctor of Philosophy**
Thesis title:	**Towards integration of optically active defects in silicon photonics**
Committee:	**Chair:** John Bechhoefer Professor, Physics
	Stephanie Simmons Supervisor Associate Professor, Physics
	Michael Thewalt Committee Member Professor Emeritus, Physics
	Simon Watkins Committee Member Professor, Physics
	Erol Girt Examiner Professor, Physics
	Rogério de Sousa External Examiner Associate Professor, Physics and Astronomy University of Victoria

Abstract

Modular quantum architectures are an encouraging means of reaching the large scales necessary to unlock the potential of quantum technologies. Silicon-based spin-photon interfaces are a potent combination for a scalable, modular architecture as they combine the long lived memories of solid state qubits, the long range networking capabilities of photons, and the CMOS compatibility and integrated photonics of silicon. In this work we push forward the understanding of two promising spin-photon interface candidates based in silicon. Firstly, we study the properties of $^{77}Se^{+}$ in a $^{\mathrm{nat}}Si$ host material to measure the coherence properties and couplings to ^{29}Si spins. We identify clock transitions with coherence times more than an order of magnitude longer compared the coherence times measured off the clock transition. The $^{77}Se^{+}$ culminates in a presentation of a proposal to utilize a $^{77}Se^{+}$-^{29}Si pair system as a spin-photon interface. Secondly, we demonstrate further steps in the integration of the T centre into a silicon-on-insulator system by incorporating ensembles into waveguide devices. We measure sharp homogeneous linewidths for waveguide ensembles and find nearly lifetime-limited homogeneous linewidths in bulk silicon samples. In both environments the T centre's transitions are sufficiently coherent to predict the success of a remote entanglement procedures using currently available silicon photonic cavities. In summary, this work continues paving the path from a qubit candidate to an integrated qubit to a concrete technological solution for both the $^{77}Se^{+}$ and T centre spin-photon interfaces.

Keywords: spin-photon interface; silicon donors; silicon colour centres; quantum information; silicon photonics

For Camille

Acknowledgements

I would like to respectfully acknowledge that SFU is on unceded Coast Salish Territory; the traditional territories of the Musqueam, Squamish, and Tsleil-Waututh Nations.

Contributions to content: Many of the results in this thesis were only possible in part thanks to the hard work of my colleagues.

For the selenium work: I thank Kevin Morse and Rohan Abraham for all the selenium work, sample mounts, and Helmholtz coils that I adopted for this work. Eduard Sauter for coming to visit SQT and helping with the experiment and the faster lock-in measurement, hope you still have the coin in the sealed ampule. Laurent Bergeron for coding LabMaster enabling all of the pulsed experiments (I appreciate the Easter eggs too).

For the T-centre work (yes I can include the dash here, deal with it): I thank Camille Bowness and Daniel Higginbottom for laying out and fabricating the Ivysaur chip upon which all my waveguide measurements were made. Camille Chartrand and Evan MacQuarrie for creating the implantation and heat treatment recipe for the base material that Ivysaur was made from. Amir Alizadeh and Camille Chartrand for the hole burning on SOI. Nicholas Brunelle for building the Stable Laser System needed for the silicon-28 hole burning.

For all the work I thank everyone who contributed to the SUPER software package enabling the control of all the instruments (in the GUI UUDDLRLRB$_z$A$_x$ start, sorry Jame someone needs to know). As well as all the technicians, Kevin Morse, Nick Lee-Hone, Myles Ruether, for building sample mounts, experimental setups, and keeping things cool. Finally, everyone who reviewed papers, this thesis, and more.

And of course I extend a hearty thank you to my supervisors for their guidance, instruction, support, and expertise: Stephanie Simmons, Michael Thewalt, Daniel Higginbottom, and Simon Watkins.

Contributions to soul: Many of the results in this thesis were only possible thanks to the hard work of my friends, family, and colleagues in keeping me motivated, cheerful, and most importantly: sane. Thank you to everyone who made the SQT lab a fantastically fun and, at times, slightly unproductive place to work. Thank you to my parents for all the encouragement and for believing in me. And finally, to Camille Chartrand who had the hardest task of all: putting up with me while I finished this thesis, I thank you for your emotional and mental support.

Finally, to you dear reader, I hope that after all this work, you find something useful or learn something new.

Table of Contents

List of Tables

List of Figures

Symbols

T_1	Population lifetime
T_2	Homogeneous coherence lifetime
T_2^*	Inhomogeneous coherence lifetime
η_{zpl}	Debye-Waller factor or zero-phonon line efficiency
η_{rad}	Radiative efficiency or quantum efficiency
Γ_{ih}	Inhomogeneous linewidth
Γ_{SD}	Long term spectral diffusion limited linewidth
Γ_{hom}	Instantaneous homogeneous linewidth
Γ_{exc}	Lifetime limited linewidth
Γ_{PD}	Pure dephasing linewidth
τ_{exc}	Excited state lifetime
σ_x	Pauli X matrix
σ_y	Pauli Y matrix
σ_z	Pauli Z matrix
$\vec{S}$	Vector of Pauli matrices acting on an electron spin
$\vec{I}$	Vector of Pauli matrices acting on a nuclear spin
B_0	Static magnetic field
B_1	Oscillating magnetic field
ω_I	Larmour frequency of nuclear spin
$\mathbf{A}$	Hyperfine tensor
$\mathbf{T}$	Dipolar interaction tensor
T	Dipolar interaction constant
a_{iso}	Isotropic Fermi contact hyperfine constant
m	Magnetic quantum number
S_0	Singlet state of a hyperfine singlet-triplet system
T_0	m$\approx$0 triplet state of a hyperfine singlet-triplet system
$\mathrm{T}_\pm$	m$\approx \pm 1$ triplet states of a hyperfine singlet-triplet system
$\mathrm{T}_0^\pm$	T_0 triplet states of an isotropic hyperfine singlet-triplet system split by an additional anisotropic hyperfine interaction
TX_0	Excitonic ground state of the T centre

TX_1	First excitonic excited state of the T centre
F_P	Purcell factor
V	Visibility
$\|\Psi^{\pm}\rangle$	Odd-parity Bell states
$\mathcal{F}$	Fidelity
R_{bath}	Radius of the bath of a CCE simulation
R_{cluster}	Radius of clusters of a CCE simulation
τ	Wait time between pulses in a Hahn-echo measurement

Chapter 1

Introduction

In this thesis, I characterize two potential candidates for the building block of future quantum computation and quantum communication technologies. This introduction chapter presents the what and why of looking for a quantum technology in the first place. Next the desired requirements for a quantum technology candidate will be outlined, concluding with a brief introduction to the candidates in question: singly-ionized selenium-77 and the T centre, two spin-photon interfaces based in silicon.

Following this introduction, Chapter 2 will discuss in detail the background theory necessary to understand the experimental work and subsequent analysis. The experimental setups and methodologies will be laid out in Chapter 3. We will discuss the models used in the results and discussions in Chapter 4. Finally, we will present the results and discussion of the $^{77}Se^{+}$ and the T centre in Chapters 5 and 6 before presenting concluding remarks in Chapter 7.

1.1 Quantum information technology

What does it mean for a system to be quantum rather than classical? Two key aspects are superposition and entanglement. Superposition allows a system to be in a linear combination of multiple states at the same time. While classical systems can be in a probabilistic combination of multiple states a superposition is a distinct phenomenon which includes a possible phase between the states — a pure quantum effect. This provides two additional degrees of freedom when describing a quantum system as opposed to a classical system. Entanglement is a phenomenon wherein two or more systems are correlated in a manner than exceeds classical correlation. An entangled state displays correlation in multiple orthogonal measurement bases such that the individual systems cannot be fully described in isolation. One of the ramifications of these additional degrees of freedom is that the number of possible configurations of a quantum system scales up very fast when more systems (e.g. more two-level systems) are added. A quantum system of just 300 two-level systems would have more states than particles in the universe [1, 2]. Any simulation of these particles would require tracking all of these states.

Two things become clear: 1) a classical computer cannot efficiently simulate large quantum systems due to the incommensurate scaling and 2) a quantum system can explore a vastly larger state-space for equal resources compared to a classical computer. The first point motivates the idea proposed by Feynman [3]: if a classical computer cannot simulate quantum systems, then use a quantum computer to simulate quantum systems. Potential simulations include novel phases of matter [4], chemical/drug simulation and synthesis [5, 6] and process engineering for more efficient nitrogen fixation [7]. But quantum computers can do even more; the second point motivates the idea to apply quantum computers to solve problems that are much more general than simulating quantum systems.

By creating a computer that uses quantum bits, qubits, rather than classical bits, the uniquely quantum properties can be harnessed for unique algorithms that can solve problems in novel ways. These algorithms scale more favourably than classical equivalents and unlock problems that would otherwise be intractable on a classical computer [8]. Examples include prime factoring [9], database searching [10], optimization [11, 12], and machine learning [13]. Importantly, to perform these algorithms a quantum computer requires a sufficient set of operations that can be performed on one or more qubits. Much like how a classical computer can build up more complicated algorithms from a small set of basic logical operations like AND, OR, and NOT, a quantum computer must be able to perform a sufficient set of basic gates to be deemed universal and capable of running any given algorithm [14]. An example of a universal gate set is the Hadamard (a single qubit operation) and the Toffoli gate (a three qubit operation) [15].

Another application of quantum information is quantum communication. In this field quantum properties are used to provide secure communication channels by leveraging the strong correlations provided by entanglement [16–18]. In one possible implementation, called quantum key distribution (QKD), this is achieved by sharing entangled particles across a quantum channel resulting in two participants sharing a system that is correlated in multiple orthogonal bases [19]. This allows a bit string to be shared by measuring the entangled particles in randomly selected bases, comparing measurement bases, and using the known correlation when the bases of the two participants match. This bit string can then be used as a single-use key guaranteeing the classical encrypted message is indecipherable to any eavesdropper on the classical channel [18]. This bit string can be proven to be private [20] as any eavesdropper measuring the entangled particles before the recipients will collapse the state, thus destroying the entanglement, and creating a signature that betrays the eavesdropper's presence to the recipients. Furthermore, an eavesdropper cannot copy the shared states to measure later due to the no-cloning theorem [21, 22]. The result is a communication channel which is provably secure by the laws of quantum mechanics.

In summary, the fields of quantum computing and quantum communication promise very exciting technological applications for quantum systems. The translation from academic work to industry application is still in early stages: small scale demonstrations of quantum computers with 10s to 100s of qubits [23, 24] and quantum key distribution modules are available to purchase [25, 26] and use over the cloud. Demonstrations, both in universities and in companies, are built on a huge range

of physical platforms. From superconductors [27] to trapped ions [28] to photons [29] to quantum dots [30], many different avenues are being pursued and studied. With such a wealth of possible platforms it is important to consider what properties a quantum technology would have in the ideal case.

1.2 The dream of scalability

At the time of writing, the record for most qubits in a universal quantum computer is 433 superconducting qubits on the IBM Osprey quantum processor [31]. Many more commercial ventures have qubit numbers in the 10s-100s of qubits including QuEra (256 trapped atoms [32]), Google (53 superconducting qubits [33]), and Quantinuum (32 charge coupled device (CCD) trapped ions [34]) with varying degrees of connectivity, gate fidelities, and applications. In contrast, a CPU contains more than a billion classical bits [35]. For some applications, quantum computers need to be operating at the same scale as classical computers. For example: by one estimate of the number of qubits needed [36], Shor's algorithm for prime factoring on a 2000 bit input would require ≈ 60 million physical qubits. Clearly there is a large divide between current technologies and the lofty goals of quantum computing. This begs the question: what is impeding quantum processors from scaling to these numbers?

One key challenge is size constraints, which may appear differently depending on the system. Two examples are as follows: a superconducting system has qubits that require a relatively large footprint (100–1000 μm scale [37]) and which require many control lines, all of which have to be cooled to milliKelvin temperatures. A limitation becomes how many qubits and control lines can be put on a chip and how many control lines can be thermalized in a cryogenic fridge while keeping high device yields and low crosstalk [38]. Ions in optical traps on the other hand can be operated without a cryostat (although they require high vacuums) but are limited by how many atoms can be put in a trap before performance is hindered [39].

One possibility to remedy this issue is *modularity*. Many architectures being considered are employing smaller processors with interconnects to build up to a much larger processor [40–43]. The natural method of mediating these interconnects (as noted in the DiVincenzo criteria [44]) is by using photons. Photons are ideal for interconnects as they are fast, easily controllable, and, other than attenuation/dispersion in a material, do not decohere. While many systems can couple to photons, few do so at energies in the telecommunication band, the most suitable band for interconnects. Superconducting qubits can be coupled via microwave photons, however, for distances beyond on-chip coupling, extensive, impractical, cryogenic microwave links are required [45]. Thus, many research groups are investigating transduction to convert from the energy scale of a qubit to the energy scale of a suitable photon for the interconnect [41]. While an active research topic, no scalable microwave to optical transducer has been demonstrated [46].

Transduction is also an exciting research direction for quantum communication. Quantum key distribution is limited by photon loss over long distances [47]. One method to circumvent this is

to use quantum repeaters wherein entanglement can be set up piece-wise between repeater stations which can be converted to end-to-end entanglement via entanglement swapping [19, 48]. These repeaters often require a stationary physical qubit to act as a memory qubit during this entanglement generation and swapping procedure. Thus, transduction from an appropriate photonic flying qubit to wavelengths suitable for a stationary quantum memory is also of great interest to quantum communication applications.

An alternative to transduction is to use a system that is a combination of both a long-lived quantum memory and a photonic link directly at wavelengths suitable for interconnects. This class of defects, known as spin-photon interfaces, is an exciting system for a modular architecture as it removes the requirement for transduction. A solid-state spin-photon interface would have the benefit of networking and modularity along with a long-lived stationary qubit that can be engineered and fabricated at scale all without a need for transduction.

1.3 Spin-photon interface

As stated, a spin-photon interface combines both a long-lived solid-state spin and a photonic degree of freedom suitable for a network compatible modular system. Across a wide variety of qubit candidates this is achieved by having spin-dependent optical transitions which can be used to create entanglement between the spin and the photon. We will discuss spin-photon interfaces in more depth in Section 2.4, here we will give some details on what properties are important for a spin-photon interface.

For starters, the ground state manifold of the system must be able to host a long-lived qubit, i.e., the spin. The coherence time of the spin must be long compared to the travel time of the photonic link used to generate the long range interactions. General details of a spin systems are provided in Section 2.3.

Secondly, the optical transition must be sufficiently coherent and sufficiently efficient, where the specifics of 'sufficient' are based on the entanglement procedure and the rates needed for the networked quantum computer. For a coherent transition, the spectral linewidth of the optical emission needs to be narrow: as close as possible to the lifetime-limited linewidth. Furthermore, the emission is ideally efficient with the majority of decays from the excited state occurring with the emission of a resonant photon, i.e., a high Debye-Waller factor and a high radiative efficiency. A 'strong' transition is also a desirable trait; a high transition dipole moment means a high interaction strength with light. General details of optical properties are provided in Section 2.2. The light-matter interactions of a spin-photon interface can be further enhance by incorporating them into optical cavities – a key component of many entanglement procedures (see Section 2.4 for more details).

For technological applications these spin and optical properties must be well studied for a robust understanding upon which engineering processes can be made. However, in many instances the exact sample in which a qubit is studied can change the properties due to isotopic and chemical purity or defects in the material. From measurements in bulk isotopically/chemically purified material, to

commercially available material, to integrated photonic devices, the properties must be mapped out at each step. The work of this thesis is the study of two candidate spin-photon interfaces at different steps along this pathway.

Solid-state spin-photon interfaces exist in a wide variety of solid-state systems. Some notable examples of solid-state spin-photon interfaces are the nitrogen-vacancy centre in diamond [49], defects in silicon-carbide [50], and rare-earth ions in crystalline hosts (e.g. Yb:YVO_4 [51], Nd:YSO [52], Er:Si [53]). The state of the art of these spin-photon interfaces is presented in Section 2.5.1. The choice of material for a quantum technology is key. Even with the modularity provided by a spin-photon interface, working with a platform that can produce the individual modular components at scale is crucial to achieve the numbers of qubits necessary for practical quantum information applications. This leads to the conclusion that a spin-photon interface in a scalable medium would be an excellent candidate to achieve quantum technologies at sufficient scales for practical applications.

1.4 Enter silicon

Classical processors are based on silicon which the global complementary metal-oxide semiconductor (CMOS) industry has forged into the defacto scalable platform through decades of research and engineering [35, 54]. A qubit native to silicon would have a huge leg up in the scaling arms race compared to other host materials. The yield and uniformity achievable in an industrial silicon foundry are unmatched. The integration of quantum systems into the foundry process has been shown to produce exceptional results as seen in the comparison of quantum dots made in academic cleanrooms and Intel's foundries [55].

Furthermore, silicon photonics is an excellent platform for the photons needed for modularity [56]. The high refractive index of silicon along with the properties of the readily-formed silicon dioxide allow for the production of high purity and highly uniform silicon-on-insulator (SOI) wafers with a thin device layer above an oxide layer atop a silicon handle. On this platform there are large libraries of low loss photonic devices, including waveguides [57], grating couplers [58], switches [59], and, crucially, optical cavities [60, 61]. Even superconducting nanowire single photon detectors can be integrated with silicon photonics [62]. For control of photonic qubits at scale, silicon photonics is a very promising platform.

Due to the many appealing aspects of silicon there are proposals to heterogeneously combine qubit systems in other host materials with silicon photonics including Er^{3+}:YSO [63] and InP/InAs quantum dots [64] evanescently coupled to cavities and waveguides. However, the renewed interest in silicon defects as spin-photon interfaces may preclude the need for these heterogeneous approaches altogether. Spin qubits in silicon such as single donors and single acceptors have been shown to possess long coherence times in their ground states [65, 66] with phosphorus breaking the world record for coherence times: 39 minutes at room temperature [67].

All these promising features of silicon outline a clear research direction: investigate spin-photon interfaces native to silicon. This has been the research direction of the Silicon Quantum Technolo-

gies (SQT) group [68] at Simon Fraser University and this is the overarching goal of this thesis work, with specific focus on the application and integration of identified spin-photon interfaces into a quantum computing architecture.

The two spin-photon interfaces identified by the SQT group and further studied in this work are the singly-ionized selenium double donor system [69] and the radiation damage T centre [70], both of which will be discussed in the following sections. Prior to this work, these centres were studied in bulk isotopically purified ^{28}Si, a so called 'semiconductor vacuum', named for the absence of interactions with spin-1/2 ^{29}Si in the crystal lattice. This purification provides two key benefits: optical linewidths much narrower than those in natural silicon due to reduced inhomogeneous broadening, and longer spin coherence times due to the absence of the nuclear spin of ^{29}Si. By working with this medium, the fundamental spin-photon interface properties can be determined by exploiting the purified environment.

While excellent for research, bulk ^{28}Si samples are not ideal for a technological application. In most implementations, the control of individual qubits and the measurement of individual photons are necessary, thus requiring single centres. These single centres must be incorporated into an integrated platform — a silicon-on-insulator platform, as described above, suitable for silicon photonics. Furthermore, the isotopic purification process is not trivial, nor are ^{28}Si SOI wafers commercially available [71]. Thus, we can consider a research pipeline towards a quantum technology starting with studies in bulk ^{28}Si samples, with the next steps going to a natural silicon environment: firstly, as a bulk sample; and secondly, as an SOI sample. The main research goals at these different steps are to understand how the different environments affect the spin-photon interfaces, both the optical transitions and the ground state structure. How can the control of these systems be optimized in the new environments? What detrimental effects are incurred by moving from ^{28}Si to a more practical, if less isotopically pure, environment? In this work, we study selenium in a bulk natural silicon sample and the T centre in an SOI platform. We work to study the applicable spin-photon properties of both centres in these new environments.

1.5 Selenium

Selenium incorporated into a substitutional site in silicon forms a double donor and, in the singly-ionized state, is a spin-photon interface. In the Se^+ charge state the remaining electron has a large binding energy which results in a hydrogenic level structure possessing bound-to-bound transitions [72]. While single acceptors/donors such as boron and phosphorus have weak bound exciton transitions [73] the chalcogen double donors possess stronger bound-to-bound transitions [69]. Furthermore, the decay was expected to have a high radiative efficiency as no phononic decays were detected [69, 74]. In the ground state the remaining electron and nuclear spins result in spin-dependent optically accessible transitions. The large binding energy results in optical transitions in the mid-infrared band: 427.3 meV (2901 nm). While not in the industry standard telecommunication bands,

the mid-infrared is not without its own extensive development [75] and importantly, mid-infrared is compatible with silicon photonics [76].

This combination garnered initial interest in the system for quantum information applications [69]. Optical control of the ground state spin manifold for initialization and readout allowed measurement of the long coherence times of the ground state spin, $T_2 = 2.14 \pm 0.04$ s, at low magnetic fields in ^{28}Si [69]. The optical properties were also measured, and a strong transition dipole moment of 1.98 ± 0.08 Debye was found. Further work measured a zero phonon line (ZPL) emission efficiency of 16 ± 1 % and a total radiative efficiency of 0.80 ± 0.09 % [77]. The low radiative efficiency limits the applications of the Se^+ centre, however, the high transition dipole moment is suitable for a cavity implementation in the strong-coupling regime [78] (see Section 2.4.3 for more details).

Thus, the next steps for the Se^+ spin-photon interface are to incorporate it into integrated silicon photonics. While much work was performed by this author on the implantation and diffusion of selenium into SOI samples, along with the design and fabrication of mid-infrared silicon photonics, this will not be the focus of this thesis. Here we focus on the intermediate step along the pipeline of studying the selenium centre in a bulk natural silicon sample. Coherence properties of the ground state manifold have only been studied in a ^{28}Si environment, here we work to determine the ground state structure, the coupling to ^{29}Si atoms, and the coherence times of the newly accessible transitions. Furthermore, we investigate the ^{29}Si atoms in the lattice as a possible additional quantum memory. We study these questions and more with a hole burning readout scheme for optical detected magnetic resonance (ODMR) (Sections 2.2.2 and 5.2) and pulsed ODMR (Sections 2.2.2 and 5.2). This work culminates in a theoretical discussion/proposal of a novel implementation scheme for the fabrication of selenium coupled to nanophotonic cavities for a quantum computing architecture (Section 5.4).

1.6 T centre

The T centre is a spin-photon interface in silicon that has recently been re-discovered as a possible qubit candidate [70]. The T centre is a multi-particle defect [79], named not for its chemical composition, but as part of an alphabetical catalogue of, at the time, unknown defects formed in silicon after radiation damage and heat treatment [80]. These 'radiation damage centres' have been known for many decades; however, their application in quantum information was only suggested recently [70]. Defect centres, such as the G centre [81] and W centre [82], have been integrated into silicon photonics [83–85] and look promising as single photon emitters. However, these centres, along with the C centre, were shown to have no available ground state spin to act as a quantum memory [86]. The T centre, on the other hand, does have a ground state spin and was shown to have spin-dependent bound excitonic transitions with favourable properties in ^{28}Si [70].

The T centre is composed of two carbon and one hydrogen atoms occupying a silicon substitutional site. In the ground state there remains a bound, unpaired, electron that was shown to have a long coherence time in ^{28}Si, 2.1 ± 0.1 ms. The hydrogen also possesses a nuclear spin measured

to have a 1.1 ± 2 s coherence time. The T centre bound exciton transition has a zero-phonon line at 935 meV (1326 nm), in the telecommunication O-band – an ideal wavelength for long-range networking. Initial measurements by Bergeron et al. [70] determined an excited state lifetime of 0.940 μs and a Debye-Waller factor of 23 ± 1 %. Measurements showed no signature of Auger recombination indicating the T centre potentially had a high radiative efficiency compared to other bound exciton transitions. Optical linewidths were determined to be narrow, < 30 MHz, in ^{28}Si, however, this was limited by inhomogeneous broadening. Following work investigated the T centre integrated into SOI wafers [87] and, subsequently, in silicon photonic devices suitable for a confocal study that identified single T centres [88] — the first all-optical measurement of isolated single spins in silicon. In these later works spectral diffusion was shown to limit the linewidths to at best 600 MHz.

Compared to selenium, the T centre is further along the technological implementation pipeline with SOI samples and silicon photonic devices already having been achieved. However, the devices studied thus far, while suitable for a confocal study, are not suitable for an integrated quantum computing technology. This thesis outlines work to integrate the T centres into a network-compatible integrated device: T centres integrated into SOI waveguides. In particular, we investigate the yet unknown optical coherence of the T centre emission in both an integrated environment (Section 6.3.1) and compare with optical coherence in a bulk ^{28}Si environment which is also measured for the first time in this work (Section 6.3.2). In both cases we determine the achievable entanglement fidelities of two T centres along with cavity parameters necessary to reach key benchmarks (Section 6.5). Finally, we demonstrate for the first time the spin control of waveguide-integrated T centres and measure a T_1 population lifetime (Section 6.4).

Chapter 2

Background Theory

Here we will lay out the relevant background theory necessary to understand the experimental results and analysis in following sections. We will begin with a discussion of optical processes and include a description of experimental methods to obtain optical spectra. We will then examine the physics of optical processes modelled as two- and three- level systems. This will lead into a discussion of magnetic resonance and phenomena present in solid-state spin systems.

From this general discussion we will then move to more specific background theory on spin-photon interfaces including cavity coupling for entanglement generation. Finally, we will present a literature review of prominent spin-photon interfaces before a discussion of the specific spin-photon interfaces studied in this work: the selenium double donor in silicon and the T centre silicon radiation damage centre.

2.1 Silicon as an optical medium

Silicon is a semiconductor with an indirect bandgap of 1.17 eV at 4.2 K [89] with a diamond cubic crystal lattice. A substitutional site in silicon will have four nearest neighbours and thus four bonds. The introduction of substitutional defects with more or less valence electrons results in defects with donor or acceptor levels within the bandgap. While the electronic properties of some of these defects have been thoroughly studied and used to great effect in electronic devices such as transistors, some defects also exhibit useful optical properties in addition to their electrical properties. Two main optical processes can occur at defects in the silicon matrix: 1, bound-to-bound transitions; and 2, excitonic transitions.

As an example of bound-to-bound transitions, consider phosphorus: in a substitutional site it will have four electrons bound to the nearest neighbours with one additional unpaired electron. At low temperatures this unpaired electron is Coulomb-bound to the nucleus and will have, between the lowest energy bound state and the ionized state (1s and the CB continuum in Fig. 2.1a), a collection of excited states not unlike a hydrogen atom in a vacuum [90] (2s, 2p, 3s, ... in Fig. 2.1a). Transitions between the ground state and these higher excited states may be driven by the absorption or emission of a photon with equal energy to the transition. These transitions are known as bound-

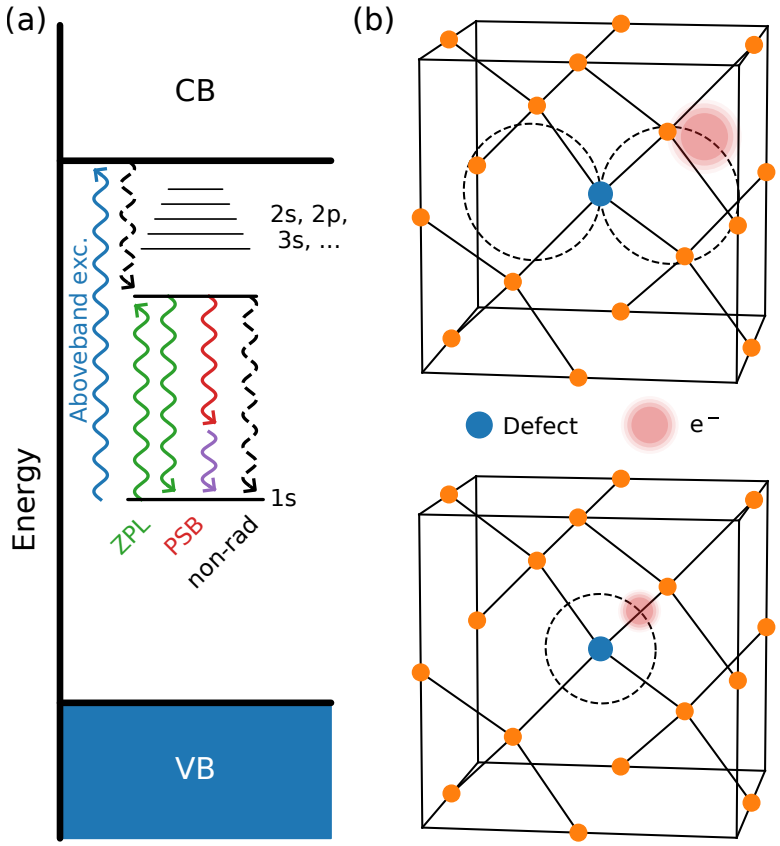

Figure 2.1: **Bound-to-bound transitions.** (a) A donor defect in silicon has a ground state within the bandgap and higher excited states up to the conduction band (exact energies not to scale). Possible radiative and non-radiative transitions can occur between the ground and first excited state including zero phonon line (ZPL) and phonon sideband (PSB) transitions. (b) A donor defect with a bound electron in the ground state (lower) and in a bound excited state (upper).

to-bound transitions as the electron remains bound in both initial and final state. An example of this is shown in Fig. 2.1.

A defect with three valence electrons will have a bound hole when in a substitutional lattice site and will have an analogous excited state spectrum to a donor. However, in this case the excited states will extend to lower energy towards the valence band. Boron is an example of such an acceptor-like defect.

While phosphorus was used as an example of a bound-to-bound transition, the transition energies are very small. This is due to the fact that the donor level of phosphorus is very close to the conduction band with only a $\sim$ 45 meV binding energy [90, 91]. To excite the donor bound electron to the conduction band is to ionize the defect – the hydrogenic spectrum of phosphorus is compressed to this small energy difference. This makes manipulating the states technically troublesome, with transitions in the 1–10 THz range, unsuitable for optical lasers. Donor, or acceptor, levels further from the band edge will have energy level spectra extending across the difference and

may have transitions with energies in the optical range allowing for more straightforward driving with more accessible laser systems.

Phosphorus and boron defects can also support the second type of optical process, a defect bound exciton transition. In silicon, excitons — electron-hole pairs bound by their Coulombic interaction — can be created in the lattice through e.g. electric injection of electrons and holes or optical excitation of valence electrons to the conduction band. These 'free excitons' are mobile quasiparticles which propagate through the silicon lattice and can bind to defects [92, 93]. These defect bound excitons will have a recombination energy lower than the silicon bandgap as the exciton has a lower energy when bound; the more tightly bound the exciton, the lower the recombination energy. Additionally, these bound excitons can be generated resonantly through optical excitation of a defect. An illustrative example is shown in Fig. 2.2a. Just as a bound electron or bound hole can possess excited states so too can a bound exciton. If the hole of a bound exciton is more tightly bound with a loosely bound electron, the electron will display an array of excited states between the bound exciton ground state and the energy needed to ionize the electron. A schematic of these higher excited states is shown in Fig. 2.2a. This is also true if the hole of the exciton is more loosely bound in the same manner.

In both bound-to-bound and excitonic transitions in silicon an array of radiative and non-radiative transitions can occur, this is shown schematically in Fig. 2.1a and Fig. 2.2a. Firstly, a system can absorb a resonant photon driving from the ground to the excited state. The strength of this transition is determined by the transition dipole moment of the transition [94]. From the excited state, the system can decay to the ground state and release either a single resonant photon or a lower energy photon along with one or more phonons or localized vibrational modes (LVM) of the defect to conserve energy/momentum. The single photon process is known as zero phonon line (ZPL) emission whereas the multi-particle emission is known as phonon sideband (PSB) emission as emitted photons are in a band to lower energies. The ratio of ZPL to all radiative emission is known as the Debye-Waller factor, or simply ZPL fraction, η_{zpl}.

In addition to radiative processes, there are also non-radiative processes. Either fully phononic, through a meta-stable state, or via an intersystem crossing (a transition from a singlet to triplet excited state configuration, e.g. as in NV centre [95]). For donors/acceptors Auger recombination [96] is another dark decay mechanism wherein the energy/momentum of the exciton recombination is transferred to the bound electron/hole, ionizing the defect. Regardless of the mechanism, these transitions are dark and emit no light. The fraction of decays that occur radiatively is known as the radiative efficiency, η_{rad}, or the quantum efficiency.

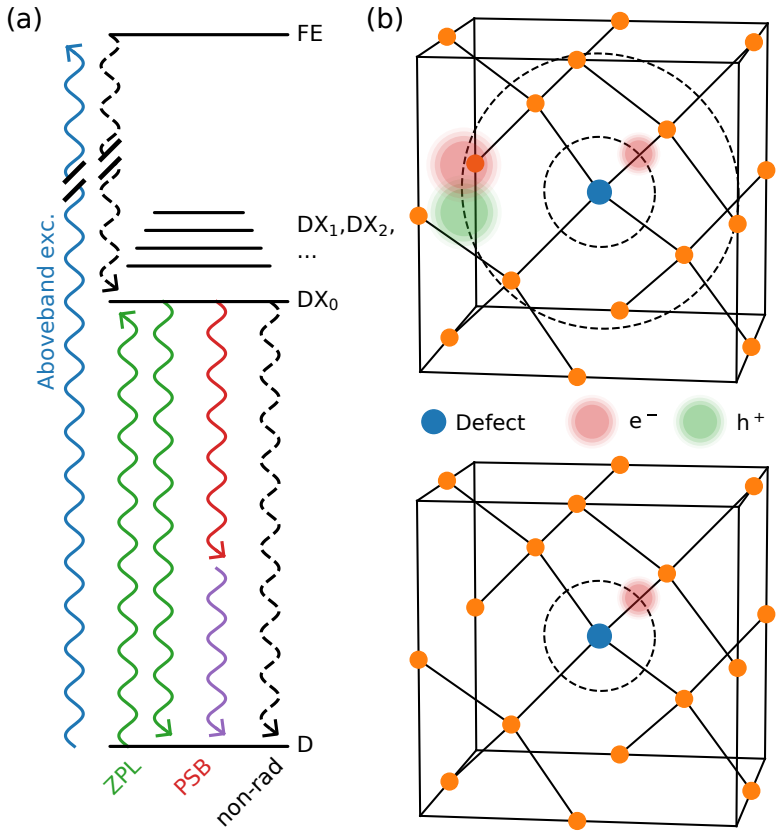

Figure 2.2: **Excitonic transitions.** (a) A defect (D) with a bound exciton state (DX_0) which is lower energy than a free exciton (FE). A variety of radiative and non-radiative transitions occur between the excitonic ground state and the defect ground state. Bound exciton excited states (DX_1, DX_2, ..) can also exist above DX_0. (b) A donor defect with a bound electron in the ground state (lower) with a bound exciton (upper).

2.2 Optical processes

In this section we will discuss, in a general sense, some of the properties of solid-state emitters. This discussion will be kept general starting from a description of broadening effects present in the spectrum of solid-state emitters and then moving onto a few key results of two- and three-level systems.

2.2.1 Linewidths

An ensemble of defects probed simultaneously in a sample will give a spectrum that is the sum of the spectra of the individual defects. As no sample and no experiment is ideal these individual spectra will have a range of energies due to differences in the local environment, be it local defects or strain [97], local isotopic composition of the lattice [86, 98, 99], or more. The resulting ensemble spectrum is characterized by the inhomogenous linewidth, Γ_{ih} as it is limited by the inhomogeneities within the sample.

In the case of a spectrum of a single defect, the same discussion as above can be considered but in the time domain rather than the spatial domain. As the local environment may vary across a sample so too can the local environment vary in time due to, for example, fluctuating charges on local traps known as charge noise [100, 101]. A spectrum will take a finite amount of time to measure and thus will be an average of the spectra of a time ensemble of the defect. This is known as spectral diffusion [102]. As spectral diffusion is a time dependent effect, any measurement of the spectral diffusion limited linewidth, Γ_{SD}, must consider the timescale of the measurement.

If then a spectrum of a single defect were to be measured 'instantaneously' (i.e. fast compared to the dynamics of the system) the linewidth would be the homogeneous linewidth, Γ_{hom}. This linewidth is the sum of two contributions: the lifetime-limited linewidth and pure dephasing linewidth. The lifetime-limited linewidth is the ultimate linewidth possible for an emitter imposed by the uncertainty principle. The emitter will spend τ_{exc} in the excited state and thus the energy-time uncertainty principle imposes a minimum linewidth of $1/(2\pi\tau_{\mathrm{exc}})$ [91]. This is also known the Fourier-transform limited linewidth as the optical spectrum will be the Lorentzian given by the Fourier-transform of the exponential lifetime decay.

In a realistic sample and environment the linewidth measured is generally larger than the lifetime limited linewidth. The remaining broadening is encompassed by the pure dephasing linewidth, Γ_{PD}, which is a measure of the dephasing experienced during the lifetime of the excited state [102, 103]. This is a measure of how coherent the transitions is — how phase stable — and is an important property for entanglement generation (coherence and decoherence are discussed in Sections 2.3.1 and 2.3.2 and entanglement generation is discussed in Section 2.4). The pure dephasing linewidth may be due to e.g. temperature effects cycling to higher excited states [70, 86]. Another possibility is fast spectral diffusion processes occurring within the timescale of the excited state lifetime, the energy shifts induced are indistinguishable from a dephasing effect.

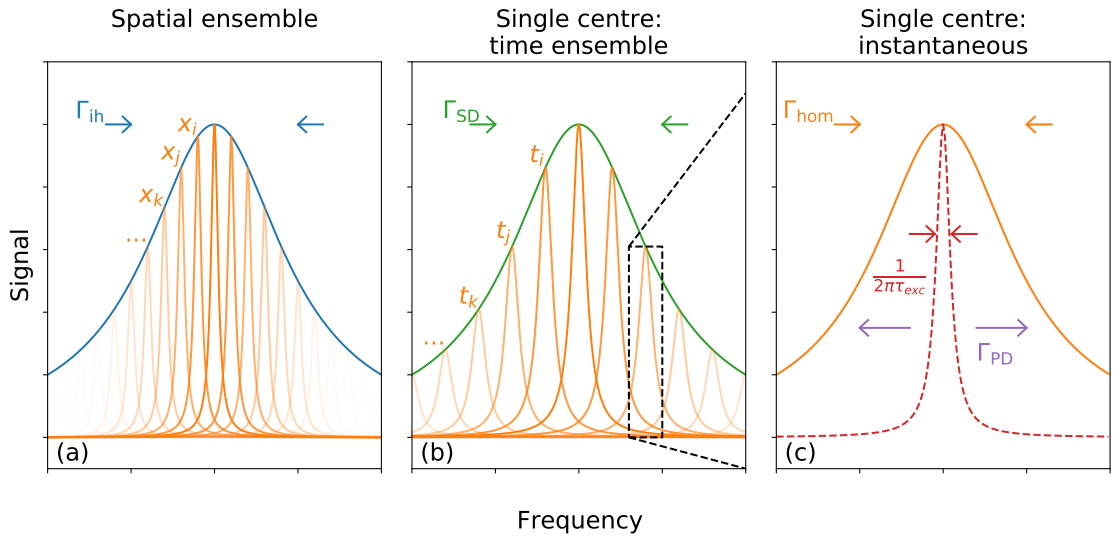

Figure 2.3: **Summary of linewidths.** (a) An ensemble of defects with an inhomogeneous linewidth, Γ_{ih}, composed of defects in different local environments, x_i. (b) a single defect will have a spectral diffusion linewidth, Γ_{SD}, composed of the defect at different times, t_i, due to a fluctuating local environment. (c) A single defect at a single time will have a homogeneous linewidth, Γ_{hom}, that is larger than the lifetime linewidth, $1/2\pi\tau_{\mathrm{exc}}$, by the pure dephasing linewidth, Γ_{PD}.

All these linewidths are summarized in Fig. 2.3. For technological applications, lower linewidths are better. A lower homogeneous linewidth is key for a coherent transition and is necessary for some entanglement generation schemes (see Section 2.4.2). A lower inhomogeneous linewidth, both spatially and temporally (i.e. SD), is beneficial for spin-photon interfaces to have the same optical properties across the many copies in a quantum technology and at all times. In the study of luminescent defects in solid state materials an understanding of all of these linewidths is necessary for the engineering of quantum information technologies that can make use of the transition of interest.

2.2.2 Saturation and hole burning

With these linewidths defined we can now model the optical dynamics of simplified systems that incorporate a subset of these broadening mechanisms. The following effects are all at the timescale of the excited state lifetime and so we can ignore effects of spectral diffusion that is slow compared to these timescales. We will consider only inhomogeneous and homogeneous linewidths in addition to the lifetime-limited linewidth.

We start our discussion with a two level system with ground state level 1 and excited state 2 (see Fig. 2.4a). In the absence of any drive on the system, there are only two rates: ω_{21} the spontaneous decay rate from level 2 to 1; and ω_{12} the spontaneous excitation rate from level 1 to 2. The spontaneous decay rate, ω_{21} is simply the inverse of the excited state lifetime. These two rates

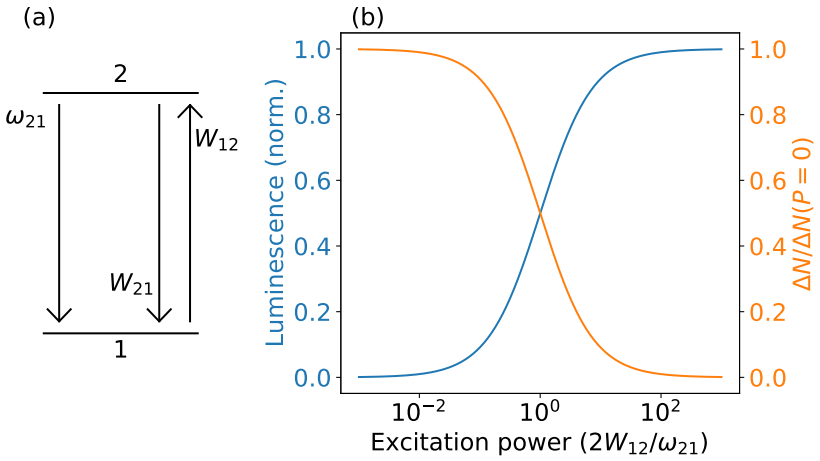

Figure 2.4: **Saturation effects of a two level system.** (a) the rates involved in a two-level system, spontaneous emission rate, ω_{ij}, and driving terms, W_{ij}. (b) Luminescence intensity and population difference versus excitation power. Saturation is defined as the point when the population difference is half of the low power population difference.

are related by the Boltzmann relation as [104]

$$\frac{\omega_{12}}{\omega_{21}} = \frac{d_2}{d_1} e^{-(E_2-E_1)/kT}. \tag{2.1}$$

Where d_i and E_i are the degeneracy and energy of level i, k is the Boltzmann constant, and T is the temperature of the system.

The systems we study in this work — optically active defects in silicon — have transitions that can be split into two regimes, infrared optical transitions and microwave transitions, corresponding to the wavelengths of light necessary to drive the transitions. In both cases, we study these systems at very low temperatures, < 4 K. In the optical regime, the energy difference between the levels are much larger than the thermal energy and thus ω_{12} can be set to zero. In the microwave regime the energy level differences are comparable to the thermal energy and thus, both rates must be considered. For the remainder of this section we will be considering only optical transitions, microwave transitions will be discussed in Section 2.3.

Resonant driving can be modelled with a driving term W_{ij} between levels i and j. This will drive stimulated transition, both upward and downward, with the two rates related as: $d_i W_{ij} = d_j W_{ji}$. All these rates are shown in Fig. 2.4a. Figure 2.4b shows the key features of the two level system as the excitation power, W_{12}, increases. First the emission from this system increases with increasing power where the emission is proportional to the population in level 2, N_2. The photons emitted per second will be $N_2 \omega_{21} \eta_{rad}$ where η_{rad} is the radiative efficiency, the fraction of decays from level 2 to level 1 that emit a photon. In practice the intensity will be scaled by experimental factors such as loss or detector efficiency, however, in all cases the emission will be proportional to N_2.

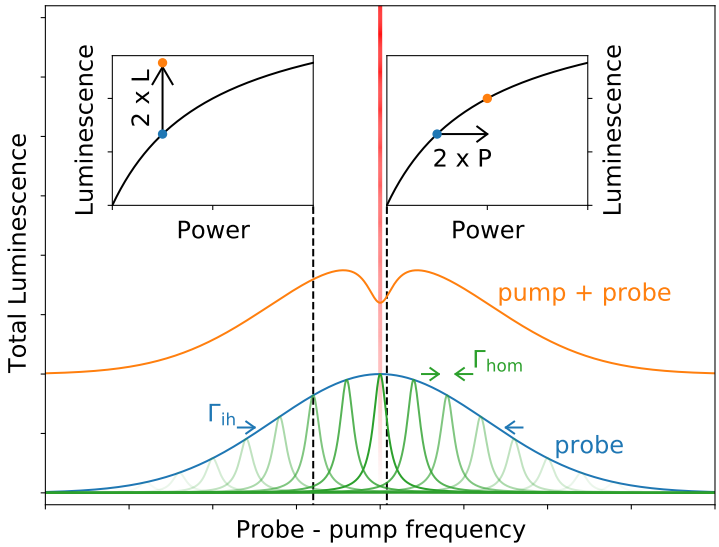

Figure 2.5: **Saturation hole burning.** One and two laser scans of an ensemble of inhomogeneously broadened defects. Individual sub-ensembles are denoted in green. When driven with a pump laser (red) and scanned with a probe laser a spectral hole appears due to saturation effects. (Left inset) When pump and probe are detuned more than Γ_{hom} the total luminescence (L) is the sum of the luminescence from the individual sub-ensembles. (Right inset) When pump and probe are detuned less than Γ_{hom} they both excite the same sub-ensemble which has a luminescence limited by the saturation curve to the luminescence at twice the power (P).

Figure 2.4b shows that the emission intensity initially increases with excitation but eventually the intensity begins to saturate. This can also be seen in the difference in population between the two levels, $\Delta N = N_1 - N_2$, as a function of power. At large power the population tends towards an even distribution between the two levels, increasing power beyond this does not increase N_2 as the drive is equally driving population down to level 1. This is used to define the saturation power, P_{sat}, as the power at which the population difference is half of the low power population difference. In terms of rates the saturation power is when $W_{12} = \omega_{21}/2$.

In practice this can be determined from the emission intensity, I, versus excitation power, P, as [104]

$$I = I_0 \frac{1}{1 + P_{\text{sat}}/P} \tag{2.2}$$

where I_0 is simply a constant.

We can now discuss a very important spectroscopic technique that will be employed repeatedly through this thesis: hole burning [104]. This two-laser technique is shown schematically in Fig. 2.5. A pump laser is tuned to the peak of an inhomogeneously broadened spectrum of an ensemble of defects, a second laser is then swept about this central pump frequency. When the two lasers are far detuned, much larger than Γ_{hom}, the lasers probe different sub-ensembles and the total luminescence

from the system is the sum of the luminescence from each sub-ensemble, see Fig. 2.5 left inset. However, when the detuning between lasers becomes comparable to the homogeneous linewidth the two lasers begin to drive the same sub-ensemble. As explained above, the luminescence of a single defect, or equivalently, a single sub-ensemble is not linear with power. In this regime the power is increased but the luminescence only increases based on the saturation curve, less than the sum of two ensembles, see Fig. 2.5 right inset. The result is that the two laser spectrum displays a 'hole' at the pump frequency of lower luminescence within the spectral region where saturation effects are at play.

What is the width of this spectral hole? As stated it is the spectral region wherein saturation effects are relevant. If the two lasers are much, much weaker than the saturation power of the defect then the saturation is only occuring when the lasers are within one homogeneous linewidth. $|f_{\mathrm{pump}} - f_{\mathrm{probe}}| < \Gamma_{\mathrm{hom}}$ and thus the hole linewidth is twice the homogeneous linewidth.

A laser tuned futher than Γ_{hom} can still drive the system appreciably if the laser has sufficiently high powers. In this case the spectral region wherein saturation effects must be considered can be much larger than the bare homogeneous linewidth. In fact the hole linewidth displays a saturation-like curve of it's own [104]:

$$\Gamma_{\mathrm{hole}} = \Gamma_{\mathrm{hom}} \left(1 + \sqrt{1 + \left(P_{\mathrm{probe}} + P_{\mathrm{pump}}\right)/P_{\mathrm{sat}}}\right) \tag{2.3}$$

It is important to consider which linewidth is being probed by this measurement method. We have referred to an ensemble of emitters, but this may be a spatial ensemble or a temporal ensemble, the explanation above is the same for both. Regardless of ensemble the saturation effect only occurs when both lasers drive the same sub-ensemble in the timescale of the excited state lifetime as the saturation effect is due to a redistribution of population into the excited state. As such the linewidth being probed is the instantaneous homogeneous linewidth. This is true for all saturation holes even in the presence other effects that might have longer timescales, eg, slow spectral diffusion, or hyperpolarization as will be discussed next.

2.2.3 Hyperpolarization

To discuss hyperpolarization we must now expand the two-level system to a three-level system, with an additional ground state, 3, that possesses an optical transition to the excited state 2. If we consider the ground states as spin states then the previous can be thought of as the zero magnetic field case while now we will talk about the at field case. This is of course a natural extension as this is the basis of a spin-photon interface. Levels 1 and 3 are the spin states separated by an energy in the microwave band, and transitions to level 2 are spin-dependent optical transitions. A level diagram with all relevant rates is shown in Fig. 2.6a. Such a level system, with all transitions being allowed, is known as a lambda system. As will be discussed in Sections 2.5.2 and 2.5.3 both the $^{77}Se^{+}$ and the T centre can be modeled as lambda systems.

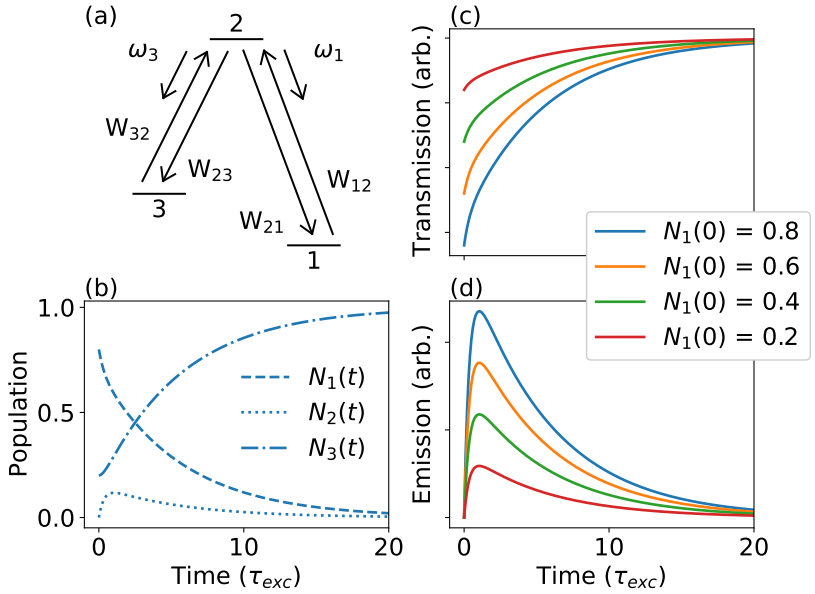

Figure 2.6: **Three-level system hyperpolarization.** (a) Rates of a three-level system. (b) Populations of the three levels when a laser drives the 1-to-2 transition. (c) Transmission of a laser tuned to transition 1-to-2 versus time for a range of starting population distributions ($N_1(0)$ in the legend). (d) Total emission from 2 when the 1-to-2 transition is driven for a range of starting population distributions (we set $\omega_1 = \omega_3$).

As before we will assume all spontaneous excitation rates to level 2 are zero as the thermal energies will be much smaller than the optical transition energies. We will also set all spontaneous decay/excitation rates between levels 1 and 3 to zero. This is due to the fact that in the systems of study ω_{13} and ω_{31} are much smaller than all other rates. The T centre has a ≈ 1 µs excited state lifetime and a decay rate in the ground state (T_1, see Section 2.3.1) greater than ≈ 16 s in ^{28}Si [70]. Likewise ^{77}Se^{+}has a excited state lifetime of ≈ 10 ns and a T_1 of ≈ 4 hours in ^{28}Si [77].

With the introduction of a third level, and if the homogeneous linewidth is small compared to the splitting between levels 1 and 3, then it will be possible to drive a single ground-to-excited-state transition with the unaddressed state being a 'dark state'. Every time a defect is excited there is a chance that it will decay to the unaddressed state, thus, after sufficient time all the population will be in the unaddressed state. This effect is known as hyperpolarization or optical pumping as a single resonant laser can pump the population into a desired state. The resulting system is said to be hyperpolarized as the population is pushed out of thermal equilibrium. This optical pumping effect can be seen in Fig. 2.6b wherein the time evolution of the three level system is simulated with a drive from level 1 to 2 turned on at time 0. The population in level 1, N_1, decreases as the population in level 3, N_3, increases as it is the dark state in this scenario. N_2 remains low for the evolution as any population will decay down to levels 1 or 2, however, for a short time at the beginning the population peaks before decaying down as the system hyperpolarizes. These decay curves in the populations are collectively known as hyperpolarization transients.

This optical hyperpolarization depends on branching ratios of the excited state back to the ground state — there must be a finite probability of decaying to the dark state for the optical pumping to occur. Branching ratios may differ due to ground state degeneracies, spin-flip selection rules, or selective cavity enhancement. The cyclicity of a transition is how many times the transition can be excited before a decay occurs to the dark state. As we will discuss in Section 2.4 cyclicity is important for spin-photon interfaces. However, here we will assume that the branching ratios between the two ground states are equal and the system has low cyclicity.

In quantum technology applications, it is necessary to measure the population in levels 1 and 3. Experimentally, N_1 and N_3 can be probed by a transmission or emission measurement. Consider the case where a laser is tuned to the 1-to-2 transition as is simulated in Fig. 2.6b and the transmission of the laser is measured versus time. When N_1 is large there will be high absorption and when N_1 is low there will be no absorption as there is nothing present to absorb the light. This is shown in Fig. 2.6c plotting the transmission versus time which shows a hyperpolarization transient. This transmission transient probes the population present in level 1 at time $t = 0$.

As stated, an emission measurement can also be used to measure the population of a state. Consider the same scenario with a laser tuned to the 1-to-2 transition, however, now we monitor the emission from the system. This is shown in Fig. 2.6d. Notice how the emission transient matches the N_2 transient in Fig. 2.6b, in fact they are directly proportional as every decay from level 2 is accompanied with the emission of a photon. Again, the hyperpolarization probes the population present in level 1 at time $t = 0$.

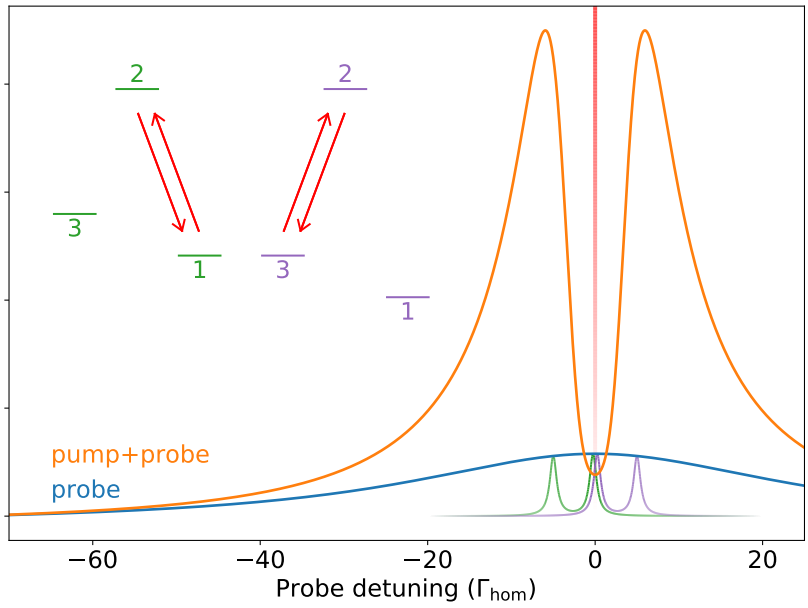

Figure 2.7: **Three-level hole burning: steady-state**. One and two laser scans of an inhomogeneously broadened ensemble of three-level defects in the steady-state regime (ground state splitting $= 5\Gamma_{\mathrm{hom}}$). Rather than a single spectral hole there are two anti-holes split by twice the ground state splitting. These anti-holes occur when both transitions of a sub-ensemble are addressed by the lasers. These sub-ensembles are shown in green and purple with slight shifts for clarity. (Inset) Level diagram of two sub-ensembles of the inhomogeneously broadened ensemble of three-level defects. The colours of the levels correspond to the spectra of the sub-ensembles shown in the main panel. These two sub-ensembles are shifted in energy such that the pump laser (red in inset and main panel) is resonant with the 1-to-2 transition for the green sub-ensemble and the 3-to-2 transition for the purple sub-ensemble.

As a further note, once the system is fully hyperpolarized at large times the system goes 'dark': there is no emission and no absorption as can be seen for large times in Fig. 2.6c and d. We now encounter an interesting dilemma: if the act of probing the system to generate luminescence causes hyperpolarization which quenches luminescence, how can a spectrum be obtained? There are a number of ways to address this issue: firstly, non-resonant excitation as in photoluminescence measurements can reveal the ground state structure without hyperpolarization as all transitions are excited. Hyperpolarization can also be avoided by addressing the dark state with an addition drive such as with two lasers each tuned to one of the two transitions or with a resonant laser and a microwave tone to drive level 1 to 3. Finally, a transient measurement, where the spectrum is measured fast compared to the hyperpolarization transient before the system is pumped to a dark state, can reveal the spectrum. In this work we will be studying three-level systems using all of these techniques.

We will now discuss how the two ground states change a hole burning measurement. We first consider hole burning in the steady-state regime where the measurement time-scale is much longer than any dynamics in the system and any spectrum is the result after the system has reached a steady-state equilibrium. We will consider an inhomogeneously broadened ensemble of emitters with Γ_{ih} larger than the ground state splitting (Δ_g) between 1 and 3 which is slightly larger than the homogeneous linewidth. Explicitly we consider $\Gamma_{\mathrm{ih}} = 50\Gamma_{\mathrm{h}}$ and $\Delta_g = 5\Gamma_{\mathrm{h}}$ and equal branching ratios to levels 1 and 3. One and two lasers scans in the steady-state regime of this ensemble of emitters are shown in Fig. 2.7. Rather than being completely dark, the one laser scan shows a weak signal. This is because there is a small overlap between the two transitions due to the finite linewidth. This overlap can be seen in the sub-ensembles plotted within the inhomogeneous line. This overlap means a single laser can drive both transitions of the lambda system – albiet weakly – and generate signal without hyperpolarizing the system.

By adding the pump laser the spectrum displays not a single hole as in the saturation case but two large 'anti-holes' at detunings equal to the 1-3 splitting. As discussed above, hyperpolarization can be avoided when two lasers are resonant with the two transitions of the lambda system. The pump will be resonant with the 1-to-2 transition of one sub-ensemble (the green sub-ensemble and levels in Fig. 2.7) and will be resonant with the 3-to-2 transition of a different sub-ensemble (the purple sub-ensemble and levels in Fig. 2.7). Thus when the probe laser addresses the green 2-to-3 transition or the purple 1-to-2 transition both transitions of these sub-ensembles will be address and there will be an increase in luminescence signal as there is no hyperpolarization and thus a high population in level 2 even in steady state.

In this steady-state hole-burning measurement there is also a small saturation hole at zero detuning. Due to the 1-3 splitting a single laser will only show luminscence from the weak driving of the overlap between the 1-2 and 3-2 transitions, but as before, increasing the power of this drive will increase the luminscence in a sub-linear fashion and thus there will still be a saturation hole. However, this hole is obscured by the large anti-holes to either side. To properly obtain the homogeneous linewidth a full rate equation model is needed, which we develop in Section 4.1.

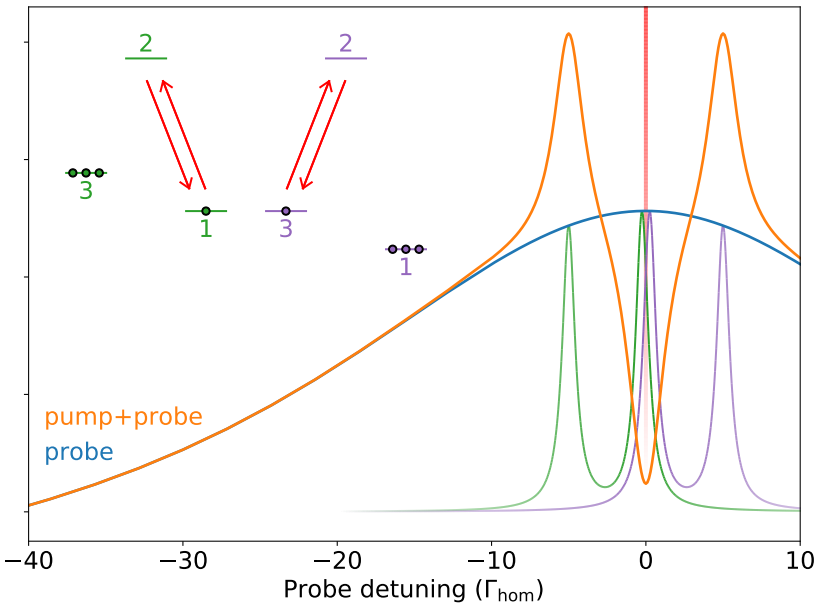

Figure 2.8: **Three-level hole burning: transient**. One and two laser scans of a inhomogeneously broadened ensemble of three-level defects in the transient regime (ground state splitting $= 5\Gamma_{\mathrm{hom}}$). In addition to a spectral hole, there are also two anti-holes split by twice the ground state splitting. These anti-holes occur when both transitions of a sub-ensemble are addressed by the lasers. These sub-ensembles are shown in green and purple with slight shifts for clarity. In the transient regime the hole is more pronounced as the probe laser is sensitive to the deficit of population in the pumped levels. (Inset) Level diagram of two sub-ensembles of the inhomogeneously broadened ensemble of three-level defects. The colours of the levels correspond to the spectra of the sub-ensembles shown in the main panel. These two sub-ensembles are shifted in energy such that the pump laser (red in inset and main panel) is resonant with the 1-to-2 transition for the green sub-ensemble and the 3-to-2 transition for the purple sub-ensemble. The colour dots denote the relative populations of the ground state levels.

We can also consider hole burning in the transient regime, i.e., not at steady state but with measurements made faster than the hyperpolarization time scale. Again we will consider an inhomogeneously broadened ensemble of emitters with $\Gamma_{\mathrm{ih}} = 50\Gamma_{\mathrm{hom}}$ and a ground state splitting $\Delta_g = 5\Gamma_{\mathrm{hom}}$ and equal branching ratios to levels 1 and 3. One and two laser scans in the transient regime are shown in Fig. 2.8. Here, there is a large signal from the single laser scan as the measurement timescale is faster than the time it would take the probe laser to pump the sub-ensembles into a dark state.

When the pump is added, a hole appears at zero detuning and two large anti-holes appear in the spectrum at $\pm\Delta_g$. We can understand these features by considering the hyperpolarization transients shown in Fig. 2.6d. In the transient regime the spectrum is measuring the emission at early times in the transient which is direct proportional to the population in the addressed state. Without the pump the populations in all the ground states of all the sub-ensembles are close to 0.5, however, the pump

hyperpolarizes the two sub-ensembles it address (green and purple sub-ensembles in Fig. 2.8). This unequal population is illustrated in the inset of Fig. 2.8. Thus when the probe addresses the depleted states (green level 1 and purple level 3) there is very low signal – a hole – as there is low population. Conversely, when the probe addresses the two high population states (green level 3 or purple level 1) there high signal – an anti-hole.

In the transient regime, the hole is not due to saturation effects as is the case in the steady-state regime nor in the case of an ensemble of two-level emitters (as discussed in Section 2.2.2). However, the hole can still provide a measure of the homogeneous linewidth as both the pump and probe must address the same sub-ensemble. Equation (2.3) still holds for hyperpolarization holes [105], although, the timescale of the linewidth measurement may not be instantaneous as in the case of a saturation hole. The appropriate timescale in this case is the ground state thermalization time, i.e., the spin T_1 lifetime (see Eq. (2.18) for more details on T_1). For more details on hole burning in the hyperpolarization regime see Ref. [106].

2.3 Spin Processes

In the previous section we discussed the dynamics and properties of optical transitions, i.e., transitions due to electronic bound-to-bound transitions or excitonic transitions. In this section we will be discussing the dynamics and properties within ground state levels. As mentioned above the ground state levels (levels 1 and 3 above) can be considered to be spin levels in a non-zero magnetic field and are the basis of a spin-photon interface. We will begin with a general discussion of these ground state levels and transitions therein, then move into a discussion of the hyperfine interaction as well as decohering interactions present in the ground state spin manifold.

2.3.1 Coherence

Firstly, we can note in what manner the ground state transition between levels 1 and 3 (see Fig. 2.6a) is different from the ground-to-excited state transitions. In the ground state the energy differences are on the order of gigahertz, in the microwave range, and at the temperatures we will be working at, the thermal decay rate back to equilibrium is much slower than the driving rate. Furthermore, spontaneous transition rates from 1-to-3 and 3-to-1 are approximately equal at the temperatures of study, thus in thermal equilibrium there is equal population in both levels 1 and 3, assuming equal degeneracies.

Most importantly, in the studies to follow the transitions from 1 to 3 will be driven in a coherent manner, in contrast to the transitions to the excited state. The rate equation models introduced thus far (see Section 2.2.3 for examples, see Section 4.1 for full details) are not the full description of these systems, they are merely a classical approximation of the systems.

In the two level rate equation two numbers are tracked, N_1 and N_2, however, with the normalization condition that $N_1 + N_2 = 1$, there's only one degree of freedom needed to describe the full system. A quantum mechanical description of the two level system requires a 2x2 complex matrix,

a density matrix, ρ. The density matrix must be Hermitian, and have a trace of one, leaving three real numbers needed to describe the system: the Bloch vector, $\vec{a}$ [107],

$$\rho = \frac{1}{2}(I + \vec{a} \cdot \vec{\sigma}), \tag{2.4}$$

where $\vec{\sigma}$ is a vector composed of the three Pauli matrices, $[\sigma_x, \sigma_y, \sigma_z]$, and the requirement that $|\vec{a}| \leq 1$. The density matrix can represent either a pure state ($|\vec{a}| = 1$) or a mixed state ($|\vec{a}| < 1$). In terms of state vectors, a pure state is a system that can be expressed by a single quantum state vector whereas a mixed state is a probabilistic combination of multiple pure states.

This vector can also be mapped to spherical coordinates in a Bloch sphere as shown in Fig. 2.9 by defining our two eigenstates $|0\rangle$ and $|1\rangle$ as the north and south poles of a sphere. An arbitrary pure state can be defined by a point on the surface of the sphere, as:

$$|\psi\rangle = \sin\frac{\theta}{2}|0\rangle + \cos\frac{\theta}{2}e^{i\phi}|1\rangle . \tag{2.5}$$

Whereas a mixed state will lie below the surface of the sphere at a location given by the Bloch vector.

In a density matrix the diagonal values are known as populations, analogous to the populations of levels in the classical description. The decidedly more quantum off-diagonal values are known as the coherences of the system. On the Bloch sphere the classical states would lie at the poles and along the Z-axis while the quantum states lie anywhere in/on the sphere.

With the addition of coherence to our system the control and dynamics become more intricate. A transition can be described as coherent if the coherences of the density matrix remain known during the transition. In the Bloch sphere representation this would be ensuring the phase information, ϕ, is not lost during the transition. Coherently driving a transition will induce a rotation about an axis in the Bloch sphere, ideally, keeping the Bloch vector at the surface of the Bloch sphere with a fixed ϕ (see Section 6.4 for more details).

In an incoherent process the phase information is lost and the transition is only a transfer of population between eigenstates. This is why the classical rate equations are valid as we are not in the regime wherein the transitions are being driven in a phase coherent manner. Such a regime is entered when the time and power of the optical drive are such that the transition can be driven faster than any decays or dephasing processes within the system, which can be achieved with fast pulsed lasers as applied to a variety of systems [108–110].

2.3.2 Decoherence

Now that we understand how coherent transitions differ from incoherent transitions, we can describe the rates and manners of manipulation of the populations/coherences within the ground state that will be relevant for the upcoming experiments in this thesis work.

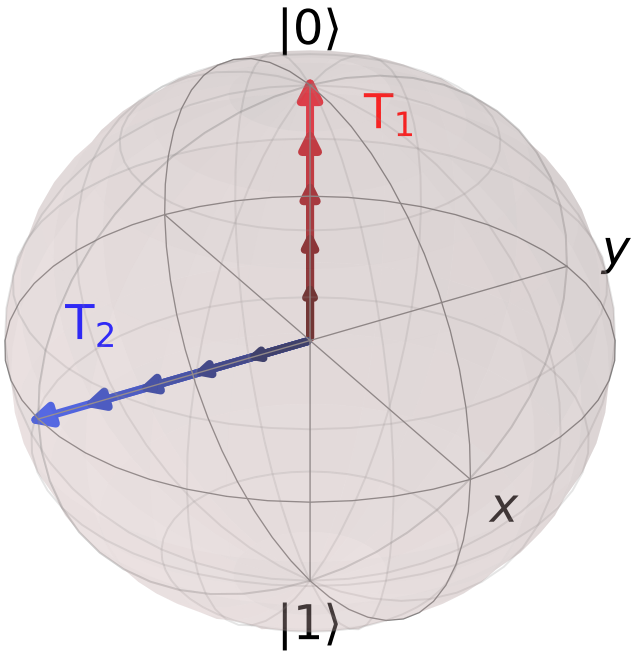

Figure 2.9: $\boldsymbol{T_1}$ **and** $\boldsymbol{T_2}$ **decays visualized.** T_1 is a decay of out-of-equilibrium populations to a statistical thermal equilibrium, in this case equal population in $|0\rangle$ and $|1\rangle$. T_2 is a temporal decay of coherence to a mixed state, a statistical mixture of $|0\rangle$ and $|1\rangle$, the origin of the Bloch sphere.

As in the optical processes there is a decay constant associated with the decay from an out of equilibrium population distribution back to equilibrium. In the optical processes model this was the spontaneous decay rate ω_{21}, in this coherent spin control model this rate is referred to as T_1. This is a decay back to a thermal statistical mixture in which the off-diagonal elements of the density matrix are zero and the populations are determined by the Boltzmann distribution based on energy spacing and temperature [104]:

$$\frac{N_2}{N_1} = e^{-(E_2-E_1)/kT}. \tag{2.6}$$

In our systems of interest, based on the operation temperatures and the energy splittings, this is a decay of populations back to a 50:50 ratio. On the Bloch sphere this can be visualized as a decay of the magnitude of the Bloch vector from a pure state on the surface of the sphere to a mixed state below the surface. This can be seen in Fig. 2.9.

By moving to the quantum mechanical description there is also the introduction of another decay rate, T_2. In the most general sense, this is a decay in the coherences of the density matrix, it is a loss of phase information about the state and can be visualized using, for example, an even superposition state on the Bloch sphere decaying to the origin as seen in Fig. 2.9. Mathematically, this can be expressed as the decay of a coherence function, $\mathcal{L}$, tracking the off-diagonal element of a density matrix ρ:

$$\mathcal{L}(t) = \frac{\langle 1| \rho(t) |0\rangle}{\langle 1| \rho(0) |0\rangle}. \tag{2.7}$$

Note that in contrast to T_1, a T_2 decay does not change the populations but may change the phase, ϕ, to an unknown value – this is equivalent to working with a fully mixed state and is not a useful resource.

As is the case with optical linewidths having different definitions, so too must the physical origins and time scales be considered for T_2 decays. Two important dephasing rates are known as T_2^* and T_2. Analogous to the optical linewidths we can think of T_2^* as an inhomogeneous ensemble dephasing (spatial or time ensemble) and the T_2 as the homogeneous dephasing rate.

Thus far we have shown states in the Bloch sphere as stationary vectors, however, in reality these vectors are precessing about the Z-axis at a frequency given by the energy splitting of the two levels, known as the Larmor precession frequency. We can move from the lab frame where the vectors are rotating and enter into the rotating reference frame to work with vectors that are stationary. When working with ensembles of spins in a physical system inhomogeneities in space or time can lead to an ensemble of frequencies, by, for example, inhomogeneities in the magnetic field for a spin with a Zeeman interaction. However, the same rotating reference frame is used for the ensemble of spins, leading to a distribution in frequencies about zero. An averaging of this ensemble magnetization reveals a decay of in-plane magnetization with a time constant denoted as T_2^*. This dephasing can be seen in Fig. 2.10a and b showing the X-projection of an ensemble of spins with different frequencies oscillating in time along with the average in-plane magnetization.

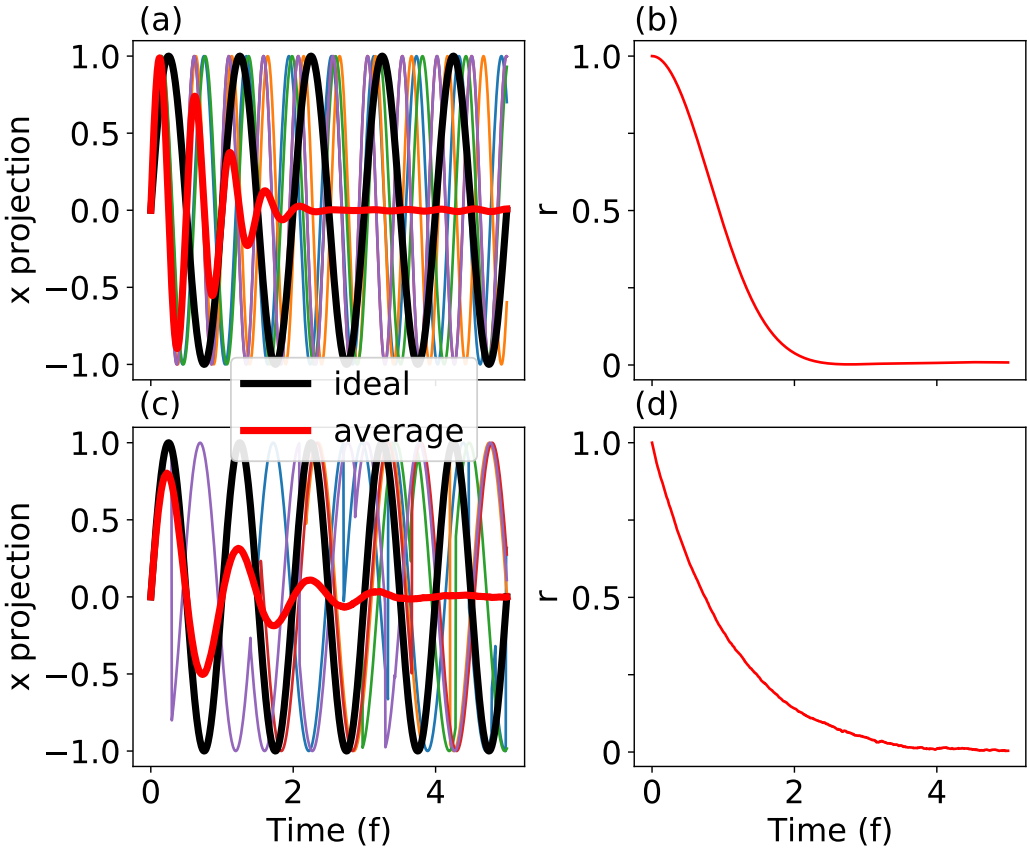

Figure 2.10: $\boldsymbol{T_2^*}$ **and** $\boldsymbol{T_2}$**.** (a) Projection along the X-axis of an ensemble of spins with a Gaussian spread of precession frequencies showing a decrease in magnetization when averaged. (b) The resulting T_2^* decay of the transverse magnetization. (c) Projection along the X-axis of an ensemble of spins undergoing phase jumps showing a decrease in magnetization when averaged. (d) The resulting T_2 decay of the transverse magnetization.

If we were to work with an ensemble with all the same frequency there would still be a decay in phase information due to stochastic variations in the local magnetic field due to environmental effects such as spin flips that cause random jumps in the phase due to spin-spin coupling [107] (see Section 2.3.5 for more detail) or phase noise from experimental hardware [67]. Averaging the ensemble over many iterations that have random phase jumps will lead to a decay of transverse magnetization as shown in Fig. 2.10c and d. This is the homogeneous phase decay, T_2.

It may seem purely theoretical to consider an ensemble with no inhomogeneities, however, there are ways to measure T_2 that cancel out inhomogeneities that might increase the phase decay. These are done by driving the transition coherently to rotate the system about the Bloch sphere such that inhomogeneities cancel out. This is known as dynamical decoupling [111] the act of interleaving rotation pulses with wait times to eliminate deleterious terms of the Hamiltonian to which a spin is subject. There are a range of dynamical decoupling pulse sequences that can extract a T_2 measurement and as such it is important to report the measurement method when reporting a T_2 value. The simplest measurement of T_2 is the Hahn-echo pulse sequence [112] the steps of which are shown in Fig. 2.11.

A requirement for a Hahn echo is the ability to rotate state vectors about the Bloch sphere. The exact definition of these rotations is given in Section 2.3.3. Here it is sufficient to known that in experiments we are able to rotate state vectors by arbitrary angles about arbitrary axes in the Bloch sphere, e.g. a π pulse about the X-axis rotates $|0\rangle$ to $|1\rangle$.

A Hahn echo experiment starts by initializing the system into an eigenstate, in this case $|0\rangle$ (Fig. 2.11a), via, for example, optical pumping to hyperpolarize the system (see Section 2.2.3). A $\pi/2$-pulse is applied to rotate the system about the X-axis to a superposition state (Fig. 2.11b). In the rotating reference frame the average magnetization will remain stationary but the components of the ensemble will start to spread out. Systems with higher frequencies (red) accumulate additional phase, while the systems with lower frequencies (blue) lose phase during the first wait period (Fig. 2.11c). After a time τ, a π-pulse is applied to rotate the system about the X-axis to invert the system (Fig. 2.11d). Now those sub-ensembles with higher frequencies will again accumulate phase which brings them back to the average phase and those systems with lower frequencies will again lose phase which brings them back to the average phase (Fig. 2.11e). After an equivalent wait time, τ, all the sub-ensembles are rephased. A final $\pi/2$-pulse (Fig. 2.11f) is applied to return the system to an eigenstate for subsequent readout, via, in our case, an optical readout pulse (Fig. 2.11g). The net result of this pulse sequence is the ensemble has 2τ of free evolution with static inhomogeneities removed.

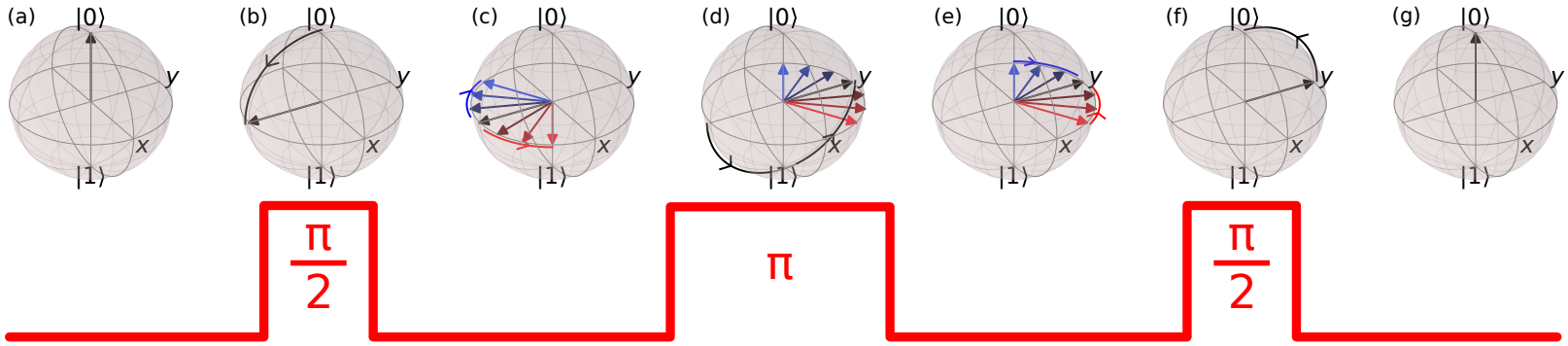

Figure 2.11: **Hahn echo pulse sequence of spatial ensemble.** (a) initialization to 0 state; (b) $\pi/2$ x-pulse; (c) dark time, individual spins precess with different frequencies (red, higher frequencies; blue, lower frequencies); (d) π x-pulse; (e) dark time, different precession frequencies rephase the spins; (f) $\pi/2$ x-pulse moves rephased spins back to an eigenstate; (g) eigenstate readout.)

2.3.3 Control

Next, let us discuss the manner in which we perform these rotation pulses. For our systems this is done by applying an oscillating magnetic field at a frequency equal to the energy difference of the two eigenstates. For a simple spin-1/2 system the oscillating magnetic field, B_1, must be perpendicular to the static magnetic field, B_0, in order to drive the transition [113]. This is necessary to drive transitions where the change in magnetic quantum number is $\Delta m = 1$ ($m = \langle\psi| \sigma_z |\psi\rangle$ where σ_z is the Pauli-Z operator). For a $\Delta m = 0$ transition the field oscillating field must be applied parallel to B_0 [114]. In the rotating reference frame the oscillating B_1 field will appear as a constant field on the equator about which the spin will precess. The exact axis will depend on the phase of the applied field.

We will consider a $\Delta m = 1$ transition: an electron spin in a static field, B_z, along the Z-axis.

$$H_0 = B_z \gamma_e \sigma_z, \tag{2.8}$$

where γ_e is the gyromagnetic ratio of the electron and σ_z is the Pauli-Z matrix. In the lab frame the spin precesses about the Z-axis with angular Larmor frequency $\omega_L = B_z\gamma_e$. Applying a MW pulse with frequency ω_{MW} and phase ϕ perpendicular to the Z-axis we get the following Hamiltonian [115]

$$H = \omega_L \sigma_z + 2\Omega(\cos(\omega_{MW} + \phi)\sigma_x + \sin(\omega_{MW} + \phi)\sigma_y) \tag{2.9}$$

where Ω is the Rabi frequency given by $\Omega = \gamma_e \left|\vec{B_1}\right|$. We can move to the rotating reference frame rotating at the drive frequency, ω_{MW}, to simplify. In this step we make use of the rotating wave approximation [115, 116] wherein terms oscillating at $\omega_L + \omega_{MW}$ are ignored as these frequencies will be much faster than any other time scale in the system and thus average to zero. We get the following Hamiltonian in the rotating reference frame

$$H_r = (\omega_L - \omega_{MW})\sigma_z + \Omega(\cos(\phi)\sigma_x + \sin(\phi)\sigma_y). \tag{2.10}$$

Thus, a MW pulse with frequency equal to the Larmor frequency appears to the spin as a constant field on the equator, inducing precession. The axis of rotation is determined by phase of the MW pulse, ϕ, and the angle of rotation, θ, is determined by the Rabi frequency and the duration of the pulse, $\theta = \Omega t/2$. A $\pi/2$ pulse about the X-axis is shown in Fig. 2.12 in both the lab frame and the rotating frame.

Experimentally, to determine a π pulse (or any angle) a Rabi pulse sequence is performed. After initialization a single MW pulse is applied then the populations are measured. Repeating this sequence changing the MW pulse duration or power results in a oscillation in the measured population as the MW transfers population back and forth between the levels.

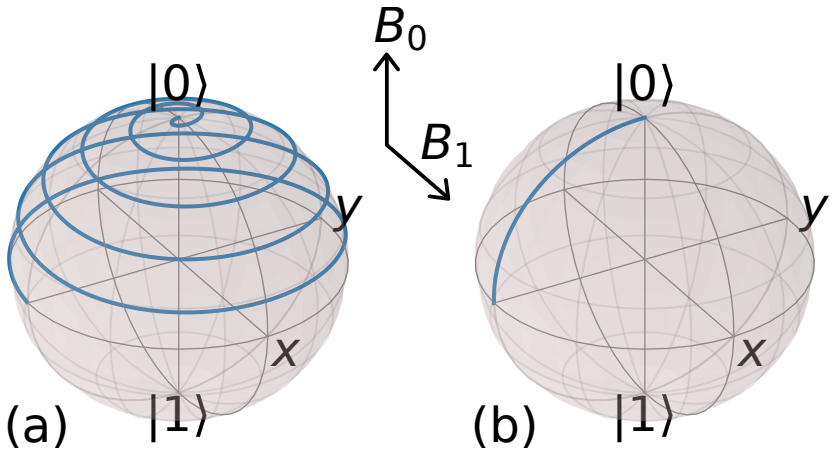

Figure 2.12: **$\pi/2$ pulse.** An oscillating microwave pulse, B_1, perpendicular to the static field, B_0, drives a rotation about the X-axis of the Bloch sphere. Trajectories starting in the $|0\rangle$ state are shown in (a) the laboratory frame, and (b) the rotating reference frame (rotating wave approximation applied).

2.3.4 Hyperfine interaction

Thus far, we have not talked in detail about the physical origins of the ground states considered. Explicit description of the ground states of the defects under study will be provided in the following sections, however, here we will consider one final aspect of the ground state applicable to both the selenium and T centre defects, as well as any defect in a spinful environment (i.e. an environment containing defects with non-zero spin): the hyperfine interaction. The following section follows the descriptions in Chapter 3.1.3 of Ref. [113].

Hyperfine interactions, $\mathcal{H}_{hf}$, in the defect systems relevant to this thesis are between the central defect electron spin, $\vec{S}$, and the nuclear spin of a nearby nuclei, $\vec{I}$, given by the hyperfine tensor, $\mathbf{A}$, as:

$$\mathcal{H}_{hf} = \vec{S}^{\,\mathsf{T}}\mathbf{A}\vec{I} \tag{2.11}$$

where $\vec{S}$ and $\vec{I}$ are vectors of the Pauli spin operators for the individual spins.

The hyperfine interaction can be split into two components, an isotropic component known as the Fermi contact interaction, and an anisotropic component, known as the dipole-dipole coupling. The Fermi contact interaction has the form:

$$H_F = a_{\text{iso}}\vec{S}^{\,\mathsf{T}}\vec{I} \tag{2.12}$$

where a_{iso} is proportional to the electron spin density at the nucleus. The dipole-dipole (or dipolar) coupling is anisotropic, depending on the orientation of the nuclear spin relative to the central spin and the static magnetic field. The dipole-dipole coupling has the form:

$$H_{\text{DD}} = \vec{S}^{\,\mathsf{T}}\mathbf{T}\vec{I} \tag{2.13}$$

where $\mathbf{T}$ is the dipolar coupling tensor which, in the principal axes of the dipolar interaction, is a diagonal tensor,

$$\mathbf{T}^d = \begin{bmatrix} -T & 0 & 0 \\ 0 & -T & 0 \\ 0 & 0 & 2T \end{bmatrix}, \tag{2.14}$$

where T is a scalar constant dependent on the system.

The dipolar coupling between electron and nuclear spins can be approximated with the electron-nuclear point-dipole formula [113].

$$\mathbf{T} = \frac{\mu_0}{4\pi\hbar} g_e \mu_B g_n \mu_N (3\vec{n}\vec{n}^{\,\mathsf{T}} - \mathbb{1})/R^3 \tag{2.15}$$

where g_e and g_n are the electron and nuclear g-factors, μ_B and μ_N are the Bohr magneton and nuclear magneton, and $\hbar$ is the reduced Plank's constant. $\vec{n}$ is the unit vector connecting the central electron and the nucleus (the static field is defined to be along the Z-axis) and R is the separation.

This hyperfine interaction is present for both the interaction of the central electron to any central nuclear spins the defect may possess, as well as with non-central nuclear spins in the environment, i.e., the spin bath.

For the spin systems we will be studying in this work the ground state structures are (ignoring bath spins) a combination of this hyperfine interaction between an electron and nuclear spin local to the defect and the Zeeman effect for each spin.

$$H = B_0 \gamma_e S_z + B_0 \gamma_n I_z + \vec{S}^{\,\mathsf{T}} \mathbf{A} \vec{I}, \tag{2.16}$$

where γ_e and γ_n are the gyromagnetic ratios of the electron and nuclear spins respectively, and $\mathbf{A}$ is the hyperfine tensor including both Fermi contact and dipole-dipole interactions.

Depending on the form of the hyperfine interaction a wealth of energy levels are possible at low magnetic fields. However, in this work we only study nuclei with spin-1/2, thus there is a common feature the hyperfine coupled systems share: they form a singlet-triplet structure at low magnetic fields. An example of an isotropic hyperfine interaction is shown in Fig. 2.13. In an isotropic system, at zero field the three higher energy states become degenerate, the triplet, and the lower energy state is a singlet of the electron and nuclear spins. At high fields, when the Zeeman energies are much larger than the hyperfine energy, the electron and nuclear spins are good quantum numbers, i.e., S_z and I_z commute with H. However, at low fields the electron and nuclear spins are no longer good quantum numbers and the eigenstates become mixtures of the spin-states and the good quantum numbers are the total angular momentum, j, and the magnetic quantum number, m.

As anisotropies are included the exact form will change but this general structure of three closely spaced levels along with a far split lone state is seen repeatedly and we make use of the labeling scheme of the isotropic case. Namely, the triplet is composed of $T_\pm$ states with $m = \pm 1$, and T_0

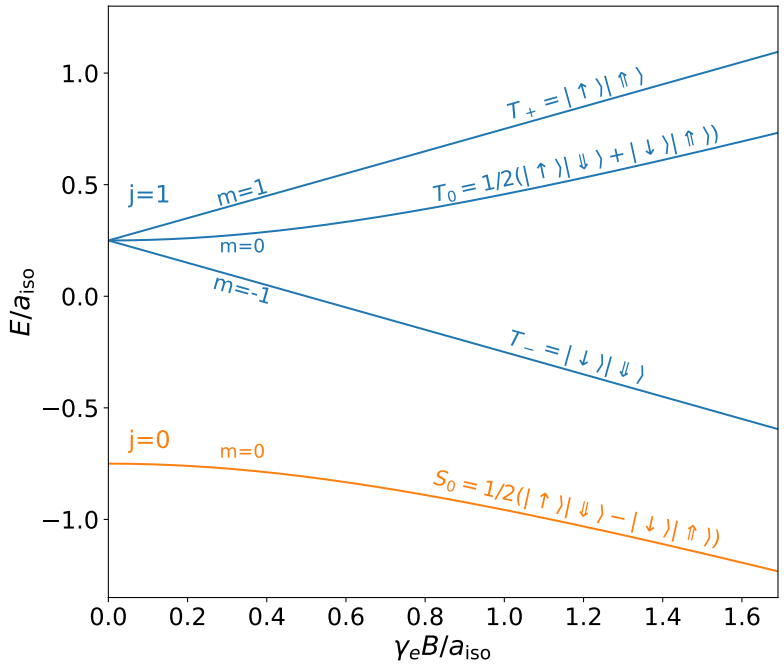

Figure 2.13: **Isotropic hyperfine for a spin-1/2 nucleus.** The low field spectrum of an isotropic hyperfine system. Energy levels are labeled and their zero-field states in terms of electron (single arrow) and nuclear spin (double arrow) are list. Zero-field j and m values are also listed.

with $m = 0$ and the singlet is labeled S_0 also with $m = 0$. These labels and quantum numbers are shown in Fig. 2.13.

As an aside, Fig. 2.13 shows a simple example of a system containing transitions of $\Delta m = \pm 1$ ($\mathrm{S}_0 \Leftrightarrow \mathrm{T}_\pm$) and transitions with $\Delta m = 0$ ($\mathrm{S}_0 \Leftrightarrow \mathrm{T}_0$). As mentioned in Section 2.3.3 the orientation of the control pulses, B_1, relative to the static field, B_0, must be picked based on the Δm of the transition: for $\Delta m = 1$ perpendicular B_0 and B_1 is required; for $\Delta m = 0$ parallel B_0 and B_1 is required [114].

2.3.5 Mechanisms of decoherence

As discussed in Section 2.3.2, decoherence (or dephasing) of the qubit causes a loss of phase information and produces a mixed state. Here we will discuss how coupling to bath spins leads to the decoherence of the qubit. This discussion is motivated by the discussion of Ref. [117]. To stay general we will discuss these interactions in terms of a 'central spin' which may be an electron spin, a nuclear spin, or any two levels in the ground state of a solid state defect, e.g., S_0 and T_0 of an electron-nuclear hyperfine coupled system. Regardless of the system we will consider a scenario where we are driving an ensemble of spins with a microwave drive in the presence of a spin-bath.

At low temperatures we can consider the qubit to be in the pure dephasing regime where $T_1 >> T_2$. We will also consider no dephasing from noisy experimental hardware. In this regime coupling to neighbouring spins in the bath via the dipolar coupling is the dominant form of decoherence. In the surrounding bath of a central spin being used as a qubit there will be three relevant defect species to consider; 1, the same species as the central spin in resonance with the microwave drive (i.e. same ground states as the central spin); 2, the same species as the central spin but not in resonance (i.e. in a different ground state outside the qubit manifold); and 3, different spins species, in silicon this is predominately ^{29}Si.

The Z-component of the dipolar coupling leads to an effective magnetic field that depends on the spin state of the bath, as the bath spins flip the central spin experiences a fluctuating magnetic field. This is known as spectral diffusion [117] similar to the spectral diffusion discussed for optical processes as in both cases time dependent fluctuations in the environment (charges or spins) lead to changes in transition energy which can cause dephasing.

In the static case without time-dependent spin flips the dipolar coupling can be corrected with a π-pulse as in the Hahn-echo pulse sequence (see Section 2.3.2). This will correct for species 2 and 3 but species 1 are resonant and will also flip during the π-pulse leading to an uncorrected difference of magnetic field before and after the π-pulse. This is known as instantaneous diffusion [113] and has a decoherence time given by:

$$\frac{1}{T_{2,ID}} = \frac{\pi\mu_0\hbar}{9\sqrt{(3)}} C \left(2\pi \frac{df}{dB_0}\right)^2 \tag{2.17}$$

where C is the concentration of resonant defects, and df/dB_0 is the derivative of the qubit transition frequency with respect to the static magnetic field, B_0.

The final decoherence effect is flip-flops, energy-conserving pairs of flips of resonant spins due to the X- and Y- components of the dipolar coupling. These flip-flops have two types, direct flip-flops that involve the central spin and indirect flip-flops that involve pairs of spins in the bath (i.e. two ^{29}Si atoms). In Ref [117] the dephasing rate of indirect flip-flops was argued to depend linearly on df/dB_0 as the two flip-flopping species are coupled by a Z dipolar term to the central spin. Direct flip-flops have no Z dipolar term and thus have no dependence df/dB_0.

The combination of these decoherence rates leads to a phenomenological model of the T_2 coherence time of a central spin [117]:

$$\frac{1}{T_2} = \frac{1}{T_{2,ID}} + \frac{1}{T_{2,iFF}} + \frac{1}{T_{2,dFF}}, \tag{2.18}$$

$$\frac{1}{T_2} = k_{ID}\left(\frac{df}{dB_0}\right)^2 + k_{iFF}\left(\frac{df}{dB_0}\right) + k_{dFF}. \tag{2.19}$$

Where $T_{2,ID}$, $T_{2,iFF}$, and $T_{2,dFF}$ are the decoherence times for the discussed mechanisms, instantaneous diffusion, indirect flip-flops and direct flip-flops respectively. k_* are phenomenological parameters. These decoherence mechanisms are illustrated schematically in Fig. 2.14.

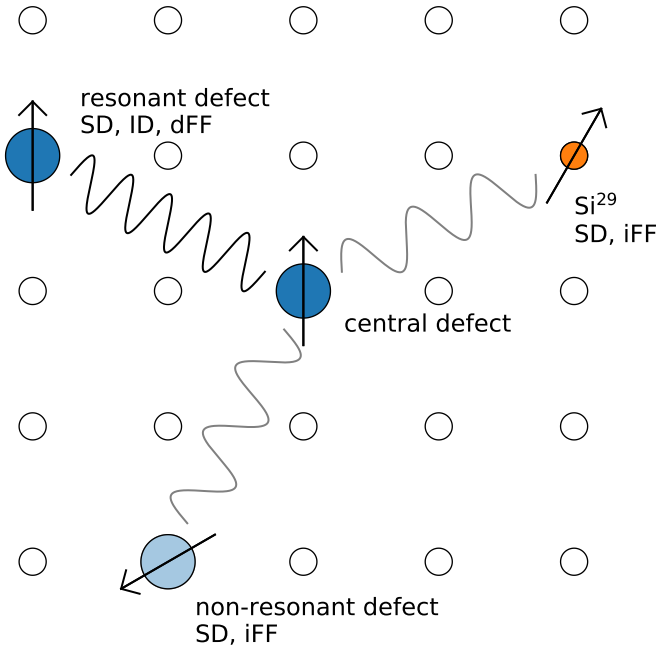

Figure 2.14: **Decoherence mechanisms.** Collection of decoherence mechanisms including spectral diffusion (SD), instantaneous diffusion (ID), and direct/indirect flip-flips (dFF, iFF) as well as the species responsible. Adapted from [117].

Here we can see that many of the dominant forms of decoherence depend on the sensitivity of the transition energy to changes in the magnetic field, df/dB_0. This leads to the idea of operating at 'clock transitions' where $df/dB = 0$ [117]. The name is derived from the use of clock transitions in atomic clocks [118] to get extremely high stabilities as the operation condition decouples the system from magnetic field fluctuations to first order.

2.3.6 Electron spin echo envelope modulation

While spinful defects in the environment can cause decoherence due to random fluctuations of the spin, some of these effects can couple coherently into the system under study and be measured in the Hahn-echo T_2 transient. One such effect is known as Electron Spin Echo Envelope Modulation (ESEEM) where oscillating spins in the environment cause oscillations in the transverse magnetization of the spin under study [119]. It has since become popular for studying hyperfine and nuclear quadrupole couplings in solids [113].

This effect was first observed by Ref. [119]. The qualitative explanation presented here follows their original description. The ESEEM effect is shown schematically in Fig. 2.15 where the central

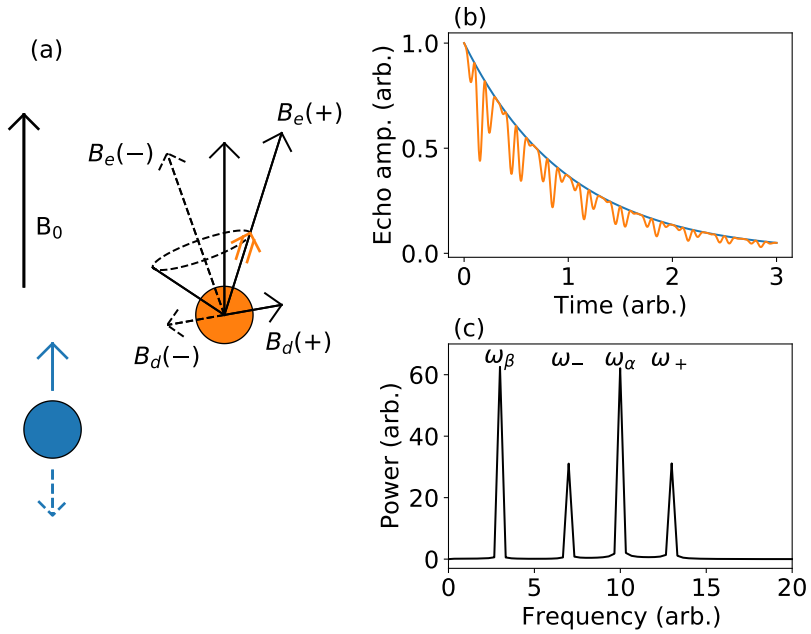

Figure 2.15: **Electron Spin Echo Envelope Modulation.** (a) A nuclear spin (orange) experiences an effective magnetic field from the central spin (blue), after the Hahn-echo spin flip of the central electron, the nuclear spin precesses about the new effective field direction (dashed). Adapted from Ref. [119]. (b) Oscillations appear in the Hahn-echo envelope due to the nuclear spin precession. (c) Fourier transform of the modulation (see text).

spin under study (blue) has a dipolar coupling to a nearby non-resonant nuclear spin (orange). Each spin experiences an additional magnetic field due to the dipolar coupling. The orientation of the central electron produces two different dipolar fields $B_d(\pm)$ at the nuclear spin depending on the spin state of the electron, aligned (+) or anti-aligned (-) to the static field, and thus two effective fields $B_e(\pm)$.

For a central electron originally in the spin up state the nuclear spin will be in an eigenstate aligned to the $B_e(+)$ axis. After applying a π-pulse to flip the spin the effective field will flip to $B_e(-)$. If the pulse is fast compared to the precession frequency of the nuclear spin then the flip will be 'instantaneous' and the nuclear spin will not change during the pulse. After the pulse the nuclear spin will precess about the new magnetic field direction as it is not in an eigenstate of the new effective field. The precessing nuclear spin leads to an oscillating dipolar field at the central electron. If the electron is then rotated $\pi/2$ the free precession signal displays interference beats in time from the nuclear precession frequency. In practice, however, these interference beats are more conveniently measured in a Hahn-echo sequence rather than a free precession.

A more quantitative description of the ESEEM process for a Hahn-echo pulse sequence results in the following description of the modulation formula of the envelope [113, 119].

$$V(t) = 1 - \frac{k}{4}[2 - 2\cos(\omega_\alpha t) - 2\cos(\omega_\beta t) + \cos(\omega_+ t) + \cos(\omega_- t)] \tag{2.20}$$

where the modulation depth, k, is:

$$k = \left(\frac{\mathcal{B}\omega_I}{\omega_\alpha \omega_\beta} \right)^2 \tag{2.21}$$

where ω_α and ω_β are the precession frequencies from the two dipolar fields induced at the nuclear spin and $\omega_\pm$ are the sum and difference of these frequencies. ω_α and ω_β are given by:

$$\omega_{\alpha,\beta} = \left[\left(\omega_I + m_s^{\alpha,\beta} \mathcal{A} \right)^2 + (m_s^{\alpha,\beta} \mathcal{B})^2 \right]^{\frac{1}{2}} \tag{2.22}$$

where ω_I is the nuclear Larmor frequency in the static magnetic field. $m_s^{\alpha,\beta}$ are the magnetic quantum numbers of the two states of the qubit. In the case of an electron these are $m_s = \pm 1/2$, in the regime where the Zeeman Hamiltonian is much larger than the hyperfine term. Finally, $\mathcal{A}$ and $\mathcal{B}$ contain the information about the dipolar coupling between the central spin and the nuclear spin, and are given by:

$$\mathcal{A} = a_{\text{iso}} + T(3\cos^2\theta - 1) \tag{2.23}$$

$$\mathcal{B} = 3T \sin\theta \cos\theta \tag{2.24}$$

where θ is the angle between the vector connecting central spin to nuclear spin and the magnetic field axis and a_{iso} and T are the parameters of the hyperfine coupline described in Section 2.3.4.

The ESEEM modulation of the exponential T_2 decay is shown in Fig. 2.15b along with the Fourier transform showing the peaks at ω_α, ω_β, and $\omega_\pm$. In practice however, a central spin will be coupled to many nuclear spins within the bath. The result is simply the product of the modulation formula for each individual nuclear spin, $V'(t) = \prod_l V_l(t)$, where each factor contains information only about the central spin and one of the nuclear spins in the bath.

2.4 Spin-photon interface

A spin-photon interface is a system that can generate some form of entanglement between a long-lived qubit state (i.e. spin) and some property of a photon. In this section we will discuss the idea of a spin-photon interface and how it can be combined with photonic cavities to create useful quantum information devices. This entanglement may be between spin and photon number [120], spin and photon frequency [121], spin and chirality of the photon [122], spin and polarization [123], or spin and a time-bin photon [124, 125]. Regardless of the physical mechanism the result is an entangled state that has a mobile photon as one of the constituent particles which can be controlled and routed either on chip or through a distributed network.

However, this spin-photon entanglement is just the first step for a quantum network or a quantum computer. What is required is the entanglement of physically separated qubits which can then be used for e.g. entanglement swapping in a quantum network or remote two qubit gates such as a teleported CNOT [126, 127] in a distributed quantum computer. Thus, the next step is to use the spin-

photon entanglement to generate spin-spin entanglement. In theory this is straightforward, it simply requires a Bell-state measurement of the photons that projects the remaining spins into an entangled state. In practice the details of the spin-photon entanglement and the manner of performing the Bell-state measurement are system dependent.

Many proposals exist for generating high fidelity remote entanglement via photons and a recurring feature of these proposals is the inclusion of photonic cavities. The use of cavities enhances the matter-light interaction of a spin-photon interface which can lead to higher entanglement rates and/or higher entanglement fidelities as is the case for emission-based entanglement schemes including Refs. [124, 125]. There are also strong-coupling entanglement schemes such as Refs. [78, 128, 129] which utilize non-linearities of the spin-cavity system to generate spin-photon entanglement. We will discuss both these cavity coupling methods for remote entanglement applications.

2.4.1 Purcell enhancement regime

A key metric for any light emitting atom or solid-state defect is the rate of emission. The emission rate determines the brightness of a centre and the rate at which a centre can be used in a quantum information processing architecture. One of the main uses of defect-cavity systems is Purcell enhancement which increases the emission rate of the defect. Furthermore, Purcell enhancement can increase the radiative efficiency and decrease the effects of spectral diffusion and decoherence. The following treatment allows us to understand this Purcell enhancement, following Ref. [130].

The origin of the spontaneous decay, Γ, from an excited state back to the ground state is coupling between the transition and the quantized vacuum radiation field, this requires a quantum electrodynamics treatment of the interaction, the result of which is

$$\Gamma = \frac{2\pi}{\hbar}\mu_{eg}^2 E_0^2 \rho(\omega_0). \tag{2.25}$$

Where μ_{eg} is the transition dipole moment of the transition from the excited state to ground state [94], E_0 is the electric field of the vacuum modes, and $\rho(\omega)$ is the photonic density of states at the location of the emitter. In a vacuum this expression becomes:

$$\Gamma_{\text{vac}} = \frac{\mu_{eg}^2 \omega_0^3}{3\pi\epsilon_0 \hbar c^3} \tag{2.26}$$

where ω_0 is the angular frequency of the transition.

From Eq. (2.25) we can see that by modifying the photonic density of states the radiative rate can be modified. The density of states of a photonic cavity mode as seen by the emitter placed at the mode maximum of the cavity is

$$\rho_c(\omega) = \frac{\kappa/(2\pi)}{(\omega - \omega_c)^2 + (\kappa/2)^2}, \tag{2.27}$$

which is a normalized Lorentzian with peak frequency ω_c and linewidth κ. The modified spontaneous emission rate for the emitter placed in a cavity is

$$\Gamma_{\text{cav}} = \frac{2\mu^2 Q}{\hbar\epsilon_0 V} \cdot \frac{(\kappa/2)^2}{(\omega_0 - \omega_c)^2 + (\kappa/2)^2}. \tag{2.28}$$

Where Q is the quality factor, ω_c/κ, and V is the modal volume of the cavity defined as the integral of the electric field $\vec{E}(\vec{r})$ within the cavity [130]:

$$V = \frac{\int \epsilon_0 |\vec{E}(\vec{r})|^2 d^3\vec{r}}{\max(\epsilon_0 |\tilde{\mathrm{E}}(\tilde{\mathrm{r}})|^2)} \tag{2.29}$$

The ratio of the decay rate in a cavity to the vacuum decay rate is the Purcell enhancement of an emitter in a cavity, with the Purcell factor, F_P given by

$$F_P = \frac{\Gamma_{\text{cav}}}{\Gamma_{\text{vac}}} = \frac{3\lambda^3}{4\pi^2} \cdot \frac{Q}{V} \cdot \frac{(\kappa/2)^2}{(\omega_0 - \omega_c)^2 + (\kappa/2)^2}. \tag{2.30}$$

On resonance ($\omega_c = \omega_0$) and accounting for the index of refraction n for an emitter in an arbitrary medium, we get

$$F_P = \frac{3}{4\pi^2} \cdot \frac{(\lambda/n)^3}{V} \cdot Q. \tag{2.31}$$

We must also consider a more realistic emitter that has, in general, more decay pathways than the resonant optical transition discussed above. This resonant transition would be the zero phonon line (ZPL) transition, however, there are also optical transitions to the phonon-sideband (PSB). ZPL to PSB fraction is captured by the Debye-Waller factor, η_{zpl}. Furthermore, there may be entirely non-radiative decay pathways, this is captured by the radiative efficiency, η_{rad}. The Purcell enhancement is a resonant effect and only enhances the radiative ZPL emission. Thus the enhanced decay rate for a given Purcell enhancement is [131]

$$\Gamma_{\text{cav}} = F_P \eta_{\text{zpl}} \eta_{\text{rad}} \Gamma_{\text{vac}} + (1 - \eta_{\text{zpl}} \eta_{\text{rad}}) \Gamma_{\text{vac}}. \tag{2.32}$$

By integrating a spin-photon interface into a cavity the rate of emission is increased as the quality factor is increased or the modal volume is decreased. This also increases the radiative component of the decay process increasing the quantum efficiency. Furthermore, a lower lifetime will decrease the time over which spectral diffusion effects can occur, decreasing the pure dephasing linewidth. Finally, as we will discuss in Section 2.4.2, the lower lifetime and lower pure dephasing linewidth increases the coherence of the emitted photon. All these benefits help generate spin-spin entanglement between spin-photon interfaces.

2.4.2 Barrett-Kok entanglement and visibility

One particularly exciting remote entanglement protocol for spin-photon interfaces utilizing emission – and is thus aided by Purcell enhancement – is the one proposed by Barrett and Kok (BK protocol) [125]. The idea is that a spin-photon Bell-state is created with the photonic degree of freedom being a time-bin photon. These photons are routed to arrive at a beamsplitter at the same time which erases which-path information. Recording photon arrivals at two detectors after the beamsplitter performs a partial Bell-state measurement with a 50% success rate. Upon a successful pattern of detector clicks (to be defined below) an entangled state is 'heralded'. This means that while the protocol is statistical in nature the success or failure is known. The click patterns herald the successful creation of an entangled state.

Depending on the pattern of detector clicks one of the odd-parity Bell states will be heralded: $|\Psi^{\pm}\rangle = 1/\sqrt{2}(|\uparrow\downarrow\rangle \pm |\uparrow\downarrow\rangle)$. However, an even-parity Bell state, $|\Phi^{\pm}\rangle = 1/\sqrt{2}(|\uparrow\uparrow\rangle \pm |\downarrow\downarrow\rangle)$, cannot be heralded hence the 50% success rate. Here odd or even parity of a Bell state is defined by the sign of a parity measurement, $\sigma_z \otimes \sigma_z$ on the state: odd for negative, even for positive.

A schematic of the BK protocol is shown in Fig. 2.16. The steps of this procedure are as follows. We assume a high cyclicity and unit efficiency: exciting a $|\uparrow\rangle$ spin will emit a photon and return to the $|\uparrow\rangle$ spin state without a spin flip.

1. Put the two spins (A and B) to superpositions states:
   $1/\sqrt{2}(|\uparrow_A\rangle + |\downarrow_A\rangle) \otimes 1/\sqrt{2}(|\uparrow_B\rangle + |\downarrow_B\rangle)$

2. Optically excite the spin-up to excited state transition and wait for emission. This will entangle each spin with the presence or absence of a photon, denoted $|1\rangle$ or $|0\rangle$ respectively:
   $1/\sqrt{2}(|\uparrow_A, 1_A\rangle + |\downarrow_A, 0_A\rangle) \otimes 1/\sqrt{2}(|\uparrow_B, 1_B\rangle + |\downarrow_B, 0_B\rangle)$

3. Perform a π-pulse to invert the spins:
   $1/\sqrt{2}(|\downarrow_A, 1_A\rangle + |\uparrow_A, 0_A\rangle) \otimes 1/\sqrt{2}(|\downarrow_B, 1_B\rangle + |\uparrow_B, 0_B\rangle)$

4. Optically excite the spin-up to excited state transition and wait for emission. Each spin will now be entangled with a time-bin photon: a single photon is emitted early, in the first excitation round ($|e\rangle \coloneqq |1, 0\rangle$), or a single photon is emitted late, in the second excitation round ($|l\rangle \coloneqq |0, 1\rangle$).
   $1/\sqrt{2}(|\downarrow_A, e_A\rangle + |\uparrow_A, l_A\rangle) \otimes 1/\sqrt{2}(|\downarrow_B, e_B\rangle + |\uparrow_B, l_B\rangle)$ =
   $1/2(|\downarrow_A\downarrow_B\rangle\,|e_A e_B\rangle + |\uparrow_A\uparrow_B\rangle\,|l_A l_B\rangle + |\uparrow_A\downarrow_B\rangle\,|l_A e_B\rangle + |\downarrow_A\uparrow_B\rangle\,|e_A l_B\rangle)$

5. Route the photons to a beamsplitter with single photon detectors on each output. If the photons are indistinguishable the measurement of one early and one late photon photon corresponds to measuring the photonic state $1/\sqrt{2}(|l_A e_B\rangle \pm |e_A l_B\rangle)$. Such a detection projects the spins to a maximally entangled, odd-parity Bell state:
   $1/\sqrt{2}(|\uparrow_A\downarrow_B\rangle \pm |\uparrow_B\downarrow_A\rangle)$.

Note, that this is a simplified description. There will be additional phases due to the relative arrival time and frequencies of the photons which lead to the following heralded state [132]

$$\frac{1}{\sqrt{2}}(|\uparrow_A\downarrow_B\rangle \pm e^{i\phi}|\uparrow_B\downarrow_A\rangle). \tag{2.33}$$

Where the plus or minus is determined by the click pattern of the two detectors and the phase is [132]

$$\phi = (\omega_A - \omega_B)(\tau_2 - \tau_1) \tag{2.34}$$

where $\omega_{A/B}$ are the photon frequencies from A and B and $\tau_{1/2}$ are the arrival times of the first and second photons.

Here we see why a high cyclicity transition is required: a high cyclicity ensures the spin becomes entangled with the presence or absence of a photon in steps 2 and 4. If the transition has low cyclicity then there is a chance that the optical excitation emits a photon but the spin flips during the excitation and decay process. This creates the state $1/\sqrt{2}(|\downarrow_A, 1_A\rangle + |\downarrow_A, 0_A\rangle)$ which has no spin-photon entanglement and will fail to generate entanglement between the two spins.

If we assume a high cyclicity transition above then the next requirement for high fidelity entanglement generation is that the two photons from each emitter are indistinguishable [103]. This means that the photons must be at the same frequency, same arrival time, and same spectral and temporal wave-packet. The indistinguishability of photons is measured by a Hong-Ou-Mandel (HOM) interference measurement [133]. If two indistinguishable photons impinge on a beamsplitter a second-order interference effect occurs resulting in both photons leaving the same port of the beamsplitter — they never leave from separate ports. Suppose a polarizer is inserted before one of the ports of the beamsplitter, as the polarization of one of the ports is rotated the incoming photons will oscillate between maximum indistinguishablility (equal polarizations) and completely distinguishable (orthogonal polarizations). Recording the coincidence counts between the two outputs of the beamsplitter there will be interference fringes as the polarization is continually rotated, the visibility of these fringes is a measure of the indistinguishability of the photons. Specifically, if N_I are the counts at maximum indistinguishability and N_D are the counts when fully distinguishable then the visibility is $V = 1 - N_I/N_D$.

The visibility can be seen as a measure of the probability that the two photons interfere as indistinguishable particles, with $1 - V$ probability that the photons act as distinguishable particles, i.e., they pass through the beamsplitter without interference. For the BK entanglement protocol, distinguishable photons result in no entanglement generation and result in the spins forming an even mixture of the two odd-parity Bell states [134]. This can be seen from Eq. (2.33) which only has odd-parity components due to the specific detector heralding pattern. Assuming everything else is perfect the resulting spin state is a probabilistic mixture of the result from the indistinguishable case — without loss of generality, the Bell state $|\Psi^+\rangle$ — and the distinguishable case — a mixture

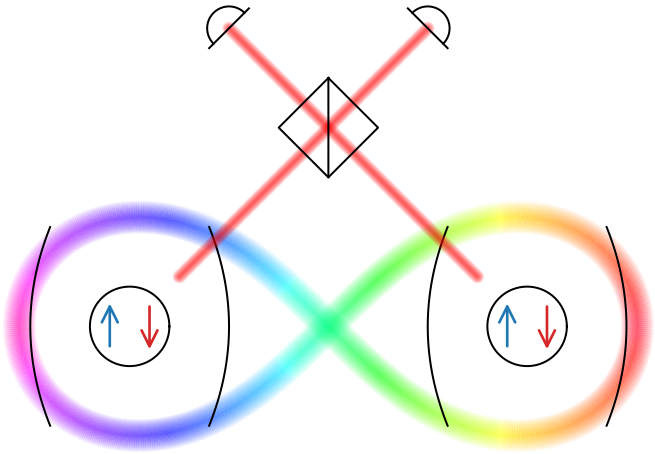

Figure 2.16: **Barrett-Kok entanglement.** Spin-dependent emission from two spin-photon interfaces interferes on a beamsplitter to eliminate which-path information. Upon the measurement of both an early and a late photon (see text) an odd parity Bell state is heralded.

of the two possible outcomes, $|\Psi^{\pm}\rangle$.

$$\rho_f = (1-V)\left(\frac{1}{2}\left|\Psi^+\right\rangle\left\langle\Psi^+\right| + \frac{1}{2}\left|\Psi^-\right\rangle\left\langle\Psi^-\right|\right) + V\left|\Psi^+\right\rangle\left\langle\Psi^+\right|. \tag{2.35}$$

The fidelity of the entangled state is on average [132]

$$\mathcal{F} = \left\langle\Psi^+\right|\rho_f\left|\Psi^+\right\rangle = \frac{1}{2} + \frac{V}{2}. \tag{2.36}$$

The visibility of two photons depends on, in the most general sense, excited state lifetime, frequency detuning, homogeneous linewidth, and spectral diffusion linewidth as discussed in Ref. [103]. Spectral diffusion can be slow compared to the operation of an emitter and thus feedback and stabilization of the transition energy can be performed via appropriate tuning mechanisms (electric-field Stark tuning [135], strain tuning [136], etc.). If spectral diffusion is controlled and made negligible the expression for the visibility is simply [137]

$$\begin{aligned} V &= \frac{\Gamma_{\text{exc}}}{\Gamma_{\text{hom}}} \\ V &= \frac{\Gamma_{\text{exc}}}{\Gamma_{\text{PD}} + \Gamma_{\text{exc}}}. \end{aligned} \tag{2.37}$$

Where Γ_{exc}, Γ_{hom}, and Γ_{PD} are the lifetime-limited, homogeneous, and pure dephasing linewidths as discussed in Section 2.2.1.

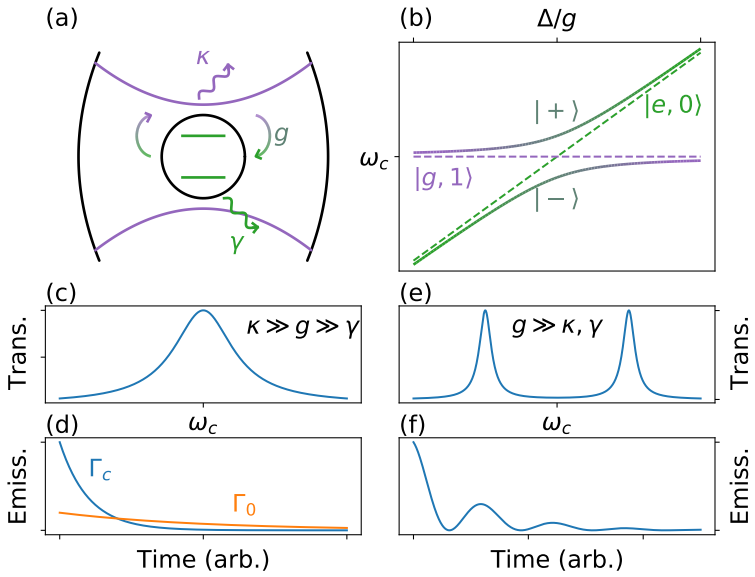

Figure 2.17: **Cavity regimes.** (a) Relevant rates in a coupled cavity-emitter system. (b) Energy levels of the bare atom (green dashed) and bare cavity (purple dashed) as well as the hybridized levels from the Jaynes-Cummings Hamiltonian (solid). Labels of the states are included (see main text for definitions). (c-d) Leaky-cavity regime showing spectra and the enhanced emission rate. (e-f) strong-coupling regime showing the split spectrum and the oscillating emission transient.

Purcell enhancement can increase the visibility of interfering photons by increasing Γ_{exc}. Increasing the lifetime-limited linewidth to be much greater than the pure dephasing linewidth the photons become more indistinguishable and result in higher visibilities and higher fidelity entanglement from the BK protocol. This higher fidelity entanglement can then be used as a resource for quantum computing and quantum communication applications.

2.4.3 Strong-coupling / high cooperativity regimes

In addition to the above discussion of Purcell enhancement and a possible entangling operations we can also consider the properties of a 'strongly-coupled' emitter-cavity system which has alternative remote entangling operations. This is in contrast to the 'leaky-cavity regime' which is the regime in which Purcell enhancement occurs. The emitter-cavity system has three relevant rates [138]: κ the loss rate of the cavity, g the emitter-cavity coupling rate, and γ the loss rate of the emitter. These rates are shown schematically in Fig. 2.17a. The leaky-cavity regime is when $\kappa \gg g \gg \gamma$. The strong-coupling regime, as the name suggests, is the regime in which the emitter-cavity coupling is the dominant rate, $g \gg \kappa, \gamma$. To understand this effect we must consider the Hamiltonian of the emitter-cavity system, the Jaynes-Cummings Hamiltonian [138]:

$$H = \omega_0 \sigma^\dagger \sigma + \omega_c a^\dagger a + g(\sigma^\dagger a + \sigma a^\dagger). \tag{2.38}$$

σ ($\sigma^\dagger$) is the atomic lowering (raising) operators of the emitter system and a ($a^\dagger$) is the annihilation (creation) operators for a photon in the cavity. ω_0 (ω_c) is the frequency of the atomic transition (cavity resonance). The two lowest, non-zero, eigenenergies, corresponding to states $|\pm\rangle$, are

$$E_\pm = \omega_c + \frac{\Delta}{2} \pm \frac{1}{2}\sqrt{(2g)^2 + \Delta^2}, \tag{2.39}$$

where $\Delta = \omega_0 - \omega_c$ is the detuning between the resonant frequencies. These energy levels are shown in Fig. 2.17b. We can consider tuning Δ via, for example, tuning the energy levels of the atomic system with magnetic fields, or tuning the cavity frequency with gas-deposition [139] or laser tuning [140]. Far from $\Delta = 0$ the eigenstates are defined by where a single quanta of energy is located: either the atomic system is in the excited state and there are no photons in the cavity, $|e, 0\rangle$; or the atomic system is in the ground state and there is one photon in the cavity, $|g, 1\rangle$. At zero detuning there is an anti-crossing where these two states mix as the quantum of energy oscillates between the cavity and the atomic systems resulting in the vacuum-Rabi splitting between the $|\pm\rangle$ states [138].

Note that there are no κ or γ terms in these expressions as these are irreversible loss terms whereas the g coupling rate is a reversible interaction. This Hamiltonian, Eq. (2.38) is true for all emitter-cavity systems but the effects of this splitting are only seen when the splitting $2g$ is much larger than the loss terms which broaden the spectra.

The differences between the Purcell and strong-coupling regimes are outlined in Fig. 2.17c-f showing the observed spectra as well as the emission time-dependence which shows oscillations in time in the strong-coupling regime [138]. This is not unexpected as (ideally) the emission time-dependence should simply be the Fourier transform of the spectrum. However, this oscillation showcases the other manner in which these regimes can be considered: the strong-coupling regime is when an excitation in the emitter-cavity system can oscillate between a photonic excitation and an emitter excitation (i.e. occupying the excited state) faster than either isolated system can lose the excitation to the environment.

Finally, we can see how a strongly coupled emitter-cavity system can be used as a spin-photon interface. If only one spin-dependent transition of an emitter is coupled to the cavity then the vacuum-Rabi splitting is only present for the coupled spin-state as shown in Fig. 2.18b. Probing the system at zero detuning would then give transmission or reflection that is dependent on the spin state. This can be used to generate entanglement and perform a full Bell state measurement [128] and can be the basis for a quantum computing architecture [78]. The schematic for this is shown in Fig. 2.18d where two strongly coupled atom cavity systems are connected by two waveguides. Injecting resonant light in the upper left waveguide, the light will only pass through the cavity to the lower waveguide (or vice versa) if the cavity is also on resonance, i.e., when the spin is up. If light is measured in the upper detector it could have been from the light passing through both cavities, $|\uparrow\uparrow\rangle$, or from passing through neither, $|\downarrow\downarrow\rangle$ thus creating an even parity Bell state. Likewise a click on the lower detector heralds an odd parity Bell state.

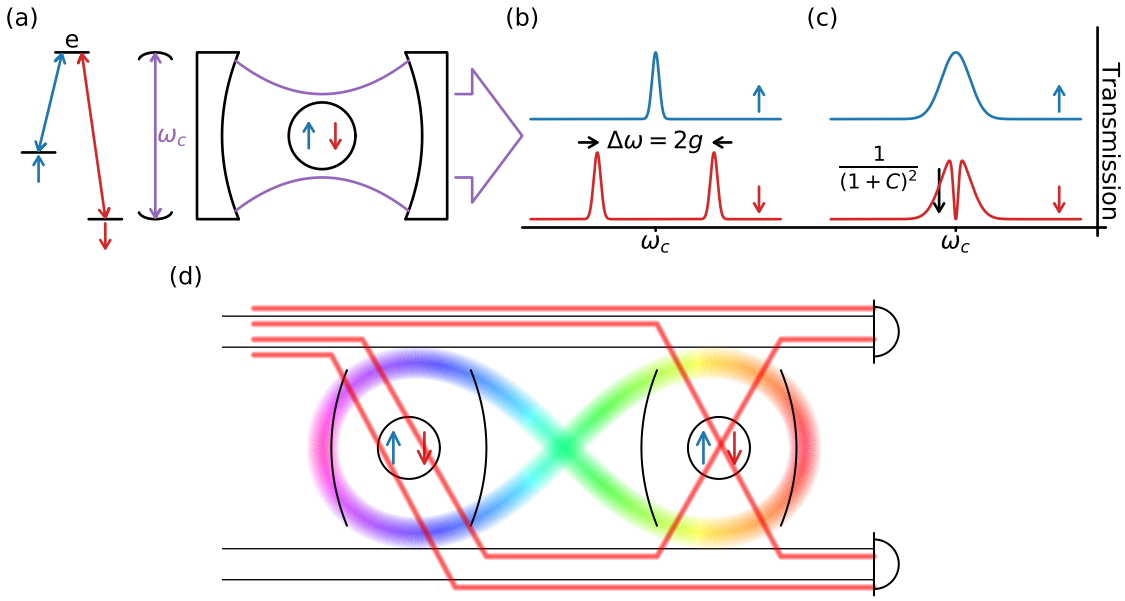

Figure 2.18: **Strong coupling entanglement.** (a) A three-level system within a cavity with one transition resonant to the cavity can exhibit spin-dependent cavity spectra. (b) Strong-coupling regime: vacuum-Rabi splitting of the cavity spectrum when the spin is in the coupled state. (c) High cooperativity regime: dipole induced transparency occurs when the spin is in the coupled state. (d) Two four-port cavity coupled spin-photon interfaces with spin-dependent cavity spectra as in (b) or (c) can generate entanglement via performing a parity measurement by probing along attached waveguides (see text).

In addition to the strong-coupling regime there is the high cooperativity regime that is in some sense between the strong-coupling and leaky-cavity regimes. The cooperativity of a cavity-atom system is a single value that captures all the relevant rates [52, 138]:

$$C = \frac{(2g)^2}{\kappa\gamma}. \tag{2.40}$$

This is a ratio of both the cavity-atom coupling to the cavity and atom decay rates. While the strong coupling regime is when $g \gg \gamma$ and $g \gg \kappa$ the high cooperativity regime is a less stringent requirement, only needing $C \gg 1$.

In this regime there is not vacuum-Rabi splitting, however, dipole induced transparency can result in a similar effect [128]. Dipole induced transparency can result in a dip in transmission that can be used for entanglement in the same manner as in the strong-coupling regime [128]. This transmission dip scales as [52]:

$$T = \frac{1}{(1+C)^2}. \tag{2.41}$$

This effect is illustrated schematically in Fig. 2.18c.

2.5 Defects of interest

We have now discussed, in a general sense, the details and features of spin-photon interfaces: the properties and dynamics of the optical transitions and the ground state spin, along with the incorporation of these interfaces into photonic cavities and use as sources for remote entanglement generation. We will now briefly discuss some spin-photon interfaces and the state of art in the literature.

Afterwards we will discuss the two specific spin-photon interfaces that will be studied for the remainder of this work: singly-ionized selenium-77 and the radiation damage centre known as the T centre. We will discuss the known properties relevant for the following work as well as provide the context for their study, the remote entanglement method most suitable, and remaining open questions.

2.5.1 Literature review

As discussed, spin-photon interfaces have the ability to generate long-range entanglement of their spin components through their photonic interface. This extremely useful ability has led to many research endeavours into many different solid-state spin-photon interface systems. Here we will discuss a few of the more developed systems.

Colour centres in diamond, especially the NV^- centre, are some of the most well studied with a nearly complete microscopic model developed back in the 1970s [141]. Composed of a substitutional nitrogen paired with a carbon vacancy, when in the negatively charged state, NV^-, the defect possesses a spin singlet in the ground state with spin-dependent transitions in the visible wave-

length, 637 nm (1.95 eV) [141]. Importantly, the NV^- centre displays optically detectable magnetic resonance (ODMR) at room temperatures with individual centres having been detected with ODMR in a room temperature confocal experiment [142].

Optically, NV^- centres possess a short excited state lifetime, ~ 10 ns [143], with a high radiative efficiency $> 70\%$ [144], although with a low Debye-Waller factor, $\sim 3\%$ [145]. The NV^- centre has been incorporated into nanophotonic waveguides [135], and cavities [131] with Purcell factors of ~ 70 [131]. High visibilities from emission of two separate NV^- centres has been measured and entanglement has been generated using the Barrett-Kok entanglement protocol [132]. In the ground state, coherence times of ≈ 1 ms have been measured at temperatures of 300 K [146]. The nuclear spin of carbon-13 in the surrounding lattice has been used as a quantum register [147] with up to 50 nuclear memories coupled to a single NV^- centre [148].

While there are many promising experimental demonstrations of NV^- centre as a spin-photon interface there are a few downsides to the NV^- center. The wavelength of the emission is not suitable for silicon photonics and the telecommunication network, requiring conversion to a longer wavelength. The Debye-Waller factor is low, with large emission into the phonon sideband. This requires photonic cavities to isolate the ZPL emission. Furthermore, due to the lack of inversion symmetry the NV^- is highly susceptible to charge noise resulting in large spectral diffusion [136]. Silicon-vacancy centres have been studied as an alternative as these have better optical properties: Debye-Waller factor of 71%, low spectral diffusion, and very coherent emission [149]. However, the SiV has worse ground state coherence properties, requiring milliKelvin temperatures for good performance [150]. Other group IV-based defects in diamond — GeV, SnV, and PbV — are also being studied [151].

Defects in silicon-carbide are a relatively recent area of study with a collection of promising spin-photon interfaces. Silicon-carbide has commercially available six inch wafers [152], it is a complementary metal-oxide-semiconductor compatible material [153, 154] and has a rapidly growing integrated photonics library[155]. As in diamond, a large range of colour centres are present in SiC [155, 156], of which the silicon vacancy centre, V_{Si}, has garnered particular interest. V_{Si} has emission at 900 nm (1.4 eV) and Debye-Waller factor of 40% at 4 K [157], and a radiative efficiency of $> 20\%$ [158]. The V_{Si} centre has the benefit of having inversion symmetry and is very insensitive to charge noise resulting in very low spectra diffusion, and a homogeneous linewidth only a factor of two larger than the lifetime-limited linewidth [159]. Coherence times (Hahn echo) at room temperature of 80–160 μs [160, 161] and coherent coupling to a ^{29}Si nuclear spin via an ESEEM signature in a Hahn-echo measurement have been measured. [159].

Single V_{Si} have been isolated and studied [159, 160]. V_{si} have been integrated into waveguides and retain their optical coherence [162] and have been integrated into cavities [50, 163, 164] showcasing a three- to ten-fold reduction in emission lifetime from Purcell enhancement and a cooperativity of 1.4 [163].

Quantum dots epitaxially grown and self-assembled on III-V semiconductor substrates can be made to emit in the telecommunication band [165–167] – along with the spin of the bound elec-

tron or hole in the dot this comprises a solid-state spin-photon interface. These dots are randomly grown resulting in a large inhomogeneous broadening in ensembles [168] due to local strain, size, etc. ZPL fraction can be 90% for InGaAs dots at 4 K [168], near unity indistinguishability has been demonstrated [169], and high quantum efficiencies have been achieved [168]. Integration into cavities (F_P=7.6) [169] with confocal access and within waveguides have also been realized [170]. The coherence times of dots have been measured to be as high as 4 μs (Hahn-echo, 4 K) with advancement in fabrication to remove lattice mismatch [171].

With their excellent optical properties a range of technical milestones have been reached including spin-photon entanglement of the emission and the spin of single carriers (electrons or holes) within the quantum dot [172, 173], the generation of entanglement between separate quantum dots [174], and to create photonic cluster states [175]. There are even commercially available products that make use of cavity coupled quantum dots for single photon emission [176]. However, some drawbacks exist: due to the random nature of the self-assembly process fabrication requires first identifying dots and then fabricating cavities and devices around the dots [168]. Furthermore, to scale up the system and integrate into silicon photonic based networks a hybrid approaches is necessary requiring evanescent coupling to silicon waveguides and cavities [64].

Rare-earth ions in crystalline hosts are another promising category of spin-photon interfaces. Rare-earth ions such as Yb, Nd, or Er possess intra-4f transitions that are well shielded by remaining valence electrons resulting in a very environmentally insensitive optical transition [177]. This insensitivity allows for the integration into a variety of crystalline hosts, including yttrium orthvanadate (YVO), yttrium orthosilicate (YSO), or silicon, without the optical properties changing appreciably. Depending on the rare-earth ion studied the optical transitions are generally in the range of 800–1000 nm (1.24–1.55 eV), however, erbium possess an optical transition near 1550 nm. The high insensitivity gives near unit radiative efficiencies [178], although at the cost of long excited state lifetimes 0.1–10 ms[179, 180]. The emission is very coherent with near lifetime-limited linewidths [179, 180]. The shielding from the environment can also produce extremely long coherence times of the ground state qubit with a six-hour coherence time at 2 K [181].

Rare earth ions have been incorporated into nanophotonic cavities, both native to the crystalline host [179], and evanescently coupled to silicon photonic cavities [63, 178]. Purcell enhancements of 700 (assuming unit radiative and ZPL efficiencies) have been achieved [178] and single centers have been identified [179, 180]. Photon mediated entanglement generation has been demonstrated with two rare-earth ions in the same cavity [182]. Finally, nuclear spins in the host lattice have been utilized as a register of quantum memory [51].

Erbium in silicon is a subset of the above but is worth mentioning in detail as it is another spin-photon interface that satisfies a lot of the ideal requirements of a scaleable spin-photon interface, as discussed in the introduction. As with the other rare earth ions, erbium in silicon possesses high radiative efficiency transition but with a transition at 1550 nm (0.8 eV) putting it directly in the C-band of telecommunication networks. The excited state transition is long, 0.1–1 ms and dependent on the sub-ensemble measured, yet can be much shorter than erbium in other crystalline hosts [183].

Erbium in silicon has been incorporated into silicon photonic waveguides [183, 184] with very narrow homogeneous linewidths, 20 kHz [183]. Single centres have been coupled to silicon photonic cavities with lifetime reductions of 60 [53].

2.5.2 Selenium

Selenium is a group-VI element which acts as a double donor when in a substitutional site in silicon [91] (shown in Fig. 2.19a). Through Fermi level tuning (e.g. boron compensation [77] or surface effects [186]) the selenium double donors can be singly ionized leaving a single unpaired electron in the ground state that is very tightly bound to the nucleus. In contrast to phosphorus, a group-V single donor in silicon with a binding energy of 45.6 meV [90, 91], Se^+ has a binding energy of 593 meV for the remaining electron [72, 91]. The high binding energy means that excited state levels are spaced such that the ground to first excited state transition is in the optical regime, 2901 nm (437 meV) [72].

In the ground state of Se^+ the electron is in a spherically symmetric 1s orbital which is split into 6 sub-levels from the six-fold valley degeneracy of the silicon conduction band [69]. Valley-orbit interactions lift this degeneracy to a singlet, 1s:A; triplet, 1s:T_2; and doublet 1s:E as shown in Fig. 2.19b. Further spin-valley interactions split the 1s:T_2 into a singlet, 1s:$T_2\Gamma_7$; and a doublet, 1s:$T_2\Gamma_8$ via a spin-valley interaction. Additional details on the orbital structure of the Se^+ system are given in Ref. [69]. Finally, the ^{77}Se isotope possesses a spin-1/2 nucleus (the only stable isotope to possess a spin) creating an isotropic hyperfine interaction with a_{iso} = 1.66 GHz [69, 98].

The ground state Hamiltonian for the $^{77}Se^+$ system — analogous to that of phosphorus — is [69, 77]

$$\mathcal{H} = \frac{g_e\mu_B}{h}B_0S_z - \frac{g_n\mu_N}{h}B_0I_z + a_{\text{iso}}\vec{S}\cdot\vec{I} \tag{2.42}$$

where g_e, and g_n are the electron and nuclear g-factors, 2.0057 and 1.07 respectively [98], and a_{iso} is the hyperfine constant, 1.66 GHz [98]. μ_B and μ_N are the Bohr and nuclear magnetons, h is the Plank constant, B_0 the static magnetic field, and $\vec{S}$ and $\vec{I}$ are the Pauli spin operators for the electron and nuclear spins.

In many ways $^{77}Se^+$is similar to phosphorus in the ground state, however, the key differences, and the reason $^{77}Se^+$was investigated, have to do with the optical transitions available. In phosphorus the only transition is a weakly bound excitonic transition that does not interact strongly with light and has very low radiative efficiency [67] due to the indirect bandgap of silicon and Auger recombination [96, 187]. $^{77}Se^+$on the other hand has a bound-to-bound optical transition that, although forbidden according to effective-mass theory, is symmetry allowed [69] and so was expected to have a high transition dipole moment. Furthermore, initial estimates expected very high radiative efficiencies [74] as a seven phonon decay would be needed for a non-radiatve decay. Both of these made $^{77}Se^+$a promising candidate for a spin-photon interface. The main drawback is the operational wavelength of 3 μm: while optical fibers and integrated photonics are available at this wavelength, detectors and lasers at this wavelength are still in their nascency compared to the in-

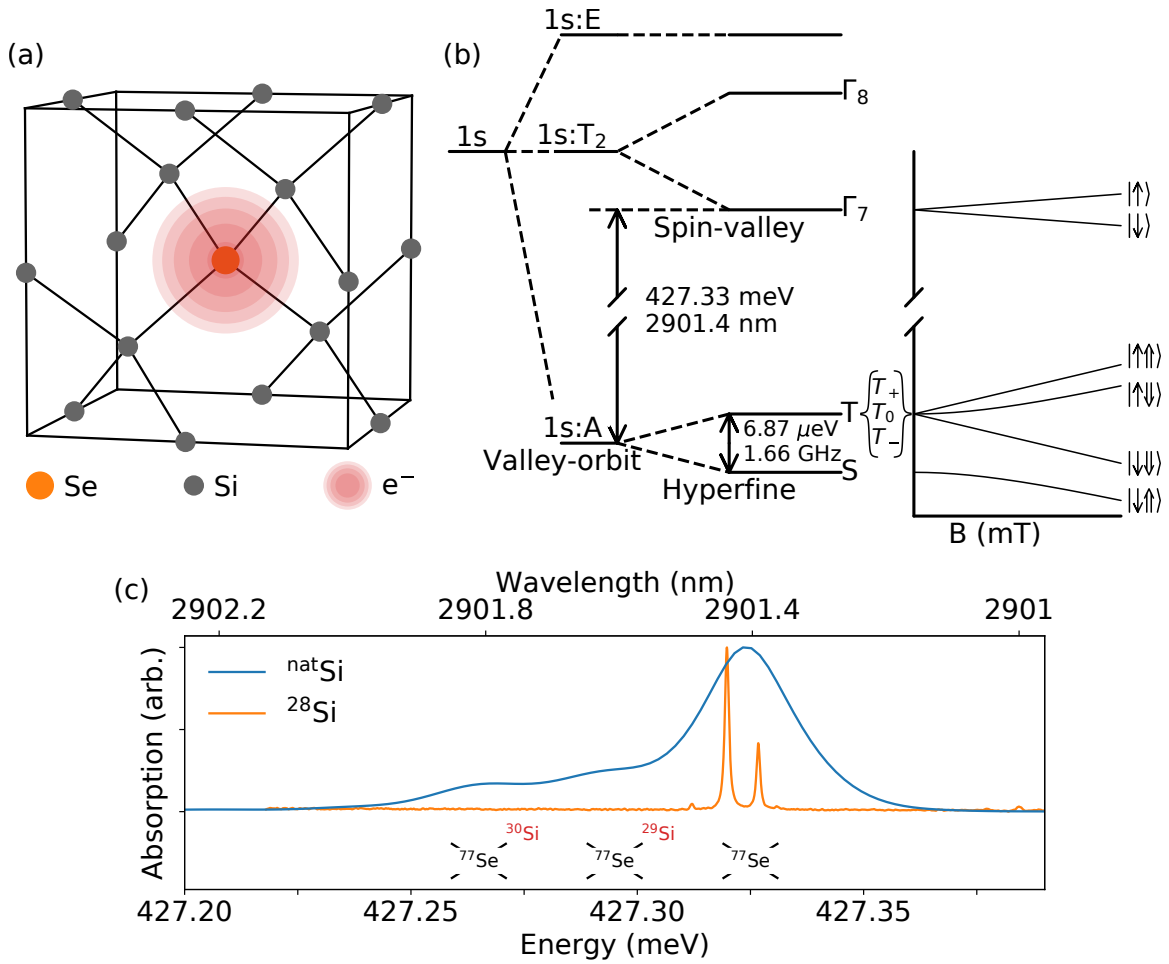

Figure 2.19: **Singly ionized selenium-77.** (a) Se^+ is a substitutional donor with a single unpaired bound electron. (b) Energy levels of $^{77}Se^+$ showing the ground state and first excited states as well as Zeeman/Hyperfine interactions at field (adapted from [185]. (c) Absorption spectrum of the $^{77}Se^+$ 1s:A to 1s:T_2:Γ_7 transition for silicon with a natural abundance of isotopes and isotopically purified ^{28}Si (note the ^{28}Si spectra is shifted in energy to account for the isotopic shift in bandgap). (Insets) Predominant nearest neighbour isotopic compositions of the three peaks in the natural silicon spectrum (^{28}Si are not labeled for simplicity).

dustry standard fiber communication bands: O-band (original-band): 1260–1360 nm, and C-band (conventional-band): 1530-1565 nm [188].

Initial studies of $^{77}Se^{+}$in isotopically purified ^{28}Si showed that in the absence of isotopic inhomogeneous broadening the hyperfine singlet and triplet states in the ground state could be resolved optically at zero field [69, 98]. The absorption spectrum in both ^{nat}Si and ^{28}Si is shown in Fig. 2.19c. Preliminary work used this fact to allow optical hyperpolarization and readout, which, along with MW drive fields, allowed coherent control of the $S_0 \Leftrightarrow T_0$ qubit (see Section 2.3.4) at low field and showed a Hahn-echo T_2 of 2.14 ± 0.04 s [69]. Further work showed a T_1 of over 4 hrs at low temperatures, 2 K, and with sufficient protection from blackbody radiation [77].

Following studies of the optical properties [77] showed a transition dipole moment of 1.96 ± 0.08 Debye indicating a strong interaction with light in absorption. Properties of the emission were also pinned down showing a Debye-Waller factor of 16 ± 1 % and a radiative efficiency of 0.80 ± 0.09 % [77]. As a spin-photon interface operating in a cavity in the strong-coupling regime (see 2.4.3) would be the most viable avenue forward, assisted by the high transition dipole moment. It was predicted that a cavity with a modal volume of $(\lambda/n)^3$ and a quality factor of 10^4 would be sufficient for a cooperativity of 1 [77].

In addition to selenium, both sulfur and tellurium are expected to have promising optical and spin properties as they are also chalcogen double donors. ^{33}S has a spin-3/2 nucleus meaning a hyperfine interaction could be optically accessible in the ground state. Further work to study ^{33}S could definitely be fruitful. ^{125}Te has a spin-1/2 and a ground state hyperfine splitting of ≈3.5 GHz and has also been studied for quantum computing [186].

The operation of the $^{77}Se^{+}$spin-photon interface in the strong-coupling regime as the basis for a networked silicon based quantum architecture is outlined in both Ref. [69] and Ref. [78]. In both cases the incorporation of $^{77}Se^{+}$into silicon photonic cavities based in a silicon-on-insulator (SOI) integrated platform is required. As commercially available SOI is predominately natural silicon rather than isotopically purified ^{28}Si, work towards studying the $^{77}Se^{+}$system in natural silicon was undertaken for this thesis work. The goals of this study were to demonstrate coherent spin control with optical initialization and readout despite the inhomogeneous linewidth obscuring the singlet-triplet splittings (see Fig. 2.19c) as well as to investigate the coherence properties of the $^{77}Se^{+}$ system in the presence of ^{29}Si spins. In fact, the ^{29}Si spins can be very close to the $^{77}Se^{+}$, the inset of Fig. 2.19c shows the nearest neighbour silicon isotopes causing shifts in the transition energy [98]. This means that those $^{77}Se^{+}$ with the highest coupling to ^{29}Si spins can be optically selected and studied for possible quantum computing applications. The results of these investigation are presented in Chapter 5.

2.5.3 T centre

In addition to defects like selenium and phosphorus which occupy a substitutional site of silicon, introduced by implanting or diffusing the element into the silicon lattice, there are radiation damage centres that are created by appropriate lattice damage and heat treatments [80, 86]. The T centre

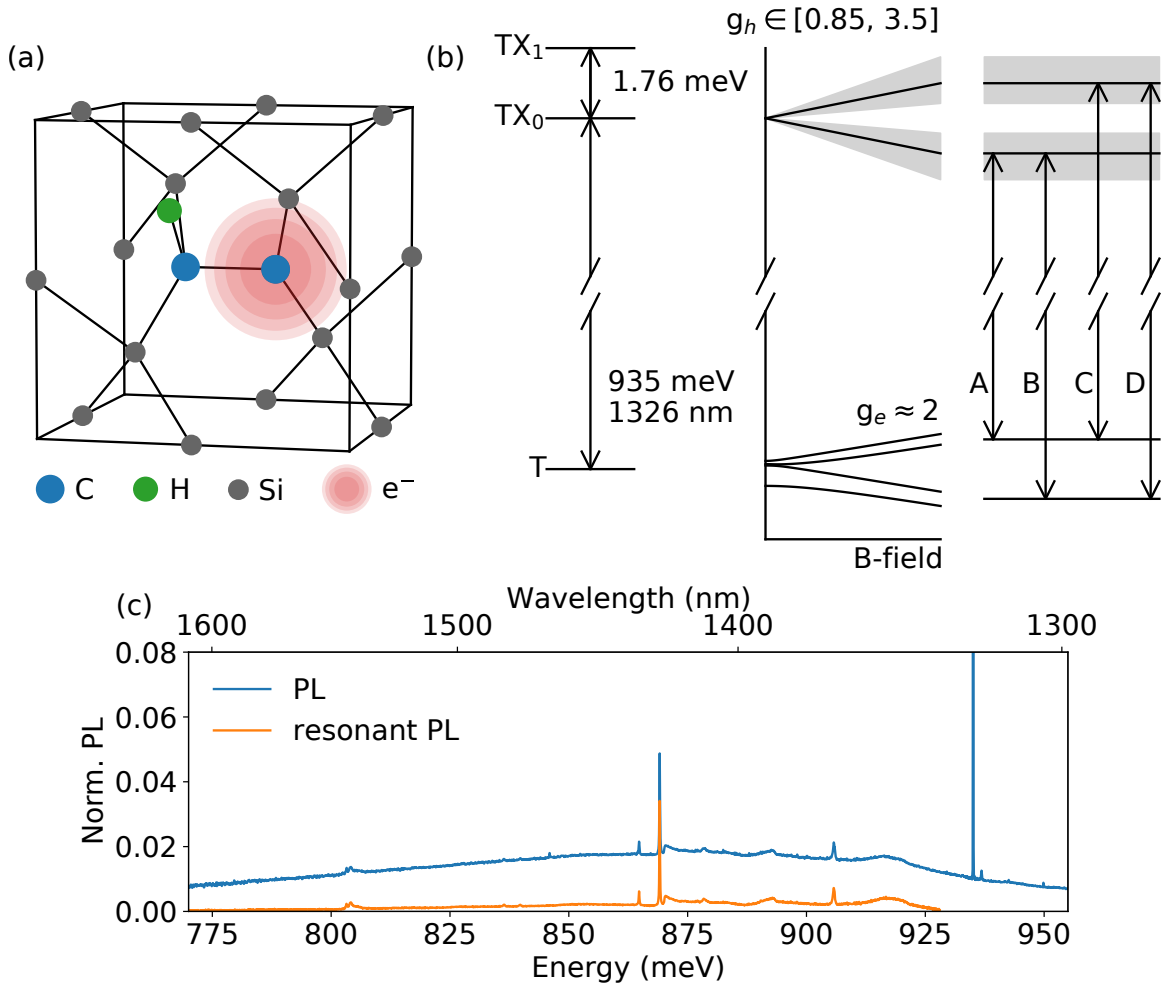

Figure 2.20: **T centre.** (a) The T centre is a carbon-carbon pair occupying a silicon substitutional site with a bonded hydrogen and an unpaired electron. (b) Energy levels of the T centre ground state and the first two bound exciton excited states. Zeeman interaction versus magnetic field is shown displaying the range of hole g-factors in the excited state from the different orientations. (c) Photoluminescence and resonant photoluminescence of the T centre (adapted from Ref. [70])

is one such defect, a multi-particle radiation damage centre [189–191], named 'T' as the chemical composition and structure were unknown at the time of its discovery. The proposed chemical composition is two inequivalent carbons occupying a substitutional site in silicon with an additional hydrogen and an unpaired electron in its ground state [191]. The chemical composition is shown in Fig. 2.20a. The T centre is capable of binding excitons which have a ZPL recombination energy of 935 meV (1326 nm) putting it in the telecommunication O-band.

While the T centre had been known and studied for many years, quantum information prospects were only realized in 2020 [70]. The unpaired electron in the ground state possesses a paramagnetic spin, which, when paired with the spin dependent excitonic transition in the telecommunication O-band, made the T centre an exciting spin-photon interface for further study.

In the bound exciton excited state the ground state electron and exciton electron pair to form a singlet, the remaining spin-3/2 hole is split by the lowered symmetry of the T centre resulting in the spin-1/2 TX_0 state and a higher energy doublet TX_1 1.76 meV above TX_0 [191], a level diagram is shown in Fig. 2.20b. The spin-1/2 TX_0 state exhibits a strong anisotropy with g_h ranging from 0.85 to 3.5, while the unpaired electron in the T centre ground state has an isotropic spin with $g_e = 2.005 \pm 8$ [70] (although a small anisotropy was recently observed [108]). The ground state electron and excited state hole splittings lead to four optical transitions labeled A, B, C, D from lowest to highest energy, this is shown in Fig. 2.20b.

Initial magnetospectroscopy of the centre revealed that there are 12 inequivalent pairs of a possible 24 T centre orientations within the silicon lattice [70, 87]. It is these orientations and the high anisotropy of the hole that leads to the large range of g_h values. In the ground state the electron was shown to have an anisotropic hyperfine interaction with the nuclear spin of the hydrogen. In the diagonal basis the hyperfine tensor is [108, 192]

$$A = \begin{bmatrix} -4.03 \pm 0.01 \text{ MHz} & 0 & 0 \\ 0 & -2.93 \pm 0.01 \text{ MHz} & 0 \\ 0 & 0 & 4.50 \pm 0.01 \text{ MHz} \end{bmatrix} \tag{2.43}$$

The energy levels at low field are shown in Fig. 2.20b.

Photoluminescence spectra are shown in Fig. 2.20c, showing both non-resonant excitation and resonant excitation (data from [70]) wherein the TX_0 transition is driven resonantly and the emission is measured with a spectrometer. In both excitation methods the PSB to lower energy is visible, although for the non-resonant excitation spectra the PSB is superimposed over broadband emission from other radiation damage centres [70, 82]. The lifetime of the transition was measured to be 940 ± 10 ns with a 0.23 ± 0.01 Debye-Waller factor [70]. The radiative efficiency has not been precisely measured only a theoretical radiative efficiency in the range of 0.19–0.72 from DFT modelling [193] and an experimental lower bound of 0.03 [88].

Thermal activation from TX_0 to TX_1 is possible for elevated temperatures leading to dephasing and large homogeneous linewidths [70]. At low temperatures below 2 K when thermal activation from TX_0 to TX_1 is frozen out the inhomogeneous linewidth in natural and isotopically purified

silicon is 6.5 GHz and 33 MHz respectively [70]. Absorption measurements determined a transition dipole moment of 0.73 ± 0.02 Debye [70] (assuming unit radiative efficiency) requiring a cavity with modal volume $(\lambda/n)^3$ and a Q factor of 10^4 to achieve a cooperativity of 1.

In addition to measuring the optical properties Bergeron et al. [70] studied the coherence properties of the ground state spins – both the unpaired electron and the hydrogen nuclear spin. In isotopically purified silicon the coherence times of the electron and nuclear spins were measured to be 2.1$\pm$0.1 ms and 1.1$\pm$0.2 s respectively, with T_1 lifetimes longer than 16 s [70].

The excellent coherence times, taken with the very appealing and technologically accessible telecommunication optical transition made the T centre an exciting candidate for quantum information studies. Further work incorporated T centres into silicon-on-insulator samples via implantation [87] and confocal measurements of SOI samples resulted in the first isolation of single spins in silicon [88].

As the basis of a quantum network, the T centre could be utilized as either an emissive defect in the Purcell regime or in a cavity-atom system in the strongly coupled regime. In either case, the T centre would need to be integrated into silicon photonic cavities and connected via waveguides. Further studies would be required to establish the coherence properties of the optical transition in integrated photonics to inform the cavities necessary for entangling procedures. While spectral diffusion linewidths have been measured in both unpatterned SOI (1 GHz) and patterned devices ($>$ 660 MHz) [87, 88] the homogeneous linewidth had not been measured. This thesis work investigates the optical properties, including the homogeneous linewidth, of integrated T centres along with comparisons to other materials.

Chapter 3

Experimental Techniques and Sample Preparation

In this chapter we will discuss the preparation process and details of the samples studied in the thesis. In addition we will discuss the experimental setups and techniques used to study the samples.

3.1 Optical spectra

In addition to the experimental details specific to the selenium and T centre work, here we will present a general discussion of optical spectra measurements. These techniques for measuring optical spectra are important for understanding the samples and the centres of interest and will be a common results among the following chapters.

Firstly, a transmission spectrum can be measured by sweeping the wavelength of a laser across a transition and measuring how much light is transmitted through the sample. An example is shown in Fig. 3.1a-b. A transmission spectrum can also be measured in a non-resonant manner by using a broadband excitation source and using a spectrometer, such as a Fourier-transform interferometer (FTIR) or grating spectrometer, to measure the transmission spectrum. A transmission spectrum, $I(\omega)$, can be converted to an absorption spectrum, $\alpha(\omega)$, as

$$\alpha(\omega) = -\frac{1}{L} \ln \frac{I(\omega)}{I_0(\omega)} \tag{3.1}$$

where L is the length of the sample measured and $I_0(\omega)$ is a reference spectrum without the sample. An absorption spectrum factors out the sample geometry and results in a spectrum that is consistent between samples that used to determine concentration of a defect via the transition dipole moment or vice versa [94, 185].

In the same manner that a transition can be studied in transmission it can also be studied in emission by sweeping a resonant laser across the transition and measuring the emission from the sample (Fig. 3.1c). The monitoring of the emission can be done in the lower energy phonon sideband as this allows the probe laser to be filtered out. The probe laser can also be removed via time-gating:

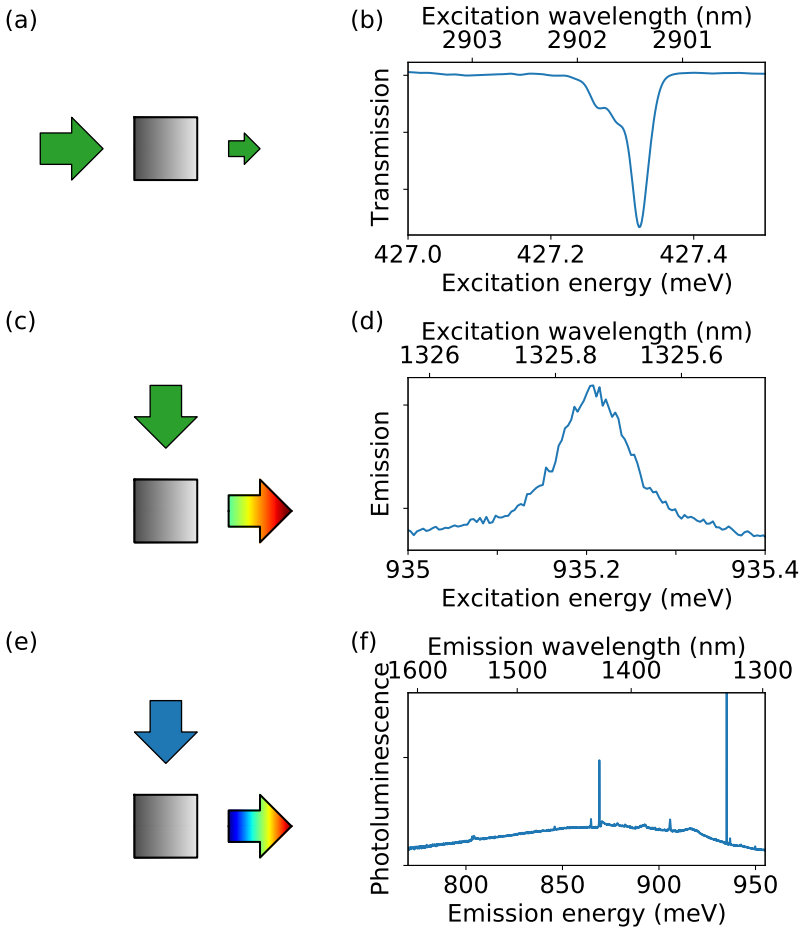

Figure 3.1: **Optical spectra.** (a) Schematic of a transmission measurement: a sample is probed with light, the ratio of output to input intensities at a given wavelength gives the transmission spectrum, (b) Selenium spectrum showed as an example spectrum. (c) Schematic of a photoluminescence excitation (PLE) spectroscopy measurement: a sample is probed with light and any resulting luminescence from the photon sideband is collected to create a spectrum. (d) T centre PLE spectrum shown as an example spectrum collecting emission in the phonon sideband. (e) Schematic of a photoluminescence (PL) measurement: a sample is illuminated with aboveband gap light driving emission from emitters in the sample. The spectrum of the emitted light gives a PL spectrum, f) T centre PL spectrum shown as an example spectrum (from [70]).

by pulsing the probe and only measuring luminescence after the pulse. In this case all emission can be recorded. This is known as photoluminescence excitation (PLE) spectroscopy, an example of which is shown in Fig. 3.1c-d.

In addition to resonant excitation, the emission of a sample may be studied non-resonantly via above bandgap excitation and photoluminescence spectroscopy. An above bandgap excitation with energy greater than the bandgap energy excites free excitons. These excitons my bind to defects where they can recombine to generate emission. Above bandgap excitation can also generate emission from bound-to-bound transitions such as in Se^+ as seen in Ref. [69]. This can be explained as follows: without excitation neutral Se will be compensated by neutral acceptors such as B to create Se^+ and B^- defects; when excited by above bandgap light, the B^- will be neutralized by the created holes from the excitation; a donor-acceptor transition can again compensate the Se^+ to Se^{++} and B to B^-; finally the Se^{++} can capture an electron from the above bandgap excitation which will undergo a phonon cascade to the first excited state of Se^+ before decaying to the ground state and emitting a photon. In either case, this is known as photoluminescence (PL). A sample is excited and a spectrum of the emitted light is measured with e.g. a FTIR or a grating spectrometer. An example is shown in Fig. 3.1e-f. Additionally, a system can also be driven resonantly with the spectrum of emission measured as above, this is known as resonant photoluminescence.

3.2 Selenium

This work aims to measure the ground state properties of the singly-ionized selenium-77 isotope system ($^{77}Se^+$) in a natural silicon environment. This requires a $^{\mathrm{nat}}$Si sample with sufficient $^{77}Se^+$ concentrations, a cryogenic environment, and a setup in which to perform optically detected magnetic resonance (ODMR).

3.2.1 Sample

The sample used was originally created for the work in Ref. [77] as part of my Masters work. The base material of the sample is a 1–5 Ω-cm P-type natural silicon wafer (0.5 mm thick), measured to have [B] = $(4.7 \pm 0.7) \times 10^{15}$ cm^{-3}. The high resistivity is selected to compensate the selenium to produce singly-ionized selenium. We perform a high temperature diffusion of selenium into the wafer at 1200 °C for 7 days with a solid $^{77}SeO_2$ diffusion source sealed together with the sample in a quartz ampule. We use $^{77}SeO_2$ as silicon sublimates intensely in selenium vapour resulting in gross physical damage to silicon surfaces whereas SeO_2 has been successfully used to diffuse into silicon without surface damage [194]. The oxygen creates a passivating SiO_2 surface through which the selenium diffuses without etching. From the solubility and diffusivity of selenium [195] we expect a nearly uniform selenium profile with a concentration $> 10^{16}$ cm^{-3} in excess of the boron concentration. We confirm the compensation of all the boron my measuring the boron split-off band hole transition, 2p′ [196], see Refs. [77, 185] for more details.

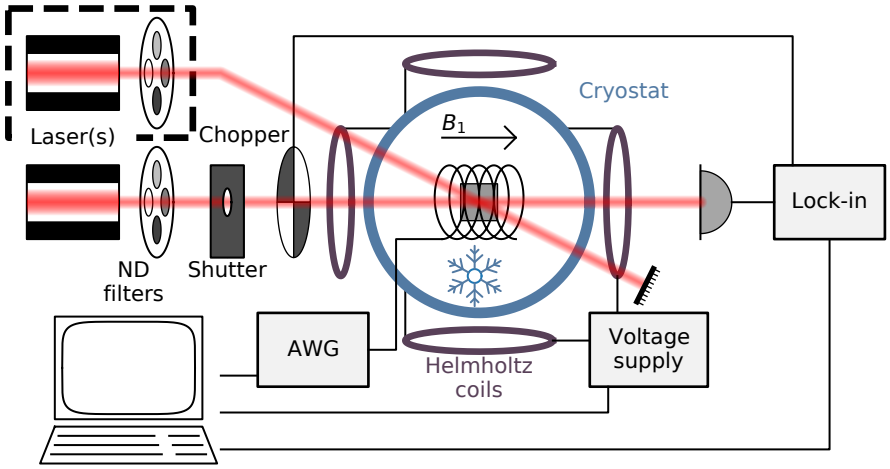

Figure 3.2: **Experimental setup for selenium studies.** Lock-in measurements are made on the transmission of light through the selenium sample with a probe laser and an optional pump laser. The sample is in a liquid helium immersion dewar, with Helmholtz coils around the sample. A resonator (illustrated as a coil around sample) is used to deliver the MW drive B_1 field, either pulsed (arbitrary waveform generator, AWG) or continuous. ND filters and a shutter allow for power control and pulsing of the laser.

After diffusion the sample was polished and etched in 10:1 HNO_3:HF to remove the surface oxide and any shallow diffused contaminants (Al, Ga, and As [185]) in the surface of the sample ($\approx$ 100 µm removed). The sample was then scribed and split into 4 pieces which were stacked to have a higher absorption of the probe laser and therefore a greater optical depth when illuminated normal to the surface.

3.2.2 Experimental setup

The experimental setup shown in Fig. 3.2 is used to perform a variety of optical and magnetic resonance measurements on the selenium sample including optical wavelength scans, hole burning, continuous wave (CW) ODMR, and pulsed ODMR.

At the center of the setup is a Janis liquid helium immersion dewar which is used to cool the sample to 1.4 K by pumping on the helium bath below the superfluid lambda transition. The sample is mounted in a loop-gap resonator to generate the B_1 field: the sample is mounted within a quartz tube (14 mm ID, $\sim$ 50 mm long) which is wrapped in copper tape with a slit cut down the length, moving a paddle with copper tape closer or further from the slit changes the capacitance of the resonator and changes the resonant frequency. The paddle is mounted such that it can be adjusted via a rod extending to the top of the sample rod for in-situ tuning. MW signals are coupled into the

resonator with a loop terminated coaxial cable. The resonator was tuned to the proper resonance after every cooldown using a network analyzer.

Surrounding the dewar are homemade Helmholtz coils – to generate the static magnetic field B_0 – positioned along two axes of the setup: parallel and perpendicular to the B_1 field. These coils are powered by an Agilent E36232A sourcemeter to provide current through the coils. The sourcemeter is, in turn, connected to the controlling PC allowing a fully remote control of the magnetic field environment. The coils were calibrated with a Gaussmeter, confirmed by the known splittings of the $^{77}Se^{+}$ T_{+-} transitions [69, 98].

MW signals to the resonator are generated using either a Agilent E8257 signal generator for CW excitation or an Agilent M8190A arbitrary waveform generator (AWG) for pulsed excitation. In both cases an optional 45 dB MW amplifier can be included to increase the power with 5, 10, 20 dB attenuators for fine tuning. The AWG was used to supply arbitrary pulsed MW waveforms to the resonator with control of both frequency and phase. For pulsed experiments a PulseBlaster is used to send triggering pulses to all relevant instruments, including the AWG, optical shutter, and lock-in.

The sample is excited optically by either one or two Nanoplus 2902 DFB diode laser with individual power control from separate ND filter wheels and individual wavelength tuning provided by either a Thorlabs ITC4001 or an SRS LDC500 laser diode controller with $approx$5 nm of tuning range. The ITC4001 was originally used but was upgraded to an SRS LDC500 as it has better current stability. The probe laser is modulated with a 1 kHz optical chopper and aligned to pass through the sample and be focused onto the detector. The probe also passes through a shutter for pulsed control. The optional pump laser is aligned to pass through the sample avoiding the detector. Transmitted light from the probe is measured with a Teledyne Judson Technologies liquid-nitrogen-cooled InSb detector with a filter (cutting off above 3 μm) within the detector also cooled by the liquid nitrogen. An external CaF_2 lens is used to focus the laser light onto the detector area. Lock-in detection is performed using a Zurich MFLI lock-in along with the 1 kHz optical chopper modulating the laser.

Continuous wave optical detected magnetic resonance

Experimentally we make extensive use of optically detected magnetic resonance (ODMR) which consists of the application of microwave (MW) frequencies to the resonator which changes the ground state populations resulting in a change in the transmission of a pump laser.

In the case of continuous wave (CW) ODMR we excite the sample with the chopped laser and apply a single MW tone to the resonator. Without the MW tone the laser will hyperpolarize the system, pumping the system into dark states resulting in low absorption, i.e., high transmission. If the MW frequency is present and resonant with any transitions between the hyperpolarized and depleted states the system will depolarize, bringing population back in resonance with the pump laser. We measure this as a reduction of transmission of the pump laser using a lock-in measurement with a long time constant relative to the chopping speed, generally 30 ms with a 12 dB/octave

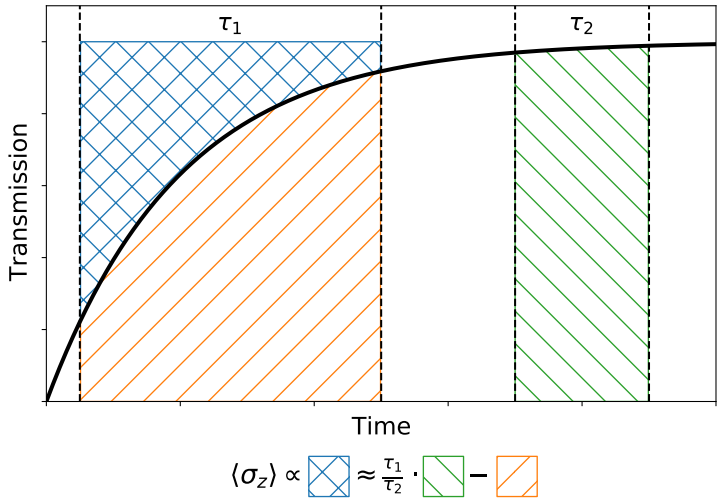

Figure 3.3: **Pulsed ODMR transient readout.** Schematic diagram of how the transient area is measured which is proportional to the population (denoted $\langle\sigma_z\rangle$) in the state the laser is resonant with. The equation shows how the area is approximated based on the area of two measurement windows.

frequency filter roll off. In this manner the MW frequency can be swept and a transmission vs MW frequency spectrum can be measured.

Pulsed ODMR

For pulsed ODMR we initially hyperpolarize the system as before, however, in this case a shutter is used to block the light while the MW pulse(s) are applied. Upon opening the shutter a subsequent hyperpolarization transient will occur, the depth of which will be a measure of the population in the addressed state (see Section 2.2.3). We take the area above the transmission transient to be proportional to the population in the addressed state. We again perform a lock-in measurement of the transmission but with a much shorter time constant, generally 2 ms with a 24 dB/octave filter roll off. To obtain the transient area – specifically the area above the transmission vs time transient (see Fig. 3.3) – we integrate the demodulated signal for a measurement window during the transient and subtract from it an integrated signal from a later measurement window after the transient has disappeared. Figure 3.3 shows a schematic diagram showing this transient measurement. The integration is either done in post-processing of the recorded demodulated signal or the demodulated signal is output from the lock-in to a voltage-to-frequency converter and a counter is used to measure output of the converter. The counts for each measurement window are an analog measure of the area below the transmission versus time transient.

The pulsed measurements we perform are Rabi measurements (see Section 2.3.3) and Hahn-echo measurements (see Fig. 2.11). A Rabi measurement allow us to calibrate the system to obtain the pulse duration for $\pi/2$ and π pulses. These calibrations depend on the transition probed, the set MW power, the cavity coupling and cavity Q factor. As such, we repeat the Rabi pulse calibration every day to account for changes during cooldown and for every magnetic field and frequency to be used.

For the Hahn-echo pulse sequences we use a method known as phase-cycling [69] to obtain echo transients. For every dark time set we measure two Hahn-echo pulse sequences with different initial $\pi/2$ pulse phases and take the difference of the transient measurements. The only difference between the two pulses is the phase of the initial $\pi/2$ pulse. As discussed in Section 2.3.3 the phase of a MW pulse changes the axis of rotation, the two phases used differ by 180 degrees to have an initial X and an initial -X pulse. These phases are set by the AWG. The result is that each pulse sequence refocuses the system to different eigenstates $\pm$Z. The two Hahn-echo signals will decay from a maximal/minimal signal to an intermediate signal. The difference signal decays from a maximum to zero. This Hahn-echo method removes any background and importantly any slow drift in the system.

3.3 T centre

In this thesis we integrate the silicon T centre with silicon photonic waveguides. This requires an SOI compatible T centre fabrication recipe, the designing and fabrication of silicon photonic devices, and a measurement apparatus able to probe the hundreds to thousands of on-chip devices at cryogenic temperatures. Here we present the fabrication steps for the SOI sample as well as a description of the photonic devices printed, and a description of the cryogenic alignment and measurement rig. Finally, descriptions of additional bulk ensemble samples and measurement procedures are discussed.

3.3.1 Integrated photonic sample

The sample creation process begins with a 8 inch wafer of Czochralski SOI with a 220 nm device layer (P-type, 50–100 Ω-cm) atop a 3 μm buried oxide layer all mounted on a 700 μm silicon handle. The T centres are generated following the recipe from Ref. [87]: a two-step carbon and hydrogen implantation scheme.

1. Carbon-12 implant at a dose of 7×10^{13} cm^{-2} and energy of 38 keV.
2. A rapid thermal anneal (RTA) at 1000 °C for 20 s in an argon background to substitutionalize the carbon.
3. Hydrogen implant at a dose of 7×10^{13} cm^{-2} and energy of 9 keV. This is to both introduce hydrogen and generate interstitial carbon.

4. The wafer is diced to 2 cm$\times$2 cm squares using a rough-cut manual cleave followed by a precision deep-etch dicing process.

5. An anneal in 100 °C de-ionized water for 1 hour to increase hydrogen concentration.

6. RTA at 405 °C for 4 minutes.

Implantation was performed by Innovion, the first rapid thermal anneal was performed by Marvell Nanofab. Simulations of the implantation profiles using the TRIM software are shown in Fig. 3.4a along with a secondary ion mass spectrometry (SIMS) measurement of the carbon before the final heat treatment. This SIMS measurement was done by EAG Laboratories. Note that the exact depth of SIMS measurement may not be accurate as there was a contamination on the surface as noted by the EAG technicians. The peak at 260 nm is indicative of the Si-SiO_2 interface.

The devices fabricated on chip are the basis for any on-chip networked architecture: photonic waveguides for routing light and a sub-wavelength grating coupler for coupling light on and off chip. The design and layout of the devices and chip was performed by my colleagues Camille Bowness and Daniel Higginbottom. The waveguides are 450 nm wide strip waveguides, selected to have minimal loss while remaining single mode at 1326 nm based on simulations using Ansys Lumerical software. The electric-field magnitude mode profile of the fundamental transverse electric (TE) mode is shown in the inset of Fig. 3.4b.

A sub-wavelength grating coupler (GC) [58] is a periodic structure of high and low index material that acts to Bragg diffract out-of-plane light to in-plane light or vice-versa. The grating is arranged in elliptical curves so the defracted light is focused onto the input of a waveguide with a tapered section to assist the mode matching. Conversely light can be outcoupled in the reverse direction. A scanning electron microscope image of an example GC device is shown in Fig. 3.4d. GC devices fabricated on this sample are full-etch GCs, low index etched sections have all silicon removed (see Fig. 3.4c) as opposed to a partial etch GC which have a set depth of silicon etched away. A full-etch device allows all fabrication to be done in one etch step rather than multiple etch steps.

The GC parameters are optimized, in simulation, for transmission either at 1326 nm the ZPL frequency (0.572 duty cycle, 0.325 fill factor, 672 nm period) or 1387 nm, the PSB frequency (0.606 duty cycle, 0.315 fill factor, 716 nm period) (see Ref. [58, 197] for parameter definition). Additionally, all the features are biased and made slightly smaller or larger ([-9, -7, -5, -4, -1, 1, 3] nm) to account for over/under etching during fabrication which can result in larger or smaller feature sizes than expected. A to-scale side-on profile of a 1326 nm device (bias = 0) is shown in Fig. 3.4c. These designs were the result of an optimization search performed on the three variables to maximize the transmission into the fundamental TE mode of the waveguide (performed in Lumerical) at the two wavelengths of interest. The GCs were design to operate at an incident angle of $38\,^{\circ}$. Fabrication of the sample was performed by Applied Nanotools using e-beam lithography with a negative photoresist (i.e. the material that remains is exposed to the e-beam), namely hydrogen silsesquioxane (HSQ).

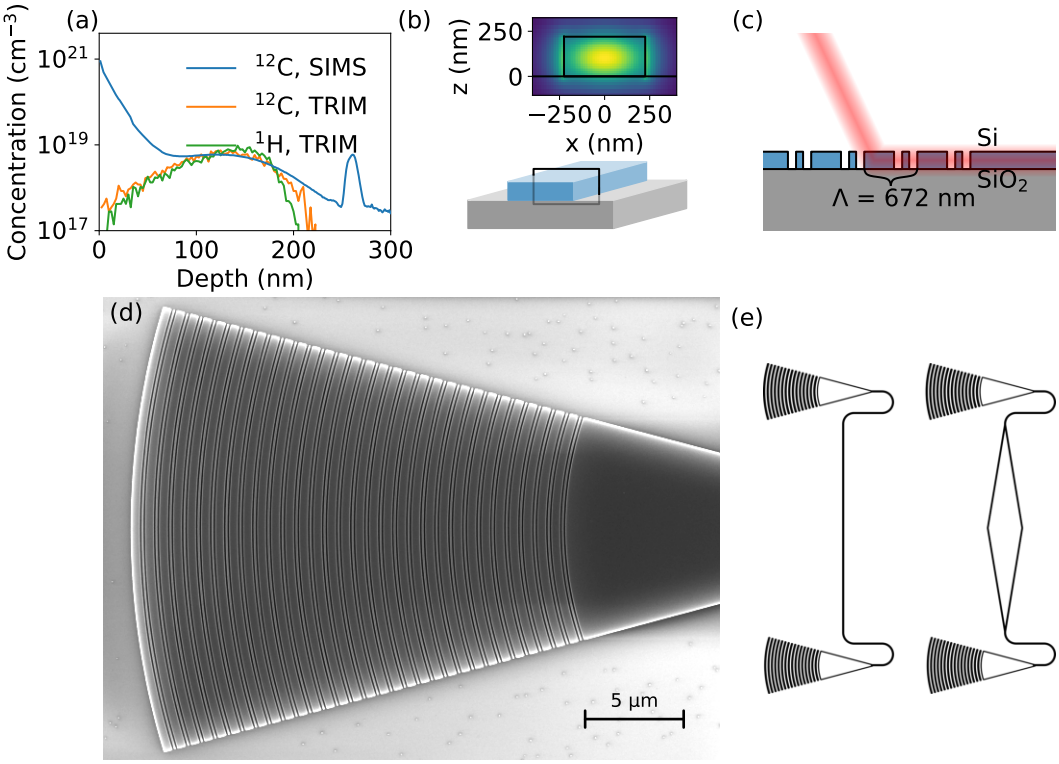

Figure 3.4: **Integrated photonic components for T centre study.** (a) Simulated implantation profiles of carbon and hydrogen (TRIM) and measured carbon profile after initial heat treatment (SIMS). (b) Waveguides are etched into the SOI wafer. (Inset) Electric field magnitude mode profile of transverse electric mode within the waveguide. (c) Side-on schematic of a grating coupler showing the sub-wavelength grating and the Bragg diffraction of light from out-of-plane to in-plane. (d) SEM image of the fabricated grating coupler used for injection of light into the waveguide. Image provided by Applied Nanotools. (e) Schematic of devices printed (not to scale). Left, waveguide device, right, taper device.

Two different waveguide devices were fabricated on the SOI sample these are shown in Fig. 3.4e. The first is a single mode waveguide connecting two different GCs separated by 254 μm, the total waveguide length is 360 μm. The second has a waveguide that tapers out to a greater width before tapering back to the single mode width. This allows an environment that is more 'bulk-like' than the narrow single mode waveguide – the T centres will be further away from interfaces that might have charge traps causing spectral diffusion. Devices that taper to a width of [1, 2, 5, 10, 15] μm are fabricated.

Both devices have the middle section loopback to align with the grating couplers. This allows for a third possible excitation pathway illuminating the middle of the waveguide/taper. This will be discussed more below, see Fig. 3.5. The grating couplers used for each device are one ZPL-GC and one PSB-GC. This combination allows for on-chip filtering when performing PLE measurements detecting on the sideband. In experiments the PSB-GC only provided ≈ 10 dB of ZPL filtering, thus necessitating additional filters on the detection pathway.

3.3.2 On-chip measurements

Coupling light in and out of these devices requires positioning optical fibers at precise locations ($\approx$ 10–20 μm vertically, $\approx$ 5–10 μm horizontally) and at a precise angle. This is achieved with a fiber block: a quartz block that holds four optical fibers at a spacing of 127 μm. This fiber block is polished to an angle of 25 degrees, which when accounting for the diffraction of the light exiting the fiber, gives a light incidence angle of $38\,^\circ$ when the fiber block surface is parallel to the surface of the chip. The fiber block was fabricated by Fibertech Optica with a mounting into a brass ferrule, it is shown schematically in Fig. 3.5b.

The fiber block addresses the requirement for a relative alignment between the fibers – a crucial requirement for multi-port devices. To position the fibers to an absolute alignment with the device, the chip is mounted on a three axis piezo-driven nanopositioner, Fig. 3.5b. Two Attocube ANPx101 and one ANPz101 stages are used as they are vacuum and low-temperature compatible. Alignment is performed with an optical microscope to confirm vertical spacing at room temperature first before cooling down the chip, Attocube, and fiber block stack. Thermal contraction of components is tracked by using a cryo-compatible reflection-based optical range finder (Philtec mDMS-RC100) which is calibrated at room temperature before the cooldown. The entire optical stack is mounted to the 1 K stage of a BlueFors dilution refrigerator with an operating temperature of ≈ 1 K (4 K) when the ^{3}He mixture is (not) circulating.

The chip was mounted to the Attocubes using a plastic clamp surrounding 3 sides of the chip leaving the optically active area exposed. The sample is clamped to a copper sample mount that had heat sinking to the 1 K BlueFors plate. The sample mount had an optional inclusion of a neodymium (NdFeB) magnet (12.7 mm diameter, 3.175 mm thick) directly below the chip. The magnetic field was measured to be ≈270 mT at room temperature and expected to be decreased to ≈230 mT at the operating temperatures due to the spin reorientation below 135 K [198]. Mounted in sample holder, at 1 K, we infer a field strength of 210 mT (see Section 6.3.3).

Figure 3.5a illustrates the optical components used for resonant optical excitation and broadband scanning for device spectroscopy. These capabilities are both provided by a Toptica CTL 1320 tunable laser locked to a Bristol 871A-NIR wavemeter with a PID loop allowing accurate wavelength sweeps (tuning range of 1300–1370 nm). ND filters allow for power control. A 99:1 splitter is used to divert the majority of the laser power to a Thorlabs PDA20CS2 photodiode to stabilize/measure the power with the $1\,\%$ used sent to devices. Polarization control is provided by a polarizing beamsplitter followed by a tunable half-wave plate. An Iridian 1326 ± 1 bandpass filter is included to remove non-resonant emission. An additional optional laser is available to be combined into the same pathway with a fiber beamsplitter. This second laser was either an identically setup Toptica CTL 1320 tunable laser or a Nanoplus 1326 DFB diode laser (with SRS LDC500 laser diode controller). In the case of the Nanoplus, ND filters and a 1326 bandpass filter are used along with a Thorlabs MX10A for its power calibrated variable optical attenuator. Both lasers have an optical modulator to provide fast optical pulsing. The modulators were either a Jenoptick electro-optic modulator (EOM) controlled by a Thorlabs MX10A or later a Brimrose acousto-optic modulator (AOM) controlled with an amplified 100 MHz frequency source (Taitien NI-100M-2900) pulsed with a high extinction RF switch (Mini-Circuits ZASWA-2-50DRA+, >90 dB extinction) to provide higher extinction. The EOM provides an extinction of 20 dB, while the AOM provides more than 60 dB. An additional above-band gap laser is used to non-resonantly excite the middle of the devices: either a 450 nm continuous wave laser (Thorlabs CPS450) or a 965 nm pulsed laser (Picoquant LDH 965).

The output light can be directed to either a single photon detector with a 1340 nm longpass filter to remove ZPL light for PLE measurements or to a high sensitivity grating spectrometer (Princeton HRS-300 grating spectrometer imaged by a Princeton NIRvana liquid-nitrogen cooled InGaAs camera) for PL spectra as shown in Fig. 3.5a. Time tagging of the single photon detector is done with a Swabian Time Tagger Ultra. The single photon detector used was an avalanche photodiode APD, (IDQ ID230 InGaAs/InP) and later upgraded to a superconducting nanowire single photon detector SNSPD, (IDQ ID281). Output from either GC could be routed to either detector system.

For pulsed measurements either an SRS DG645 digital delay generator or a PulseBlaster TTL generator was used to trigger relevant instruments with TTL pulses including the AOMs/EOMs and the time tagger.

3.3.3 Bulk measurements

Bulk T centre sample measurements were performed by mounting samples in a stress-free manner to the end of a sample rod which is cooled in a Janis VariTemp or Cryo Industries of America variable temperature liquid helium dewar (< 1.4 K). Bulk photoluminescence is measured by exciting the sample with a 200 mW 532 nm CW laser, 8 mm spot size, and the emission is collected and routed to a Bruker IFS125HR interferometer with a Ge-diode detector. Specifics of the bulk samples used and the hole-burning measurement details are outlined below.

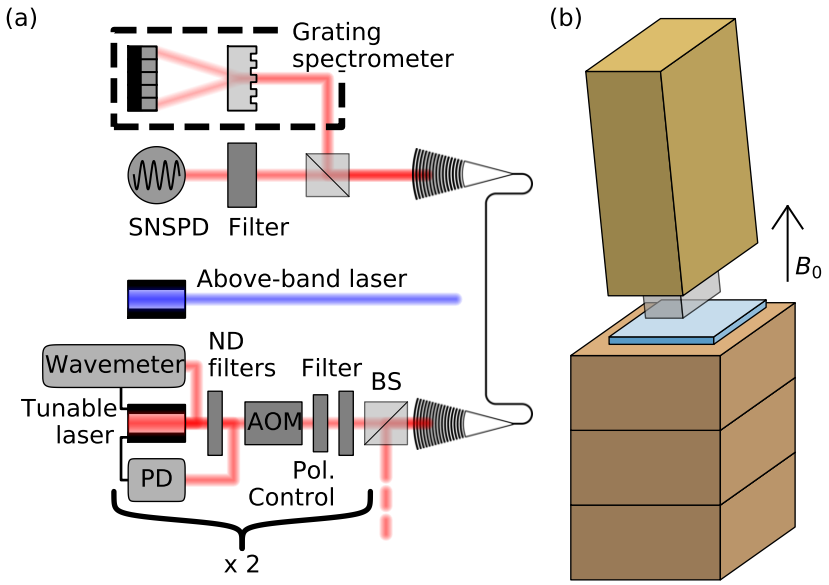

Figure 3.5: **Experimental setup for T centre studies.** (a) Waveguide devices (not to scale) are probed with either an above bandgap laser or a tunable 1326 nm laser. The tunable laser uses a wavemeter and a photodiode (PD) for wavelength and power stability. Power and polarization are controlled with ND filters and polarization optics and a bandpass filter is used to remove non-resonant light. The tunable laser can also be pulsed with an AOM. Upto two of these tunable laser setups can be combined with a beamsplitter (BS). Emission from T centres is collected from the output GC and directed to either a single-photon detector with filtering or a grating spectrometer. (b) The SOI chip is mounted to the top of a stack of Attocube XYZ piezo stages to align to a fiber block. The plastic top hat is omitted for clarity (see text). An optional permanent magnet mounted below the wafer creates a vertical field as shown.

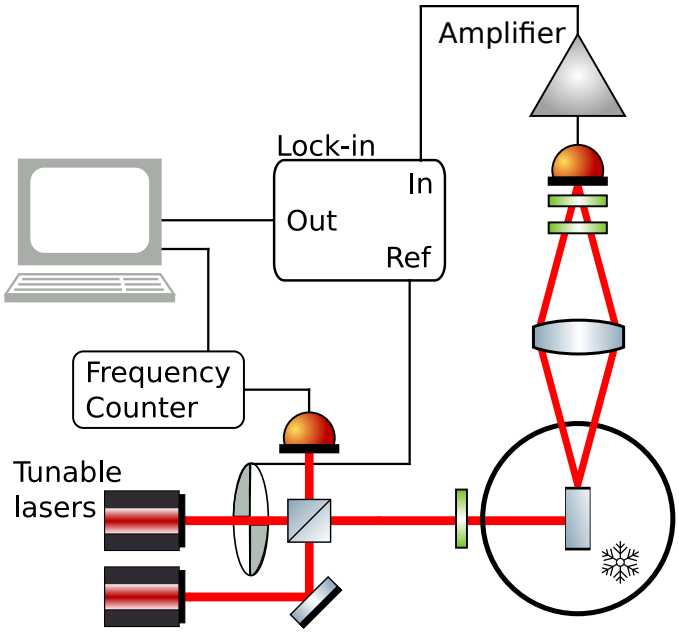

Figure 3.6: **Bulk SOI hole burning.** Two tunable lasers excited a cryogenically cooled SOI sample. Their frequency difference is measured with a fast detector and a frequency counter. The luminescence is filtered and focused to a detector before a lock-in measurement is made using the chopper as reference.

Bulk silicon-on-insulator

An unpatterned SOI T centre sample was prepared from a commercially available Czochralski silicon-on-insulator (220 nm device layer, 3 µm buried oxide layer, 700 µm silicon handle) wafer (P-type, 50–100 Ω-cm. Carbon-13 was implanted with a dose of 7×10^{13} cm^{-2} at 38 keV with a following 1000 °C RTA for 20 seconds in argon. Hydrogen was then implanted at a dose of 7×10^{13} cm^{-2} at 9 keV with a following 100 °C anneal in de-ionized water for 1 hour and a 420 °C RTA for 3 minutes.

Hole burning on this sample was performed by my collegues Amir Alizadeh and Camille Chartrand with a setup as shown in Fig. 3.6 (figure from Ref. [199]). Two Toptica CTL 1320 tunable lasers were combined in a fiber beamsplitter and aligned to a liquid helium cooled sample in a reflective pocket. A pick-off from the fiber was sent to a fast detector (MenloSystems FPD610-FC-NIR, DC-600 MHz) to measure the beat frequency of the two lasers with an Agilent DSO0954A oscilloscope acting as a frequency counter. The beat frequency gives the detuning between pump and probe lasers. A lock-in measurement is made by modulating the probe light with an optical chopper. The luminescence from the sample is filtered with a 1340 nm longpass filter and a 1375 ± 25 nm bandpass filter to remove ZPL laser light and Raman excitation then focused onto a Ge diode detector. The signal was amplified by a Ithaco 1201 preamplifier and then measured with a Princeton Applied Research 5210 lock-in amplifier.

Bulk ^{28}Si

The bulk ^{28}Si sample is from the Avogadro Project [200] with a 99.995 $\%$ ^{28}Si isotopic purity, an oxygen concentration less than 10^{14} cm^{-3}, and a carbon concentration less than 5×10^{14} cm^{-3}. Rather than implantation, the T centres were generated via electron radiation with a ionizing radiation dose of 320 kGy and energy 10 MeV. A 100 °C anneal in de-ionized water for 17 hours was then followed by a sequence of anneals on a hotplate: 300 °C for 30 min, 350 °C for 30 min, 400 °C for 60 min and 450 °C for 50 min. This sample was created as a result of the work from Ref. [70].

The hole-burning setup for the bulk ^{28}Si sample is shown in Fig. 3.7. The measurement is performed in a similar manner to the bulk SOI hole burning with the main difference being the laser system used to excite the sample. In this case a stable laser system (linewidth < 2.6 kHz), developed by my colleague Nicholas Brunelle, see Ref. [108], is used to generate the pump and probe fields. The output of the stable laser system is split into two paths which are each modulated by iXblue MPZ-LN-10 phase EOMs controlled by Stanford Research Systems SG386 signal generators to provide frequency tuning. A single modulation sideband is selected via filtering with Light Machinery etalons (80 GHz FSR, >100 finesse). The output is power-stabilized and amplified before exciting the sample. As before, filtering on the luminscence is done to remove ZPL laser light and Raman excitation from the sample before focusing the light onto a Ge diode detector. After preamplification a lock-in measurement is made using an additional slow modulation of one of the phase EOMs as reference.

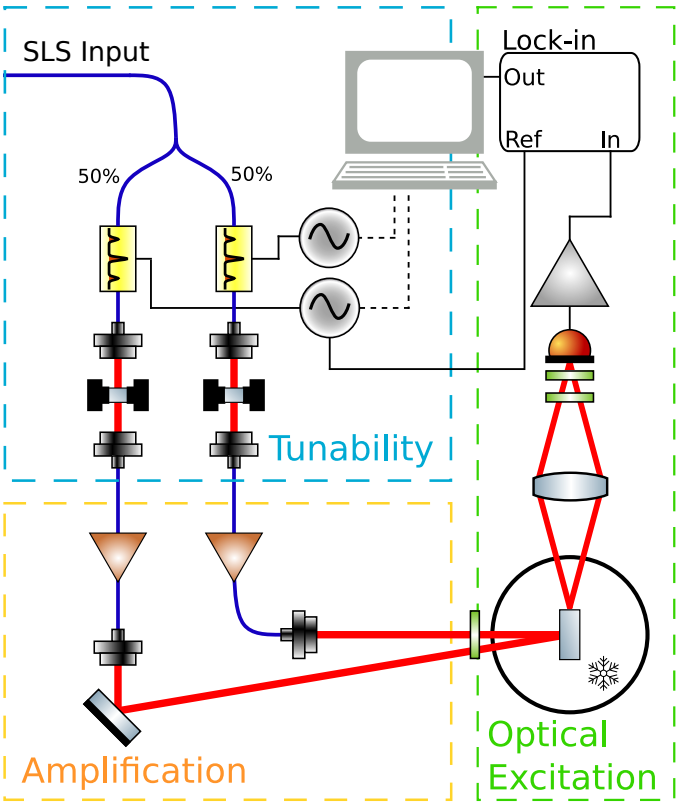

Figure 3.7: **Bulk ^{28}Si hole burning.** Input laser light from the stable laser system (SLS, see text) is split and modulated with phase EOMs. Single sidebands are isolated with etalons then amplified before excited the cryogenically cooled sample. The luminescence is filtered and focused to a detector before a lock-in measurement is made using an additional slow modulation of one of the EOMs as a reference. Figure modified from Ref. [108].

Chapter 4

Analysis Techniques and Simulations

4.1 Rate equation model

The simulated spectra shown in Section 2.2.2 and in upcoming chapters make use of a rate equation model to simulate the dynamics of a multi-level system. Here we will walk through the details of the model, and the Python code which is included in Appendix Section A.1.

We make use of a classical rate equation model as a full quantum mechanical description of the system, such as a master equation model, would be unnecessarily complex. Equivalent to a master equation in the high-decoherence limit, the rate equation matches the experiments which drive and measure the systems in an incoherent manner.

We will keep the description general for a system with n_g ground states (indexed with the subscript i_g), n_e excited states (indexed with the subscript i_e), n_l driving fields (indexed with the subscript i_l), and level degeneracies d_j (indexed with the corresponding ground or excited state subscript). To simplify, we will make the assumption that there is no population transfer between excited states and no population transfer between ground states. This assumes that the T_1 lifetimes within the excited and ground state manifolds are much longer than optical driving and decay rates. Much of the details of the dynamics are informed by the discussion in Ref. [104].

The rate equation is:

$$\begin{bmatrix} \vdots \\ \dot{N}_{i_e} \\ \vdots \\ \vdots \\ \dot{N}_{i_g} \\ \vdots \end{bmatrix} = \begin{bmatrix} & & \\ [M^{ee}] & & [M^{eg}] \\ & & \\ & & \\ [M^{ge}] & & [M^{gg}] \\ & & \end{bmatrix} \begin{bmatrix} \vdots \\ N_{i_e} \\ \vdots \\ \vdots \\ N_{i_g} \\ \vdots \end{bmatrix} \tag{4.1}$$

Where N_{i_e} (N_{i_g}) are the populations within the excited (ground) states. The coefficient matrix can be broken into four sub-matrices for the different driving terms, excited to excited, excited to ground,

etc. These sub-matrices are defined as:

$$\begin{aligned}
[M^{ee}]_{i_e,i_e} &= \mathrm{diag}\Big(\sum_{i_g} -W_{i_e,i_g} - \omega_{i_g}\Big) \\
[M^{gg}]_{i_g,i_g} &= \mathrm{diag}\Big(\sum_{i_e} -W_{i_g,i_e}\Big) \\
[M^{eg}]_{i,j} &= W_{i_e,j_g} + \omega_{j_g} \\
[M^{ge}]_{i,j} &= W_{i_g,j_e}
\end{aligned} \tag{4.2}$$

,

where a sum over i_e (i_g) denotes a sum over all the excited (ground) state indices. $W_{i,j}$ and ω_j are the driving and decay rates respectively from state i to j. The upward and downward driving rates are related based on the degeneracies of the involved levels as

$$W_{ij} = \frac{d_j}{d_i} W_{ji}. \tag{4.3}$$

The degeneracies also determine the relative spontaneous decay rates based on the total excited state decay rate, ω, weighted by the relative degeneracy of a ground state to the total number ground states:

$$\omega_{i_g} = \frac{d_{i_g}}{\sum_{j_g} d_{j_g}} \omega. \tag{4.4}$$

The driving rates, W_{ij}, are determined by the power of the driving field expressed as the effective Rabi frequency, and the spectral overlap of the transition. This overlap is modeled by multiplying the driving rate by a Lorentzian prefactor, $L(f, \Gamma)$, with a linewidth, Γ given by the homogeneous linewidth of the transition Γ_{hom}. The frequency, f, of the Lorentzian prefactor is determined by: the frequency of the driving field(s), $\{f_{i_l}\}$; the relative detunings of the excited state and ground state being addressed, Δ_e and Δ_g; as well as the detuning of the sub-ensemble from the inhomogeneous distribution, f_{ih}. For n_l lasers with frequencies $\{f_{i_l}\}$ and resonant driving rates $\{W_{i_l}\}$ the total driving will be the sum of all the driving rates from all the driving fields

$$W_{i_g,j_e}(\vec{f_l}, \vec{W_l}, f_{\mathrm{ih}}) = \sum_{i_l} L(f_{i_l} - f_{\mathrm{ih}} - \Delta_{i_g} - \Delta_{i_e}, \Gamma_{\mathrm{hom}}) W_{i_l}. \tag{4.5}$$

With the matrix differential equation established, the time evolution of the system can be solved numerically to obtain the population in each level as a function of time. To obtain an optical spectrum we take the signal, $S(\vec{f_l}, t_i, t_f)$, to be proportional to the population in the excited states. In a PLE measurement the excited state population will be proportional to the emission rate of photons and any detector signal. In a transmission measurement the excited state population will be proportional to the amount of light absorbed. We integrate this population over all sub-ensembles by numerically integrating over all inhomogeneous detunings, f_{ih}, weighted by the inhomogeneous lineshape given by a normalized Gaussian-Lorentzian sum, $I(f, m, \Gamma)$, with a linewidth given by the

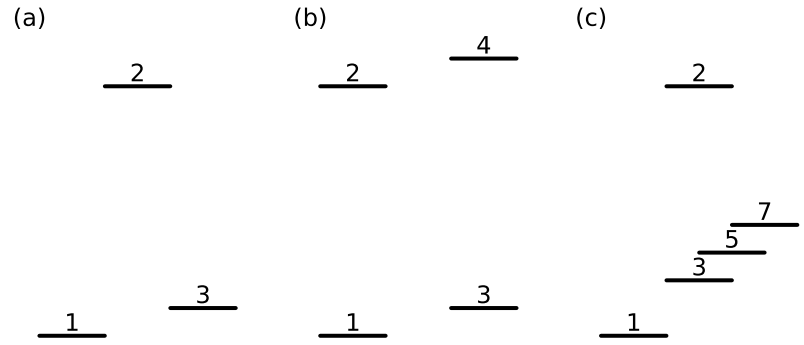

Figure 4.1: **Energy levels for steady-state solutions.** Energy level arrangements for which steady-state solutions are determined (see text). Excited state levels are indexed with even numbers, ground state levels are indexed with odd numbers. (a) Three-level system, two ground states and one excited state as in the case of the T centre in ^{28}Si at zero magnetic field assuming an isotropic hyperfine interaction. (b) Four-level system, two ground states and two excited states as in the case of T centre in a $^{\mathrm{nat}}$Si at non-zero magnetic field. (c) Five-level system, four ground states and one excited state as in the case of the T centre in ^{28}Si at zero magnetic field assuming an anisotropic hyperfine interaction.

inhomogeneous linewidth, Γ_{ih}, and m, a parameter between 0 and 1 for the Gaussian-Lorentzian proportion. A Gaussian-Lorentzian sum is used as different broadening mechanisms can lead to Gaussian lineshapes, Lorentzian lineshapes or a combination of the two [97, 201].

The signal function will depend on the evolution with time and so we integrate it over a time period $[t_i, t_f]$ to match the experimental conditions. The final expression for the signal is:

$$S(\vec{f_l}, t_i, t_f) = \int_{-\infty}^{\infty} I(f_{\mathrm{ih}}, m, \Gamma_{\mathrm{ih}}) \int_{t_i}^{t_f} \sum_{i_e} N_{i_e}(t) dt \; df_{\mathrm{ih}}. \tag{4.6}$$

For the initial state we use a thermal equilibrium state with population evenly distributed in the ground states as is the case for the systems and temperatures of study.

4.1.1 Steady-state solutions

Often the spectrum is taken on a timescale much longer than any dynamics of the system. In this case the signal can be taken to be the population in the excited states in steady-state. The left-hand side of Eq. (4.1) can be taken to be zero and the matrix equation can be solved analytically with the added constraint that the sum of all populations is unity. Practically this is a much easier regime to model as the computational time is much lower when the time evolution is not required. In steady-state Eq. (4.6) becomes

$$S(\vec{f_l}) = \int_{-\infty}^{\infty} I(f_{\mathrm{ih}}, m, \Gamma_{\mathrm{ih}}) \sum_{i_e} N_{i_e}^{SS} \; df_{\mathrm{ih}}. \tag{4.7}$$

Where $N_{i_e}^{SS}$ is the population in the i_e excited state in steady state. We list here the steady state solutions for different combinations of excited and ground state levels that are used in the main text.
Three-level system with ground states levels 1, 3, and excited state level 2. See Fig. 4.1a for the level diagram. This rate equation is used to simulate the T centre at zero magnetic field in ^{28}Si with the assumption of an isotropic hyperfine interaction, see Section 6.3.2. As an example here is the rate equation in matrix form to be solved with the sub-matrices highlighted along with the requirement that $N_{\mathrm{tot}} = N_1 + N_2 + N_3$ is conserved.

$$\begin{bmatrix} \dot{N}_2 \\ \dot{N}_1 \\ \dot{N}_3 \\ N_{\mathrm{total}} \end{bmatrix} = \begin{bmatrix} 0 \\ 0 \\ 0 \\ 1 \end{bmatrix} = \begin{bmatrix} \begin{bmatrix} -W_{21} - W_{23} - \omega_1 - \omega_3 \end{bmatrix} & \begin{bmatrix} W_{12} & W_{32} \end{bmatrix} \\ \begin{bmatrix} W_{21} + \omega_1 \\ W_{23} + \omega_3 \end{bmatrix} & \begin{bmatrix} -W_{12} & 0 \\ 0 & -W_{32} \end{bmatrix} \\ 1 & 1 \quad 1 \end{bmatrix} \begin{bmatrix} N_2 \\ N_1 \\ N_3 \end{bmatrix} \tag{4.8}$$

Solving for N_2 in steady state, N_2^{SS},

$$N_2^{SS} = \frac{W_{12}W_{32}}{W_{12}W_{32} + W_{12}(W_{23} + \omega_3) + W_{32}(W_{21} + \omega_1)}. \tag{4.9}$$

Four-level system with ground state levels 1, 3, and excited state levels 2, 4. See Fig. 4.1b for the level diagram. This rate equation is used to simulate the T centre in a $^{\mathrm{nat}}$Si waveguide in an applied magnetic field, see Section 6.3.3. Equal ground state degeneracies and thus $\omega_{ij} = \bar{\omega} \equiv 1/(2\tau_{\mathrm{exc}})$. This is the steady-state solution for the population in both excited states. Used in Section 6.3.3

$$\begin{aligned} \sum_{i_e=2,4} N_{i_e}^{SS} = \frac{} {} & W_{12}W_{14}W_{32} + W_{12}W_{14}W_{34} + W_{12}W_{32}W_{34} + W_{12}W_{34}\bar{\omega} \\ & + W_{14}W_{32}W_{34} + W_{14}W_{32}\bar{\omega} + W_{12}W_{32}\bar{\omega} + W_{14}W_{34}\bar{\omega} \\ & \overline{2W_{12}W_{14}W_{32} + 2W_{12}W_{14}W_{34} + W_{12}W_{14}\bar{\omega} + 2W_{12}W_{32}W_{34} + 3W_{12}W_{32}\bar{\omega}} \\ & + 2W_{12}W_{34}\bar{\omega} + W_{12}\bar{\omega}^2 + 2W_{14}W_{32}W_{34} + 2W_{14}W_{32}\bar{\omega} + 3W_{14}W_{34}\bar{\omega} \\ & + W_{14}\bar{\omega}^2 + W_{32}W_{34}\bar{\omega} + W_{32}\bar{\omega}^2 + W_{34}\bar{\omega}^2 \end{aligned} \tag{4.10}$$

Five-level system with ground state levels 1, 3, 5, 7, and excited state level 2. See Fig. 4.1c for the level diagram. Equal ground state degeneracies and thus $\omega_{ij} = \bar{\omega} \equiv 1./(4\tau_{\mathrm{exc}})$. Used to simulate the T centre at zero magnetic field in ^{28}Si with an anisotropic hyperfine interaction in the ground state, see Section 6.3.2.

$$N_2^{SS} = \frac{W_{12}W_{32}W_{52}W_{72}}{\begin{aligned}&W_{12}W_{23}W_{52}W_{72} + W_{12}W_{25}W_{32}W_{72} + W_{12}W_{27}W_{32}W_{52} \\ &+ W_{12}W_{32}W_{52}W_{72} + W_{12}W_{32}W_{52}\bar{\omega} + W_{12}W_{32}W_{72}\bar{\omega} \\ &+ W_{12}W_{52}W_{72}\bar{\omega} + W_{21}W_{32}W_{52}W_{72} + W_{32}W_{52}W_{72}\bar{\omega}\end{aligned}} \tag{4.11}$$

4.1.2 Spectral diffusion

While not considered in any of the results to be discussed, we also include in the rate equation code a method for modeling time dependent spectral diffusion. We include a time dependent detuning, $f_{\mathrm{SD}}(t)$, of the driving rates to account for a time dependent transition energy. Equation (4.5) becomes

$$W_{i_g,j_e}(\vec{f_l}, \vec{W_l}, f_{\mathrm{ih}}, t) = \sum_{i_l} L(f_{i_l} - f_{\mathrm{SD}}(t) - f_{\mathrm{ih}} - \Delta_{i_g} - \Delta_{i_e}, \Gamma_{\mathrm{hom}}) W_{i_l}. \tag{4.12}$$

The exact form of $f_{\mathrm{SD}}(t)$ will depend on the system being studied, we have in the code an implementation of a simple model for spectral diffusion. We assume the spectral diffusion can be defined by a single time scale, τ_{SD}, and a single linewidth, Γ_{SD}. During the time evolution of the system every τ_{SD} seconds the detuning is updated to a random value drawn from a Gaussian distribution with mean 0 and linewidth Γ_{SD} [202]. Due to the random nature of this spectral diffusion model we also include the ability to average the resulting spectrum over multiple iterations.

Figure 4.2 shows an example of a spectrum that could not be modelled without time dependent spectral diffusion: single centre hole burning. In this example we consider a two level system with no inhomogeneous broadening, only a homogeneous linewidth and a spectral diffusion linewidth, nevertheless, the pump-probe measurement reveals a saturation hole. In this case the hole is burnt into the temporal ensemble rather than the spatial ensemble. The pump plus probe spectrum is much noisier than the probe only spectrum due to the large fluctuations in signal from the transition energy fluctuation between being on and off resonance with the pump laser, we show a smoothed (Savitzky-Golay filter) spectrum for clarity.

4.2 Cluster correlation expansion

In Section 2.3.5 a phenomenological understanding of the T_2 coherence via df/dB and the coupling of different spin dynamics in the bath is discussed. In the following experimental results, extrapolations from measured coherence times are performed, however, this is not possible with this phenomenological model without multiple well characterized samples. Instead we present here an alternate model for simulating decoherence using time evolution of the qubit spin-bath coupled system.

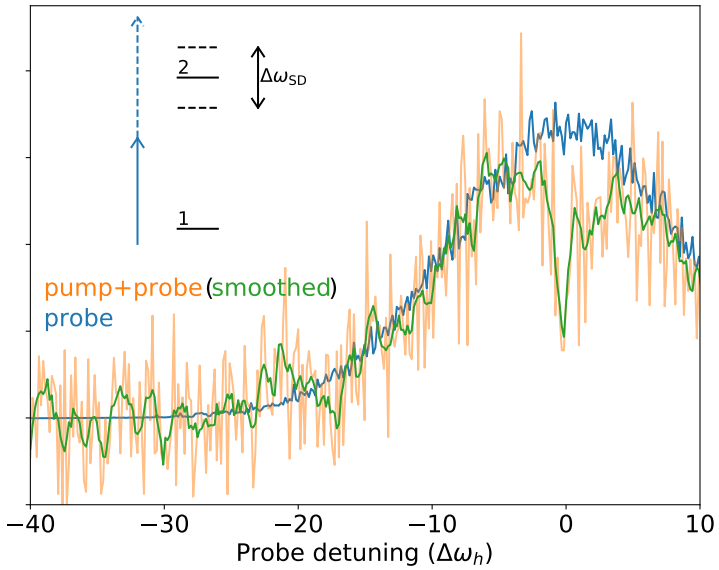

Figure 4.2: **Single-centre hole burning.** Model of a hole burning measurement of a single centre (i.e. no inhomogeneous broadening) with a time dependent spectral diffusion linewidth 20 times larger than the homogeneous linewdith. (Inset) Level diagram of the system showing the excited state level energy shifting due to spectral diffusion.

Cluster correlation expansion (CCE) is a technique for simulating the dephasing of a qubit in the presence of a spin bath [203, 204]. In this work we make use of the PyCCE python package [205] to perform the CCE calculations for our defined qubit systems. Here we present the theoretical description of the modeling procedure following the documentation of PyCCE [206].

As described in Section 2.3.2 a Hahn-echo T_2 measures the loss of a qubit's coherence due to losing the phase of the superposition state. In the pure dephasing regime, $T_1 >> T_2$, the decoherence is captured entirely by the evolution of the off diagonal elements of the qubit's density matrix, $\rho(t)$. Thus we can define a coherence function as

$$\mathcal{L}(t) = \frac{\langle 1|\, \rho(t)\, |0\rangle}{\langle 1|\, \rho(0)\, |0\rangle}. \tag{4.13}$$

Cluster correlation expansion (CCE) is a method of modeling this coherence function for a central spin (any two levels of a spin system) when coupled to a bath of nuclear spins in the environment (as discussed in Section 2.3.4). In general these baths are composed of many spins so a full description of all spins is impractical on a classical computer. Hence, the main idea of CCE is to factorize the bath-induced decoherence into irreducible contributions from smaller clusters within the spin bath

$$\mathcal{L} = \prod_C \tilde{L}_C = \prod_i \tilde{L}_{\{i\}} \prod_{i,j} \tilde{L}_{\{ij\}} \ldots \tag{4.14}$$

Here i, j are indices of the bath spins within the cluster, with $\{i\}$ denoting clusters of single bath spins, $\{i,j\}$ denoting clusters of pairs of bath spins, etc. Each cluster contribution is defined recursively by the sub-clusters within:

$$\tilde{L}_C = \frac{L_C}{\prod_{C'} \tilde{L}_{C'}}. \tag{4.15}$$

L_C is the coherence function of the central spin interacting only with the bath spins in cluster C and $\tilde{L}_{C'}$ is the contribution from a subcluster $C' \subset C$.

For example the contribution from a cluster of a single spin is simply the coherence function for a bath with one isolated spin,

$$\tilde{L}_i = L_i, \tag{4.16}$$

and the contribution from a cluster of two spins is,

$$\tilde{L}_{ij} = \frac{L_{ij}}{\tilde{L}_i \tilde{L}_j}. \tag{4.17}$$

By truncating the expansion in Eq. (4.14) to a cluster of size N the coherence function can be approximated with only simulations of a maximum bath size N, rather than the full bath size. The maximum cluster size considered is the order of the CCE approximation, i.e. CCE-2 only considers up to pairs of bath spins, and CCE-3 only considers up to triplets of spin baths. CCE is shown schematically in Fig. 4.3.

The simulation is set up by defining a maximum size of the spin bath surrounding the central spin and populating it randomly with spins limited to appropriate crystallographic locations. Clusters, up to the selected order, are defined for sets of bath spins within a given physical cluster size (these dimensions are shown in Fig. 4.3). To achieve sufficient convergence a high enough max cluster size should be selected along with an average over an appropriate number of random realizations of the spin bath.

Finally, the coherence function for a given spin bath is defined as follows. The total Hamiltonian of the system is split into two components conditional on the state of the central spin

$$H_C = |0\rangle \langle 0| H_C^0 + |1\rangle \langle 1| H_C^1. \tag{4.18}$$

Where H_C^α is the effective Hamiltonian acting on the bath when the central spin is in the $|\alpha\rangle$ eigenstate of the central spin. The coherence function for this cluster is determined by the time evolution of the spin-bath density matrix, ρ_C as:

$$L_C(t) = Tr[U_C^0(t) \rho_C U_C^{1\dagger}(t)]. \tag{4.19}$$

Where $U_C^\alpha(t)$ is the time evolution operator for the effective Hamiltonian, H_C^α, and the given number of decoupling pulses. For a Hahn-echo pulse sequence, i.e. single pulse applied at t_1, the time

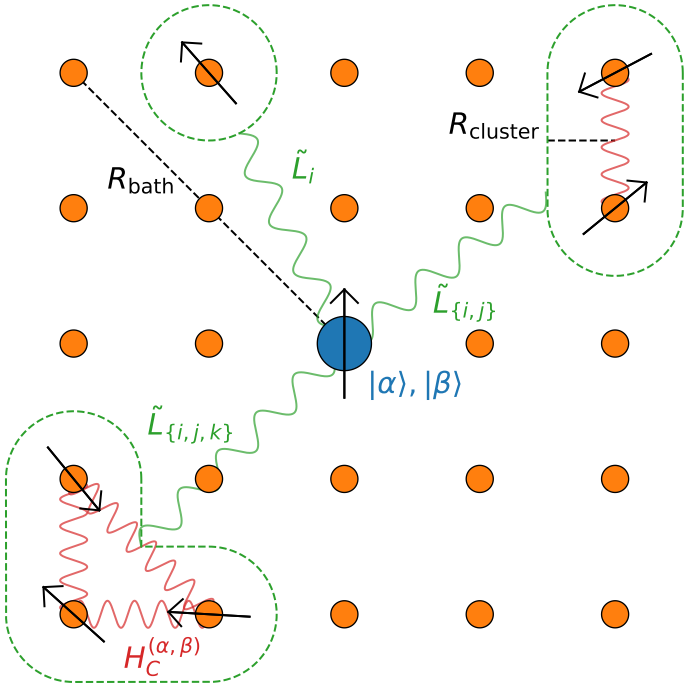

Figure 4.3: **Schematic of CCE.** The decoherence of a central spin (states α and β in a bath of six spins is approximated by considering the decoherence clusters of size one ($\tilde{L}_i$), two ($\tilde{L}_{\{i,j\}}$), and three ($\tilde{L}_{\{i,j,k\}}$) as described in the text. R_{bath} and R_{cluster} set the size of the simulation and the range of interactions to consider. Interactions within a cluster are the spin-dependent Hamiltonians $H_C^{(\alpha/\beta)}$.

evolution operators are:

$$U_C^0(t) = e^{-i/\hbar H_C^1(t_t - t_1)} e^{-i/\hbar H_C^0(t_1)}, \tag{4.20}$$

$$U_C^1(t) = e^{-i/\hbar H_C^0(t_t - t_1)} e^{-i/\hbar H_C^1(t_1)}, \tag{4.21}$$

$$\tag{4.22}$$

where t_t is the total time of the evolution.

The definition described in this section for the coherence function is known as conventional CCE with other choices for the time evolution of the coherence function possible [205]. Furthermore, different dynamics can be modeled with different number of re-focusing pulses, different pulse lengths and different delay times.

Chapter 5

Results and Discussion: Selenium

Armed with a natural silicon sample diffused with selenium we can now begin to examine the $^{77}Se^{+}$ system in the nuclear spin bath from the natural abundance of ^{29}Si. We begin by examining the spectral properties of the ^{nat}Si:^{77}Se system including a two laser hole burning measurement. Next we perform continuous-wave (CW) optically detected magnetic resonance (ODMR) investigating the ground state Hamiltonian of the ^{nat}Si:^{77}Se system. Moving to pulsed ODMR we measure the effect of the ^{29}Si via electron spin echo envelope modulation (ESEEM) and assess the coherence properties of the clock transitions available. Finally, we present a proposal for the use of a paired $^{77}Se^{+}$-^{29}Si system in a cavity-coupled quantum computing architecture.

5.1 Hole burning

Shown in Fig. 5.1 is a one laser absorption scan of the selenium 1s:A$\Leftrightarrow$1s:T_2:Γ_7 transition along with a two laser pump-probe hole-burning measurement performed on the primary optical peak. Measurements done at zero-field. As discussed in Section 2.5.2 the three optical peaks in this spectrum are due to the primary isotopic composition of the four silicon nearest neighbours to the selenium defect. The lower insets in Fig. 5.1a show the primary isotopic combinations. Specifically these are four ^{28}Si, three ^{28}Si and one ^{29}Si, and three ^{28}Si and one ^{30}Si (or two ^{28}Si and two ^{29}Si). We will refer to these optical peaks as the ^{28}Si optical peak, ^{29}Si optical peak, and ^{30}Si optical peak.

In this natural silicon sample we are unable to resolve the zero-field hyperfine splitting in the ground state due to the inhomogeneous broadening. We perform hole burning measurements at zero applied magnetic field (background field $\lesssim 0.5$ G) to demonstrate that we can hyperpolarize a subensemble despite the inhomogeneous broadening. There are clear anti-holes as well as a hole indicating the singlet and triplet levels are well separated relative to the homogeneous linewidths and showcasing the ability to hyperpolarize the ensemble system into the singlet state and the triplet states, noting that the triplet manifold is not a true triplet (see Sec. Section 2.3.4). The exact energy levels of the singlet-triplet and the hyperfine interaction will be investigated in Section 5.2.1. The splitting between the anti-holes matches a ground state splitting of 1.73 ± 0.01 GHz which is close to the expected $^{77}Se^{+}$ hyperfine coupling of 1.66 GHz [65, 98]. ODMR measurements in Section 5.2

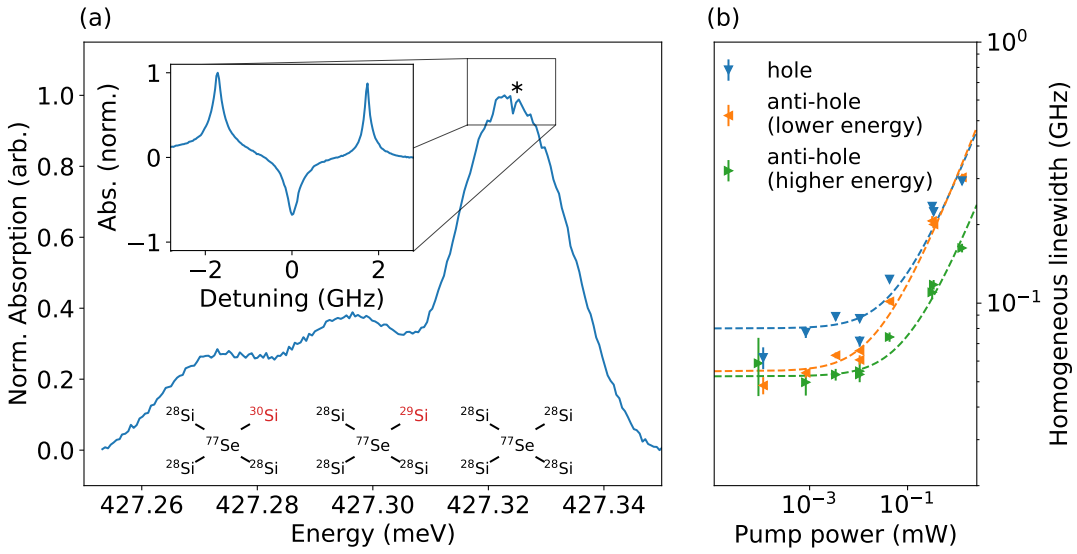

Figure 5.1: **Hole burning.** (a) Single laser optical absorption spectrum of the $^{\mathrm{nat}}$Si:^{77}Se 1s:A$\leftrightarrow$1s:T$_2$:Γ_7 showing the three optical peaks corresponding (primarily) to the three isotopic nearest neighbours as shown in the lower insets. The dip in the ^{28}Si optical peak denoted with a $*$ is due to residual hyperpolarization in the system from a previous measurement. (Inset) Hole burning spectrum of the main peak showing a hole and anti-holes. (b) Hole and anti-hole linewidths versus pump power showing extrapolated low power linewidths of 80 ± 6 MHz (hole, blue), 55 ± 3 MHz (low energy anti-hole, orange), and 52 ± 2 MHz (high energy anti-hole, green) with the lowest linewidth measured to be 48 ± 4 MHz (lower energy anti-hole).

confirm the singlet-triplet splitting is consistent with the 1.66 GHz from literature, we attribute this discrepancy in the optical measurement to the calibration from laser current/temperature to wavelength.

The ability to hyperpolarize the system is important for the following ODMR measurements which will allow us to further measure the energy levels of the ground state. Here we have shown that despite the large inhomogeneous linewidth we are still able to address the unresolved ground states.

Even though there is hyperpolarization occurring we are still able to obtain a single laser spectrum. One might expect that due to hyperpolarization and the small homogeneous linewidth (< 62 MHz, value determined below) that a single laser scan would have almost no absorption signal. While this is true in the steady-state regime, we work here in the transient regime wherein we are able to obtain a signal at each wavelength step before the system has fully hyperpolarized. This is due to having a very low laser power, 0.6 μW, 3 mm spot size, and scanning the wavelength relatively fast, 50 ms per wavelength point, compared to the hyperpolarization time of > 200 ms (see Fig. 5.2). We can see that the hole burning spectrum qualitatively matches the transient hole burning depicted in Fig. 2.8.

Due to working in the transient regime, the hole we are seeing is not solely a saturation hole, it is a measure of the depleted population in the remaining dark state after hyperpolarization due to the CW pump laser. Nevertheless measuring the hole linewidth as a function of power can still reveal the homogeneous linewidth [207]. In this case the time scale of this homogeneous linewidth is the ground state T_1 lifetime, not the 'instantaneous' time scale for a saturation hole (see Section 2.2.2). There is likely slow spectral diffusion contributing to this homogeneous linewidth. The T_1 lifetime has been measured to be up to 4.6 ± 1.5 h [77] with sufficient shielding from blackbody radiation. In this setup we forgo this shielding and measure a T_1 lifetime of 35 ± 2 s as shown in Fig. 5.2. In fact, fast, low power scans immediately after the pump laser has been on for a long time show a hole as it has not healed yet – this is present in the one laser scan in Fig. 5.1a as a dip in the ^{28}Si peak denoted with a star.

Once hyperpolarized via hole burning we measure the temporal decay back to thermal equilibrium, Fig. 5.2. The system is hyperpolarized with an optical pulse from a single laser after which the system is allowed to evolve in the dark by blocking the laser with a shutter. The remaining population in the addressed state is measured with another laser pulse after this variable dark time. The transient area (see Fig. 5.2 inset) is a measure of the population that has returned to the addressed state.

Shown in Fig. 5.1b is the homogeneous linewidth measured from the hole and anti-holes as a function of pump power. These linewidths are fit with Eq. (2.3). The extrapolated low power linewidths differ between hole and anti-holes, however, at the lowest powers measured all features begin to have nominally similar linewidths: minimum hole linewidth is 62 ± 6 MHz, and anti-hole linewidths of 48 ± 4 MHz and 50 ± 6 for lower and higher energies respectively. The lower energy anti-hole has a saturation power of 0.010 ± 0.02 mW while the higher energy anti-hole has 0.04 ± 0.01 mW. This asymmetry is not unexpected as the ground state of $^{77}Se^{+}$ is an asymmetric singlet-triplet. The hole, which is addressing both the singlet and triplet, is correspondingly an intermediate saturation power, 0.024 ± 0.007 mW, approximately equal to the average of the anti-hole saturation powers.

The lifetime limited linewidth, based on the 7.7 ± 0.4 ns excited state lifetime [77], is 21 ± 1 MHz. The lowest measured homogeneous linewidth we measure is within a factor of 2–3 of the lifetime-limited linewidth, indicating this is a very coherent transition. This homogeneous linewidth is an upper bound as the timescale for this homogeneous linewidth is the T_1 lifetime meaning slow spectral diffusion may be increasing the linewidth we measure. These holes measured in natural silicon wafers are consistent with the hole burning results reported by Morse et al. [69] in bulk ^{28}Si (< 29 MHz) from which we can conclude that this difference in samples has not had a large effect on the linewidth.

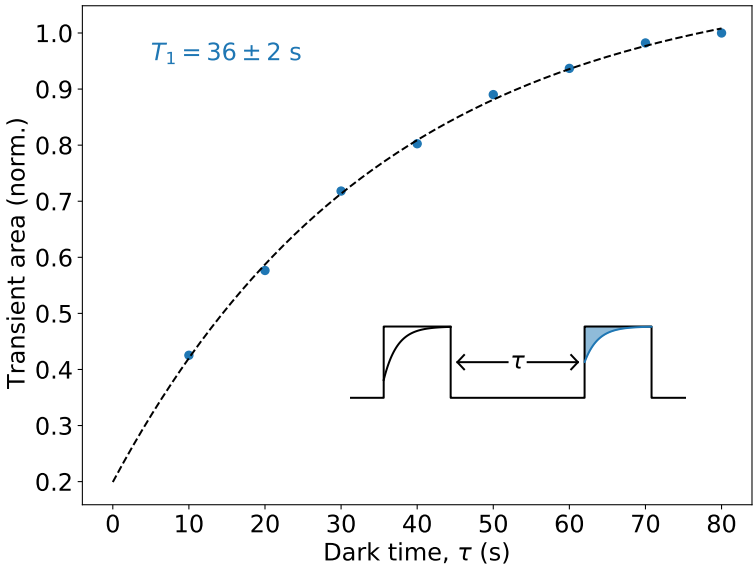

Figure 5.2: $\mathbf{T_1}$. Population decay of the singlet-triplet transition. (Inset) Pulse sequence used for the measurement: an initialization pulse, a variable dark time, then a readout pulse. The blue transient area is the readout signal. Transients are approximately 100 ms long.

5.2 ODMR

With our ability to hyperpolarize the system we are now able to perform ODMR by driving the resonator with a microwave (MW) tone and sweeping its frequency. When resonant with a transition in the ground state the MW tone will depolarize the system leading to more absorption of the laser light and thus a decrease in transmission.

In this section we use ODMR to measure the ground state structure as a function of magnetic field and, furthermore, as a function of the isotopic surroundings. We can perform different variations of an ODMR experiment by varying the experimental configuration, by picking one of the three isotopic peaks the pump laser is resonant with, and one of two MW drive orientations (parallel or perpendicular to the static magnetic field B_0. Figure 5.3 shows the ODMR spectrum at a few magnetic field magnitudes for the six setups described.

As will be shown in the following section, these transitions are all between the singlet state(s) and the individual components of the triplet state. We can associate the observed ODMR transitions to T_0-like transitions at ≈1.66 GHz that have minimal sensitivity to the magnetic field, and $T_\pm$-like transitions on either side of the T_0-like transitions that split outward with increasing magnetic field.

The ^{28}Si optical peak (Fig. 5.3 a, b) showcases familiar features as expected from the $^{77}Se^+$ Hamiltonian (see [69]): $T_\pm$ lines are present, splitting linearly with the magnetic field in addition to a T_0-like peak that doesn't shift significantly with magnetic field as expected for the S_0-T_0 transition. The nominal labelling of transitions as T_0-like or $T_\pm$-like is shown in Fig. 5.3 b and apply to the

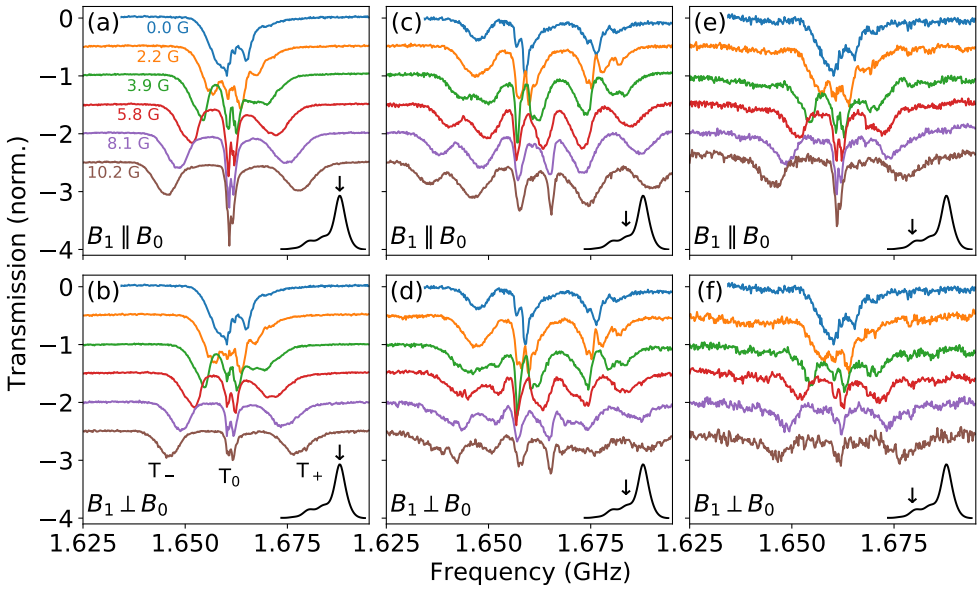

Figure 5.3: **ODMR spectra.** ODMR spectra of the three optical peaks for parallel and perpendicular B-field arrangements. Insets illustrate which spectral peak is probed (a-b: ^{28}Si peak; c-d: ^{29}Si peak; e-f: ^{30}Si peak) as well as the magnetic field orientations (a, c, e: $B_1 \parallel B_0$; b, d, f:$B_1 \perp B_0$). The zero-field transmission is scaled to be normalized and all other spectra are scaled by the same amount then offset for clarity. The optical peaks determine the isotopic composition of the nearest neighbours, while the B-field orientation illustrates the Δm of the transitions. The transitions in all six panels map roughly onto the singlet to triplet transitions, T_0 and $T_\pm$, which are labelled explicitly in (b).

ODMR from all three optical peaks. Where the transitions deviate from the expected form is in the structure present in the T_0-like transition with at least two separate transitions present – these will be discussed in the following section. As expected based on the S_0-T_0 transition having $\Delta m = 0$, the T_0-like peak is stronger when $B_1 \parallel B_0$ and is much reduced when $B_1 \perp B_0$.

Interestingly, the $T_\pm$ peaks do not have significantly different amplitudes between the two different B-field orientations despite the S_0-$T_\pm$ transition having a $\Delta m = \pm 1$ predicting a perpendicular alignment to be preferred. While the transition can be driven in CW ODMR we observe that coherent Rabi oscillations are only possible when the field is oriented perpendicular as expected. Coherent control of these MW transitions is discussed in Section 5.3.

The ^{29}Si optical peak (Fig. 5.3 c, d) displays a much more involved ODMR spectrum, showing at least three distinct peaks at zero field which split to six separated peaks under an applied B-field. At this optical peak there is a ^{29}Si atom in the nearest neighbour position to the selenium which is clearly introducing a large hyperfine coupling which introduces more non-degenerate transitions to the expected singlet-triplet structure. The system is now composed of three spin-1/2 particles leading to eight energy levels. As we will see in the next section the singlet-like levels are nearly degenerate and so six transitions are resolvable from the six 'triplet'-like levels to the averaged singlet-like level. Again we see for the S_0-T_0-like transitions a parallel field is preferred indicating these are $m \approx 0$ transitions. The magnetic quantum number of these transitions is investigated further in Section 5.2.1. As in the case of the ^{28}Si optical peak we can identify T_0- and $T_\pm$-like transitions. The central two peaks near 1.66 GHz shift minimally with B-field and are thus T_0-like, while the outer four transitions are $T_\pm$-like as they split to higher and lower energies nearly linearly with applied magnetic field.

Finally, the ^{30}Si optical peak (Fig. 5.3e, f), despite lower signal, can be seen to be very similar to the ^{28}Si optical peak. This is expected as ^{30}Si has no spin. The ^{30}Si optical peak also contains those selenium centres with two ^{29}Si atoms in the nearest neightbours, however, such centers will have much lower concentrations and are not resolved in the spectra measured.

5.2.1 Hamiltonian determination

We have now seen that the ODMR of the ^{28}Si optical peak and ^{29}Si optical peak display ground state structures that deviate, in different ways, from the $^{77}Se^+$ ground state seen in previous work in ^{28}Si [69]. Here we investigate the ground state energies more thoroughly via ODMR and magnetic field sweeps to higher fields and at higher resolution. We will no longer consider the ^{30}Si optical peak as it appears to have the same structure as the ^{28}Si optical peak but with lower signal.

Further investigation is necessary as an exact mapping of the ground state will be needed to inform which of the energy levels will be used as a qubit and to determine the optimal field for their use. Furthermore, the coupling to ^{29}Si atoms is clearly affecting the ground state structure which leads to an exciting possibility of using a ^{29}Si nuclear spin as a quantum memory. Nuclear qubits in the bath have been used as quantum registers in other material to great effect [51, 208].

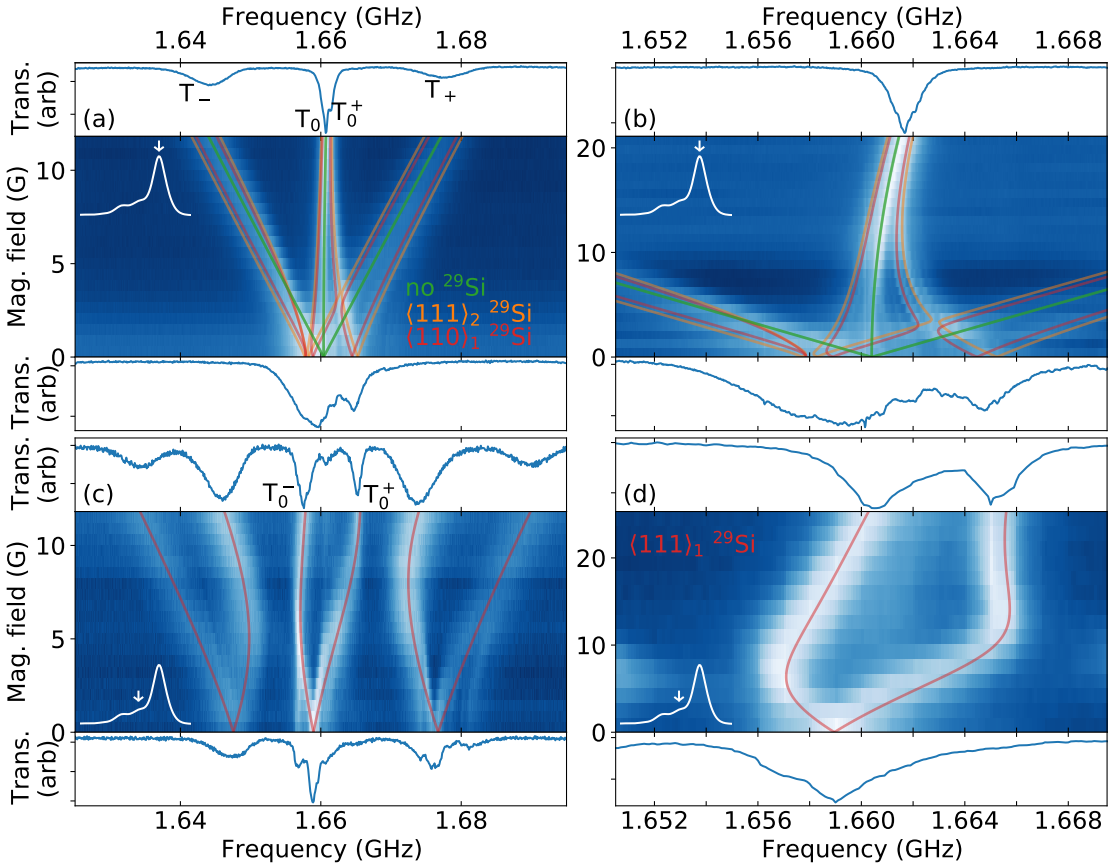

Figure 5.4: **ODMR versus magnetic field.**ODMR spectra as a function of magnetic field with a slice at zero applied magnetic field (lower inset) and a slice at the maximum applied magnetic field (upper inset). (a) Primary ^{28}Si optical peak, transitions for different orientations of ^{29}Si (further than NN) along with the uncoupled case are plotted (see text and Table 5.1 for details). Upper inset labels the primary ODMR peaks (see text for labelling definitions). (b) same as (a) going to higher fields and at a higher resolution. (c) ^{29}Si optical peak with transitions for a $\langle 111\rangle_1$ ^{29}Si plotted (see text and Table 5.1 for details). Upper inset labels the two primary ODMR peaks. (d) same as (c) going to higher fields and at a higher resolution.

The ODMR spectra for the ^{28}Si and ^{29}Si optical peaks are shown in Fig. 5.4 in two regimes, lower resolution frequency scans measuring all the transitions, as well as higher resolution scans to higher fields focusing on the T_0-like lines. In all cases we additionally plot the energy levels from the Hamiltonian of a $^{77}Se^+$ system with a hyperfine coupling to a ^{29}Si atom. The exact form of the hyperfine coupling will depend on the position of the ^{29}Si relative to the central $^{77}Se^+$ defect, e.g. the ^{29}Si optical peak will have a coupling to a nearest neighbour ^{29}Si while the ^{28}Si optical peak will have coupling to ^{29}Si atoms further than the nearest neighbours. In general, the Hamiltonian is

$$H = B_0\gamma_e S_z + B_0\gamma_n I_z + B_0\gamma_{29} I_z^{29} + a_{77}\vec{S}^{\,\mathsf{T}} \cdot \vec{I} + \vec{S}^{\,\mathsf{T}}\mathbf{A}\vec{I^{29}}, \tag{5.1}$$

where $\vec{S}$, $\vec{I}$, and $\vec{I^{29}}$ are vectors of the Pauli matrices for the electron, ^{77}Se nuclear spin, and the ^{29}Si nuclear spin. Likewise γ_e, γ_n, and γ_{29} are the gyromagnetic ratios for the three spin species: 28.07 GHz/T, -8.156 MHz/T, and -8.458 MHz/T respectively. a_{77} is the isotropic hyperfine coupling between electron and ^{77}Se nuclear spin and $\mathbf{A}$ is the anisotropic hyperfine tensor between the electron and ^{29}S nuclear spin.

From Ref. [209] we have a tabulation of the anisotropic hyperfine couplings to ^{29}Si with different crystalographic symmetries – a subset of which are shown in Table 5.1. The labelling of the different ^{29}Si centres is determined first by the crystallographic symmetry and secondly by the magnitude of equivalent symmetry centres, e.g., the label $\langle 110\rangle_1$ would denote the strongest coupling ^{29}Si centre with $\langle 110\rangle$ symmetry.

In addition to the ^{29}Si centre involved we will also introduce a further labelling convention for those hyperfine couplings sufficient to split the T_0 line. We will label the two lines $T_0^{\pm}$ for the higher and lower energy transitions. We keep the standard T_0 label for those sub-ensembles without sufficient hyperfine coupling. When appropriate we will also refer to the coupled ^{29}Si to further differentiate lines, e.g. $\langle 111\rangle_1$ T_0^+ versus $\langle 111\rangle_2$ T_0^+. These labels are shown in Fig. 5.4. Note that in the upper inset of Fig. 5.4a the T_0^- line is not resolved as it overlaps with the T_0 of the unsplit sub-ensembles. Labelling with the nuclear spin state of the ^{29}Si would be appropriate as well, however, the exact nuclear spin of an energy changes with field as will be discussed below.

To assign a ^{29}Si centre to the results we see, we take, for simplicity, the three centres that have the highest magnitude of hyperfine interaction, namely, $\langle 111\rangle_1$, $\langle 111\rangle_2$, and $\langle 110\rangle_1$ from Table 1 in Ref. [209] with hyperfine parameters a_{iso} and T (see Section 2.3.4) as shown in Table 5.1. However, the tabulated values in Ref. [209] have a sign ambiguity where only the relative sign between a_{iso} and T is measured. These results resolve this sign ambiguity: the ODMR spectra are only fit well with the negative of the tabulated a_{iso} and T (appropriate signs are shown in Table 5.1).

Finally, we neglect the singlet splitting to simplify the analysis of the data in Fig. 5.4 as in all cases the S_0-like states are split much less than the triplet-like states and much less than the linewidths of the ODMR transitions (see Fig. 5.5 as an example of the splitting present). It is likely that in all cases we are at least partially driving transitions from both the S_0-like states, although the

Label	a_{iso} (MHz)	T (MHz)	Orientation
$\langle 111\rangle_1$	-28.89	-12.52	111
$\langle 111\rangle_2$	-9.63	-0.57	111
$\langle 110\rangle_1$	-7.54	-0.52	110

Table 5.1: **Hyperfine values.** The three highest magnitude hyperfine interactions as determined by Ref. [209] along with the labels we will use the remainder of the thesis. The labels are based on the identified crystallographic symmetry and the subscript denotes the magnitude of coupling, e.g., $\langle 110\rangle_1$ denotes the strongest coupling ^{29}Si centre with $\langle 110\rangle$ symmetry. The absolute values are from Ref. [209], however, the signs are determined from this work.

exact Δm character will play a role as will be discussed below. For all Hamiltonians we average the singlet-like energy levels when determining the transitions.

The $\langle 111\rangle_1$ ^{29}Si is clearly from a nearest neighbour site; it has the correct orientation and the largest coupling strength. This is confirmed by performing a one parameter fit to the ODMR spectra obtained on the ^{29}Si optical peak. The one free parameter is the isotropic hyperfine coupling of electron and nucleus of the $^{77}Se^+$ centre as this simply sets the overall energy level of the splitting. This is shown in Fig. 5.4c and d showing good agreement with the data.

For the ^{28}Si optical peak the ODMR spectra contains contributions for all locations of ^{29}Si (other than nearest neighbour) to varying degrees. To simplify we consider only the next two highest hyperfine coupled ^{29}Si atoms with all other contributions being considered to have negligible hyperfine coupling. These are shown in Fig. 5.4a and b after a one parameter fit as above to set the overall energy level of the system. This does capture the predominate features of the ODMR spectra, $T_\pm$, as well as the primary features in the T_0-like transition. The primary T_0 peak is due to an uncoupled (or negligibly coupled) $^{77}Se^+$ defect. Additionally, the two side peaks in the T_0 line are well matched by the $\langle 111\rangle_2$ and $\langle 110\rangle_1$ coupled ^{29}Si. At ≈5 G the predicted transitions of $\langle 111\rangle_2$ and $\langle 110\rangle_1$ match the two peaks to higher energy of the T_0 line. There are likely further elements from other ^{29}Si hyperfine couplings with weaker couplings, however, these are not as clearly resolved within the ODMR linewidths.

We average the two S_0-like states when determining the transition energies from the Hamiltonian for simplicity of comparison with the spectra, however, the S_0-like states differ in a more important way than the small energy difference – the magnetic quantum number, m, i.e., the net spin of all constituent particles. Figure 5.5 shows the energy levels of the $\langle 111\rangle_1$ ^{29}Si coupled system along with a colour coding based on the m value of the state at the given magnetic field. Explicitly we determine the eigenstates of the Hamiltonian of a $^{77}Se^+$ coupled to a $\langle 111\rangle_1$ ^{29}Si and determine the expectation value of the sum of Pauli-Z operator for each spin species. We plot the $\langle 111\rangle_1$ coupled system as it has the largest splittings for clarity but the salient features are consistent for the other ^{29}Si couplings.

In Fig. 5.5 we can see that from the singlet states to the T_0-like transitions there are both $\Delta m \approx 0, \pm 1$ transitions. Thus, it is likely that only a single branch of S_0-like states is being driven in either S_0-$T_0^\pm$ transition. As well, we might expect that regardless of B-field orientation there will be a

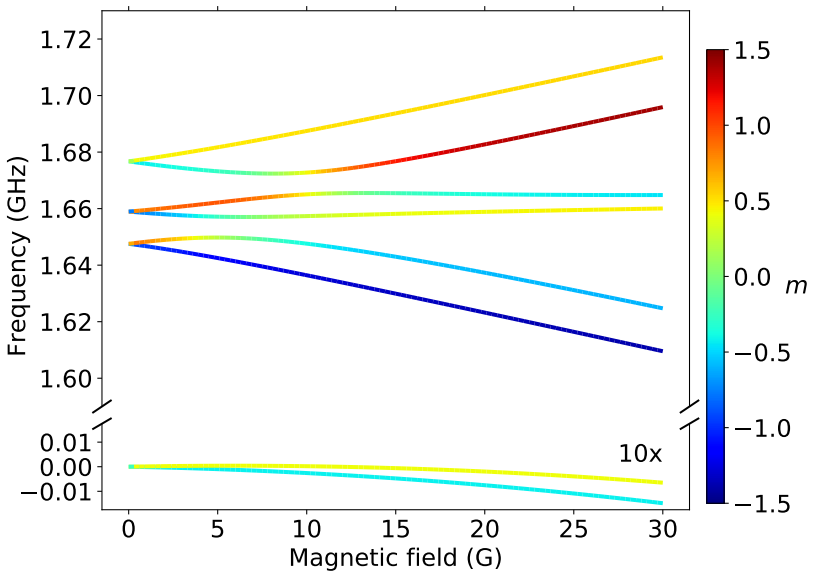

Figure 5.5: $\langle \mathbf{111} \rangle_\mathbf{1}$ **magnetic quantum number.** The transition frequencies from the $\langle 111 \rangle_1$ ^{29}Si Hamiltonian (see Eq. (5.1)) color-coded by the magnetic quantum number, m, i.e., the net spin of all constituent particles. All frequencies are referenced to the lowest energy level at zero-field. Note the broken axis, the energies in the lower axis are scaled up by a factor of 10 to show the two levels.

S_0-$T_0^{\pm}$ transition that can be driven, however, from Fig. 5.3b, e, we see that the perpendicular case was weaker than the parallel case. The difference may be due to the fact that in the perpendicular case the $\Delta m = 1$ is coming entirely from the flipping of the ^{29}Si nuclear spin which has a much smaller gyromagnetic ratio than an electron and so the weaker ODMR peak may be indicating the lower sensitivity to the drive field rather than anything about selection rules.

Each pair of levels – the $T_\pm$-like pair, T_0-like pair, and S_0-like pair – all differ by $\Delta m = 1$ indicating that the difference may be primarily a ^{29}Si spin flip. Figure 5.6 shows that in fact, at most magnetic fields this is exactly the case and that the ^{29}Si nuclear spin is almost always a good quantum number. This is exciting as it opens up the possibility of using the ^{29}Si nuclear spin as an additional qubit while remaining in the low-field regime. As mentioned before, coupling to bath spins have been leveraged to gain additional quantum memories. Furthermore, while a bare or weakly coupled ^{29}Si nuclear spin would have a linear dependence on magnetic field from the Zeeman effect, here we see that in the T_0 manifold the difference in energy is sub-linear, and in fact possesses clock transitions, which may be used to enhance the nuclear spin coherence. This will be discussed further in Section 5.3.2.

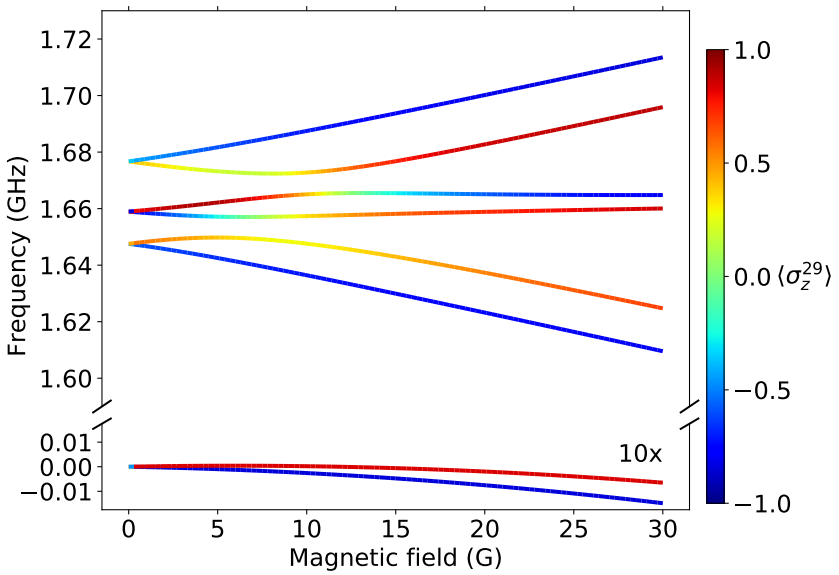

Figure 5.6: $\langle \mathbf{111} \rangle_{\mathbf{1}}$ **^{29}Si spin composition.** The energies levels from the $\langle 111 \rangle_1$ ^{29}Si Hamiltonian (see Eq. (5.1)) color-coded by the expectation value of only the ^{29}Si spin. Except at $\approx$ 10 G the nuclear spin is a good quantum number. Note the broken axis, the energies in the lower axis are scaled up by a factor of 10 to show the two levels.

5.3 Pulsed ODMR

With the ground state fully mapped out for both the ^{28}Si and ^{29}Si optical peaks we can now move from continuous wave ODMR to pulsed ODMR wherein we probe the temporal dynamics of the qubits defined by the different transitions identified in the previous section, namely, T_-, T_0, T_0^+ for the ^{28}Si optical peak, and T_0^+ and T_0^- for the ^{29}Si optical peak. As stated before, this investigation will inform the optimal operation points for a ^{77}Se spin system in natural silicon. Furthermore, we aim to investigate clock transitions within these different ground state manifolds.

For all pulsed ODMR experiments Rabi pulses sequences are done every day to calibrate π pulse lengths. This is done for every transition frequency at every magnetic field to be investigated. This ensures that any changes in the resonator cavity or Q-factor day to day or any other coupling changes are compensated.

5.3.1 Electron spin echo envelope modulation

As discussed in Section 2.3.6, ^{29}Si nuclear spins in the bath couple to the central spin during a Hahn echo measurement leading to oscillations in the transient. Here we investigate electron spin echo envelope measurement (ESEEM) of the transitions of interest. Due to low optical signal from the ^{29}Si optical peak we focused on the ^{28}Si optical peak for these measurements. High resolution Hahn echo measurements are shown in Fig. 5.7 along with their Fourier transform power spectra.

The measurement of Hahn-echo transients is performed as described in Section 3.2.2, however, note that we plot the Hahn echo results versus τ rather than the full dark time, 2τ.

The most prominent ESEEM features are seen in the T_- transient (Fig. 5.7a, b) with much higher modulation depth than the T_0 or T_0^+ transients. We are in the regime where $\mathcal{B}$ (see Eq. (2.23)) is much less than the Larmor frequency of ^{29}Si, thus, when the magnetic number of the two states is close to zero, as is the case for the T_0 and T_0^+ transitions, the ESEEM modulation frequencies are approximately equal to the Larmor frequency of ^{29}Si, $\omega_{\alpha,\beta} \approx \omega_I$. As well the modulation depth, $k<$ is much less than 1 (see Eq. (2.21)). The result is that driving the T_0 and T_0^+ result in low ESEEM modulation, whereas the $T_\pm$ levels with $m = \pm 1$ have much higher modulation depths

With a high Δm the T_- transition shows near 100% modulation of the envelope with frequencies at multiples of the ^{29}Si Larmor frequency, 8.46 MHz/T [210]. This measurement is repeated at multiple magnetic fields (Fig. 5.7c inset) and the peak frequencies in the power spectrum are plotted versus magnetic field. Overlaying the expected Larmor frequencies of ^{29}Si (no fit parameters) show excellent agreement. We can compare this result to literature by recognizing that, at low field, the singlet and $T_\pm$ levels are identical to the levels of an NV^- center: a spin-1 system with a zero-field splitting which splits the spin ± 1 levels from the spin 0 level. Van Oort et al. [211] see ESEEM results that are near identical to these results but with the ^{13}C Larmor frequency as the modulation frequency.

The ESEEM of the T_0 and T_0^+ levels (Fig. 5.7d-g) are more subtle with lower modulation depths due to the Δm of the transition being lower. In this case the power spectra show distinct features without repetition as seen for $T_\pm$. T_0 shows a low frequency peak and a peak at $2\omega_{29}$ while the T_0^+ shows two peaks centred on at ω_{29}.

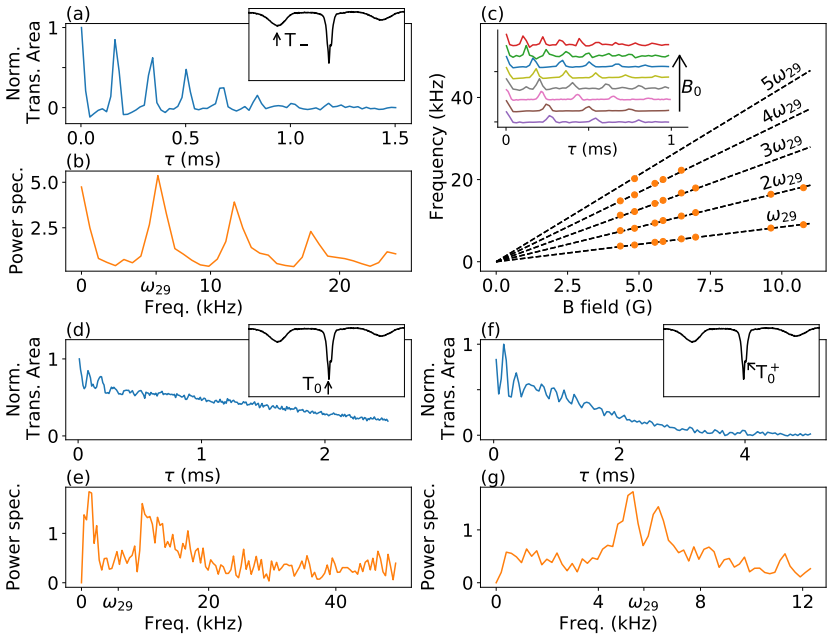

Figure 5.7: **ESEEM experiments.** Hahn-echo decay curves probing different ODMR transitions (ODMR spectra in insets) of the ^{28}Si optical peak, plotted versus τ, half the total dark time, 2τ. All Hahn-echo measurements shown are at 7 G B-field. (a-b) Hahn-echo decay and Fourier transform for the T_- transition ($B_0 \perp B_1$). (c) Peak frequencies of the T_- power spectra at different magnetic fields (decays shown in inset). Dashed lines are multiples of Larmor frequencies. (d-e) Hahn-echo decay and Fourier transform for the T_0 transition ($B_0 \parallel B_1$). (f-g) Hahn-echo decay and Fourier transform for the T_0^+ transition ($B_0 \parallel B_1$).

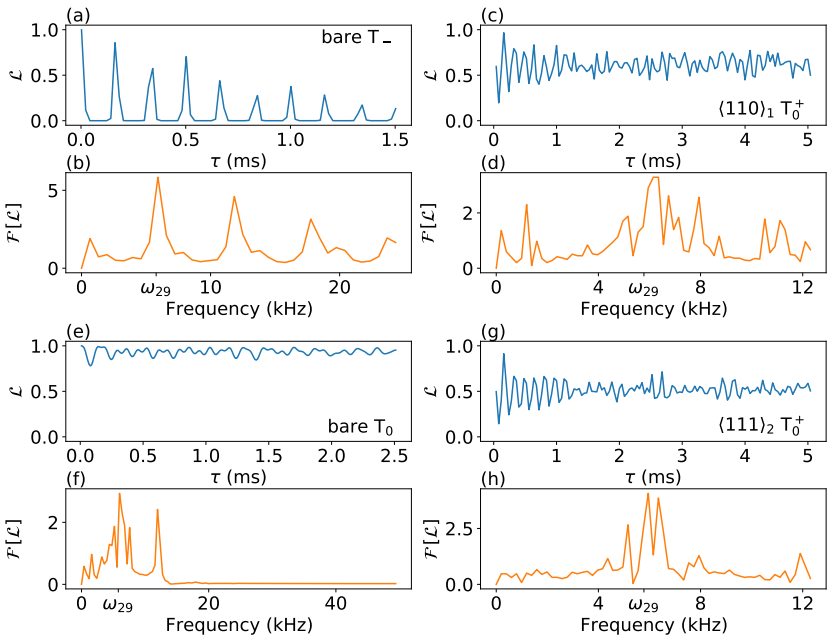

Figure 5.8: **ESEEM simulations.** Coherence function and power spectrum for different central spins simulated using PyCCE at first order. Coherence functions are plotted versus τ, half the total dark time, 2τ. (a-b) The T_- transition of a bare $^{77}Se^+$ center. (c-d) The T_0^+ transition of a $\langle 110 \rangle_1$ coupled center. (e-f) the T_0 transition of a bare $^{77}Se^+$ center. (c-d) The T_0^+ transition of a $\langle 111 \rangle_2$ coupled center.

We can understand these results further by comparing to simulations. In Section 2.3.6 we outline the procedure to model ESEEM oscillations in a Hahn-echo coherence transient for a central spin with modulation from many nuclear spins. However, cluster correlated expansion (CCE, see Section 4.2) can also be used to model the ESEEM oscillations. CCE-1 reduces to ESEEM, considering the effects of the central spin coupled to only and a single bath spin. Each bath spin is considered separately with the modulation from each bath spin multiplied together.

With this motivation we perform CCE-1 simulations of the transitions of interest within a bath of ^{29}Si atoms with a 4.7% density. We make use of the PyCCE package [205] to encode the Hamiltonian and level structure of our central spin, generate properly placed ^{29}Si atoms for 100 random realizations of a lattice and to perform the evolution and generation of the coherence function $\mathcal{L}$. We consider a bath with a radius of 8 nm and we consider a cluster cutoff radius of 1 nm. We consider the T_0, and T_- of a bare $^{77}Se^+$, and T_0^+ transitions for both a $\langle 111\rangle_2$ and a $\langle 110\rangle_1$ coupled ^{29}Si to form the central spin. The results of these simulations are shown in Fig. 5.8. Note that CCE-1 models the modulation but not the exponential decay due to the loss of coherence on a T_2 time scale.

For the T_0 and T_- transitions we consider just a $^{77}Se^+$ defect with no ^{29}Si coupling as the central spin. From Fig. 5.4 there is some contribution from coupled $^{77}Se^+$-^{29}Si centres, however, we assume that the bare uncoupled transition is dominant based on these weakly coupled centres being the most common. The T_0^+ ODMR line is composed of two primary centres: a $^{77}Se^+$ coupled to either a $\langle 111\rangle_2$ or a $\langle 110\rangle_1$ ^{29}Si. We consider these two cases separately when defining the central spin. In both cases we choose the appropriate S_0 sub-level such that the central spin simulated is a $\Delta m \approx 0$ transition as this should be the dominant transition in the experiment due to the parallel B_0-B_1 arrangement.

We can see immediately that the T_- simulation matches the data very well showing the peaks at multiples of ω_{29} (Fig. 5.8a-b). In the coherence the peaks do decrease at longer τ values despite there being no loss of coherence in simulation, this may be to due to the modulation frequencies washing out. This washing out effect is present in the other results as the modulation depths drop off with longer evolution times. This may indicate that the Hahn echo result is limited by the spin-bath oscillations not the intrinsic coherence time of the transition.

The T_0 simulation (Fig. 5.8e-f) has the low modulation depth as seen in the data along with the spike in frequency at $2\omega_{29}$. However, there is a large amount of power at ω_{29} that doesn't match the data. It is not clear why this additional power is not seen in experiment.

The T_0^+ simulations (Fig. 5.8c-d and g-h) both have large power at ω_{29} as seen in the data. However, the $\langle 111\rangle_2$ coupled transition more closely matches the data. It is likely then that the $\langle 111\rangle_2$ coupled centers are the primary constituent of the T_0^+ line, consistent with the larger coupling, and the higher detuning from T_0 and the higher signal strength. For the following discussion and simulations we will consider that the T_0^+ is exclusively due to $\langle 111\rangle_2$ coupled centers.

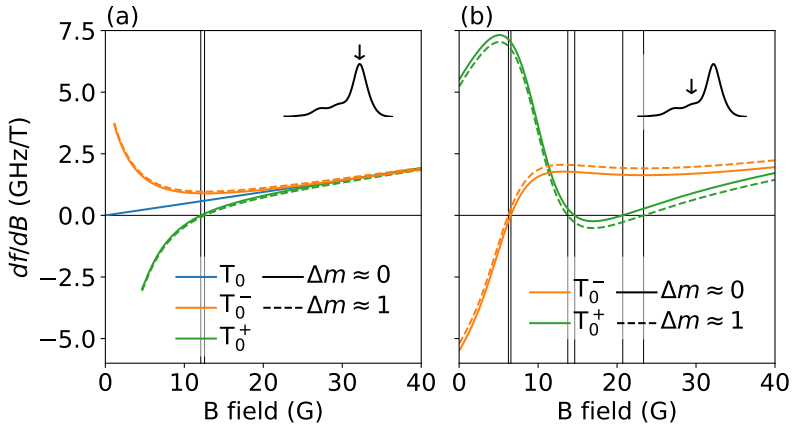

Figure 5.9: **Clock transitions.** df/dB_0 of transitions of interest for the two optical peaks as shown in the insets. (a) df/dB_0 of the bare T_0 and the two $\langle 111\rangle_2$ $T_0^{\pm}$ transitions. For the latter transitions both the $\Delta m \approx 0, 1$ branches are plotted. Curves are cut off where anti-crossings occur at low B-field (see Fig. 5.4). (b) The $T_0^{\pm}$ transitions of the $\langle 111\rangle_1$ system for both $\Delta m \approx 0, 1$. Clock transitions occurring where $df/dB_0 = 0$ are marked with vertical lines.

5.3.2 Clock transitions

As discussed in Section 2.3.5 many forms of decoherence are dependent on df/dB_0, the sensitivity of the transition energy to the external magnetic field. This motivates the search for operational sweet spots, known as clock transitions (CTs) [212], where df/dB_0 goes to zero.

In the previous section we mapped out the transition energies versus magnetic field. Armed with the model Hamiltonian we can determine the CTs available in the system and measure T_2 coherence times on and off the CTs. Figure 5.9 shows df/dB_0 versus magnetic field for the primary peak transitions: the ^{28}Si T_0, the $\langle 111\rangle_2$ ^{29}Si $T_0^{\pm}$, and the $\langle 111\rangle_1$ ^{29}Si $T_0^{\pm}$.

The T_0 transition, which is the standard S_0-T_0 transition of an isotropic hyperfine system, only has a CT at zero field. This has been shown to be an excellent CT in selenium [69] and in phosphorus [65]. However, this CT is at zero-field exactly, thus, there are limitation on how close to the CTs the B-field can be set while still being able to resolve the T_0 transition from the overlapping with $T_{\pm}$ at low field [65]. The inability to drive only the S_0-T_0 transition lowers the accessibility of this CT. In our sample, the overlap of T_0 with $T_{\pm}$ occurs below ≈ 5 G. Nevertheless, we investigate this line as a comparison for other CTs such as the T_0^+ transition which exhibits a CT above 10 G making it accessible for a T_2 measurement or for use as a qubit. The additional hyperfine coupling to the $\langle 111\rangle_2$ ^{29}Si introduces more accessible CTs.

The hyperfine coupling to a $\langle 111\rangle_1$ ^{29}Si also introduces CTs as seen in Fig. 5.9b. In addition to being at $B_0 > 0$, the $\langle 111\rangle_1$ ^{29}Si coupling has two additional benefits. Firstly, due to the larger interaction strength of the hyperfine coupling, the individual transitions are even more split than those of the ^{28}Si optical peak allowing for easier resolution of the individual transitions. Secondly, the optical isotopic shift results in an optical peak where (nearly) all centres have the same domi-

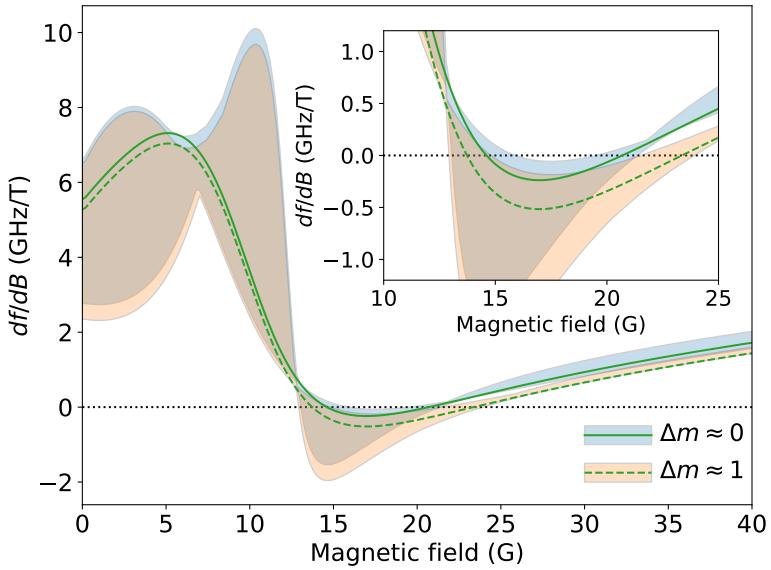

Figure 5.10: ***df/dB*$_0$ at different angles.** The df/dB_0 of the T_0^+ transitions of the $\langle 111 \rangle_1$ transition along with upper and lower bounds at each field value for a collection of B_0 angles. The green lines are when B_0 is along the $\langle 111 \rangle$ crystal axis as in Fig. 5.9. The steep drop at $\approx$ 13 G is due to an anti-crossing that apprears at certain angles.

nate hyperfine coupling to ^{29}Si. In contrast, the ^{28}Si optical peak has multiple different hyperfine couplings present in addition to a dominate signal from a sub-ensemble with negligible hyperfine coupling.

Looking closer at the $\langle 111 \rangle_1$ T_0^+ transition there are two CTs at $\approx$ 14 G and $\approx$ 22 G. Here we see a possible issue: as the 'T_0^+' transition is actually two transitions with $\Delta m = 0$ or 1 with CTs at slightly different magnetic fields, we may be unable to exactly probe the system at df/dB_0 = 0. The $\Delta m = 1$ transition should be sub-dominant given $B_0 \parallel B_1$ however it could have deleterious effects, this will be discussed further below.

Due to the anisotropy of the hyperfine tensor of the interaction with the ^{29}Si $\langle 111 \rangle_1$ we have an additional knob to control the system: the angle of static field relative to the $\langle 111 \rangle$ direction. While this will have a multitude of effects including changing transition energies and magnetic fields at which CTs occur, a possibly very exciting outcome would be if the two CTs of a single Δm branch become a single CT with d^2f/dB_0^2=0. This would result in a CT that is insensitive to magnetic fields at both first and second order, possibly increasing coherence times dramatically.

Figure 5.10 shows the df/dB_0 of the T_0^+ transitions for a multitude of different B-field angles sampling across all possible directions. Unfortunately, as can be seen from the inset, there is never an angle where the CT has both df/dB_0=0 and d^2f/dB^2=0. Nevertheless the peak $|df/dB_0|$ between the two CTs drops by a factor of ≈ 4 (≈ 3) for the $\Delta m \approx 0$ ($\Delta m \approx 1$) transition. If in application the exact magnetic field cannot be set then minimizing $|df/dB_0|$ across this band may be favourable.

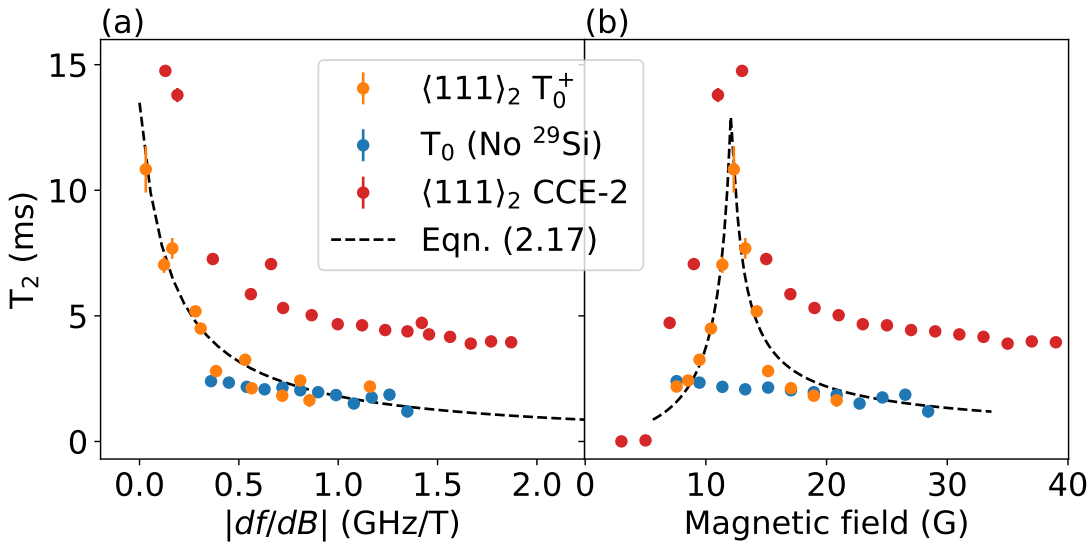

Figure 5.11: **Clock transition: ^{28}Si optical peak.** Hahn-echo T_2 lifetimes versus (a) $|df/dB_0|$ and (b) magnetic field for the primary ODMR peaks, T_0 (blue) and T_0^+ (orange), for the ^{28}Si optical peak. $|df/db|$ in (a) is determined from the corresponding Hamiltonian (T_0^+ transition of a $\langle 111\rangle_2$ ^{29}Si coupled system, orange, and the T_0 transition of an uncoupled system, blue) at the experimentally set magnetic field values shown in (b). Dashed lines are a fit to Eq. (2.18). Simulated Hahn-echo T_2 values from CCE-2 (red) are included as well.

Coherence times: ^{28}Si optical peak

To assess these CTs we performed a Hahn-echo T_2 measurement for the four lines of interest for a range of magnetic fields up to 30 G. Of particular interest is the dependence of the Hahn-echo T_2 on df/dB_0 and to determine how much enhancement is possible by operating at the CTs. Furthermore, with four possible transitions with which to use as a qubit we aim to determine which has the most promising features for future use as a qubit.

For each magnetic field and drive frequency we first perform a Rabi pulse sequence to obtain calibrated π and $\pi/2$ pulses. The measurement of the Hahn-echo transient is performed as described in Section 3.2.2.

Figure 5.11 shows the same dataset of T_2 times for the transitions of the ^{28}Si optical peak plotted both versus $|df/dB_0|$ and versus magnetic field. For each of the two ODMR peaks, the uncoupled T_0 and $\langle 111\rangle_2$ ^{29}Si coupled T_0^+, $|df/dB_0|$ is calculated using the Hamiltonian in Eq. (5.1) with the corresponding hyperfine values. When determining the transition energy we use the branch of S_0 that results in a transition with $\Delta m = 0$ as we expect this to be the dominant transition for the magnetic field orientation ($B_0 \parallel B_1$).

As predicted the T_0 transition shows minimal increase in coherence times as the low $|df/dB_0|$ regime at low magnetic field cannot be accessed. The T_0^+ transition on the other hand shows a clear

peak in coherence time of 10.8 ± 0.9 ms at 12.3 G, a factor of 7 times greater than when measured off the CT. A dramatic increase and thus an ideal operation point for use as a qubit.

The coherence times versus $|df/dB_0|$ of the $\langle 111 \rangle_2$ T_0^+ line are fit with Eq. (2.18) shown as a dashed line in Fig. 5.11. For this fit we allow for a correction factor to the experimentally set magnetic field to account for any errors in the field calibration because a slight error in magnetic field can skew $|df/dB_0|$ substantially when near a CT. This correction factor is an additional fit parameter. From the fit we determine:

$$\begin{aligned} k_{ID} &= 0 \pm 200 \text{ kHz}/\gamma_e^2, \\ k_{iFF} &= 13 \pm 4 \text{ kHz}/\gamma_e, \\ k_{dFF} &= 0.07 \pm 0.02 \text{ kHz}, \end{aligned} \tag{5.2}$$

where here we are normalizing by the electron spin dipole moment, γ_e. k_* are the proportionality constants for the different decoherence mechanisms introduced in Section 2.3.2: instantaneous diffusion, indirect flip-flops and direct flip-flops.

As a comparison for these values we can determine an expected k_{ID} from the approximate Se^+ concentration. As an upper bound we can consider all boron has compensated one-to-one a Se^0 to Se^+, thus [Se^+] = [B] = $(4.7 \pm 0.7) \times 10^{15}$ cm^{-3}. This would give k_{ID} ≈4 kHz/γ_e^2 which is much smaller than the errorbars of this fit indicating this dataset is insufficient to accurately measure k_{ID}. A method such as tip-angle [69, 77] might be better suited.

k_{iFF} is very large compared to those determined in Ref. [66] (10–30 Hz/γ_e) which investigated Bi donors in ^{28}Si. This is expected as their sample was in isotopically purified material (100 ppm ^{29}Si) whereas here we have a natural abundance ($\approx 5\%$ ^{29}Si), 500 times larger, which agrees with the 500–1000 times larger k_{iFF}. k_{dFF} is quite large as compared to Ref. [66] (1–6 Hz) which may be due to the much higher concentration of resonant Se^+ centres.

In addition to fitting with Eq. (2.18) we also compare the T_2 times to the expected coherence times from CCE-2 simulations. We simulate Hahn-echo T_2 coherence decays for a $\langle 111 \rangle_2$ $^{77}Se^+$-^{29}Si pair system in a bath of ^{29}Si spins with a 4.7% isotopic abundance. These simulations are done in the same manner as the simulations in Section 2.3.6 however we use a cluster size of two to capture the decoherence from the spin bath. As before we make use of the PyCCE package [205] and average the one-pulse coherence function over 50 random realizations of the lattice. We consider a bath with a radius of 8 nm and we consider a cluster cutoff radius of 1 nm. After averaging the coherence function over all lattice realizations we fit the result with a stretched exponential [66] to obtain a Hahn-echo T_2.

The simulations show qualitative agreement with the data but with higher coherence time across the board. This may be due to the high concentration of selenium centres limiting the experimental results, an effect that is not included in the simulations. The maximum T_2 is determined by k_{dFF} which is predominately set by the concentration of resonant Se^+ centres. Another possibility is that the T_0^+ transition isn't fully resolved from the T_0 transition of the uncoupled Se^+ centres nor the

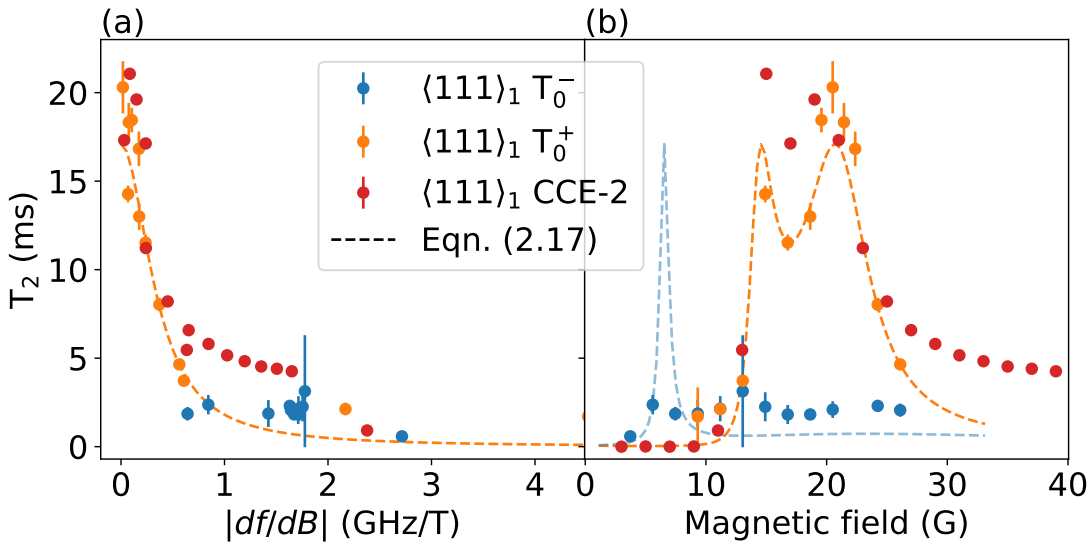

Figure 5.12: **Clock transition: ^{29}Si optical peak.** Hahn-echo T_2 lifetimes versus (a) $|df/dB_0|$ and (b) magnetic field for the two primary ODMR peaks, T_0^+ and T_0^-, for the ^{29}Si optical peak. df/dB_0 is derived from the Hamiltonian determined in Section 5.2.1. Dashed lines are a fit to Eq. (2.18). Simulated Hahn-echo T_2 values from CCE-2 are included as well.

$\langle 110\rangle_1$ T_0^+ line, either of which may hinder the coherence by driving multiple transitions simultaneously.

Coherence times: ^{29}Si optical peak

In the same manner as the previous section, we study the coherence times of the two primary ODMR transitions, $\langle 111\rangle_1$ $T_0^\pm$, for the ^{29}Si optical peak. Figure 5.12 show the T_2 coherence times measured for the $\langle 111\rangle_1$ $T_0^\pm$ transitions of the ^{29}Si optical peak. Again we display the coherence times versus the magnetic field set during the experiment and versus the calculated $|df/dB_0|$ from the Hamiltonian, Eq. (5.1), and the corresponding hyperfine values as well as using the $\Delta m = 0$ branch of S_0 due to the magnetic field orientation ($B_0 \parallel B_1$).

The T_0^+ transition shows very clear enhancement of the coherence times at the two CTs with a maximum measured $T_2 = 20.3 \pm 1.5$ ms at 20.5 G, a 12 times enhancement over the non-CT magnetic field values. Compared to the coherence times measured for the bare uncoupled Se defect there is a factor of 9 increase. On the other hand the T_0^- transition shows no enhancement at the expected CT at ≈ 7 G – this will be discussed later.

Again we fit the $\langle 111\rangle_1$ T_0^+ results with Eq. (2.18) in the same manner as above. We obtain:

$$\begin{aligned} k_{ID} &= 390 \pm 180 \text{ kHz}/\gamma_e^2, \\ k_{iFF} &= 0 \pm 3 \text{ kHz}/\gamma_e, \\ k_{dFF} &= 0.06 \pm 0.01 \text{ kHz}, \end{aligned} \tag{5.3}$$

where we are normalizing by the electron spin dipole moment, γ_e.

Here we now see very different results as compared to the $\langle 111\rangle_2$ T_0^+ fit result. The k_{ID} value indicates a concentration 100 times larger than would be expected based on the upper bound on the Se^+ concentration. The exact source of this $|df/db|^2$ dependent decoherence unknown.

k_{iFF} is lower than the $\langle 111\rangle_2$ T_0^+ fit result, although not to a significant extent given the large error bars. The k_{iFF} values should be about the same as the two systems are in the same isotopic environment. It could be that the large k_{ID} is obscuring the smaller effect of the k_{iFF} leading to an underestimate in the fit result. The dataset may be insufficient to determine both accurately. k_{dFF} is approximately the same as before, consistent with the hypothesis that the limitation being the ^{29}Si in the environment.

To get an estimate of T_2 versus magnetic field for the T_0^- transition (which showed no enhancement) we take the fit parameters from the T_0^+ versus df/dB_0 dataset (Eq. (5.3)) and apply them to the T_0^- transition. We make the assumption that the two transitions will have the same sensitivity to the environment as they are merely different ground state manifolds of the same sub-ensemble of centres. Thus the only difference in the predicted T_2 times is that we use the $|df/dB_0|$ values from the $S_0 \leftrightarrow T_0^-$ transition (using the $\Delta m = 0$ branch). This is plotted as a blue dashed line in Fig. 5.12b showing that the experimental data points likely missed the much sharper CT which could explain the lack of T_2 enhancement seen for the T_0^- transition. This shows that the T_0^+ transition is a better manifold for a qubit as the CT enhancement over a much broader band in magnetic field rather than a very sharp enhancement.

Finally, we use the same CCE-2 simulation method as above but for the ^{29}Si coupled in the nearest neighbour position. In this case the modelled coherence times agree quite well as seen in Fig. 5.12. The exact positions of the peak coherence are slightly shifted compared to experiment but the magnitude of the max coherence agrees within our experimental error. The offsets of the peaks could be due the calibration of the magnetic field at the sample, from the fitting above the optimal correction factor for the magnetic field was 10% higher than the experimentally determined value. Higher than in the previous section which was measured on a different day indicating the need for more frequent field calibrations.

As the simulations only consider a single centre, the agreement between simulations and experiment means the high selenium concentration isn't limiting the coherence times. Nor are we being limited by poor selectivity of the transition being driven: the T_0^+ transition is well separated from any other transition. Furthermore, the simulations only drive the $\Delta m = 0$ branch from S_0. Exper-

imentally, we cannot resolve the two branches and yet the agreement with simulations suggest we are not being limited by driving these two Δm branches.

The simulated coherence times also seem to match the fast quadratic drop off with $|df/dB_0|$ without a large offset as seen in the $\langle 111\rangle_2$ comparison. This could mean that the k_{ID} and k_{dFF} effects are well captured by the spin bath alone and the concentration of ^{77}Se$^+$-^{29}Si centres is sub-dominant. This is in contrast to the comparison of simulations to data for the $\langle 111\rangle_2$ T_0^+ transition in the ^{28}Si optical peak which suggested the concentration of Se centres was having a non-negligible effect. This makes sense as these ^{77}Se$^+$-^{29}Si pairs are only 5% of the centres and therefore a lower concentration of *resonant* defects in the bulk. The spin-bath being the dominant factor could help explain the high k_{ID} despite the concentration being lower than the ^{28}Si optical peak. Furthermore, the agreement between simulations and our experimental results show that we are not limited by the overlap of the S_0 levels. We are not driving two transitions in a manner that is lowering coherence possibly due to the magnetic field orientation doing a good job of selecting a single Δm branch.

The peak coherence times of both simulations and experimental results for the $\langle 111\rangle_1$ T_0^+ transition are larger than the $\langle 111\rangle_2$ T_0^+ transition. The fact that the simulations match the experiments means this difference isn't due to the concentration of Se centres. It could be due to a higher order effect: the second derivative of frequency with respect to magnetic field is smaller for the $\langle 111\rangle_1$ T_0^+ transition than the $\langle 111\rangle_2$ T_0^+ transition (see Fig. 5.9) which could be limiting the coherence of the latter.

Nuclear-like transitions

In addition to providing more accessible CTs for the ^{77}Se$^+$ hyperfine qubit, the presence of a ^{29}Si is itself an additional qubit available to be used in the system. As shown in Fig. 5.6 the transition between the $\langle 111\rangle_1$ T_0^+ and T_0^- states is nominally a ^{29}Si nuclear spin flip. This is promising as nuclear spins in silicon and other solid state systems have been shown to possess much higher coherence times as compared to the central optically accessible spin [51, 67, 70, 208, 213]. The presence of two available qubits in one center has promising applications for a memory/client architecture suitable for distributed quantum computing [214]. The optically active $S_0 \leftrightarrow T_0^+$ transition can act as a broker spin-photon interface for long range entanglement, while the ^{29}Si nuclear spin can act as a long lived memory qubit for storage during entanglement operations.

These transitions are not solely from a nuclear spin flip as the system is highly coupled at these low fields and the nuclear spin is not a good quantum number. However, as stated above, the nuclear-like transitions may still have long coherence times. While attempts were made to drive these nuclear-like transitions, no coherent Rabi oscillations were observed. Here we present the results of our models and simulations created to provide a prediction of the nuclear-like coherence times and any possibility of CTs.

Figure 5.13a shows df/dB_0 of the $T_0^- \leftrightarrow T_0^+$ transitions showcasing CTs at ≈ 11 and ≈ 67 G. By inspecting the Δm characteristic of the transitions we see that while the higher field is a $\Delta m = 1$

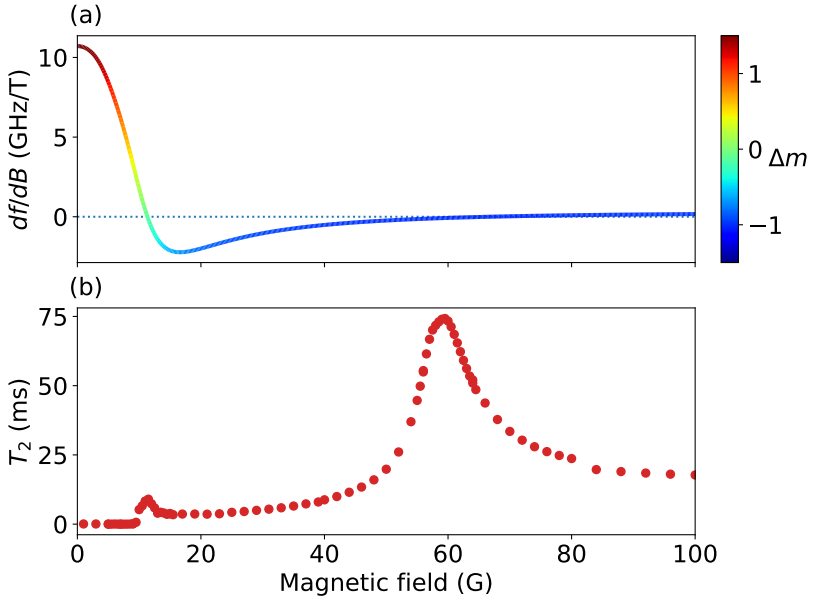

Figure 5.13: **Nuclear-like clock transition.** (a) df/dB_0 versus magnetic field for the $T_0^- \leftrightarrow T_0^+$ transition coloured by the Δm of the transition. (b) Hahn-echo T_2 coherence times from CCE-2 simulations with a natural abundance of ^{29}Si.

indicating a nuclear spin-flip as the nominal transition, the lower field is $\Delta m = 0$ indicating that the transition is between a non-trivial composition of all three spins.

Figure 5.13b shows the simulated coherence times based on CCE-2 utilizing 50 random lattice realizations with a bath radius of 8 nm and a cluster radius of 1 nm with a 4.7% ^{29}Si abundance. The coherence decays are each fit with a stretched exponential and the Hahn-echo T_2 coherence time is extracted for each magnetic field. Here we see that the two CTs have very different enhancements of the coherence despite both having $df/dB_0 = 0$, clearly the second order dependence on magnetic field (d^2f/dB_0^2) is coming into play [66], as was suggested for the different peak coherence times in Section 2.3.1. The higher field CT has a very low d^2f/dB_0^2 as the transition is approaching that of an uncoupled ^{29}Si. As the field increases df/dB_0 approaches a constant value equal to the ^{29}Si Larmor frequency of ≈ 8.46 MHz/T.

The use of both the central spin microwave CT and this nuclear spin radio frequency CT may prove challenging as they occur as different magnetic fields. Optimization of the integrated system will be needed to have both a long lived memory qubit and a broker qubit with sufficient coherence times. In any case, experimental work will be necessary to measure the coherence time of this nuclear-like transition for which these Δm values will help inform the resonator geometry for future studies.

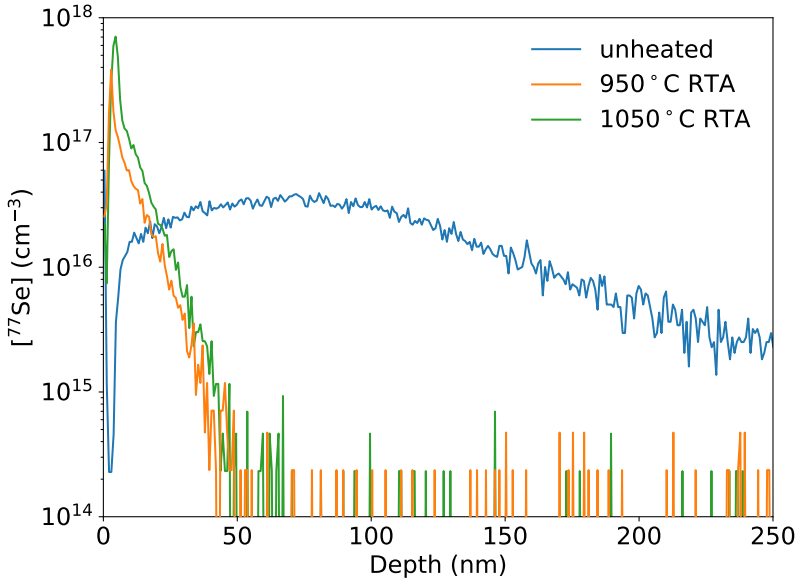

Figure 5.14: **Out-diffusion of implanted selenium.** Secondary Ion Mass Spectroscopy (SIMS) measurement of selenium implanted silicon before and after heat treatment.

5.4 Proposal

We can now take what we've learned and consider applying it to a quantum technology application. Specifically, we have measure the hyperfine interaction between $^{77}Se^{+}$ and nearest neighbour ^{29}Si and how the system possesses, not only a long lived clock transition, but also an addition nuclear spin qubit. As discussed previously, the most suitable application for selenium is the incorporation into silicon photonic cavities in the strong-coupling regime to generate photon mediated remote entanglement [78, 128]. Cavity parameters have already been determined based on the optical properties of the Se^{+} 1s:A $\Leftrightarrow$ 1s:T_2:Γ_7 transition [77]. Here we propose the integration of a $^{77}Se^{+}$-^{29}Si pair into the cavity rather than a bare $^{77}Se^{+}$ defect. This method results in two qubits coupled to the cavity that could form the basis of a client-memory system [214]. Furthermore, we will demonstrate that this proposal is advantageous from a fabrication standpoint and even from a coherence properties standpoint.

Incorporating selenium into the mode maximum of a cavity is non-trivial. Morse et al. [69] proposed implantation of selenium, however, selenium is a large atom that experiences significant out-diffusion after implantation with low uptake into substitutional sites [215, 216]. Furthermore, careful Fermi-level engineering is needed to produce selenium in the proper charge state, requiring co-implantation and uptake into the lattice or other methods [186]. These issues make it a challenging prospect to incorporate a single selenium in a substitutional site, in the proper charge state, in the mode maximum of a photonic cavity. As an example of the difficulties of the implantation

procedure, Fig. 5.14 shows the issue of out-diffusion with selenium implantation. This captures just one of the fabrication difficulties without addressing the issues of Fermi-level engineering.

The conventional method for incorporating selenium in a cavity would be to lower the final concentration of selenium in the material until on average the number of selenium atoms in the mode maximum is on the order of one. This may be accomplished by lower fluences of selenium implantation or lower concentration diffusion processes. Both of these methods have their fabrication difficulties, not least of which being confirming selenium concentrations. Working with $^{77}Se^{+}$-^{29}Si pairs would mean that the selenium concentration could be 20 times larger than the desired result and using the 5% abundance of ^{29}Si to reduce the effective concentration. The 20x increase in selenium concentration would increase the signal of concentration calibration measurements – an important step for determining optimal implantation/annealing recipes. It may even assist with fabrication constraints as it is easier to implant 10–100s of ions rather than 1–10s of ions [217].

If we now consider a ^{28}Si isotopically purified material there are yet more possible benefits for the fabrication of $^{77}Se^{+}$-^{29}Si pairs. While not commercially available, isotopically purified silicon can be obtained at wafer scales for silicon spin qubits [71] and isotopically purified SOI material is starting to be investigated for optically active silicon defects [218]. The benefits to coherence times and linewidths are well known [69, 70, 86, 98, 99] so we will consider the scenario where the benefits of utilizing ^{28}Si SOI outweigh the fabrication issues. We will consider an SOI sample with a 99.95% ^{28}Si isotopic purity. This is below the purity achieved in bulk samples, e.g. samples from the Avogadro Project [200] with a 99.995 $\%$ ^{28}Si, but is the state of the art for molecular beam epitaxy ^{28}silicon-on-insulator wafers [218].

For a ^{28}Si SOI sample we suggest modifying the incorporation procedure as follows: perform high concentration implantation or diffusion to have selenium in the correct charge state in the sample *without* the aim of having only a single Se^{+} (or $^{77}Se^{+}$-^{29}Si pair) in the mode maximum – aim to have high concentration throughout. For reference 10–100 selenium atoms in the mode maximum of a cavity with modal volume $(\lambda/n)^3$ is a concentration of $\approx 10^{13} - 10^{14}$ cm^{-3}, this is much lower than the concentrations of Se in the samples studied in this work, $\approx 10^{15}$ cm^{-3}. Next perform deterministic single ion implantation (or low fluence) implantation of ^{29}Si ions into the mode maximum of the cavities. This placement along with the high concentration of selenium will result in the deterministic placement of an $^{77}Se^{+}$-^{29}Si pair into the mode maximum. ^{29}Si deterministic placement is much easier than deterministic Se^{+} placement as 1) ^{29}Si will be much more readily incorporated into the lattice rather than out-diffusion as is the case for selenium, and 2) the implantation of ^{29}Si will not effect the Fermi level nor does it require a co-implantation to properly incorporate it. This process is shown schematically in Fig. 5.15a.

As established in Fig. 2.19c the optical transition of an $^{77}Se^{+}$-^{29}Si pair is well resolved from the unpaired Se centres. This means the precisely placed $^{77}Se^{+}$-^{29}Si pair will not be obscured by the spectra of the background Se^{+}. Figure 5.15b shows a $^{77}Se^{+}$ spectrum in 99.991% ^{28}Si [69] which has a purely Lorentzian linewidth of 0.87 μeV. At the relative detuning from ^{28}Si optical peak to the ^{29}Si optical peak this Lorentzian has an amplitude over three order of magnitude lower than the

maximum. Thus, there will be a negligable amount of bare $^{77}Se^+$ centres resonant with the $^{77}Se^+$-^{29}Si pairs. The optical cavity can simply be shifted from the bare ^{28}Si $^{77}Se^+$ spectrum as shown in Fig. 5.15b comparing to a cavity with a Q-factor of 10^4 (the requirement for C=1 [77]).

We can also consider the detrimental effects of higher selenium concentration on the spin coherence time. The results of this work has shown that the $\langle 111 \rangle_1$ T_0^+ coherence is not limited by the concentration of selenium in the surroundings as evidenced by the good agreement with the single defect simulations (see Section 2.3.1). The samples studied in this work have 10–100 times more selenium than we are proposing here. Furthermore, decoherence from instantaneous diffusion and direct flip-flops depend on resonant defects. The $^{77}Se^+$-^{29}Si pair qubit levels are detuned from the bare Se^+ $S_0 \leftrightarrow T_0$ transition by $\approx$4 MHz which may be sufficient to avoid decreases to coherence, although more work is necessary to confirm this hypothesis.

Finally, we can consider the achievable spin coherence times possible for an integrated $^{77}Se^+$-^{29}Si pair as compared to a bare $^{77}Se^+$ – specifically when operating at clock transitions. In the case of a natural silicon environment we have shown via experiments and simulations that the clock transitions available to the coupled system outstrip the coherence times of the bare Se^+, by a factor of 9 (see Section 2.3.1). For the comparison between a $^{77}Se^+$-^{29}Si pair and bare $^{77}Se^+$ defect in the case of an isotopically purified sample we must consider that the implantation of ^{29}Si is introducing spins into the lattice, making a locally worse spin bath. To this end we investigate CCE-2 simulations of the $\langle 111 \rangle_1$ T_0^+ coherence in environments with different ^{29}Si concentrations, simulating a $^{77}Se^+$-^{29}Si pair created by different doses of ^{29}Si. We compare these results in Fig. 5.15 along with the bare $^{77}Se^+$ T_0 transition in an environment with 0.05% ^{29}Si (the state of art for SOI isotopic purity [218]). The spin coherences were simulated with CCE-2 using PyCCE [205] using 50 random realizations of the spin bath. For each ^{29}Si concentration the bath size and cluster radius are scaled to have the same number of bath spins and same number of cluster pairs on average. For a natural concentration of 4.7% we use a bath size of radius 8 nm and a cluster size of 1 nm. We can see that by limiting the concentration of implanted ^{29}Si to 2–5 times the background we can achieve coherence times that are comparable to the bare Se^+ the background spin bath.

When comparing these results note that the CT of bare ^{28}Si $^{77}Se^+$ is misleading as the zero-field coherence time is experimentally inaccessible. As shown in Section 5.2.1 and Section 5.3.2 the T_0 transition of bare Se^+ cannot be driven at low fields due to the overlap with the $T_\pm$ transitions. This is true even in isotopically purified material as seen in Ref. [65] where going to yet lower magnetic fields did not monotonically improve the coherence times. This is not a problem for $^{77}Se^+$-^{29}Si system as the finite field means all transitions are well resolved. Thus, despite the worse spin-bath from the ^{29}Si implantation the spin coherence times of a $^{77}Se^+$-^{29}Si pair can exceed that of an isolated $^{77}Se^+$ centre.

In summary, we believe working with a $^{77}Se^+$-^{29}Si pair presents an advantageous system to work with compared to a bare Se^+. An additional qubit, a more straight-forward fabrication procedure, and competitive coherence times all make this a promising platform for an integrated silicon-photonics based quantum technology. Future work includes the integration of $^{77}Se^+$-^{29}Si pairs into

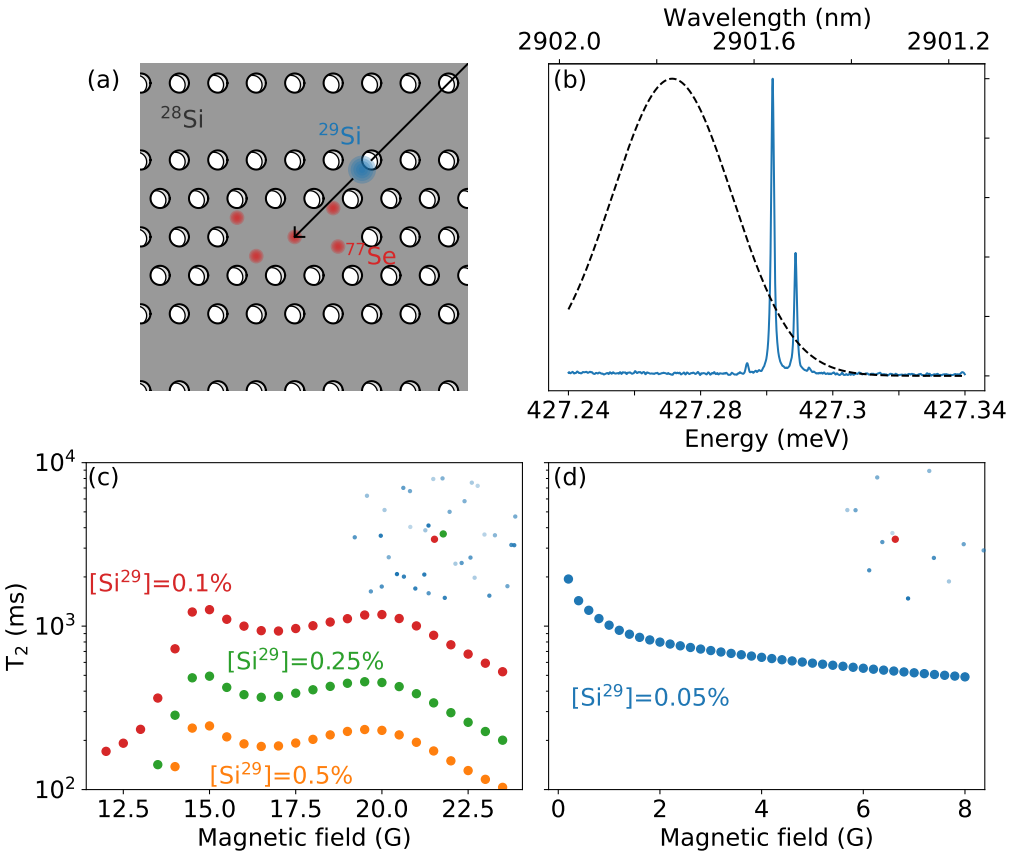

Figure 5.15: **^{77}Se^{+}-^{29}Si quantum technology**. (a) A silicon photonic crystal cavity [219] and adjacent waveguides illustrating a schematic diagram for the fabrication of cavity-coupled ^{77}Se^{+}-^{29}Si pairs: firstly, incorporate high concentrations of ^{77}Se in the correct charge state, secondly, perform deterministic implantation of ^{29}Si into this high ^{77}Se background. (b) ^{77}Se spectra in 99.991% ^{28}Si [69] along side the profile of a Q=10^4 cavity centred on the ^{29}Si optical peak. (c) CCE-2 simulated T_2 coherence versus magnetic field of a coupled ^{77}Se^{+}-^{29}Si system (T_0^+ transition) in different isotopic environments. The inset shows the environment of a ^{77}Se^{+}-^{29}Si pair (red-green) and the bath ^{29}Si (blue). (d) CCE-2 simulated T_2 coherence of a bare Se system (T_0 transition) in a high purity isotopic environment. The inset shows the environment of a bare Se (red) and the bath ^{29}Si (blue).

cavities and integrated photonics as well as a study of the spin coherence time of the local ^{29}Si nuclear spin. Cavity integrated $^{77}Se^{+}$-^{29}Si centres, acting as client-broker pairs, can enable an on-chip quantum computer as proposed by as proposed by Morse et al. [69] and Yan et al. [78] or even across multiple chips in a distributed quantum computing application.

Chapter 6

Results and Discussion: T centre

The state of the art at the time of this thesis work is implantation into SOI samples and preliminary work with integrated devices, however, the optical properties of T centres in this new environment are not known. Here we present our work on waveguide-integrated T centres including waveguide spectroscopy, lifetime measurements, and hole burning. We examine the waveguide sample at both zero-field and in a magnetic field, the latter of which enables spin control for a T_1 measurement. Additionally, we present hole burning measurements of T centres in bulk ^{28}Si to provide a measure of the possible linewidth in more ideal conditions. Finally, we present an outlook of the use of the T centre in an integrated photonic cavity for quantum networking prospects.

6.1 Waveguide spectroscopy

We confirm the presence of T centres within the waveguides with PL measurements using CW above-bandgap light (450 nm) illuminating the centre of the waveguide and measuring the luminescence with a grating spectrometer. The measured PL from both the ZPL GC and the PSB GC are shown in Fig. 6.1a along with a PL measurement of the unpatterned SOI material measured with a Fourier transform infrared spectrometer. There is a clear signature of T centres within the waveguides, with a strong ZPL line and the phonon sideband to lower energies showing the L_1 local vibrational mode at 906 meV [70, 191].

We use the grating spectrometer at a higher grating density to obtain a high resolution PL spectrum centered at the ZPL to attempt to measure the TX_1 transition. As the TX_1 level can be thermally populated at elevated temperatures the ratio of TX_0 to TX_1 integrated emission can be used to assess the temperature of the sample [190]. As shown in Fig. 6.1c there is no sign of emission from TX_1 in PL, indicating the temperature of the sample is lower that 4K (limited by the noise of the spectrum). As a comparison we measure pulsed PLE with the detector only triggered when the laser is off (to remove background) to obtain a PLE spectrum of the TX_1 level, this is shown in Fig. 6.1c. The splitting between TX_0 and TX_1 is measured to be 1.75 ± 0.1 meV, consistent with the splitting seen in Ref. [70].

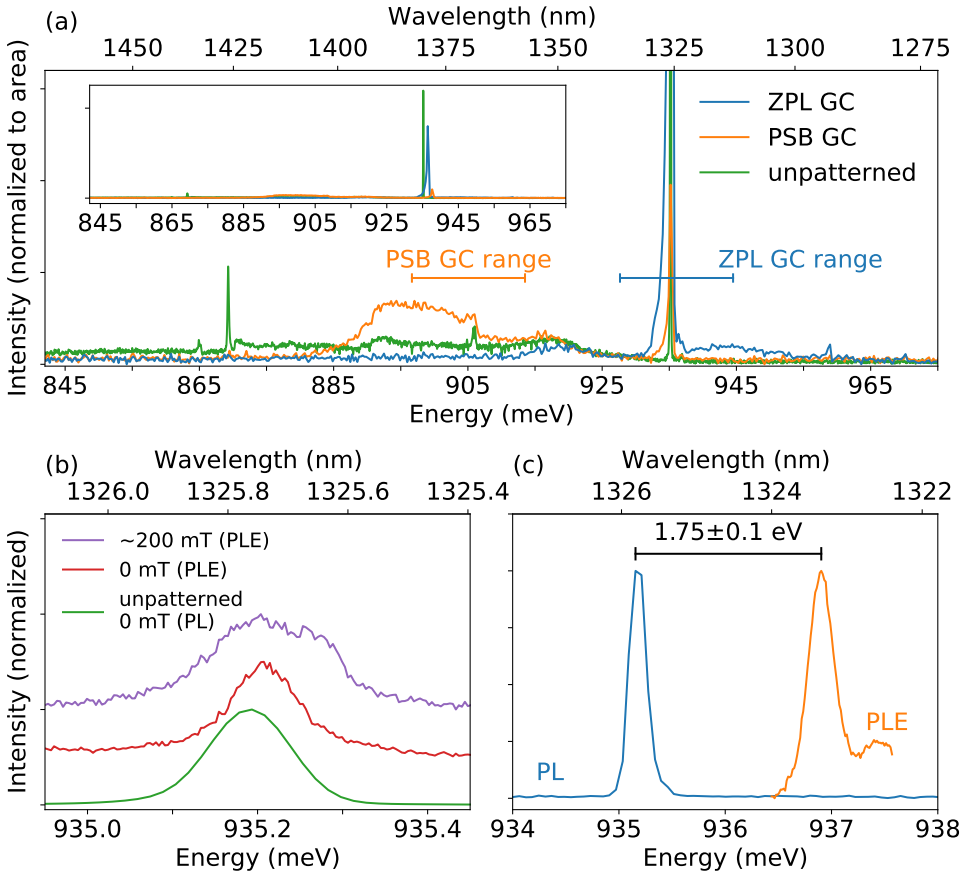

Figure 6.1: **Waveguide spectroscopy.** (a) Above-bandgap PL spectra of the unpatterned SOI material compared to the emission from the ZPL and PSB GCs. The approximate transmission ranges of the PSB and ZPL GCs are shown with horizontal bars. (Inset) Area normalized spectra showing ZPL relative to the PSB. ZPL GC and PSB GC spectra are shifted 10 and 20 meV respectively for clarity. (b) PLE spectra of waveguide integrated T centres at zero field and at a ∼200 mT magnetic field compared to the PL spectra of the unpatterned material. (c) High resolution PL from the ZPL GC in the region of the ZPL along with a higher energy PLE scan showing the TX_1 transition. The lack of TX_1 in PL indicates $T < 2$ K.

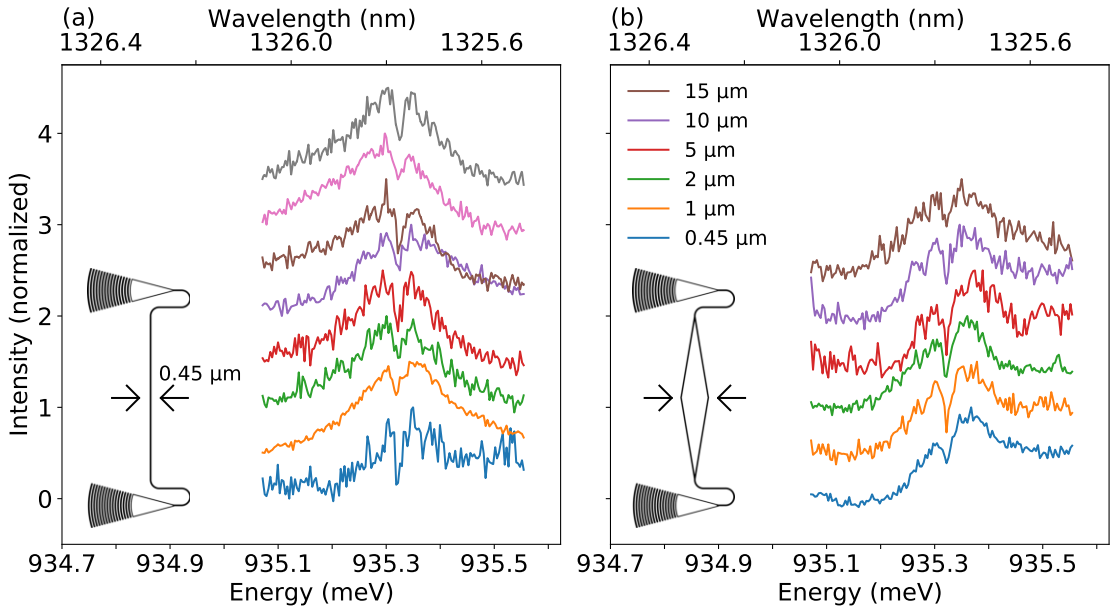

Figure 6.2: **Device survey.** Hole burning spectra of (a) a range of 0.45 µm wide waveguides devices and (b) a range of tapered devices with varying taper widths. The presence of PLE and spectral holes confirm the presence of integrated T centres across all probed devices.

We next measure a CW PLE spectrum to get a higher resolution spectrum of the ZPL line, measured with a single photon detector, as shown in Fig. 6.1b. Here we see an inhomogeneously broadened spectrum of an ensemble of T centres, we expect approximately 600 T centres based on concentration estimate from similar material [88]. We compare the PLE of this ensemble to a high resolution PL spectrum of the unpatterned material. This PL spectrum is measured with a 200 mW 532 nm CW excitation laser and the resulting luminesnce spectrum is measured by a Bruker FTIR. Compared to the PL spectra of the unpatterned material with linewidth 27.3 ± 0.2 GHz (0.1129 ± 0.00008 meV) the waveguide ensemble has a slightly narrower linewidth of 22.7 ± 0.3 GHz (0.0939 ± 0.0012 meV). In both cases the linewidths are much larger than seen in bulk natural silicon (approximately 7 GHz [70, 87]) due to implantation damage [87] and random strain from the silicon-silicon oxide interface in the SOI sample [79]. However, the two linewidths are nominally the same indicating the narrow waveguide environment does not add significant strain to the T centres and the fabrication procedure may in fact release some strain [220]. Under-etching the waveguides may reduce the strain even further – a topic for future work.

We also measured the PLE spectrum with the photonic chip mounted atop a neodymium magnet. In this case the inhomogeneous linewidth is 39.6 ± 0.5 GHz (0.164 ± 0.002 meV), however, we expect that this broadening is not due to the magnetic field and instead is due to strain on the sample from the mounting method. The study of the sample in a magnetic field is continued in Sections 6.3.3 and 6.4 where this will be discussed further.

While the remainder of the work on this chip will be performed on this particular device, we confirm the presence of T centres within additional devices, both waveguide and taper devices, by performing pump-probe hole burning measurements. A collection of these measurements are shown in Fig. 6.2. Of the 13 devices measured we see clear signs of T centres in all 13 indicating a high yield of T centre integrated photonic devices.

6.2 Waveguide lifetime

We next investigate the time-dependence of the T centre emission and measure the excited luminescence lifetime using a pulsed excitation and time tagging measurement. We excite the T centres both non-resonantly with an above-band 980 nm pulsed laser exciting the middle of the waveguide and with resonant light driving the ZPL pulsed with an EOM amplitude modulator.

For the above-band excitation we observe an emission lifetime of $0.96 \pm 0.01\mu$s which agrees with the lifetime measured in bulk ^{28}Si samples [70]. With the resonant excitation pathway we first measure at a wavelength detuned from the T centre PLE peak to get a measure of the background and then again resonant with the PLE peak. The two histograms of timetags are normalized and then the background is subtracted from the resonant histogram and the resulting exponential decay is fit. With this resonant excitation scheme we measure a shorter lifetime reduced by 16 percent to $0.81 \pm 0.01\mu$s. Both resonant and non-resonant results are shown in Fig. 6.3. This resonant excitation was repeated at multiple different wavelengths as shown in Fig. 6.4a which shows no dependence on the excitation wavelength.

There exist a variety of mechanisms through which the T centre may exhibit a reduced excited state lifetime including stimulated emission [104], Purcell enhancement [130, 221], and superradiance [222]. Stimulated emission is the process through which an excited T centre can have emission induced by the presence of a resonant light field. We conclude that this hypothesis is unlikely to be correct by measuring the luminescence lifetime across a range of pump powers and find that there is no dependence on the emission lifetime as shown in Fig. 6.4b. This power dependence study is repeated resonantly driving the TX_1 line, Fig. 6.4c, again showing no trends with power and giving an average lifetime of 0.858 ± 0.002 μs.

Purcell enhancement is described in Section 2.4.1 and is generally associated with cavity devices, however, simple photonic structures have been shown to theoretically Purcell enhance T centres by changing the local density of states within the device. Higginbottom et al. [88] predict Purcell enhancement (>3) in puck structures with dimensions on the same order of magnitude as the waveguide devices.

We assess the Purcell enhancement hypothesis by performing FDTD simulations of dipoles within a waveguide using Ansys Lumerical. A dipole within the waveguide will have a Purcell factor dependent on where in the waveguide it is located as shown in Fig. 6.5a-c. An ensemble throughout the waveguide will display an effective Purcell factor that is a weighted average across the waveguide. The weighting will be both the strength of the excitation mode profile of the first TE

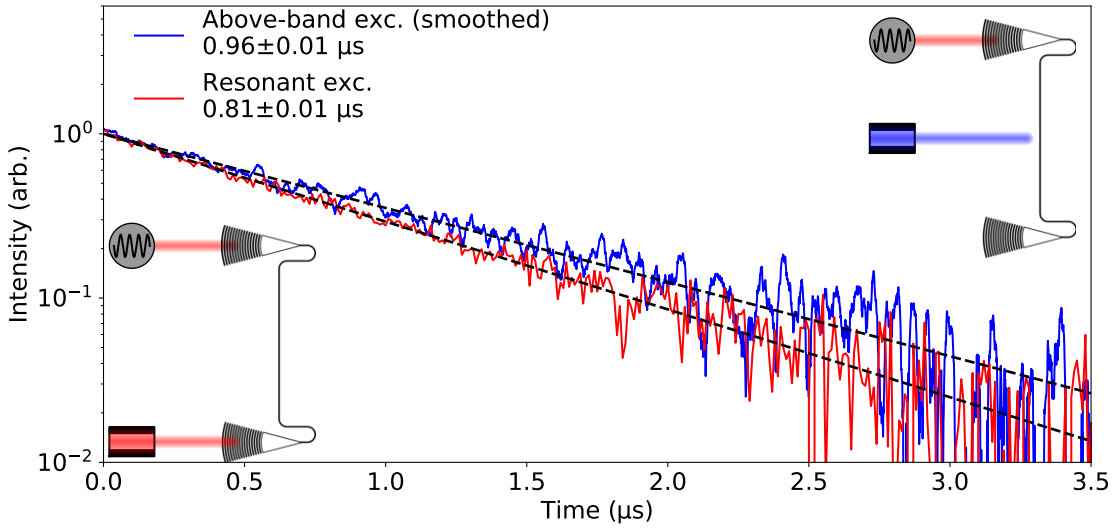

Figure 6.3: **Excited state lifetime.** The luminescence lifetime of waveguide integrated T centres probed with non-resonant, above-bandgap, light (blue) excited as shown in the upper inset and with resonant ZPL light (red) excited as shown in the lower inset. The luminescence decay of the above-band excitation has been smoothed with a Savitzky-Golay filter.

waveguide mode (Fig. 3.4b) as well as the coupling of the dipole's emission to the same mode as shown in Fig. 6.5d-f. We simulate all of these for three orthogonal dipole orientations and determine the effective Purcell factor. Examples of these simulations are shown in Fig. 6.5 for a dipole oriented normal to the SOI sample Fig. 6.5a; in the plane of the sample, orthogonal to the axis of the waveguide Fig. 6.5b; and in the plane of the sample and along the axis of the waveguide Fig. 6.5c. The effective Purcell factor for these orientations are 0.81, 0.91, and 0.72 respectively. These effective Purcell factors assume a uniform distribution of T centres through the waveguide, it is possible that a non-uniform distribution may weight the high Purcell factors differently.

We can also determine the expected effective Purcell enhancement when exciting with above-band light. In this case we take the excitation to be uniform across the waveguide rather than as a specific mode. However, the spatially dependent Purcell factors and the coupling to the first TE mode are the same. In this case the effective Purcell factor for the three orientations are 0.82, 0.90, and 0.74. These values correspond closely to those determined in the resonant case. We conclude that regardless of the distribution of T centres, Purcell enhancement is unlikely to match the lifetime results we are measuring.

Another possible explanation for the enhanced emission rate is superradiance [222], wherein a coherent interaction between excited centres induces a faster decay. This has been seen in whispering-gallery-mode cavities with defects in SiC [164] and may be present in the waveguide. If this is the case this is promising for a technological application that would require an ensemble working coherent together as is the case for a memory or transduction device as discussed in Ref [223].

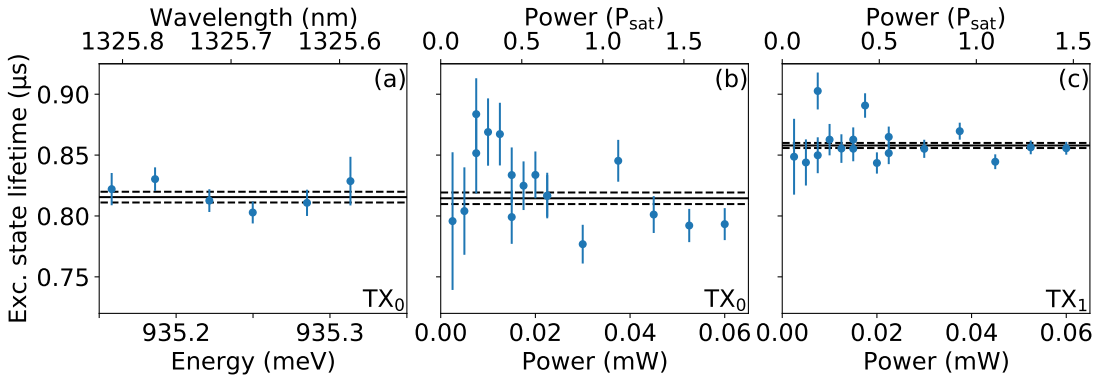

Figure 6.4: **Lifetime versus wavelength and power.** (a) Lifetime of the TX_0 versus wavelength showing no dependence. Lifetime of the (b) TX_0 and (c) TX_1 states versus power with nominal lifetimes of 0.81 ± 0.01 μs and 0.858 ± 0.002 μs respectively.

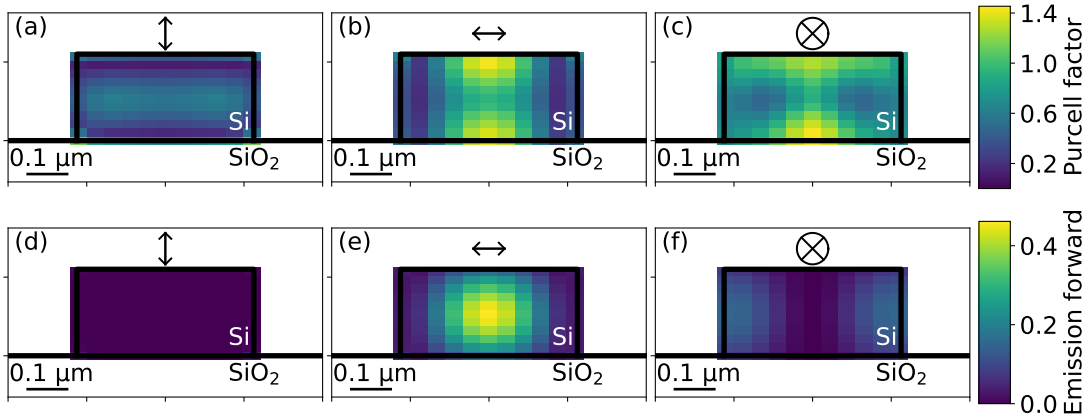

Figure 6.5: **Purcell factor and transmission simulations.** Lumerical simulations of a dipole oriented as shown in a waveguide showing (a-c) the Purcell factor and (d-f) the transmission into the fundamental TE mode.

A final explanation is that the resonant excitation is not enhanced, but the non-resonant excitation is suppressed, both in this measurement and in the bulk sample measurement in Ref. [70]. If the excitons created from above-bandgap excitation bind in a high energy level there could also be a rate limiting chain of decays to return to the TX_0 state before decaying with a detectable photon. We have seen that resonantly exciting to TX_1 adds 50 ns to the decay time (see Fig. 6.4). Decaying from yet higher excited states may explain the time difference between resonant and non-resonant excitation.

6.3 Hole burning

As discussed in Section 2.4.2 a key metric for the remote entanglement of emitters based on the Barrett-Kok protocol is the homogeneous linewidth or 'instantaneous' homogeneous linewidth. This can be determined via a hole burning measurement. Here we present hole burning measurements on a number of T centre ensembles in different samples and environments. While the exact lasers used may differ between experimental setups, the procedures are all the same as described in Section 2.2.2: a variable-power pump laser is turned to the peak of the inhomogeneously broadened line and a low power probe is swept about this pump energy revealing a hole and possible anti-holes. Exact experimental details for each sample and system are described in Section 3.3.

6.3.1 Waveguide: Zero-field

We start by investing the waveguide ensemble studied in the previous sections (Section 6.1 and Section 6.2) at zero applied magnetic field (Earth field < 0.05 mT). Resonant light is coupled through the ZPL GC and the emission is measured by a SNSPD through the PSB GC after filtering out remaining ZPL light. An example of spectral hole burning in this sample is shown in Fig. 6.6b. This spectra is generated by sweeping the probe laser with and without the pump laser and dividing the two spectra after removing the offset from pump excitation. The hole is fit with a Gaussian-Lorentzian sum to get the hole linewidth, which we take to be twice the homogeneous linewidth at the set pump power (see Section 2.2.2).

This hole measurement and fitting procedure is repeated for many different pump powers to generate a power dependence of the homogeneous linewidth. For each power the hole burning measurement is repeated multiple times with the hole fit with a Gaussian-Lorentz sum. The hole linewidth is determined by a weighted averaging over these datasets, weighted by the inverse variance of the fitting error. The dependence of the average homogeneous linewidth (half the average hole linewidth) on pump power is shown at both 1.2 K and 4.3 K in Fig. 6.6a. In each case the dependence is fit with Eq. (2.3) to extract a low power linewidth. At 4.3 K the lowest measured homogeneous linewidth (low power extrapolated value) is 590 ± 30 MHz (470 ± 30). This linewidth is limited by thermal dephasing to the TX_1 as has been seen in the broadening of ensemble linewidths in ^{28}Si [70]. From Ref. [70], the expected linewidth at this temperature is 260 MHz, lower than what we observe in the waveguide ensemble. This difference isn't due to a different TX_0 to TX_1 split as

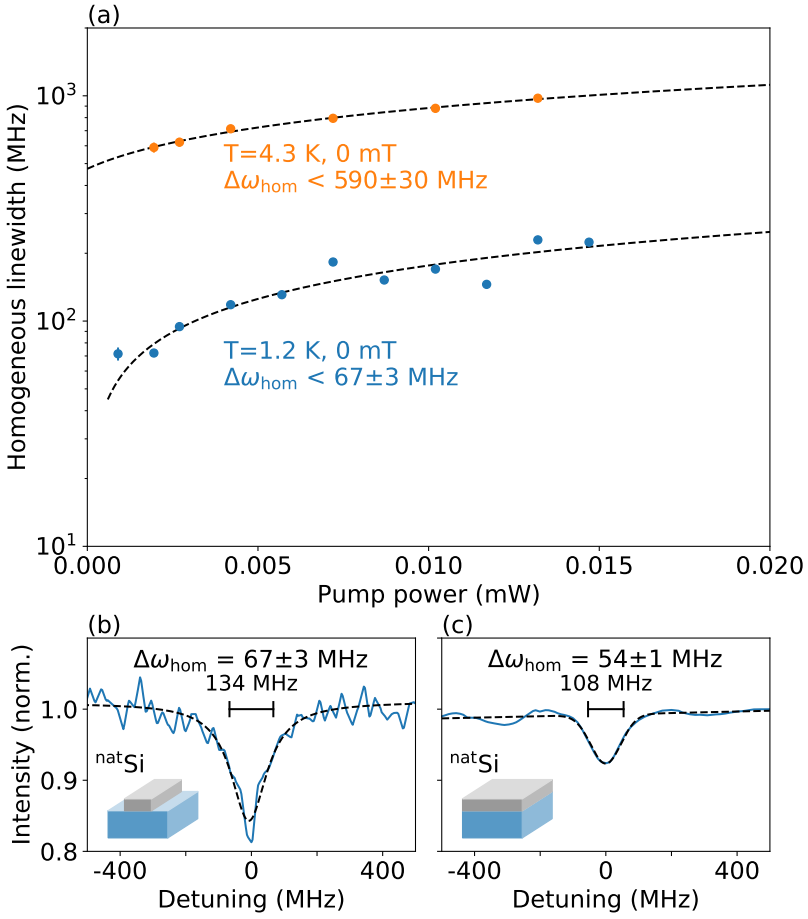

Figure 6.6: **Zero-field waveguide hole burning.** (a) Hole linewidth versus pump power for a waveguide ensemble at zero field at 1.2 K and at 4.3 K. Trends have been fit with Eq. (2.3). (b) An example of a hole burning spectrum of the waveguide ensemble. (c) A hole burning spectrum of unpatterned SOI material with the same implantation and annealing procedure as our main sample.

PLE measurements showed the splittings are the same between the waveguide and bulk ensembles (see Fig. 6.1c). It could be due to a different phonon density of states in the nanophotonic waveguide as compared to the macroscopic bulk sample.

At 1.2 K, below the thermal activation temperature the lowest measured homogeneous linewidth is 67 ± 3 MHz with a low power extrapolated linewidth of 4 ± 4 MHz. Low SNR prohibited measuring to lower powers and the sharp drop off at low powers is not well measured hence the large errorbars on the extrapolated value. Nevertheless, from the lowest measured linewidth as an upper bound we can confidently state that the instantaneous homogeneous linewidth is on the order of 10s of MHz, nearly two orders of magnitude lower than previous estimates [87, 88].

A comparison before and after fabrication is done by measuring a low power hole burning spectrum on unpatterned SOI material as shown in Fig. 6.6c displaying an instantaneous linewidth

of 54 ± 1 MHz. Limited SNR prohibited measuring the power dependence of the homogeneous linewidth thus we can only use this as an upper bound of the unpatterned material. Of note are the lineshapes of the two holes measured in waveguide and unpatterned samples: Lorentzian and Gaussian respectively. This discrepancy may be indicating a difference in the spectral diffusion environment. The typical lineshape is Lorentzian [104] however Gaussian linewidths have in seen in other solid state platforms due to spectral diffusion [202, 224].

These measured linewidths are very promising and actually significantly less than previous measurements of the homogeneous linewidth of the T centre. Ref. [87] investigated the linewidth using a method that hyperpolarized the T centres as the magnetic field was swept and measured a homogeneous linewidth of 1 GHz in SOI, and Ref. [88] investigated single T centres measuring a minimum homogeneous linewidth of 660 MHz. The key difference between these previous approaches and the approach presented here is the relevant time scales of the measurements. Here we measure the *instantaneous* homogeneous linewidth with a timescale set by the excited state lifetime (~ 1 µs) whereas Refs. [87, 88] measure the long-time homogeneous linewidth with times scales set by the T_1 lifetime and the spectrum acquisition time respectively, both much longer than the excited state lifetime. The time scale sets what spectral diffusion the measurement is sensitive to: the instantaneous homogeneous linewidth is a measure of the fast spectral diffusion and intrinsic dephasing whereas the long-time homogeneous linewidth is also sensitive to slower spectral diffusion effects. For technological applications, the instantaneous homogeneous linewidth is the key metric for high fidelity remote entanglement generation as will be discussed further in Section 6.5.

While the linewidth measured in this integrated waveguide is promising, there is a lot of room for improvement as no optimization has been performed on the e.g. implantation and annealing steps, on the fabrication steps, or on the base material – simply commercially available material. Here we have demonstrated a robust method of determining the key metric for future applications – a method that can be used for future studies on material development and improvements to spectral diffusion. As a comparision we can measure the instantaneous homogeneous linewidth in an isotopically purified sample with T centres in the bulk, far from interfaces as a measure of the optical coherence possible in a more ideal environment. To this end we consider T centre ensembles in bulk ^{28}Si.

6.3.2 Bulk ^{28}Si: Zero-field

In Ref. [87] the spectral diffusion linewidth of bulk samples were found to be significantly less than in SOI samples. This comparison to bulk samples provides a benchmark of what is possible for an optimized integrated sample. Here we investigate the hole burning linewidth of a bulk ^{28}Si sample to compare to the waveguide linewidth measured. The details of the ^{28}Si sample are listed in Section 3.3.3, however, of note is that T centres are generated via irradiation with electrons rather than implantation as is the case for the SOI/waveguide samples studied. Implantation has been shown to increase the inhomogeneous linewidth in bulk samples [87]. An irradiated sample may have more favourable optical properties in addition to being isotopically pure and having T centres far from surfaces.

Hole burning spectra of the bulk ^{28}Si sample at zero field are shown in Fig. 6.7 at a range of relative pump/probe powers, $P_{\mathrm{rel}} = P_{\mathrm{pump}}/P_{\mathrm{probe}}$, with a fixed probe power of 62 μW. In contrast to the saturation hole burning measured in waveguides Section 6.3.1, here the hole burning spectra are in the hyperpolarization regime (see Section 2.2.3).

The T centre is known to have an anisotropic hyperfine coupling between the unpaired electron and the hydrogen nucleus with a coupling strength of approximately 1–5 MHz [70]. At zero field this will lead to a splitting in the ground state on the order of the hyperfine coupling. In the waveguide sample the homogeneous linewidth was larger than this ground state splitting at the powers measured and so only saturation was occurring, not hyperpolarization. In this bulk ^{28}Si sample the presence of anti-holes indicates that the homogeneous linewidth is less than the ground state splitting to produce hyperpolarization (see Section 2.2.3).

In order to extract the homogeneous linewidth we make use of the rate equation model introduced in Section 4.1. With a hyperfine interaction between the electron and hydrogen we expect a singlet-triplet structure at zero field (the exact structure will be discussed below). As such we use a three-level steady-state solution Eq. (4.9).

As power broadening from the pump can lead to larger linewidths than the intrinsic homogeneous linewidth we fit all five spectra simultaneously. The free parameters are the homogeneous linewidth, the ground state splitting, and the inhomogeneous linewidth. Additionally, the absolute power of the pump and probe was a free parameter for each dataset, i.e., a conversion from the measured power to the driving rate of the system. After fitting, we confirm that the ratio of pump/probe powers for each dataset agrees with the expected ratio from lab measurements. We include as a fit parameter a scaling factor as a conversion from the equation's output signal to the measured detector signal. Finally, an offset value is included to account for any offsets in the measured results.

In addition to the nominal ground-state splitting we must account for the degeneracies of the two ground states. At the time of measuring these spectra the exact hyperfine tensor had not been determined, only that it was anisotropic. Depending on the exact form of the hyperfine tensor two doublets or a singlet-triplet were both possible in the ground state [225]. From the asymmetry between the two holes in these hole burning spectra, Fig. 6.7, we can rule out the doublet-doublet case, however, a singlet-triplet or an inverted singlet-triplet could both be possible. The fitting was repeated for both possible degeneracies. Agreement with the collected data was only possible when the three-fold degenerate level was higher in energy than the singly degenerate level. This level structure is shown in the inset of Fig. 6.7.

These fits are shown in Fig. 6.7 along with the single laser scan. In addition to the ground state degeneracies, the fits return a nominal ground state splitting of 3.85 ± 0.01 MHz, a value that was later confirmed in Refs. [108, 192]. Finally the homogeneous linewidth was determined to be 0.69 ± 0.01 MHz, only a factor of 4 from the lifetime limited linewidth of 0.17 MHz (0.20 MHz) based on the above-band excitation (resonant excitation) lifetime. As discussed in Section 2.4.2 a homogeneous linewidth equal to the lifetime limited linewidth results in indistinguishable emission

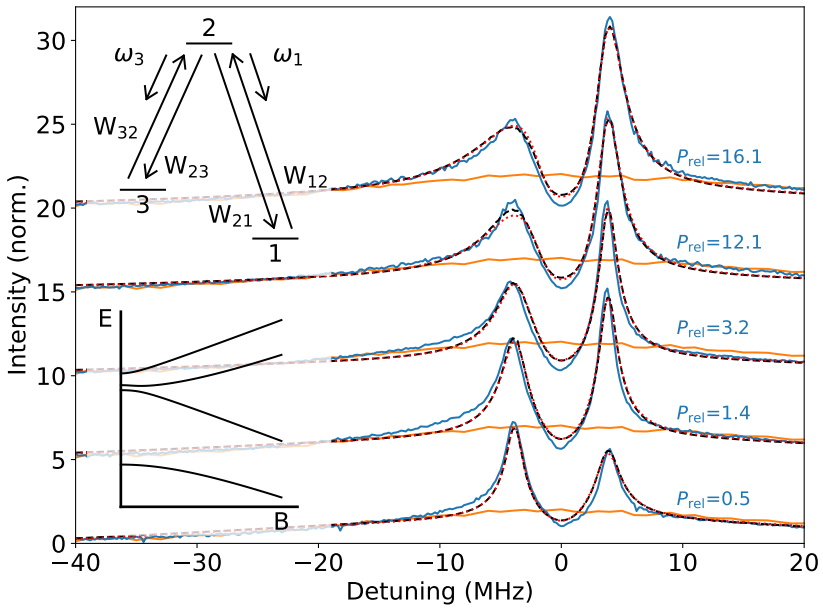

Figure 6.7: **Bulk ^{28}Si hole burning.** Hole burning spectra of a bulk ^{28}Si sample at zero field at different pump powers given by $P_{\text{rel}} = P_{\text{pump}}/P_{\text{probe}}$. A one laser scan is shown in orange. All spectra are normalized to 1 at -20 MHz detuning, far from the hole and anti-holes. Black dashed lines are a simultaneous fit with the rate equation model from Section 4.1 for an isotropic hyperfine with nominal splitting as a free parameter and rates as shown in upper inset. Red dotted lines are a simultaneous fit using the full anisotropic hyperfine as shown in the lower inset. Extracted homogeneous linewdiths are 0.69 ± 0.01 MHz and 0.43 ± 0.03 MHz respectively.

and high fidelity entanglement generation. The exact visibility achievable by this highly coherent transition will be discussed in Section 6.5.

During the writing of this thesis the nominal ground state splitting and relative degeneracies of the ground state were confirmed via ODMR measurements of the ground state at low magnetic fields (in the same manner as the $^{77}Se^{+}$ ground state was measured, Chapter 5). The hyperfine tensor was determined to be [108, 192]

$$A = \begin{bmatrix} -4.03 \pm 0.01 \text{ MHz} & 0 & 0 \\ 0 & -2.93 \pm 0.01 \text{ MHz} & 0 \\ 0 & 0 & 4.50 \pm 0.01 \text{ MHz} \end{bmatrix}. \tag{6.1}$$

This hyperfine tensor leads to a ground state with four non-degenerate levels with a ladder of splittings of 3.48, 0.235, and 0.55 MHz (see the lower inset of Fig. 6.7). This more precise ground state can be implemented in the rate equation model using the steady-state equation Eq. (4.11) and the fitting procedure repeated as above. In this case the ground state is fixed per the tensor with no free parameters. The homogeneous linewidth in this scenario is found to be 0.43 ± 0.03 MHz, only 2.5 times larger than the lifetime limited value. This fit is shown as well in Fig. 6.7. While the out-

puts of the fitting procedures are nominally the same, in the degenerate case a larger homogeneous linewidth is needed to compensate for the state splitting that is neglected.

From the linewidth versus temperature model developed in Ref. [70] a homogeneous linewidth of 0.43 ± 0.03 MHz corresponds to a temperature of ≈ 1.7 K if the zero temperature linewidth is taken to the be the lifetime limited linewidth. This is hotter than our experimental temperature of 1.4 K meaning the additional broadening is not purely a thermal effect. At 1.4 K we would expect a linewidth of 0.2 MHz in the ideal scenario, thus, ≈ 0.230 MHz of dephasing broadening is still present in the system.

6.3.3 Waveguide: At-field

We now return to the ensemble T centre waveguide sample. In addition to the zero-field waveguide hole burning presented above we can repeat the measurements in the presence of a magnetic field. Practical applications of the T centre will likely operate at an elevated magnetic field in order to have the electron spin-states optically resolved. Here we remount the waveguide sample atop a magnet (as described in Section 3.3) and align to the same waveguide device in order to begin preliminary work on the manipulation of the spin states.

In a magnetic field the ground and excited states split into four transitions A-D (see Fig. 2.20). From the permanent magnet cooled to 1 K we expect $B_0 \approx$200 mT oriented normal to the SOI wafer along $\langle 100 \rangle$. With a g-factor of 2 the ground state splits by $\Delta_{\mathrm{g}} = 6$ GHz. For this field orientation there are two orientational subsets each with a separate hole g-factor in the excited state: $g_{\mathrm{h}}^{1,2} = 0.91, 2.55$, with degeneracies 4 and 8 respectively [87]. This leads to splittings in the excited state of $\Delta_{\mathrm{e}}^{1} = 3$ GHz or $\Delta_{\mathrm{e}}^{2} = 8$ GHz. Thus we expect to have well-resolved spin-dependent transitions, relative to the long-term homogeneous linewidth ($\approx$1 GHz [87]) which is sufficient to generate hyperpolarization.

A one laser PLE spectrum compared to the unpatterned PL spectrum is shown in Fig. 6.1b. The linewidth, 39.6 ± 0.5 GHz (0.164 ± 0.002 meV), is broader than both the unpatterned material and the zero-field spectrum of the same waveguide. While the field does cause splitting, a single laser scan should not be sensitive to this splitting as the well-split lines and the slow wavelength sweep will hyperpolarize the system and not generate a PLE signal in steady state. We attribute this broadening to strain in the sample. As the magnet is housed in a pocket within the copper sample mount, nearly flush to the surface of the mount, the sample is in contact with both the copper mount and the magnet. Differential contraction of the sample mount and the magnet will force the sample to be bent about the magnet as the edges of the sample are clamped to the copper mount.

We perform steady-state hole burning on the waveguide ensemble resulting in the spectrum shown in Fig. 6.8a. Here we see yet another different form of a hole burning spectrum, there are both anti-holes split by $\sim$ 12 GHz and a hole at zero detuning. We are no longer in the fully hyperpolarization nor fully saturation regime but rather in an intermediate regime.

We investigate this saturation hole by measuring the hole linewidth as a function of pump power as before, and fit the results to Eq. (2.3). This is shown in Fig. 6.8b showing a good agreement. The

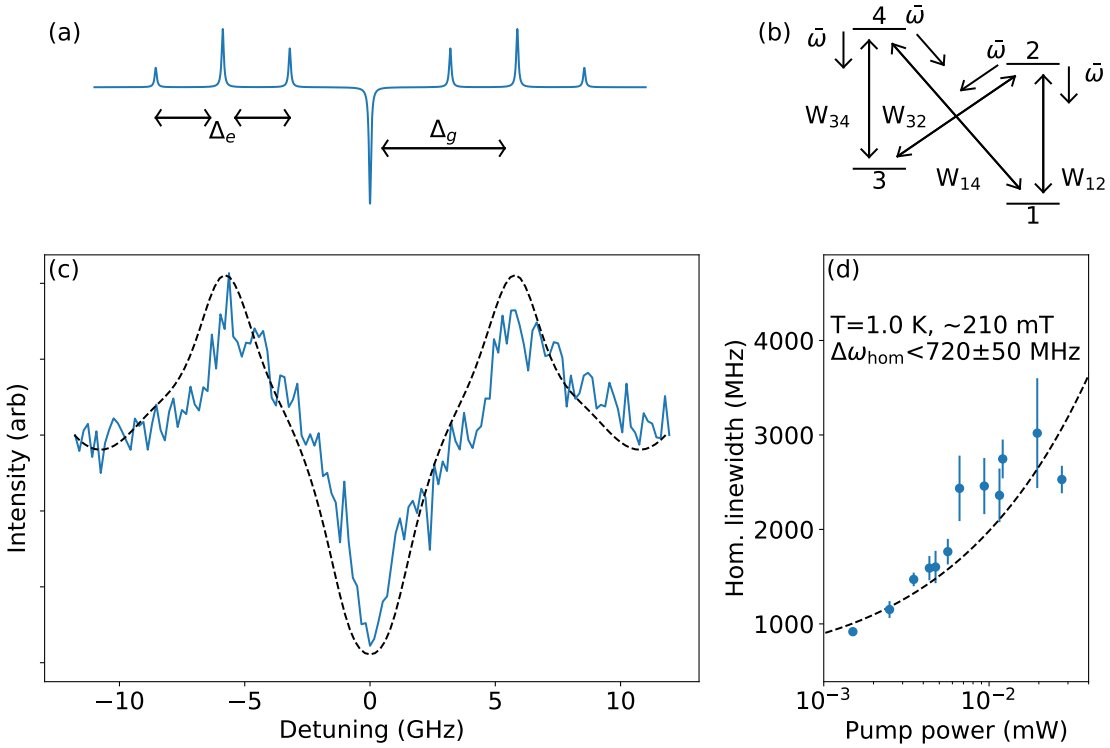

Figure 6.8: **At-field waveguide hole burning.** (a) Expected anti-hole locations relative to the hole for a T centre with $g_h = 0.91$ at 210 mT. Linewidths are made narrow for clarity. (b) Four level rate equation model showing all relevant rates. (c) A hole burning spectrum of an ensemble of T centres within a waveguide in a ∼210 mT magnetic field along the $\langle 100 \rangle$ crystal axis along with a zero parameter fit to the rate equation model (dashed). (b) Hole linewidth versus pump power fit with Eq. (2.3).

narrowest hole measured gives a homogeneous linewidth of 720 ± 50 GHz while the extrapolated low power linewidth is determined to be 590 ± 40 GHz, more than an order of magnitude larger than the zero field homogeneous linewidth. Two possible explanations are as follows: firstly, at field a higher linewidth is expected as the saturation hole is only present when driving the overlap of the two transitions. Thus, the dominant contribution to the saturation hole is from those sub-ensembles that have a large overlap, i.e., a homogeneous linewidth on the order of the B-C transitions splitting. Secondly, as the sample is expected to be strained the sensitivity of the T centres to spectral diffusion, or even the magnitude of the spectral diffusion could be larger than in the unstrained case. If this spectral diffusion were on the timescale of the excited state lifetime this would result in a larger homogeneous linewidth.

We now consider the anti-holes of the hole burning spectrum. In general, anti-holes should be present at $\pm\Delta_{\mathrm{g}}, \pm\Delta_{\mathrm{BC}} = \pm|\Delta_{\mathrm{g}} - \Delta_{\mathrm{e}}|$, and $\pm\Delta_{\mathrm{AD}} = \pm(\Delta_{\mathrm{g}} + \Delta_{\mathrm{e}})$ [106], these are shown schematically in Fig. 6.8a. We attribute the anti-holes to the ground state splitting which is confirmed by a zero parameter fit (shown in Fig. 6.8a). We use a four level system with rates as shown in the inset of Fig. 6.8a along with the nominal splittings and orientations as mentioned above. We also use the expected low power homogeneous linewidth, 590 ± 40 GHz, and the experimental laser powers scaled by the saturation power obtained from the fit to Eq. (2.3). We use the rate equation described in Section 4.1 using the four-level steady state solution Eq. (4.10).

The output of the model is normalized in the same manner as the data and plotted in dashed lines in Fig. 6.8a showing good qualitative agreement both with the anti-hole positions and with the relative ratios of anti-holes to the saturation hole. This zero parameter fit uses $B_0 = 210$ mT based on the 12 GHz anti-hole splitting and known electron g-factor of 2 [70] and is consistent with the permanent magnet used, measured to be 270 mT at room temperature and expected to be 230 mT when accounting for the spin reorientation below 135 K [198]. This zero parameter fit confirms the anti-hole splitting as primarily coming from the ground state splitting, as opposed to an excited state splitting or a combination of the two as listed above. This allows for optical control of the ground spin state which will be leveraged in the following section.

Finally, we repeated the hole burning and low power extrapolation at different wavlengths as shown in Fig. 6.9 plotted along with the one laser PLE spectrum. At lower energies, towards the nominally unshifted peak in the unpatterned material, the homogeneous linewidth gets smaller. This could indicate that the sub-ensembles at lower energy in the spectrum are less strained and thus begin to approach the unstrained homogeneous linewidth. This highlights the need for low strain mounting methods but also highlights the possibility of using strain, or perhaps electric field, to modify the T centre's sensitivity to spectral diffusion.

6.4 Waveguide spin control

Despite not having the spin states resolved within the inhomogeneous linewidth, this hole burning approach is sufficient to initialize and read-out the spin state of a sub-ensemble as was used to

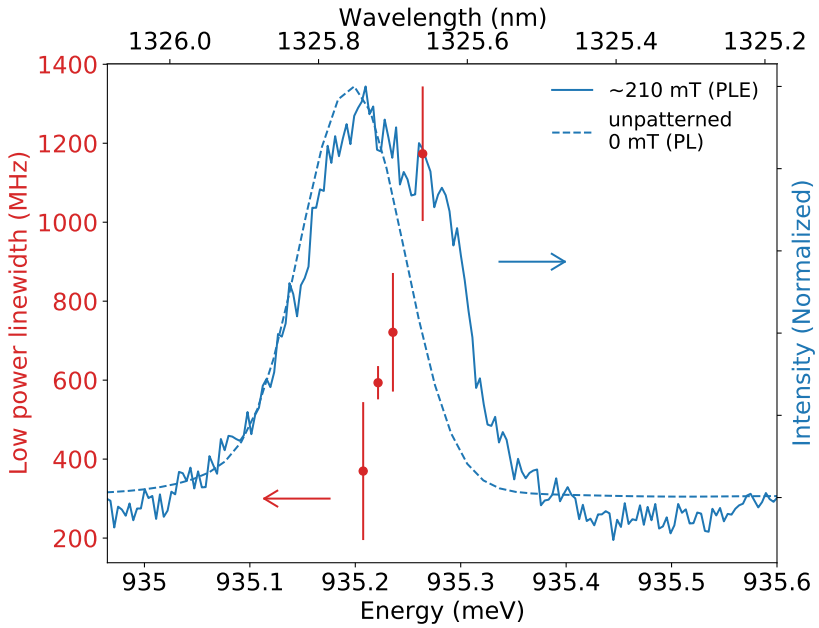

Figure 6.9: **Homogeneous linewidth versus wavelength.** Low power hole linewidth versus pump wavelength (red, left axis) along with the one laser PLE of the at field waveguide integrated ensemble and PL from the unpatterned material (blue, right axis).

great effect in the selenium chapter, Chapter 5. In the present setup there is no resonator or coil for arbitrary electron spin control. However, initialization and readout is sufficient to perform a population lifetime (T_1) measurement.

The hole burning spectrum from above is shown again in Fig. 6.10a along with insets illustrating the hyperpolarization occurring in the system and the laser energies used to address the two spin states. By pulsing a laser at one of these energies and measuring the time trace of the PLE emission a hyperpolarization transient can be seen super-imposed on the background emission in the inset of of Fig. 6.10b. The area of this transient is used as a measure of the population in the addressed spin state (see Section 2.2.3).

The full pulse sequence for the T_1 measurement is shown in the inset of Fig. 6.10b which can be split into three sections: initialization, wait, and readout. In each section a combination of 10 µs pulses are applied. The initialization pulse on λ_1 hyperpolarizes the system, the system is then allowed to evolve for the dark time, during which the system will decay into a mixed state of both spin states. Finally, the readout phase measures the remaining population in the initial state using four pulses as follows: first, a pulse on λ_2 measures the hyperpolarization transient; second, the pulse is repeated at the same wavelength which shows no hyperpolarization transient as the system is already hyperpolarized, the area between these two pulses is the 'data' transient. In order to normalize this data transient to the zero-delay transient, a reference transient is measured by re-initializing the system with the third pulse, this time on the initializing wavelength, λ_1, and immediately following with the fourth pulse, with wavelength λ_2 to measure a hyperpolarization

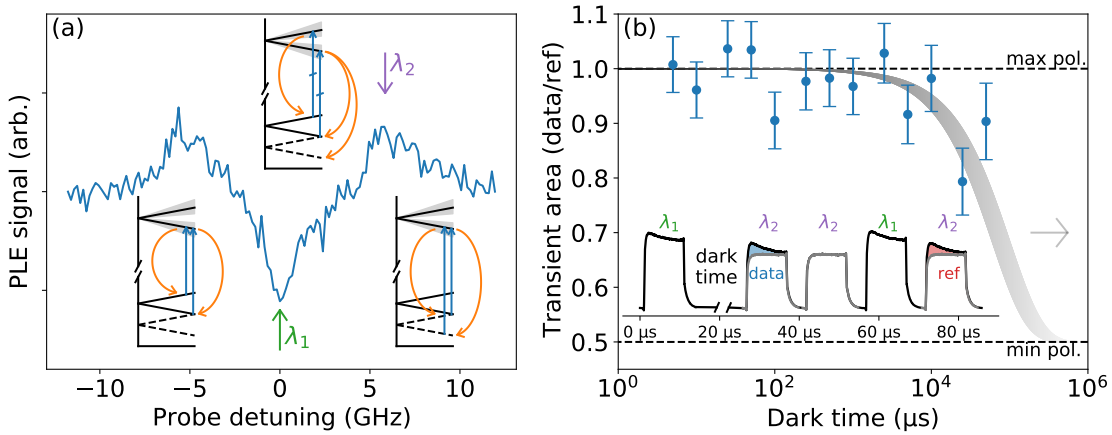

Figure 6.10: **Waveguide T_1 lifetime.** (a) Hole burning spectrum with insets showcasing the states being addressed with the pump and probe lasers (blue) and the resulting decays (orange) leading to the saturation hole and hyperpolarization or anti-holes. Solid and dashed lines illustrate different sub-ensembles addressed by the lasers. (b) T_1 population lifetime: the decay of the hyperpolarization tranisent versus dark time between intialization and readout. (Inset) Pulse sequence used to measure the transient decay, after an initialization and variable dark time the state is readout by taking the area of two subsequence pulses on λ_2 (blue), is referenced by an initialization and immediate readout with no dark time (red). The population lifetime is measured to be $> 80 \pm 20$ ms.

transient. The area between the fourth pulse and second pulse in the readout train give the 'reference' transient. By comparing the data transient to the reference transient a normalized measure of the spin population is determined, one that is free from slow drifts in the experimental conditions. These pulses, wavelengths, and transients are shown in the inset of Fig. 6.10b.

The ratio of data and reference transient areas versus dark time is shown in Fig. 6.10b showing the beginning of an exponential decay from a fully out of equilibrium state to a fully mixed state (the thermal equilibrium value). While a decay in polarization is only tentative based on the data collected we can extract a decay time to place a lower bound on the T_1 lifetime. The decay time is measured to be 80 ± 20 ms. While this is much less than measured in bulk ^{28}Si [70] (>16 s) it does place a higher bound than previous measurements on integrated T centres (1 ms [88]) due to having higher extinction optical modulation. We expect the lifetime is limited due to leaked light during the dark time resulting in a weak field driving the system to a mixed state. Attempts to repeat this measurement at lower optical power were inconclusive due to the prohibitively long times necessary for sufficient averaging at the longest dark times. Nevertheless, this experiment demonstrates spin control in an integrated waveguide format with sufficiently long T_1 times to perform MW spin control. This initialization and readout scheme will be important for future work.

6.5 Outlook

We have successfully integrated T centre ensembles into silicon networked nanophotonic devices, a crucial step toward creating a networked on-chip quantum computer or even a remote network of quantum computing arrays. The next step towards this quantum computing architecture is to integrate T centres into cavities to enhance the light-matter interaction of the spin-photon interface, the final goal being to remotely entangle physically separated T centres. As described in Section 2.4.2 the Barrett-Kok (BK) entanglement protocol is one possible remote entanglement procedure. This procedure depends crucially on the one of the key results of this work: the instantaneous homogeneous linewidth.

The fidelity of entanglement created by the BK protocol depends on the Hong-Ou-Mandel interference visibility of the two T centre photons (see Section 2.4.2). This visibility is a measure of the indistinguishability of the two photons and in general depends the wavelength detuning of the two emitters, the lifetimes, the instantaneous homogeneous linewidth (Γ_{hom}), the lifetime limited linewidth (Γ_{exc}), and the slow spectral diffusion [103]. Here we have measured for the first time the homogeneous linewidth in both an ideal case (bulk ^{28}Si) and in a more realistic, albeit unoptimized, case (integrated waveguides) and can begin to make predictions of the interference visibility possible for two T centres. We will make the assumption that the slow spectral diffusion is zero. While this has been measured in integrated devices to be on the order of GHz [87, 88], we will make the assumption that in a mature technology fast feedback will be available to compensate for slow drifts from spectral diffusion [134, 226]. Thus the visibility simplifies to $\Gamma_{\mathrm{exc}}/\Gamma_{\mathrm{hom}}$ [137].

By integrating the T centres into nanophotonic cavities, Purcell enhancement will decreases the emission lifetime thus increasing the lifetime limited linewidth as described in Eq. (2.32). The visibility as a function of Purcell enhancement is shown in Fig. 6.11. Key thresholds on the visibility are plotted as well. Firstly, we can consider the minimum visibility required to violate Bell's inequality. Consider the density matrix, ρ_f, obtained after an BK entanglement attempt, Eq. (2.35), and the expression for fidelity in terms of visibility, Eq. (2.36), we can write ρ_f as (see Eq. (2.35))

$$\rho_f = (1-V)\left(\frac{1}{2}\left|\Psi^+\right\rangle\left\langle\Psi^+\right| + \frac{1}{2}\left|\Psi^-\right\rangle\left\langle\Psi^-\right|\right) + V\left|\Psi^+\right\rangle\left\langle\Psi^+\right|. \tag{6.2}$$

Bell's inequality, specifically the CHSH inequality [107, 227]

$$\langle A_0 \otimes B_0\rangle + \langle A_0 \otimes B_1\rangle + \langle A_1 \otimes B_0\rangle - \langle A_1 \otimes B_1\rangle \leq 2, \tag{6.3}$$

where we choose as our observables

$$\begin{aligned} &A_0 = \sigma_z; A_1 = -\sigma_x; \\ &B_0 = -\frac{\sigma_x + \sigma_z}{\sqrt{2}}; B_1 = \frac{\sigma_x - \sigma_z}{\sqrt{2}}. \end{aligned} \tag{6.4}$$

For ρ_f we obtain for Bell's inequality

$$\sqrt{2}V + \sqrt{2} \leq 2. \tag{6.5}$$

which is violated for $V > \sqrt{2} - 1 \approx 0.41$, or in terms of fidelity (see Eq. (2.36)), Bell's inequality is violated for $\mathcal{F} > 1/\sqrt{2} \approx 0.71$. This threshold is plotted in Fig. 6.11.

We also consider thresholds for quantum computing. Li and Benjamin [214] outline the thresholds for errors in the entanglement channel for a distributed quantum computing (DQC) architecture with nodes of N qubits referred to as DQC-N. The T centre possesses two spins, electron and hydrogen, with up to two additional spins by incorporating carbon-13 [70]. Thus, a single T centre can play the role of a single node in DQC-2 to DQC-4. We include in Fig. 6.11 the thresholds in visibility to reach the necessary entanglement fidelities for DQC-N with the assumption of a 0.1% error probability for local operations (rotations, two-qubit gates, or measurements). The local gate error sets the required fidelities for DQC-N and is a relevant breakpoint for the implementations studied in Ref. [214].

Furthermore, as described in Eq. (2.32) the lifetime reduction for a given Purcell enhancement depends on the radiative lifetime of the coupled emitter. The exact radiative efficiency is not known but we include plots for unit radiative efficiency, a lower bound based on theoretical work, 19% [193], and a lower bound based on experimental work, 3% [88].

From the Purcell factor we can also determine the cavity Q-factor necessary from Eq. (2.31) assuming a modal volume of $\frac{1}{2}(\lambda/n)^3$. For all combinations of linewidth and radiative efficiencies we see that the Bell violation and DQC-4 thresholds are achievable with routinely available cavity parameters [60, 61, 228]. The Q-factors needed for DQC-3 and DQC-2 for the lowest measured waveguide-integrated T centres linewidths at 3% efficiency start to become prohibitively high ($Q > 10^6$). The ^{28}Si linewidth, on the otherhand, can achieve the DQC-2 bound with with modest Q-factors ($< 10^5$) for all radiative efficiencies considered.

In addition to increasing visibility the Purcell enhancement also increases the emission rate. While the base lifetime (1 μs) of the T centre is much faster than other telecommunication band single photon emitters like erbium it is quite slow compared to nominal telecommunication data transfer rates, more than GHz. For the Bell violation threshold the lifetimes are reduced to 3 ns (60 ns) for the measured (inferred low power) waveguide integrated T centres. For the ^{28}Si T centres only a small Purcell enhancement and a modest Q-factor is required to violate Bell's inequality putting the lifetime at 880 ns, although in this case further speed ups are straightforward. This puts the operation rate of a T centre based technology at 10–100 MHz. This can be further improved via, for instance, time multiplexing with additional T centres and fast switches, all straight-forward with integrated silicon photonics at telecommunication wavelengths [56].

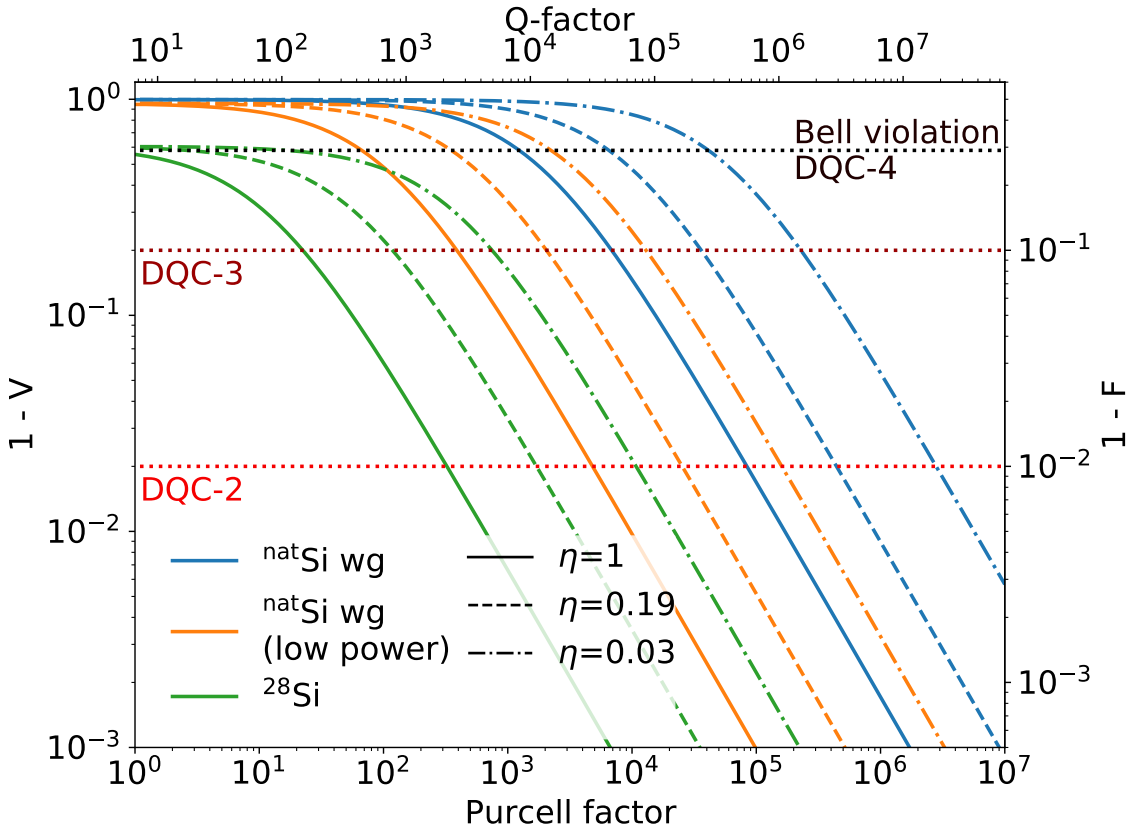

Figure 6.11: **Cavity enhanced visibilities.** One minus expected visibility (one minus fidelity, right axis) versus Purcell factor for three different homogeneous linewidth values and three different radiative efficiencies. The Q-factor axis assumes a $\frac{1}{2}(\lambda/n)^3$ modal volume. Important visibility/fidelity thresholds are labeled with horizontal lines (see text). Note that Bell violation and DQC-4 thresholds overlap with DQC-4 being slightly lower.

Chapter 7

Conclusions and future work

We have studied two silicon-based spin-photon interfaces for their capability to be incorporated into integrated silicon photonics for quantum information applications. For both the Se^+ and T centre spin-photon interfaces we progress along the research pipeline from ^{28}Si to natural silicon to an integrated platform. These crucial steps study the relevant properties in a technologically applicable environment: ground state structure and spin control/coherence properties, and optical transition linewidths and optical coherence properties. This research provides proposals and outlooks for a Se^+ or T centre based quantum technology integrated into silicon photonic cavities.

We study $^{77}Se^+$ in a natural silicon environment as a stepping stone towards a natural silicon SOI integrated platform. We map out the ground state manifold and the interactions of silicon-29 spins in the environment to generate a full description of the ground state Hamiltonian. From this we identify and evaluate clock transitions finding enhanced spin coherence times that are shown to be optimal for this isotopic environment based on simulations.

We present a proposal on the use and fabrication of a $^{77}Se^+$-^{29}Si pair into a silicon photonic cavity. By extrapolating simulations to different isotopic environments we assess the viability of this proposal as compared to a bare $^{77}Se^+$ qubit. We find that the $^{77}Se^+$-^{29}Si pair is a promising system to incorporate into a silicon photonic cavity. Not only does a $^{77}Se^+$-^{29}Si pair provide an additional qubit for broker-client protocols but it also simplifies fabrication procedures and provides enhanced spin coherence times.

Not only can the selenium centre be incorporated into silicon photonic devices as the next step of the proposed research pipeline but $^{77}Se^+$-^{29}Si pairs can also be considered as the primary candidate for integration. In an integrated environment or in a bulk sample the nuclear-like transition of the $\langle 111 \rangle_1$ ^{29}Si can be investigated, both on and off the demonstrated clock transitions.

We incorporate, for the first time, the T centre into network-compatible integrated photonic waveguides as a big step towards an integrated T centre quantum technology. We study the coherence properties of the optical transition: with hole burning measurements on an ensemble we determine bounds on the homogeneous linewidth that are an order of magnitude lower than previous bounds. Repeated measurements on other materials, including a bulk ^{28}Si sample, reveal very coherent transitions with nearly transform-limited linewidths.

With our measurements of the coherence of the T centres' optical transition we were able to establish the level of indistinguishability achievable in different environments. We forecast what cavity parameters and Purcell enhancements are necessary for different entanglement fidelity thresholds. In all cases, current fabrication procedures [60, 61] are sufficient to achieve the necessary entanglement fidelities for distributed quantum computing.

The next step for the T centre is the incorporation into photonic cavities, a comparable environment considering nanobeam cavities have similar dimensions. This work is already being undertaken [229]. Additionally, improvements need to be pursued to reduce the effects of spectral diffusion from the material or to use active feedback to improve spectral coherence. Ground state coherence may be studied with the inclusion of on-chip microwave lines to drive the spin and probe the T_2 coherence times within integrated devices. Alternate isotopic T centres can also be studied for the use of the carbon-13 spins as work towards higher node size for distributed quantum computing.

Bibliography

[1] P. (https://physics.stackexchange.com/users/24142/pulsar). "Dumbed-down explanation how scientists know the number of atoms in the universe?" eprint: https://physics.stackexchange.com/q/68346. (), [Online]. Available: https://physics.stackexchange.com/q/68346.

[2] S. Lloyd, "Computational capacity of the universe," *Physical Review Letters*, vol. 88, p. 4, 23 2002, ISSN: 10797114. DOI: 10.1103/PhysRevLett.88.237901.

[3] R. P. Feynman, "Simulating physics with computers," *International Journal of Theoretical Physics*, vol. 21, 6 1982.

[4] G. Semeghini *et al.*, "Probing topological spin liquids on a programmable quantum simulator," *Science*, vol. 374, no. 6572, pp. 1242–1247, 2021.

[5] A. Aspuru-Guzik, A. D. Dutoi, P. J. Love, and M. Head-Gordon, "Simulated quantum computation of molecular energies," *Science*, vol. 309, no. 5741, pp. 1704–1707, 2005.

[6] G. A. Quantum *et al.*, "Hartree-fock on a superconducting qubit quantum computer," *Science*, vol. 369, no. 6507, pp. 1084–1089, 2020. DOI: 10.1126/science.abb9811. eprint: https://www.science.org/doi/pdf/10.1126/science.abb9811. [Online]. Available: https://www.science.org/doi/abs/10.1126/science.abb9811.

[7] M. Reiher, N. Wiebe, K. M. Svore, D. Wecker, and M. Troyer, "Elucidating reaction mechanisms on quantum computers," *Proceedings of the National Academy of Sciences of the United States of America*, vol. 114, pp. 7555–7560, 29 Jul. 2017, ISSN: 10916490. DOI: 10.1073/pnas.1619152114.

[8] S. Jordan, *Quantum algorithm zoo*, Oct. 2022. [Online]. Available: https://quantumalgorithmzoo.org/.

[9] P. W. Shor, "Algorithms for quantum computation: Discrete logarithms and factoring," in *Proceedings 35th annual symposium on foundations of computer science*, Ieee, 1994, pp. 124–134.

[10] L. K. Grover, "A fast quantum mechanical algorithm for database search," in *Proceedings of the twenty-eighth annual ACM symposium on Theory of computing*, 1996, pp. 212–219.

[11] D. Bulger, "Quantum basin hopping with gradient-based local optimisation," *arXiv preprint quant-ph/0507193*, 2005.

[12] E. Farhi, J. Goldstone, and S. Gutmann, "A quantum approximate optimization algorithm," *arXiv preprint arXiv:1411.4028*, 2014.

[13] S. Lloyd, M. Mohseni, and P. Rebentrost, "Quantum algorithms for supervised and unsupervised machine learning," *arXiv preprint arXiv:1307.0411*, 2013.

[14] C. P. Williams, "Quantum gates," in *Explorations in Quantum Computing*. London: Springer London, 2011, pp. 51–122, ISBN: 978-1-84628-887-6. DOI: 10.1007/978-1-84628-887-6_2. [Online]. Available: https://doi.org/10.1007/978-1-84628-887-6_2.

[15] D. Aharonov, "A simple proof that toffoli and hadamard are quantum universal," *arXiv preprint quant-ph/0301040*, 2003.

[16] C. H. Bennett and G. Brassard, "Quantum cryptography: Public key distribution and coin tossing," *arXiv preprint arXiv:2003.06557*, 2020.

[17] G. Brassard, "Brief history of quantum cryptography: A personal perspective," in *IEEE Information Theory Workshop on Theory and Practice in Information-Theoretic Security, 2005.*, IEEE, 2005, pp. 19–23.

[18] N. Gisin and R. Thew, "Quantum communication," *Nature photonics*, vol. 1, no. 3, pp. 165–171, 2007.

[19] S. Muralidharan, L. Li, J. Kim, N. Lütkenhaus, M. D. Lukin, and L. Jiang, "Optimal architectures for long distance quantum communication," *Scientific Reports*, vol. 6, Feb. 2016, ISSN: 20452322. DOI: 10.1038/srep20463.

[20] D. Deutsch, A. Ekert, R. Jozsa, C. Macchiavello, S. Popescu, and A. Sanpera, "Quantum privacy amplification and the security of quantum cryptography over noisy channels," *Physical review letters*, vol. 77, no. 13, p. 2818, 1996.

[21] J. L. Park, "The concept of transition in quantum mechanics," *Foundations of Physics*, vol. 1, 1 1970.

[22] W. K. Wootters and W. H. Zurek, "A single quantum cannot be cloned," *Nature*, vol. 299, pp. 802–803, 5886 1982, ISSN: 1476-4687. DOI: 10.1038/299802a0. [Online]. Available: https://doi.org/10.1038/299802a0.

[23] J. Chow, O. Dial, and J. Gambetta, "Ibm quantum breaks the 100-qubit processor barrier," *IBM Research Blog*, 2021.

[24] *IonQ Aria*, 2023. [Online]. Available: https://ionq.com/quantum-systems/aria.

[25] *Xg series: The first comprehensive range of quantum key distribution solutions*, Apr. 2023. [Online]. Available: https://www.idquantique.com/quantum-safe-security/xg-series-qkd/.

[26] *Digital solutions: Quantum key distribution*, 2023. [Online]. Available: https://asia.toshiba.com/qkd.

[27] A. A. Houck, J. Koch, M. H. Devoret, S. M. Girvin, and R. J. Schoelkopf, "Life after charge noise: Recent results with transmon qubits," *Quantum Information Processing*, vol. 8, pp. 105–115, 2-3 Jun. 2009, ISSN: 15700755. DOI: 10.1007/s11128-009-0100-6.

[28] J. I. Cirac and P. Zoller, "Quantum computations with cold trapped ions," *Physical review letters*, vol. 74, no. 20, p. 4091, 1995.

[29] E. Knill, R. Laflamme, and G. J. Milburn, "A scheme for efficient quantum computation with linear optics," *Nature*, vol. 409, pp. 46–52, 6816 2001, ISSN: 1476-4687. DOI: 10.1038/35051009. [Online]. Available: https://doi.org/10.1038/35051009.

[30] L. M. K. Vandersypen and M. A. Eriksson, "Quantum computing with semiconductor spins," *Physics Today*, vol. 72, no. 8, pp. 38–45, Aug. 2019, ISSN: 0031-9228. DOI: 10.1063/PT.3.4270. eprint: https://pubs.aip.org/physicstoday/article-pdf/72/8/38/10122763/38_1_online.pdf. [Online]. Available: https://doi.org/10.1063/PT.3.4270.

[31] *Ibm unveils 400 qubit-plus quantum processor and next-generation ibm quantum system two*, Nov. 2022. [Online]. Available: https://newsroom.ibm.com/2022-11-09-IBM-Unveils-400-Qubit-Plus-Quantum-Processor-and-Next-Generation-IBM-Quantum-System-Two.

[32] *Aquila, our 256-qubit quantum computer*, 2023. [Online]. Available: https://www.quera.com/aquila.

[33] F. Arute *et al.*, "Quantum supremacy using a programmable superconducting processor," *Nature*, vol. 574, pp. 505–510, 7779 Oct. 2019, ISSN: 14764687. DOI: 10.1038/s41586-019-1666-5.

[34] S. Moses *et al.*, "A race track trapped-ion quantum processor," *arXiv preprint arXiv:2305.03828*, 2023.

[35] M. Roser, H. Ritchie, and E. Mathieu, *What is moore's law?* Mar. 2023. [Online]. Available: https://ourworldindata.org/moores-law.

[36] A. G. Fowler, M. Mariantoni, J. M. Martinis, and A. N. Cleland, "Surface codes: Towards practical large-scale quantum computation," *Physical Review A*, vol. 86, no. 3, p. 032 324, 2012.

[37] R. Barends *et al.*, "Coherent josephson qubit suitable for scalable quantum integrated circuits," *Physical Review Letters*, vol. 111, 8 Aug. 2013, ISSN: 00319007. DOI: 10.1103/PhysRevLett.111.080502.

[38] J. Niu *et al.*, "Low-loss interconnects for modular superconducting quantum processors," *Nature Electronics*, Mar. 2023, ISSN: 25201131. DOI: 10.1038/s41928-023-00925-z.

[39] P. Murali, D. M. Debroy, K. R. Brown, and M. Martonosi, "Architecting noisy intermediate-scale trapped ion quantum computers," in *2020 ACM/IEEE 47th Annual International Symposium on Computer Architecture (ISCA)*, IEEE, 2020, pp. 529–542.

[40] C. Monroe *et al.*, "Large-scale modular quantum-computer architecture with atomic memory and photonic interconnects," *Physical Review A - Atomic, Molecular, and Optical Physics*, vol. 89, 2 Feb. 2014, ISSN: 10502947. DOI: 10.1103/PhysRevA.89.022317.

[41] D. Awschalom *et al.*, "Development of quantum interconnects (quics) for next-generation information technologies," *PRX Quantum*, vol. 2, 1 Jan. 2021, ISSN: 26913399. DOI: 10.1103/PRXQuantum.2.017002.

[42] M. Pompili *et al.*, "Realization of a multinode quantum network of remote solid-state qubits," *Science*, vol. 372, pp. 259–264, 2021. [Online]. Available: https://www.science.org.

[43] T. Đorđević *et al.*, "Entanglement transport and a nanophotonic interface for atoms in optical tweezers," *Science*, vol. 373, no. 6562, pp. 1511–1514, 2021.

[44] D. P. DiVincenzo, "The physical implementation of quantum computation," *Fortschritte der Physik*, vol. 48, pp. 771–783, 9-11 2000, ISSN: 00158208. DOI: 10.1002/1521-3978(200009)48:9/11<771::AID-PROP771>3.0.CO;2-E.

[45] S. Storz *et al.*, "Loophole-free bell inequality violation with superconducting circuits," *Nature*, vol. 617, pp. 265–270, 7960 May 2023, ISSN: 14764687. DOI: 10.1038/s41586-023-05885-0.

[46] N. Lauk *et al.*, "Perspectives on quantum transduction," *Quantum Science and Technology*, vol. 5, 2 Mar. 2020, ISSN: 20589565. DOI: 10.1088/2058-9565/ab788a.

[47] S. Pirandola, R. Laurenza, C. Ottaviani, and L. Banchi, "Fundamental limits of repeaterless quantum communications," *Nature Communications*, vol. 8, 2017, ISSN: 20411723. DOI: 10.1038/ncomms15043.

[48] C. Jones, D. Kim, M. T. Rakher, P. G. Kwiat, and T. D. Ladd, "Design and analysis of communication protocols for quantum repeater networks," *New Journal of Physics*, vol. 18, 8 Aug. 2016, ISSN: 13672630. DOI: 10.1088/1367-2630/18/8/083015.

[49] S. Prawer and I. Aharonovich, *Quantum information processing with diamond: principles and applications*. Elsevier, 2014.

[50] D. M. Lukin *et al.*, "4h-silicon-carbide-on-insulator for integrated quantum and nonlinear photonics," *Nature Photonics*, vol. 14, pp. 330–334, 5 May 2020, ISSN: 17494893. DOI: 10.1038/s41566-019-0556-6. [Online]. Available: https://doi.org/10.1038/s41566-019-0556-6.

[51] A. Ruskuc, C. J. Wu, J. Rochman, J. Choi, and A. Faraon, "Nuclear spin-wave quantum register for a solid-state qubit," *Nature*, vol. 602, pp. 408–413, 7897 Feb. 2022, ISSN: 14764687. DOI: 10.1038/s41586-021-04293-6.

[52] T. Zhong, J. M. Kindem, E. Miyazono, and A. Faraon, "Nanophotonic coherent light-matter interfaces based on rare-earth-doped crystals," *Nature Communications*, vol. 6, Sep. 2015, ISSN: 20411723. DOI: 10.1038/ncomms9206.

[53] A. Gritsch, A. Ulanowski, and A. Reiserer, "Purcell enhancement of single-photon emitters in silicon," *Optica*, vol. 10, p. 783, 6 Jun. 2023. DOI: 10.1364/optica.486167.

[54] I. Cutress, *Intel's process roadmap to 2025: With 4nm, 3nm, 20a and 18a?!* Jul. 2021. [Online]. Available: %7Bhttps://www.anandtech.com/show/16823/intel-accelerated-offensive-process-roadmap-updates-to-10nm-7nm-4nm-3nm-20a-18a-packaging-foundry-emib-foveros%7D.

[55] A. M. Zwerver *et al.*, "Qubits made by advanced semiconductor manufacturing," *Nature Electronics*, vol. 5, pp. 184–190, 3 Mar. 2022, ISSN: 25201131. DOI: 10.1038/s41928-022-00727-9.

[56] L. Chrostowski and M. Hochberg, *Silicon Photonics Design From Devices to Systems*. Cambridge University Press, 2015. [Online]. Available: http://example.com/history_of_time.pdf.

[57] G. Z. Mashanovich, G. T. Reed, B. D. Timotijevic, and S. P. Chan, "Silicon photonic waveguides," in *Silicon Photonics*. John Wiley and Sons, Ltd, 2008, ch. 2, pp. 15–46, ISBN: 9780470994535. DOI: https://doi.org/10.1002/9780470994535.ch2. eprint: https://onlinelibrary.wiley.com/doi/pdf/10.1002/9780470994535.ch2. [Online]. Available: https://onlinelibrary.wiley.com/doi/abs/10.1002/9780470994535.ch2.

[58] Y. Wang *et al.*, "Design of broadband subwavelength grating couplers with low back reflection," *Optics Letters*, vol. 40, p. 4647, 20 Oct. 2015, ISSN: 0146-9592. DOI: 10.1364/ol.40.004647.

[59] X. Tu, C. Song, T. Huang, Z. Chen, and H. Fu, "State of the art and perspectives on silicon photonic switches," *Micromachines*, vol. 10, 1 Jan. 2019, ISSN: 2072666X. DOI: 10.3390/mi10010051.

[60] P. B. Deotare, M. W. McCutcheon, I. W. Frank, M. Khan, and M. Lončar, "High quality factor photonic crystal nanobeam cavities," *Applied Physics Letters*, vol. 94, 12 2009, ISSN: 00036951. DOI: 10.1063/1.3107263.

[61] K. Ashida *et al.*, "Ultrahigh-q photonic crystal nanocavities fabricated by cmos process technologies," *Optics Express*, vol. 25, p. 18 165, 15 Jul. 2017, ISSN: 10944087. DOI: 10.1364/oe.25.018165.

[62] M. K. Akhlaghi, E. Schelew, and J. F. Young, "Waveguide integrated superconducting single-photon detectors implemented as near-perfect absorbers of coherent radiation," *Nature Communications*, vol. 6, Sep. 2015, ISSN: 20411723. DOI: 10.1038/ncomms9233.

[63] A. M. Dibos, M. Raha, C. M. Phenicie, and J. D. Thompson, "Atomic source of single photons in the telecom band," *Physical Review Letters*, vol. 120, 24 Jun. 2018, ISSN: 10797114. DOI: 10.1103/PhysRevLett.120.243601.

[64] J. H. Kim, S. Aghaeimeibodi, C. J. Richardson, R. P. Leavitt, D. Englund, and E. Waks, "Hybrid integration of solid-state quantum emitters on a silicon photonic chip," *Nano Letters*, vol. 17, pp. 7394–7400, 12 Dec. 2017, ISSN: 15306992. DOI: 10.1021/acs.nanolett.7b03220.

[65] K. J. Morse *et al.*, "Zero-field optical magnetic resonance study of phosphorus donors in 28-silicon," *Physical Review B*, vol. 97, 11 Mar. 2018, ISSN: 24699969. DOI: 10.1103/PhysRevB.97.115205.

[66] G. Wolfowicz, C. P. Anderson, B. Diler, O. G. Poluektov, F. J. Heremans, and D. D. Awschalom, "Vanadium spin qubits as telecom quantum emitters in silicon carbide," *Science Advances*, vol. 6, 18 Apr. 2020, ISSN: 23752548. DOI: 10.1126/sciadv.aaz1192. [Online]. Available: http://advances.sciencemag.org/.

[67] K. Saeedi *et al.*, "Room-temperature quantum bit storage exceeding 39 minutes using ionized donors in silicon-28," *Science*, vol. 342, 6160 Dec. 2013. DOI: 10.1126/science.1239584. [Online]. Available: http://science.sciencemag.org/content/342/6160/830/tab-pdf.

[68] *Silicon quantum technology*, Accessed: 2023-06-21. [Online]. Available: https://www.sfu.ca/physics/siliconquantum/.

[69] K. J. Morse *et al.*, "A photonic platform for donor spin qubits in silicon," *Science advances*, vol. 3, no. 7, e1700930, 2017.

[70] L. Bergeron *et al.*, "Silicon-integrated telecommunications photon-spin interface," *PRX Quantum*, vol. 1, p. 020 301, 2 Oct. 2020. DOI: 10.1103/prxquantum.1.020301. [Online]. Available: https://journals.aps.org/prxquantum/abstract/10.1103/PRXQuantum.1.020301.

[71] V. Mazzocchi *et al.*, "99.992% 28 si cvd-grown epilayer on 300 mm substrates for large scale integration of silicon spin qubits," *Journal of Crystal Growth*, vol. 509, pp. 1–7, Mar. 2019, ISSN: 00220248. DOI: 10.1016/j.jcrysgro.2018.12.010.

[72] H. Grimmeiss, E. Janzén, and K. Larsson, "Multivalley spin splitting of 1 s states for sulfur, selenium, and tellurium donors in silicon," *Physical Review B*, vol. 25, no. 4, p. 2627, 1982.

[73] D. Karaiskaj *et al.*, "Photoluminescence of isotopically purified silicon: How sharp are bound exciton transitions?" *Physical Review Letters*, vol. 86, no. 26, p. 6010, 2001.

[74] A. Hoffmann, L. Podlowski, R. Heitz, I. Broser, and H. G. Grimmeiss, "Calorimetric absorption spectroscopy of deep donors in silicon at mk temperatures," 21st International Conference on the Physics of Semiconductors, 1992.

[75] J. Haas and B. Mizaikoff, "Advances in mid-infrared spectroscopy for chemical analysis," *Annual Review of Analytical Chemistry*, vol. 9, no. 1, pp. 45–68, 2016, PMID: 27070183. DOI: 10.1146/annurev-anchem-071015-041507. eprint: https://doi.org/10.1146/annurev-anchem-071015-041507. [Online]. Available: https://doi.org/10.1146/annurev-anchem-071015-041507.

[76] T. Hu *et al.*, "Silicon photonic platforms for mid-infrared applications," *Photon. Res.*, vol. 5, no. 5, pp. 417–430, Oct. 2017. DOI: 10.1364/PRJ.5.000417. [Online]. Available: https://opg.optica.org/prj/abstract.cfm?URI=prj-5-5-417.

[77] A. Deabreu *et al.*, "Characterization of the si: Se+ spin-photon interface," *Physical Review Applied*, vol. 11, 4 Apr. 2019, ISSN: 23317019. DOI: 10.1103/PhysRevApplied.11.044036.

[78] X. Yan, W. Asavanant, H. Kamakari, J. Wu, J. F. Young, and R. Raussendorf, "A quantum computer architecture based on silicon donor qubits coupled by photons," *Advanced Quantum Technologies*, vol. 3, p. 2 000 011, 11 Nov. 2020, ISSN: 2511-9044. DOI: 10.1002/qute.202000011. [Online]. Available: https://onlinelibrary.wiley.com/doi/10.1002/qute.202000011.

[79] A. Safonov, E. C. Lightowlers, and G. Davies, "Carbon-hydrogen deep level luminescence centre in silicon responsible for the t-line," in *Defects in Semiconductors 18*, ser. Materials Science Forum, vol. 196, Trans Tech Publications Ltd, Nov. 1995, pp. 909–914. DOI: 10.4028/www.scientific.net/MSF.196-201.909.

[80] G. Davies, "The optical properties of luminescence centres in silicon," *Physics reports.*, vol. 176, pp. 83–188, 3 1989, ISSN: 03701573.

[81] C. Beaufils *et al.*, "Optical properties of an ensemble of g-centers in silicon," *Physical Review B*, vol. 97, 3 Jan. 2018, ISSN: 24699969. DOI: 10.1103/PhysRevB.97.035303.

[82] G. Davies, E. C. Lightowlers, and Z. E. Ciechanowskat, "The 1018 mev (w or 11) vibronic band in silicon," *J. Phys. C: Solid State Phys*, vol. 20, pp. 191–205, 1987.

[83] W. Redjem *et al.*, "Single artificial atoms in silicon emitting at telecom wavelengths," *Nature Electronics*, vol. 3, pp. 738–743, 12 Dec. 2020, ISSN: 25201131. DOI: 10.1038/s41928-020-00499-0.

[84] M. Prabhu *et al.*, "Individually addressable and spectrally programmable artificial atoms in silicon photonics," *Nature Communications*, vol. 14, 1 Dec. 2023, ISSN: 20411723. DOI: 10.1038/s41467-023-37655-x.

[85] A. N. Tait *et al.*, "Microring resonator-coupled photoluminescence from silicon w centers," *JPhys Photonics*, vol. 2, 4 Jul. 2020, ISSN: 25157647. DOI: 10.1088/2515-7647/ab95f2.

[86] C. Chartrand *et al.*, "Highly enriched si 28 reveals remarkable optical linewidths and fine structure for well-known damage centers," *Physical Review B*, vol. 98, 19 Nov. 2018, ISSN: 24699969. DOI: 10.1103/PhysRevB.98.195201.

[87] E. R. MacQuarrie *et al.*, "Generating T centres in photonic silicon-on-insulator material by ion implantation," *New Journal of Physics*, vol. 23, 10 Oct. 2021, ISSN: 13672630. DOI: 10.1088/1367-2630/ac291f.

[88] D. B. Higginbottom *et al.*, "Optical observation of single spins in silicon," *Nature*, vol. 607, pp. 266–270, 7918 Jul. 2022, ISSN: 14764687. DOI: 10.1038/s41586-022-04821-y.

[89] W. Bludau, A. Onton, and W. Heinke, "Temperature dependence of the band gap of silicon," *Journal of Applied Physics*, vol. 45, pp. 1846–1848, 4 1974, ISSN: 00218979. DOI: 10.1063/1.1663501.

[90] P. T. Greenland *et al.*, "Coherent control of rydberg states in silicon," *Nature*, vol. 465, pp. 1057–1061, 7301 Jun. 2010, ISSN: 00280836. DOI: 10.1038/nature09112.

[91] B. Pajot, *Optical Absorption of Impurities and Defects in Semiconducting Crystals*. Springer, 2010. DOI: 10.1007/b135694.

[92] R. Knox, "Introduction to exciton physics," in *Collective Excitations in Solids*, Springer, 1983, pp. 183–245.

[93] B. Laurich, H. Hillmer, and A. Forchel, "Optical time-of-flight investigation of the exciton transport in silicon," *Journal of Applied Physics*, vol. 61, pp. 1480–1485, 4 1987, ISSN: 00218979. DOI: 10.1063/1.338080.

[94] R. C. Hilborn, "Einstein coefficients, cross sections, f values, dipole moments, and all that," *arXiv preprint physics/0202029*, 2002.

[95] M. L. Goldman *et al.*, "State-selective intersystem crossing in nitrogen-vacancy centers," *Physical Review B - Condensed Matter and Materials Physics*, vol. 91, 16 Apr. 2015, ISSN: 1550235X. DOI: 10.1103/PhysRevB.91.165201.

[96] W. Schmid, "Auger lifetimes for excitons bound to neutral donors and acceptors in si," *physica status solidi (b)*, vol. 84, no. 2, pp. 529–540, 1977. DOI: https://doi.org/10.1002/pssb.2220840216. eprint: https://onlinelibrary.wiley.com/doi/pdf/10.1002/pssb.2220840216. [Online]. Available: https://onlinelibrary.wiley.com/doi/abs/10.1002/pssb.2220840216.

[97] A. M. Stoneham, "Shapes of inhomogeneously broadened resonance lines in solids," *Reviews of Modern Physics*, vol. 41, pp. 82–108, 1 Jan. 1969. DOI: 10.1103/RevModPhys.41.82. [Online]. Available: https://link.aps.org/doi/10.1103/RevModPhys.41.82.

[98] M. Steger *et al.*, "High-resolution absorption spectroscopy of the deep impurities s and se in 28si revealing the 77se hyperfine splitting," *Physical Review B - Condensed Matter and Materials Physics*, vol. 80, 11 Sep. 2009, ISSN: 10980121. DOI: 10.1103/PhysRevB.80.115204.

[99] M. Steger *et al.*, "Reduction of the linewidths of deep luminescence centers in si28 reveals fingerprints of the isotope constituents," *Physical Review Letters*, vol. 100, 17 Apr. 2008, ISSN: 00319007. DOI: 10.1103/PhysRevLett.100.177402.

[100] C. P. Anderson *et al.*, "Electrical and optical control of single spins integrated in scalable semiconductor devices," *Science*, vol. 366, pp. 1255–1230, 2019. DOI: 10.1126/science.aax9406. [Online]. Available: http://science.sciencemag.org/.

[101] D. Bluvstein, Z. Zhang, and A. C. Jayich, "Identifying and mitigating charge instabilities in shallow diamond nitrogen-vacancy centers," *Physical Review Letters*, vol. 122, 7 Feb. 2019, ISSN: 10797114. DOI: 10.1103/PhysRevLett.122.076101.

[102] A. Tokmakoff, *Time-dependent quantum mechanics and spectroscopy*, Nov. 2014. [Online]. Available: https://tdqms.uchicago.edu/.

[103] B. Kambs and C. Becher, "Limitations on the indistinguishability of photons from remote solid state sources," *New Journal of Physics*, vol. 20, 11 Nov. 2018, ISSN: 13672630. DOI: 10.1088/1367-2630/aaea99.

[104] A. E. Siegman, *Lasers*. University Science Books, 1986, ISBN: 0935702113.

[105] A. Yang, M. Steger, T. Sekiguchi, M. L. Thewalt, J. W. Ager, and E. E. Haller, "Homogeneous linewidth of the 31p bound exciton transition in silicon," *Applied Physics Letters*, vol. 95, 12 2009, ISSN: 00036951. DOI: 10.1063/1.3238268.

[106] M. Nilsson, L. Rippe, S. Kröll, R. Klieber, and D. Suter, "Hole-burning techniques for isolation and study of individual hyperfine transitions in inhomogeneously broadened solids demonstrated in pr 3+:y2sio5," *Physical Review B - Condensed Matter and Materials Physics*, vol. 70, pp. 1–11, 21 2004, ISSN: 1550235X. DOI: 10.1103/PhysRevB.70.214116.

[107] M. A. Nielsen and I. L. Chuang, *Quantum Computation and Quantum Information: 10th Anniversary Edition*. Cambridge University Press, 2010. DOI: 10.1017/CBO9780511976667.

[108] N. Brunelle, "All-optical manipulation and hyperfine characterization of silicon T-centres," M.S. thesis, Simon Fraser University, 2023.

[109] D. Press, T. D. Ladd, B. Zhang, and Y. Yamamoto, "Complete quantum control of a single quantum dot spin using ultrafast optical pulses," *Nature*, vol. 456, pp. 218–221, 7219 Nov. 2008, ISSN: 14764687. DOI: 10.1038/nature07530.

[110] C. G. Yale *et al.*, "All-optical control of a solid-state spin using coherent dark states," *Proceedings of the National Academy of Sciences of the United States of America*, vol. 110, pp. 7595–7600, 19 May 2013, ISSN: 00278424. DOI: 10.1073/pnas.1305920110.

[111] L. Viola, E. Knill, and S. Lloyd, "Dynamical decoupling of open quantum systems," *Physical Review Letters*, vol. 82, no. 12, p. 2417, 1999.

[112] F. Bloch and ; E. L. Hahn, "Spin echoes," *Phys. Rev*, vol. 70, p. 297, 1946.

[113] A. Schweiger and G. Jeschke, *Principles of pulse electron paramagnetic resonance*. Oxford university press, 2001.

[114] M. E. Hayden and W. N. Hardy, "Atomic hydrogen-deuterium mixtures at 1 kelvin: Recombination rates, spin-exchange cross sections, and solvation energies," *Journal of Low Temperature Physics*, vol. 99, 5 1995.

[115] J. Baugh *et al.*, "Quantum information processing using nuclear and electron magnetic resonance: Review and prospects," *arXiv preprint arXiv:0710.1447*, 2007.

[116] K. Fujii, "Introduction to the rotating wave approximation (rwa): Two coherent oscillations," *Journal of Modern Physics*, vol. 08, pp. 2042–2058, 12 2017, ISSN: 2153-1196. DOI: 10.4236/jmp.2017.812124.

[117] G. Wolfowicz *et al.*, "Atomic clock transitions in silicon-based spin qubits," *Nature Nanotechnology*, vol. 8, pp. 561–564, 8 2013, ISSN: 1748-3395. DOI: 10.1038/nnano.2013.117. [Online]. Available: https://doi.org/10.1038/nnano.2013.117.

[118] P. C. Haljan, P. J. Lee, K. A. Brickman, M. Acton, L. Deslauriers, and C. Monroe, "Entanglement of trapped-ion clock states," *Physical Review A - Atomic, Molecular, and Optical Physics*, vol. 72, 6 2005, ISSN: 10941622. DOI: 10.1103/PhysRevA.72.062316.

[119] L. Rowan, E. Hahn, and W. Mims, "Electron-spin-echo envelope modulation," *Physical Review*, vol. 137, no. 1A, A61, 1965.

[120] R. E. Evans *et al.*, "Photon-mediated interactions between quantum emitters in a diamond nanocavity," *Science*, vol. 362, no. 6415, pp. 662–665, 2018.

[121] W. B. Gao, P. Fallahi, E. Togan, J. Miguel-Sanchez, and A. Imamoglu, "Observation of entanglement between a quantum dot spin and a single photon," *Nature*, vol. 491, pp. 426–430, 7424 Nov. 2012, ISSN: 00280836. DOI: 10.1038/nature11573.

[122] P. Lodahl *et al.*, "Chiral quantum optics," *Nature*, vol. 541, pp. 473–480, 7638 Jan. 2017, ISSN: 14764687. DOI: 10.1038/nature21037.

[123] L.-M. Duan and H. J. Kimble, "Scalable photonic quantum computation through cavity-assisted interactions," *Phys. Rev. Lett.*, vol. 92, p. 127 902, 12 Mar. 2004. DOI: 10.1103/PhysRevLett.92.127902. [Online]. Available: https://link.aps.org/doi/10.1103/PhysRevLett.92.127902.

[124] C. Cabrillo, J. I. Cirac, P. Garcia-Fernandez, and P. Zoller, "Creation of entangled states of distant atoms by interference," *Physical Review A*, vol. 59, no. 2, p. 1025, 1999.

[125] S. D. Barrett and P. Kok, "Efficient high-fidelity quantum computation using matter qubits and linear optics," *Physical Review A - Atomic, Molecular, and Optical Physics*, vol. 71, 6 Jun. 2005, ISSN: 10502947. DOI: 10.1103/PhysRevA.71.060310.

[126] Y.-F. Huang, X.-F. Ren, Y.-S. Zhang, L.-M. Duan, and G.-C. Guo, "Experimental teleportation of a quantum controlled-not gate," *Phys. Rev. Lett.*, vol. 93, p. 240 501, 24 Dec. 2004. DOI: 10.1103/PhysRevLett.93.240501. [Online]. Available: https://link.aps.org/doi/10.1103/PhysRevLett.93.240501.

[127] S. Daiss *et al.*, "A quantum-logic gate between distant quantum-network modules," *Science*, vol. 371, no. 6529, pp. 614–617, 2021. DOI: 10.1126/science.abe3150. eprint: https://www.science.org/doi/pdf/10.1126/science.abe3150. [Online]. Available: https://www.science.org/doi/abs/10.1126/science.abe3150.

[128] E. Waks and J. Vuckovic, "Dipole induced transparency in drop-filter cavity-waveguide systems," *Physical Review Letters*, vol. 96, 15 2006, ISSN: 00319007. DOI: 10.1103/PhysRevLett.96.153601.

[129] J. Kerckhoff, L. Bouten, A. Silberfarb, and H. Mabuchi, "Physical model of continuous two-qubit parity measurement in a cavity-qed network," *Physical Review A - Atomic, Molecular, and Optical Physics*, vol. 79, 2 Feb. 2009, ISSN: 10502947. DOI: 10.1103/PhysRevA.79.024305.

[130] D. Wang, "Cavity quantum electrodynamics with a single molecule: Purcell enhancement, strong coupling and single-photon nonlinearity," *Journal of Physics B: Atomic, Molecular and Optical Physics*, vol. 54, 13 Jul. 2021, ISSN: 13616455. DOI: 10.1088/1361-6455/abf6e1.

[131] A. Faraon, C. Santori, Z. Huang, V. M. Acosta, and R. G. Beausoleil, "Coupling of nitrogen-vacancy centers to photonic crystal cavities in monocrystalline diamond," *Physical Review Letters*, vol. 109, 3 Jul. 2012, ISSN: 00319007. DOI: 10.1103/PhysRevLett.109.033604.

[132] H. Bernien *et al.*, "Heralded entanglement between solid-state qubits separated by three metres," *Nature*, vol. 497, pp. 86–90, 7447 2013, ISSN: 00280836. DOI: 10.1038/nature12016.

[133] C. K. Hong, Z. Y. Ou, and L. Mandel, "Physical review letters measurement of subpicosecond time intervals between two photons by interference," *VOLUME*, vol. 59, 1987.

[134] H. Bernien, L. Childress, L. Robledo, M. Markham, D. Twitchen, and R. Hanson, "Two-photon quantum interference from separate nitrogen vacancy centers in diamond," *Physical Review Letters*, vol. 108, 4 Jan. 2012, ISSN: 00319007. DOI: 10.1103/PhysRevLett.108.043604.

[135] E. R. Schmidgall *et al.*, "Frequency control of single quantum emitters in integrated photonic circuits," *Nano Letters*, vol. 18, pp. 1175–1179, 2 Feb. 2018, ISSN: 15306992. DOI: 10.1021/acs.nanolett.7b04717.

[136] B. A. McCullian, H. F. Cheung, H. Y. Chen, and G. D. Fuchs, "Quantifying the spectral diffusion of n- v centers by symmetry," *Physical Review Applied*, vol. 18, 6 Dec. 2022, ISSN: 23317019. DOI: 10.1103/PhysRevApplied.18.064011.

[137] J. Bylander, I. Robert-Philip, and I. Abram, "Interference and correlation of two independent photons," *European Physical Journal D*, vol. 22, pp. 295–301, 2 2003, ISSN: 14346060. DOI: 10.1140/epjd/e2002-00236-6.

[138] A. Reiserer and G. Rempe, "Cavity-based quantum networks with single atoms and optical photons," *Reviews of Modern Physics*, vol. 87, pp. 1379–1418, 4 Dec. 2015, ISSN: 15390756. DOI: 10.1103/RevModPhys.87.1379.

[139] G. Zhang, Y. Cheng, J. P. Chou, and A. Gali, "Material platforms for defect qubits and single-photon emitters," *Applied Physics Reviews*, vol. 7, p. 31 308, 3 Sep. 2020, ISSN: 19319401. DOI: 10.1063/5.0006075. [Online]. Available: https://doi.org/10.1063/5.0006075.

[140] M. Kazemi, "Laser-assisted selective tuning of silicon nanophotonic structures," M.S. thesis, Simon Fraser University, 2020.

[141] G. Davies and M. F. Hamer, "Optical studies of the 1.945 ev vibronic band in diamond," *Proc. E. Soc. Lond.A*, vol. 348, pp. 285–298, 1976. [Online]. Available: https://royalsocietypublishing.org/.

[142] A. Gruber, A. Dräbenstedt, C. Tietz, L. Fleury, J. Wrachtrup, and C. V. Borczyskowski, "Scanning confocal optical microscopy and magnetic resonance on single defect centers," *Science*, vol. 276, pp. 2012–2014, 5321 Jun. 1997, ISSN: 00368075. DOI: 10.1126/science.276.5321.2012. [Online]. Available: http://science.sciencemag.org/.

[143] Collins, A. T, M. F. Thomaz, and M. I. B. Jorge, "Luminescence decay time of the 1.945 ev centre in type ib diamond," *J. Phys. C: Solid State Phys*, vol. 16, pp. 2177–2181, 1983.

[144] I. P. Radko *et al.*, "Determining the internal quantum efficiency of shallow-implanted nitrogen-vacancy defects in bulk diamond," *Optics Express*, vol. 24, p. 27 715, 24 Nov. 2016, ISSN: 10944087. DOI: 10.1364/oe.24.027715.

[145] A. Alkauskas, B. B. Buckley, D. D. Awschalom, and C. G. V. D. Walle, "First-principles theory of the luminescence lineshape for the triplet transition in diamond nv centres," *New Journal of Physics*, vol. 16, 2014, ISSN: 13672630. DOI: 10.1088/1367-2630/16/7/073026.

[146] N. Bar-Gill, L. M. Pham, A. Jarmola, D. Budker, and R. L. Walsworth, "Solid-state electronic spin coherence time approaching one second," *Nature Communications*, vol. 4, 2013, ISSN: 20411723. DOI: 10.1038/ncomms2771.

[147] M. V. G. Dutt *et al.*, "Quantum register based on individual electronic and nuclear spin qubits in diamond," *Science*, vol. 316, pp. 1312–1316, 5829 2007. DOI: 10.1126/science.1139831. [Online]. Available: https://www.science.org/doi/abs/10.1126/science.1139831.

[148] G. van de Stolpe *et al.*, "Mapping a 50-spin-qubit network through correlated sensing," *arXiv preprint arXiv:2307.06939*, 2023.

[149] L. J. Rogers *et al.*, "Multiple intrinsically identical single-photon emitters in the solid state," *Nature Communications*, vol. 5, Aug. 2014, ISSN: 20411723. DOI: 10.1038/ncomms5739.

[150] D. D. Sukachev *et al.*, "Silicon-vacancy spin qubit in diamond: A quantum memory exceeding 10 ms with single-shot state readout," *Physical Review Letters*, vol. 119, 22 Nov. 2017, ISSN: 10797114. DOI: 10.1103/PhysRevLett.119.223602.

[151] C. Bradac, W. Gao, J. Forneris, M. E. Trusheim, and I. Aharonovich, "Quantum nanophotonics with group iv defects in diamond," *Nature Communications*, vol. 10, 1 Dec. 2019, ISSN: 20411723. DOI: 10.1038/s41467-019-13332-w.

[152] D. M. Lukin, M. A. Guidry, and J. Vučković, "Silicon carbide: From abrasives to quantum photonics," *Optics and Photonics News*, vol. 32, no. 3, pp. 34–41, 2021.

[153] M. Bhatnagar and B. J. Baliga, "Comparison of 6h-sic, 3c-sic, and si for power devices," *IEEE TRANSACTIONS ON ELECTRON DEVICES*, vol. 40, 3 1993.

[154] G. Liu and B. Jacquier, *Spectroscopic properties of rare earths in optical materials*. Springer Science & Business Media, 2005, vol. 83.

[155] S. Majety, P. Saha, V. A. Norman, and M. Radulaski, "Quantum information processing with integrated silicon carbide photonics," *Journal of Applied Physics*, vol. 131, 13 Apr. 2022, ISSN: 10897550. DOI: 10.1063/5.0077045.

[156] S. Castelletto and A. Boretti, "Silicon carbide color centers for quantum applications," *JPhys Photonics*, vol. 2, 2 Mar. 2020, ISSN: 25157647. DOI: 10.1088/2515-7647/ab77a2.

[157] R. Nagy *et al.*, "Quantum properties of dichroic silicon vacancies in silicon carbide," *Physical Review Applied*, vol. 9, 3 Mar. 2018, ISSN: 23317019. DOI: 10.1103/PhysRevApplied.9.034022.

[158] N. Morioka *et al.*, "Spin-optical dynamics and quantum efficiency of a single v1 center in silicon carbide," *Phys. Rev. Appl.*, vol. 17, p. 054 005, 5 May 2022. DOI: 10.1103/PhysRevApplied.17.054005. [Online]. Available: https://link.aps.org/doi/10.1103/PhysRevApplied.17.054005.

[159] R. Nagy *et al.*, "High-fidelity spin and optical control of single silicon-vacancy centres in silicon carbide," *Nature Communications*, vol. 10, 1 Dec. 2019, ISSN: 20411723. DOI: 10.1038/s41467-019-09873-9.

[160] M. Widmann *et al.*, "Coherent control of single spins in silicon carbide at room temperature," *Nature Materials*, vol. 14, pp. 164–168, 2 2015, ISSN: 14764660. DOI: 10.1038/nmat4145.

[161] S. G. Carter, O. O. Soykal, P. Dev, S. E. Economou, and E. R. Glaser, "Spin coherence and echo modulation of the silicon vacancy in 4h-sic at room temperature," *Physical Review B - Condensed Matter and Materials Physics*, vol. 92, 16 Oct. 2015, ISSN: 1550235X. DOI: 10.1103/PhysRevB.92.161202.

[162] C. Babin *et al.*, "Fabrication and nanophotonic waveguide integration of silicon carbide colour centres with preserved spin-optical coherence," *Nature Materials*, vol. 21, pp. 67–73, 1 2022, ISSN: 1476-4660. DOI: 10.1038/s41563-021-01148-3. [Online]. Available: https://doi.org/10.1038/s41563-021-01148-3.

[163] J. L. Zhang *et al.*, "Strongly cavity-enhanced spontaneous emission from silicon-vacancy centers in diamond," *Nano Letters*, vol. 18, pp. 1360–1365, 2 Feb. 2018, ISSN: 15306992. DOI: 10.1021/acs.nanolett.7b05075.

[164] D. M. Lukin *et al.*, "Optical superradiance of a pair of color centers in an integrated silicon-carbide-on-insulator microresonator," *arXiv preprint arXiv:2202.04845*, 2022.

[165] M. Benyoucef, M. Yacob, J. Reithmaier, J. Kettler, and P. Michler, "Telecom-wavelength (1.5 μm) single-photon emission from inp-based quantum dots," *Applied Physics Letters*, vol. 103, no. 16, 2013.

[166] M. Paul *et al.*, "Single-photon emission at 1.55 μm from movpe-grown inas quantum dots on ingaas/gaas metamorphic buffers," *Applied Physics Letters*, vol. 111, no. 3, 2017.

[167] A. Musiał *et al.*, "High-purity triggered single-photon emission from symmetric single inas/inp quantum dots around the telecom c-band window," *Advanced Quantum Technologies*, vol. 3, no. 2, p. 1 900 082, 2020.

[168] P. Senellart, G. Solomon, and A. White, "High-performance semiconductor quantum-dot single-photon sources," *Nature Nanotechnology*, vol. 12, pp. 1026–1039, 11 2017, ISSN: 1748-3395. DOI: 10.1038/nnano.2017.218. [Online]. Available: https://doi.org/10.1038/nnano.2017.218.

[169] N. Somaschi *et al.*, "Near-optimal single-photon sources in the solid state," *Nature Photonics*, vol. 10, pp. 340–345, 5 May 2016, ISSN: 17494893. DOI: 10.1038/nphoton.2016.23.

[170] M. Arcari *et al.*, "Near-unity coupling efficiency of a quantum emitter to a photonic crystal waveguide," *Phys. Rev. Lett.*, vol. 113, p. 093 603, 9 Aug. 2014. DOI: 10.1103/PhysRevLett.113.093603. [Online]. Available: https://link.aps.org/doi/10.1103/PhysRevLett.113.093603.

[171] L. Zaporski *et al.*, "Ideal refocusing of an optically active spin qubit under strong hyperfine interactions," *Nature Nanotechnology*, vol. 18, pp. 257–263, 3 2023, ISSN: 1748-3395. DOI: 10.1038/s41565-022-01282-2. [Online]. Available: https://doi.org/10.1038/s41565-022-01282-2.

[172] K. De Greve *et al.*, "Quantum-dot spin–photon entanglement via frequency downconversion to telecom wavelength," *Nature*, vol. 491, no. 7424, pp. 421–425, 2012.

[173] W. Gao, P. Fallahi, E. Togan, J. Miguel-Sánchez, and A. Imamoglu, "Observation of entanglement between a quantum dot spin and a single photon," *Nature*, vol. 491, no. 7424, pp. 426–430, 2012.

[174] R. Stockill *et al.*, "Phase-tuned entangled state generation between distant spin qubits," *Physical review letters*, vol. 119, no. 1, p. 010 503, 2017.

[175] I. Schwartz *et al.*, "Deterministic generation of a cluster state of entangled photons," *Science*, vol. 354, no. 6311, pp. 434–437, 2016. DOI: 10.1126/science.aah4758. eprint: https://www.science.org/doi/pdf/10.1126/science.aah4758. [Online]. Available: https://www.science.org/doi/abs/10.1126/science.aah4758.

[176] *Quandela technology*, 2023. [Online]. Available: https://www.quandela.com/technology/.

[177] C. W. Thiel, T. Böttger, and R. Cone, "Rare-earth-doped materials for applications in quantum information storage and signal processing," *Journal of luminescence*, vol. 131, no. 3, pp. 353–361, 2011.

[178] M. Raha, S. Chen, C. M. Phenicie, S. Ourari, A. M. Dibos, and J. D. Thompson, "Optical quantum nondemolition measurement of a single rare earth ion qubit," *Nature Communications*, vol. 11, 1 Dec. 2020, ISSN: 20411723. DOI: 10.1038/s41467-020-15138-7.

[179] T. Zhong *et al.*, "Optically addressing single rare-earth ions in a nanophotonic cavity," *Physical Review Letters*, vol. 121, 18 Oct. 2018, ISSN: 10797114. DOI: 10.1103/PhysRevLett.121.183603.

[180] J. M. Kindem, A. Ruskuc, J. G. Bartholomew, J. Rochman, Y. Q. Huan, and A. Faraon, "Control and single-shot readout of an ion embedded in a nanophotonic cavity," *Nature*, vol. 580, pp. 201–204, 7802 Apr. 2020, ISSN: 14764687. DOI: 10.1038/s41586-020-2160-9.

[181] M. Zhong *et al.*, "Optically addressable nuclear spins in a solid with a six-hour coherence time," *Nature*, vol. 517, pp. 177–180, 7533 Jan. 2015, ISSN: 14764687. DOI: 10.1038/nature14025.

[182] A. Ruskuc, C.-J. Wu, J. Choi, S. Hermans, and A. Faraon, "Heralded entanglement of single rare-earth ion qubits," *Bulletin of the American Physical Society*, 2023.

[183] A. Gritsch, L. Weiss, J. Früh, S. Rinner, and A. Reiserer, "Narrow optical transitions in erbium-implanted silicon waveguides," *Physical Review X*, vol. 12, 4 Oct. 2022, ISSN: 21603308. DOI: 10.1103/PhysRevX.12.041009.

[184] I. R. Berkman *et al.*, "Observing er3+ sites in si with an in situ single-photon detector," *Physical Review Applied*, vol. 19, 1 Jan. 2023, ISSN: 23317019. DOI: 10.1103/PhysRevApplied.19.014037.

[185] A. DeAbreu, "Optical characterization of the Si:Se+ spin-photon interface," M.S. thesis, Simon Fraser University, 2018.

[186] M. Šimėnas *et al.*, "Near-surface te+ 125 spins with millisecond coherence lifetime," *Physical Review Letters*, vol. 129, 11 Sep. 2022, ISSN: 10797114. DOI: 10.1103/PhysRevLett.129.117701.

[187] P. Dean, J. Haynes, and W. Flood, "New radiative recombination processes involving neutral donors and acceptors in silicon and germanium," *Physical Review*, vol. 161, no. 3, p. 711, 1967.

[188] *Glossary: Optical communication band*, 2023. [Online]. Available: https://www.fiberlabs.com/glossary/optical-communication-band/.

[189] N. S. Minaev and A. V. Mudryi, "Thermally-induced defects in silicon containing oxygen and carbon," *physica status solidi (a)*, vol. 68, pp. 561–565, 2 Dec. 1981. [Online]. Available: https://onlinelibrary.wiley.com/doi/full/10.1002/pssa.2210680227%20papers3://publication/doi/10.1002/pssa.2210680227.

[190] E. Irion, N. Burger, K. Thonke, and R. Sauer, "The defect luminescence spectrum at 0.9351 ev in carbon-doped heat-treated or irradiated silicon," *Journal of Physics C: Solid State Physics*, vol. 18, no. 26, p. 5069, Sep. 1985. DOI: 10.1088/0022-3719/18/26/018. [Online]. Available: https://dx.doi.org/10.1088/0022-3719/18/26/018.

[191] A. Safonov, E. Lightowlers, G. Davies, P. Leary, R. Jones, and S. Öberg, "Interstitial-carbon hydrogen interaction in silicon," *Physical review letters*, vol. 77, no. 23, p. 4812, 1996.

[192] J. Kanaganayagam, "Thesis work in progress," M.S. thesis, Simon Fraser University, 2023.

[193] D. Dhaliah, Y. Xiong, A. Sipahigil, S. M. Griffin, and G. Hautier, "First-principles study of the T center in silicon," *Physical Review Materials*, vol. 6, 5 May 2022, ISSN: 24759953. DOI: 10.1103/PhysRevMaterials.6.L053201.

[194] C.-S. Kim, E. Ohta, and M. Sakata, "Electrical properties of selenium-diffused silicon," *Japanese Journal of Applied Physics*, vol. 18, no. 5, p. 909, May 1979. DOI: 10.1143/JJAP.18.909. [Online]. Available: https://dx.doi.org/10.1143/JJAP.18.909.

[195] P. Pichler, *Intrinsic point defects, impurities, and their diffusion in silicon*. Springer Science & Business Media, 2012.

[196] Z. Yu, Y. Huang, and S. Shen, "Spin-orbit splitting of the valence bands in silicon determined by means of high-resolution photoconductive spectroscopy," *Physical Review B*, vol. 39, no. 9, p. 6287, 1989.

[197] T. Richards, "Mid-ir waveguides and grating couplers for 2.7-2.9 um," M.S. thesis, Simon Fraser University, 2018.

[198] K. Tokuhara, Y. Ohtsu, F. Ono, O. Yamada, M. Sagawa, and Y. Matsuura, "Magnetization and torque measurements on nd2fe14b single crystals," *Solid State Communications*, vol. 56, pp. 333–336, 4 1985, ISSN: 0038-1098. DOI: https://doi.org/10.1016/0038-1098(85)90396-5. [Online]. Available: https://www.sciencedirect.com/science/article/pii/0038109885903965.

[199] A. DeAbreu *et al.*, "Waveguide-integrated silicon T centres," *Optics Express*, vol. 31, p. 15 045, 9 Apr. 2023, ISSN: 10944087. DOI: 10.1364/oe.482008.

[200] G. G. Devyatykh *et al.*, "High-purity single-crystal monoisotopic silicon-28 for precise determination of avogadro's number," *Doklady Chemistry*, vol. 421, pp. 157–160, 1 Jul. 2008, ISSN: 00125008. DOI: 10.1134/S001250080807001X.

[201] A. L. Stancik and E. B. Brauns, "A simple asymmetric lineshape for fitting infrared absorption spectra," *Vibrational Spectroscopy*, vol. 47, no. 1, pp. 66–69, 2008, ISSN: 0924-2031. DOI: https://doi.org/10.1016/j.vibspec.2008.02.009. [Online]. Available: https://www.sciencedirect.com/science/article/pii/S0924203108000453.

[202] G. Sallen *et al.*, "Subnanosecond spectral diffusion measurement using photon correlation," *Nature Photonics*, vol. 4, pp. 696–699, 10 Oct. 2010, ISSN: 17494885. DOI: 10.1038/nphoton.2010.174.

[203] W. Yang and R. B. Liu, "Quantum many-body theory of qubit decoherence in a finite-size spin bath," *Physical Review B - Condensed Matter and Materials Physics*, vol. 78, 8 Aug. 2008, ISSN: 10980121. DOI: 10.1103/PhysRevB.78.085315.

[204] W. Yang and R. B. Liu, "Quantum many-body theory of qubit decoherence in a finite-size spin bath. ii. ensemble dynamics," *Physical Review B - Condensed Matter and Materials Physics*, vol. 79, 11 Mar. 2009, ISSN: 10980121. DOI: 10.1103/PhysRevB.79.115320.

[205] M. Onizhuk and G. Galli, "Pycce: A python package for cluster correlation expansion simulations of spin qubit dynamics," *Advanced Theory and Simulations*, vol. 4, 11 Nov. 2021, ISSN: 25130390. DOI: 10.1002/adts.202100254.

[206] M. Onizhuk, *Pycce: A python package for cce simulations*, 2021. [Online]. Available: https://pycce.readthedocs.io/en/latest/index.html.

[207] A. Yang, M. Steger, T. Sekiguchi, M. L. W. Thewalt, I. Ager J. W., and E. E. Haller, "Homogeneous linewidth of the P31 bound exciton transition in silicon," *Applied Physics Letters*, vol. 95, no. 12, p. 122 113, Sep. 2009, ISSN: 0003-6951. DOI: 10.1063/1.3238268. eprint: https://pubs.aip.org/aip/apl/article-pdf/doi/10.1063/1.3238268/14421051/122113_1_online.pdf. [Online]. Available: https://doi.org/10.1063/1.3238268.

[208] A. Reiserer *et al.*, "Robust quantum-network memory using decoherence-protected subspaces of nuclear spins," *Physical Review X*, vol. 6, 2 2016, ISSN: 21603308. DOI: 10.1103/PhysRevX.6.021040.

[209] S. Greulich-Weber, J. R. Niklas, and J.-M. Spaeth, "Letter to the editor endor investigation of se+ in silicon," *J. Phys. C: Solid State Phys*, vol. 17, pp. 911–914, 1984.

[210] R. K. Harris, E. D. Becker, S. M. Cabral de Menezes, R. Goodfellow, and P. Granger, "Nmr nomenclature. nuclear spin properties and conventions for chemical shifts (iupac recommendations 2001)," *Pure and Applied Chemistry*, vol. 73, no. 11, pp. 1795–1818, 2001.

[211] E. V. Oort and M. Glasbeek, "Optically detected low field electron spin echo envelope modulations of fluorescent n-v centers in diamond," *Chemical Physics*, vol. 143, pp. 131–140, 1990.

[212] G. Wolfowicz *et al.*, "Quantum guidelines for solid-state spin defects," *Nature Reviews Materials*, vol. 6, pp. 906–925, 10 Oct. 2021, ISSN: 20588437. DOI: 10.1038/s41578-021-00306-y. [Online]. Available: https://www.nature.com/articles/s41578-021-00306-y.

[213] J. J. Pla *et al.*, "Coherent control of a single si 29 nuclear spin qubit," *Physical Review Letters*, vol. 113, 24 Dec. 2014, ISSN: 10797114. DOI: 10.1103/PhysRevLett.113.246801.

[214] Y. Li and S. C. Benjamin, "High threshold distributed quantum computing with three-qubit nodes," *New Journal of Physics*, vol. 14, Sep. 2012, ISSN: 13672630. DOI: 10.1088/1367-2630/14/9/093008.

[215] J. Gyulai, O. Meyer, R. D. Pashley, and J. W. Mayer, "Lattice location and dopant behavior of group ii and vi elements implanted in silicon," *Radiation Effects*, vol. 7, pp. 17–24, 1-2 1971. DOI: 10.1080/00337577108232560. [Online]. Available: https://doi.org/10.1080/00337577108232560.

[216] H. S. Wong, L. Chan, G. Samudra, and Y. C. Yeo, "Effective schottky barrier height reduction using sulfur or selenium at the nisi/n-si (100) interface for low resistance contacts," *IEEE Electron Device Letters*, vol. 28, pp. 1102–1104, 12 Dec. 2007, ISSN: 07413106. DOI: 10.1109/LED.2007.910003.

[217] D. N. Jamieson *et al.*, "Deterministic atom placement by ion implantation: Few and single atom devices for quantum computer technology," in *2016 21st International Conference on Ion Implantation Technology (IIT)*, 2016, pp. 1–6. DOI: 10.1109/IIT.2016.7882858.

[218] Y. Liu, S. Rinner, T. Remmele, O. Ernst, A. Reiserer, and T. Boeck, "28silicon-on-insulator for optically interfaced quantum emitters," *Journal of Crystal Growth*, vol. 593, Sep. 2022, ISSN: 00220248. DOI: 10.1016/j.jcrysgro.2022.126733.

[219] R. Shankar, R. Leijssen, I. Bulu, and M. Lončar, "Mid-infrared photonic crystal cavities in silicon," *Opt. Express*, vol. 19, no. 6, pp. 5579–5586, Mar. 2011. DOI: 10.1364/OE.19.005579. [Online]. Available: https://opg.optica.org/oe/abstract.cfm?URI=oe-19-6-5579.

[220] M. Prabhu, C. Errando-Herranz, L. D. Santis, I. Christen, C. Chen, and D. R. Englund, "Individually addressable artificial atoms in silicon photonics," *arXiv preprint*, pp. 1–14, 2022. [Online]. Available: http://arxiv.org/abs/2202.02342.

[221] M. Pelton, "Modified spontaneous emission in nanophotonic structures," *Nature Photonics*, vol. 9, pp. 427–435, 7 Jun. 2015, ISSN: 17494893. DOI: 10.1038/nphoton.2015.103.

[222] R. H. Dicke, "Coherence in spontaneous radiation processes," *Physical review*, vol. 93, no. 1, p. 99, 1954.

[223] D. B. Higginbottom *et al.*, "Memory and transduction prospects for silicon t center devices," *PRX Quantum*, vol. 4, no. 2, p. 020 308, 2023.

[224] A. Berthelot *et al.*, "Unconventional motional narrowing in the optical spectrum of a semiconductor quantum dot," *Nature Physics*, vol. 2, pp. 759–764, 11 2006, ISSN: 17452481. DOI: 10.1038/nphys433.

[225] J. Kanaganayagam, Personal communication, Dec. 2021.

[226] V. M. Acosta *et al.*, "Dynamic stabilization of the optical resonances of single nitrogen-vacancy centers in diamond," *Physical Review Letters*, vol. 108, 20 May 2012, ISSN: 00319007. DOI: 10.1103/PhysRevLett.108.206401.

[227] J. F. Clauser, M. A. Horne, A. Shimony, and R. A. Holt, "Proposed experiment to test local hidden-variable theories," *Phys. Rev. Lett.*, vol. 23, pp. 880–884, 15 Oct. 1969. DOI: 10.1103/PhysRevLett.23.880. [Online]. Available: https://link.aps.org/doi/10.1103/PhysRevLett.23.880.

[228] W. Xie, P. Verheyen, M. Pantouvaki, J. Van Campenhout, and D. Van Thourhout, "Efficient resonance management in ultrahigh-q 1d photonic crystal nanocavities fabricated on 300 mm soi cmos platform," *Laser & Photonics Reviews*, vol. 15, no. 2, p. 2 000 317, 2021. DOI: https://doi.org/10.1002/lpor.202000317. eprint: https://onlinelibrary.wiley.com/doi/pdf/10.1002/lpor.202000317. [Online]. Available: https://onlinelibrary.wiley.com/doi/abs/10.1002/lpor.202000317.

[229] L. Stott, “Purcell enhancement of the silicon T centre,” M.S. thesis, Simon Fraser University, 2022.

Appendix

A.1 Code

```
import matplotlib.pyplot as plt
import numpy as np
import time
from scipy.integrate import solve_ivp

class rate_equation:
    def __init__(self):
        pass

    def set_spectral_properties(self, texc, hom_lw, inhom_lw, gs_shifts,
                                es_shifts, degeneracies):
        """Set the physical properties of the measured ensemble of emitters.

        texc: excited state lifetime (in seconds)
        hom_lw: instantaneous homogeneous linewidth (in Hz)
        inhom_lw: inhomogeneous linewidth (in Hz)
        gs_shifts: array of energy shifts for the ground state levels (in Hz)
        es_shifts: array of energy shifts for the excited state levels (in Hz)
        degeneracies: array of two arrays of the degeneracies of the ground and
                                                excited states, eg [[n1, n3], [
                                                n2]]
        """
        self.texc = texc
        self.hom_lw = hom_lw
        self.inhom_lw = inhom_lw
        self.gs_shifts = gs_shifts
        self.n_gs = len(gs_shifts)
        self.es_shifts = es_shifts
        self.n_es = len(es_shifts)
        self.degeneracies = degeneracies

        assert hom_lw >= 1./2/np.pi/texc
        assert inhom_lw >= inhom_lw

    def set_time_dependent_properties(self, sd_lw, tjump, initial_state):
        """Set the properties of the measured ensemble of emitters needed for
                                                the time dependent rate
                                                equations.

        sd_lw: spectral diffusion linewidth (in Hz)
        tjump: time scale of the random jumps of the spectral diffusion (in
                                                seconds)
```

```
        initial_state: array of two arrays of the initial population
                                                distribution eg. a three level
                                                lambda system in a
            mixed state in the ground states is [[0.5, 0.5], [0]]
        """
        self.sd_lw = sd_lw
        self.tjump = tjump
        self.initial_state = [val for val in initial_state[1]] + [val for val in
                                                 initial_state[0]]
        self.jdetuning = 0
        self.tprevious = 0

    def def_steady_state(self, ss_function, indexing=1):
        """Define the steady-state solution for the population in the excited
                                                state(s) as a function of the
                                                driving
            rates W[i,j] and the spontaneous decay rates w[i].

        ss_function: a function that takes as inputs an array of driving rates
                                                and an array of decay rates. Eg.
                                                 for a
        three level lambda system the ss_function is as follows (Note that here
                                                we use an indexing starting with
                                                 one.):

        def my_ss_function(W, w):
            NSS = W[1,2]*W[3,2] / (W[1,2]*W[3,2] + W[1,2]*(W[2,3] + w[3]) + W[3,
                                                    2]*(W[2,1] + w[1]))
            return NSS

        indexing: set 0 or 1 indexing. Python is natively 0 indexing but rate
                                                equations are often 1 indexing.
                                                If set to 1
            additional rows and columns will be added to W and w to make them 1
                                                    indexing.
        """
        if indexing == 0:
            self.ss_function = ss_function
        elif indexing == 1:
            def wrapped_ss_function(Win, win):
                W = np.empty(shape=(Win.shape[0]+1, Win.shape[1]+1, Win.shape[2]
                                                        , Win.shape[3]))
                W[1:, 1:, :, :] = Win
                w = np.concatenate(([0], win))
                return ss_function(W, w)
            self.ss_function = wrapped_ss_function
        else:
            raise ValueError('indexing must be 0 or 1')

    def get_spectrum_time_dep(self, probe_ee, probe_power, pump_e, pump_power,
                              inhom_ee, dtime, integ_time, prefactor, offset,
                                                                    navg):
        """Obtain the time dependent spectrum of the defined ensemble of
                                                emitters with the given laser
                                                parameters.

        probe_ee: array of energies of the probe laser, points at which the
                                                spectrum is measured (in Hz)
```

```
        probe_power: power of the probe laser (in Hz) (1/2/texc is saturation
                                                power)
        pump_e: energy of the pump laser (in Hz), pump_e = 0 is the center of
                                                the distribution
        pump_power: power of the pump laser (in Hz) (1/2/texc is saturation
                                                power)
        inhom_ee: sample points to integrate over for each probe energy value (
                                                in Hz). This should be dense
                                                compared to the
            homogeneous linewidth and should extend beyond the limits of
                                                    probe_ee
        dtime: two tuple of times, initial and final time at which to solve the
                                                rate equation
        integ_time: time points at which to evalute rate equation, at a given
                                                probe energy the signal is
                                                integrated over
            these time points.
        prefactor: scaling factor of the resulting spectrum (useful as a fitting
                                                 parameter)
        offset: value added to the resulting spectrum (useful as a fitting
                                                parameter)
        navg: number of times to repeat the model to get an average
        """
        self.dtime = dtime
        self.integ_time = integ_time
        self.power1 = probe_power
        self.power2 = pump_power
        self.pump_e = pump_e
        self.dmatrix = None
        spectrum = np.zeros_like(probe_ee)
        dt = time.time()
        for n in range(navg):
            for i, prob_e in enumerate(probe_ee):
                spectrum[i] += self.average_over_inhom_dist(prob_e, inhom_ee)
        spectrum /= navg
        print(time.time() - dt)
        return prefactor*spectrum + offset

    def get_spectrum_steady_state(self, probe_ee, probe_power, pump_e,
                                            pump_power,
                                    inhom_ee, peak_offset, prefactor, offset):
        """Obtain the steady state spectrum of the defined ensemble of emitters
                                                with the given laser parameters.

        probe_ee: array of energies of the probe laser, points at which the
                                                spectrum is measured (in Hz)
        probe_power: power of the probe laser (in Hz) (1/2/texc is saturation
                                                power)
        pump_e: energy of the pump laser (in Hz), pump_e = 0 is the center of
                                                the distribution
        pump_power: power of the pump laser (in Hz) (1/2/texc is saturation
                                                power)
        inhom_ee: sample points to integrate over for each probe energy value (
                                                in Hz). This should be dense
                                                compared to the
            homogeneous linewidth and should extend beyond the limits of
                                                    probe_ee
```

```
        peak_offset: detuning of the pump laser from the peak of the inhom line
                                                    (in Hz).
        prefactor: scaling factor of the resulting spectrum (useful as a fitting
                                                    parameter)
        offset: value added to the resulting spectrum (useful as a fitting
                                                    parameter)
        """
        out1, out2 = np.meshgrid(probe_ee, inhom_ee, indexing='ij')
        l1_ih_ee = out1 - out2

        out1, out2 = np.meshgrid(pump_e, inhom_ee, indexing='ij')
        l2_ih_ee = out1 - out2

        W = np.empty((self.n_gs+self.n_es, self.n_gs+self.n_es,) + l1_ih_ee.
                                                    shape)
        for igs in range(self.n_gs):
            for jes in range(self.n_es):
                W[2*igs, 2*jes+1] = probe_power * self.amp_lor(l1_ih_ee +
                                                        self.gs_shifts[
                                                        self.es_shifts[
                                                        1,
                                                        0,
                                                        self.hom_lw) + \
                                    pump_power * self.amp_lor(l2_ih_ee +
                                                        self.gs_shifts[igs
                                                        self.es_shifts[jes
                                                        1,
                                                        0,
                                                        self.hom_lw)
                W[2*jes+1, 2*igs] = self.degeneracies[0][igs]/self.degeneracies[
                                                    1][jes]*W[2*igs, 2*jes+1
                                                    ]

        w = 1./self.texc

        wg = np.zeros(self.n_gs+self.n_es)
        for igs in range(self.n_gs):
            wg[2*igs] = self.degeneracies[0][igs] / np.sum(self.degeneracies[0][
                                                    :]) * w

        NSS = self.ss_function(W, wg)
```

```
        return offset + prefactor*np.trapz(self.amp_lor(inhom_ee, 1, peak_offset
                                                        , inhom_lw) * NSS, inhom_ee,
                                                        axis=-1)

    def amp_lor(self, x, a0, b0, c0):
        """Lorentzian function.

        x: list of points at which to calculate the Lorentzian
        a0: Lorentzian amplitude
        b0: centre of Lorentzian
        c0: FWHM of Lorentzian
        """
        return a0 / (1 + 4 * ((np.array(x) - b0) / c0)**2)

    def reinit(self, prob_e, inhom_offset):
        """Internal function to reinitialize the system and set the probe energy
        """
        self.prob_e = prob_e
        self.inhom_offset = inhom_offset
        self.tprevious = 0
        self.jdetuning = 0
        self.dmatrix = None

    def jump_detuning(self, t):
        """Internal function used to update the SD detuning if it's been long
                                                        enough since the last SD jump.
        """
        if t - self.tprevious > self.tjump:  # update jump detuning if it's been
                                                        long enough
            self.jdetuning = np.random.normal(loc=0, scale=self.sd_lw / 2.355)
            self.tprevious = t
        return self.jdetuning

    def build_rates(self, t):
        """Internal function to build the driving and decay rates from internal
                                                        parameters.
        """
        detuning = self.inhom_offset + self.jump_detuning(t)

        W = np.empty((self.n_gs+self.n_es, self.n_gs+self.n_es))
        for igs in range(self.n_gs):
            for jes in range(self.n_es):
                W[2*igs, 2*jes+1] = self.power1 * self.amp_lor(self.prob_e +
                                                                self.gs_shifts[
                                                                self.es_shifts[
                                                                detuning,
                                                                1,
                                                                0,
```

```
                                                    self.hom_lw) + \
                                    self.power2 * self.amp_lor(self.pump_e +
                                                    self.gs_shifts[
                                                    self.es_shifts[
                                                    detuning,
                                                    1,
                                                    0,
                                                    self.hom_lw)
            W[2*jes+1, 2*igs] = self.degeneracies[0][igs]/self.degeneracies[
                                                    1][jes]*W[2*igs, 2*jes+1
                                                    ]

    w = 1./self.texc

    wg = np.empty(self.n_gs)
    for igs in range(self.n_gs):
        wg[igs] = self.degeneracies[0][igs] / np.sum(self.degeneracies[0][:]
                                                ) * w

    return W, wg

def build_driving_matrix(self, t):
    """Internal function used to build the driving matrix at time t from
                                            internal parameters.
    """
    W, wg = self.build_rates(t)

    Mee = np.diag(np.sum(-W[1::2, 0::2] - wg, axis=1))
    Mgg = np.diag(np.sum(-W[0::2, 1::2], axis=1))
    Meg = np.empty((self.n_es, self.n_gs))
    Mge = np.empty((self.n_gs, self.n_es))

    for i in range(Meg.shape[0]):
        for j in range(Meg.shape[1]):
            Meg[i,j] = W[1::2,0::2][i,j] + wg[j]
    for i in range(Mge.shape[0]):
        for j in range(Mge.shape[1]):
            Mge[i,j] = W[0::2,1::2][i,j]

    dmatrix = np.empty((self.n_gs+self.n_es, self.n_gs+self.n_es))
    dmatrix[0:self.n_es, 0:self.n_es] = Mee
    dmatrix[self.n_es:, self.n_es:] = Mgg
    dmatrix[0:self.n_es, self.n_es:] = Meg
    dmatrix[self.n_es:, 0:self.n_es] = Mge

    self.dmatrix = dmatrix.T

    return dmatrix.T
```

```
    def driving(self, t, A):
        """Internal function for applying the driving matrix.
        """
        # check if the matrix needs to be rebuilt
        if t - self.tprevious > self.tjump or self.dmatrix is None:
            mat = self.build_driving_matrix(t)
        else:
            mat = self.dmatrix
        # print(mat)
        # print(A)
        # print(np.dot(mat, A))
        # assert False
        return np.dot(mat, A)

    def average_over_inhom_dist(self, prob_e, inhom_ee):
        """Internal function for averaging the time dependent result over the
                                                inhomogeneous linewidth
        """
        A0 = self.initial_state
        signal = np.empty(inhom_ee.size)
        for i, inhom_offset in enumerate(inhom_ee):
            self.reinit(prob_e, inhom_offset)
            driving = solve_ivp(self.driving, (self.dtime[0], self.dtime[-1]),
                                                    A0, t_eval=self.integ_time)
            # print(driving['y'])
            # assert False
            signal[i] = np.mean(driving['y'][0:self.n_es,:].flatten())
        if inhom_ee.size == 1:
            return signal
        else:
            return np.trapz(self.amp_lor(inhom_ee, 1, 0, self.inhom_lw) * signal
                                                    , inhom_ee)

if __name__ == '__main__':

    create_figure_2p8 = False
    create_figure_2p9 = False
    create_figure_4p1 = False

    if create_figure_2p8:
        # define the steady state function
        def ss_function_2_ground_1_excited(W, w):
            NSS = W[1,2]*W[3,2] / (W[1,2]*W[3,2] + W[1,2]*(W[2,3] + w[3]) + W[3,
                                                    2]*(W[2,1] + w[1]))
            return NSS

        # define the spectral properties of the ensemble
        texc = 0.940e-6
        psat = 1./texc/2
        inhom_lw = 50e6
        hom_lw = 1e6
        gs_shifts = [-5e6/2, 5e6/2]
        es_shifts = [0]
        degeneracies = [[1, 1], [2]]

        # create the rate equation instance
        rate_inst = rate_equation()
```

```
    # set the spectral properties
    rate_inst.set_spectral_properties(texc=texc,
                                      hom_lw=hom_lw,
                                      inhom_lw=inhom_lw,
                                      gs_shifts=gs_shifts,
                                      es_shifts=es_shifts,
                                      degeneracies=degeneracies)
    # set the steady state function
    rate_inst.def_steady_state(ss_function_2_ground_1_excited, indexing=1)

    # define the probe energy and inhomogeneous linewidth points to
                                            integrate over
    probe_ee = np.linspace(-1*inhom_lw, 1*inhom_lw, 301)
    inhom_ee = np.linspace(-3*inhom_lw, 3*inhom_lw, 1001)

    # obtain a one laser scan
    spectrum_1l = rate_inst.get_spectrum_steady_state(probe_ee=probe_ee,
                                                      probe_power=psat/10,
                                                      pump_e=0,
                                                      pump_power=0,
                                                      inhom_ee=inhom_ee,
                                                      peak_offset = 0,
                                                      prefactor = 1,
                                                      offset = 0)
    # obtain a two laser scan
    spectrum_2l = rate_inst.get_spectrum_steady_state(probe_ee=probe_ee,
                                                      probe_power=psat/10,
                                                      pump_e=0,
                                                      pump_power=psat/10,
                                                      inhom_ee=inhom_ee,
                                                      peak_offset = 0,
                                                      prefactor = 1,
                                                      offset = 0)

    plt.figure()
    plt.plot(probe_ee, spectrum_1l - np.min(spectrum_1l), label='probe')
    plt.plot(probe_ee, spectrum_2l - np.min(spectrum_2l), label='pump+probe'
                                                )
    plt.show()

if create_figure_2p9:
    # define the spectral properties of the ensemble
    texc = 1e-6
    psat = 1./texc/2
    hom_lw = 1e6
    inhom_lw = 50e6
    gs_split = 5e6
    gs_shifts = [-gs_split/2, gs_split/2]
    es_shifts = [0]
    hom_lw = 1e6
    degeneracies = [[1, 1], [2]]

    # create the rate equation instance
    rate_inst = rate_equation()
    # set the spectral properties
    rate_inst.set_spectral_properties(texc=texc,
                                      hom_lw=hom_lw,
                                      inhom_lw=inhom_lw,
```

```
                                        gs_shifts=gs_shifts,
                                        es_shifts=es_shifts,
                                        degeneracies=degeneracies)
        # set the properties for the time dependent evolution
        rate_inst.set_time_dependent_properties(sd_lw=0,
                                                tjump=np.inf,
                                                initial_state=[[0.5, 0.5], [0]])

        # define the probe energy and inhomogeneous linewidth points to
                                                integrate over
        # make the probed points more sparse far from the pump laser
        probe_ee = np.concatenate((np.linspace(-2*inhom_lw, -2*gs_split, 25), np
                                                .linspace(-2*gs_split, 2*
                                                gs_split, 101)))
        inhom_ee = np.arange(-4*inhom_lw, 4*inhom_lw, hom_lw/2)

        # define what time range to solve for and what time range to integrate
        # in this case the signal is the integration for the latter half of the
                                                evolution time
        dtime=[0, 40*texc]
        integ_time = np.linspace(20*texc, 40*texc, 11)

        # obtain a one laser scan
        spectrum_1l = rate_inst.get_spectrum_time_dep(probe_ee=probe_ee,
                                                      probe_power=psat/10,
                                                      pump_e=0,
                                                      pump_power=0,
                                                      inhom_ee=inhom_ee,
                                                      dtime=dtime,
                                                      integ_time=integ_time,
                                                      prefactor=1,
                                                      offset=0,
                                                      navg=1)
        # # obtain a two laser scan
        spectrum_2l = rate_inst.get_spectrum_time_dep(probe_ee=probe_ee,
                                                      probe_power=psat/10,
                                                      pump_e=0,
                                                      pump_power=psat/10,
                                                      inhom_ee=inhom_ee,
                                                      dtime=dtime,
                                                      integ_time=integ_time,
                                                      prefactor=1,
                                                      offset=0,
                                                      navg=1)

        plt.figure()
        plt.plot(probe_ee, spectrum_1l - np.min(spectrum_1l))
        plt.plot(probe_ee, spectrum_2l - np.min(spectrum_2l))

        plt.show()

    if create_figure_4p1:
        # define the spectral properties of the ensemble
        texc = 0.940e-6
        psat = 1./texc/2
        inhom_lw = 50e6
        hom_lw = 1e6
        sd_lw = 20e6
```

```
        gs_shifts = [0]
        es_shifts = [0]
        degeneracies = [[1,], [1,]]

        # create the rate equation instance
        rate_inst = rate_equation()
        # set the spectral properties
        rate_inst.set_spectral_properties(texc=texc,
                                          hom_lw=hom_lw,
                                          inhom_lw=inhom_lw,
                                          gs_shifts=gs_shifts,
                                          es_shifts=es_shifts,
                                          degeneracies=degeneracies)
        # set the properties for the time dependent evolution
        rate_inst.set_time_dependent_properties(sd_lw=sd_lw,
                                                tjump=5*texc,
                                                initial_state=[[1], [0]])

        # define the probe energy and inhomogeneous linewidth points to
                                                integrate over
        probe_ee = np.linspace(-2*sd_lw, 2*sd_lw, 501)
        inhom_ee = np.array([0])

        # define what time range to solve for and what time range to integrate
        # in this case the signal is the integration for the latter half of the
                                                evolution time
        dtime=[0, 40*texc]
        integ_time = np.linspace(20*texc, 40*texc, 11)

        # obtain a one laser scan
        spectrum_1l = rate_inst.get_spectrum_time_dep(probe_ee=probe_ee,
                                                      probe_power=psat/5,
                                                      pump_e=0,
                                                      pump_power=0,
                                                      inhom_ee=inhom_ee,
                                                      dtime=dtime,
                                                      integ_time=integ_time,
                                                      prefactor=1,
                                                      offset=0,
                                                      navg=500)
        # obtain a two laser scan
        spectrum_2l = rate_inst.get_spectrum_time_dep(probe_ee=probe_ee,
                                                      probe_power=psat/5,
                                                      pump_e=0,
                                                      pump_power=psat,
                                                      inhom_ee=inhom_ee,
                                                      dtime=dtime,
                                                      integ_time=integ_time,
                                                      prefactor=1,
                                                      offset=0,
                                                      navg=500)

        plt.figure()
        plt.plot(probe_ee, spectrum_1l - np.min(spectrum_1l))
        plt.plot(probe_ee, spectrum_2l - np.min(spectrum_2l))

        plt.show()
```